Principles

Optical Quantum Computers

A Route to Practical Continuous Variable Quantum Information Processing

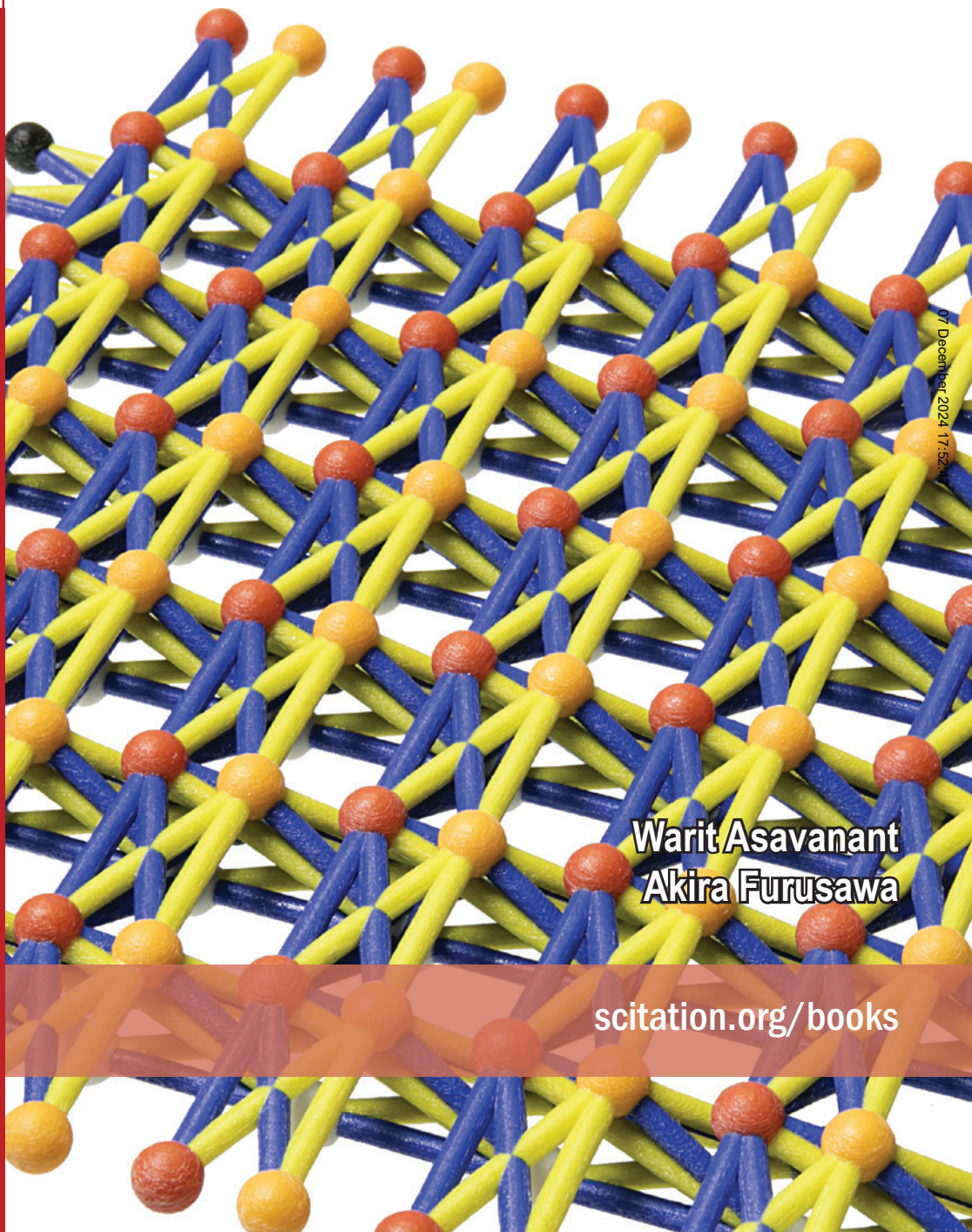

07 December 2024 17:52:

Warit Asavanant
Akira Furusawa

scitation.org/books

AIP Publishing

Optical Quantum Computers

07 December 2024 17:52:47

07 December 2024 17:52:47

scitation.org/books

Optical Quantum Computers

A Route to Practical Continuous Variable Quantum Information Processing

Warit Asavanant
The University of Tokyo, Bunkyo-ku, Tokyo 113-8654, Japan

Akira Furusawa
The University of Tokyo, Bunkyo-ku, Tokyo 113-8654, Japan
RIKEN Center for Quantum Computing, Wako, Saitama 351-0198, Japan

07 December 2024 17:52:47

AIP Publishing Books
A publication of AIP Publishing
Melville, New York

Copyright © 2022 AIP Publishing LLC
All rights reserved. No part of this publication may be reproduced, stored in a retrieval system, or transmitted, in any form or by any means, electronic, mechanical, photocopying, recording or otherwise, except as permitted by law.

To obtain permission to reuse material from this title, contact AIP Publishing at rights@aip.org. Additional rights and permissions information is available at: https://publishing.aip.org/resources/researchers/rights-and-permissions/permissions/.

First edition, published 2022.

Library of Congress Control Number: 2021947655

ISBN: 978-0-7354-2404-3 (Softcover)
ISBN: 978-0-7354-2407-4 (Online)
ISBN: 978-0-7354-2405-0 (ePub)
ISBN: 978-0-7354-2406-7 (ePDF)

Set in 10/13pt MinionPro by Nova Techset Private Limited, Bengaluru & Chennai, India, and bound by The Sheridan Group, USA

The publisher and authors cannot guarantee the accuracy of this work. Readers of scientific texts should not rely on any third-party text, or the statements and conclusions embodied in such work, without independently confirming hypotheses, factual statements, and conclusions. The publisher does not endorse organizations, institutions, or companies that may be referenced herein.

Published by AIP Publishing
1305 Walt Whitman Road, Suite 300, Melville, NY 11747-4300, USA

07 December 2024 17:52:47

PREFACE

This book was written during difficult times, that is, when the global COVID-19 pandemic was at its peak. First, we pay our condolences to those families whose members have died because of COVID. We believe that with the resilience and constant development of science and technology, humanity can be saved from pandemics such as these and progress toward a bright future.

Quantum computation is expected to increase computational power and speed, which will greatly benefit society. When we ponder about this, it is quite fascinating how we are no longer simply giving explanations for quantum phenomena but are now able to control the quantum system for our benefits and needs. Among many systems, the optical system is one of the most promising and unique systems. Nowadays, telecommunications is largely supported by optical communications, allowing us to connect with people across the globe. Similarly, many unique features of optical quantum computation stem from the fact that the optical system is a propagating wave, while most physical systems for realizing qubits are based on stationary systems. In this book, we will discuss these fascinating developments in optical quantum computation with a focus on the continuous-variable approach. We hope that readers will enjoy reading this book as much as we enjoyed writing it.

Without the help and support of many people, we would not have been able to write this book. In particular, we would like to thank all members, students, and staff of the Furusawa–Yoshikawa Laboratory at the University of Tokyo. Being surrounded by bright minds has allowed us to constantly broaden our horizons and deepen our understanding of quantum computation. Also, many of the experimental data presented in this book are taken from our students, as also the representations of the current developments in optical quantum computation. We hope that after reading this book, readers will feel satisfied that we have conveyed the essence of optical quantum computation that we have painstakingly studied over the years.

07 December 2024 17:52:47

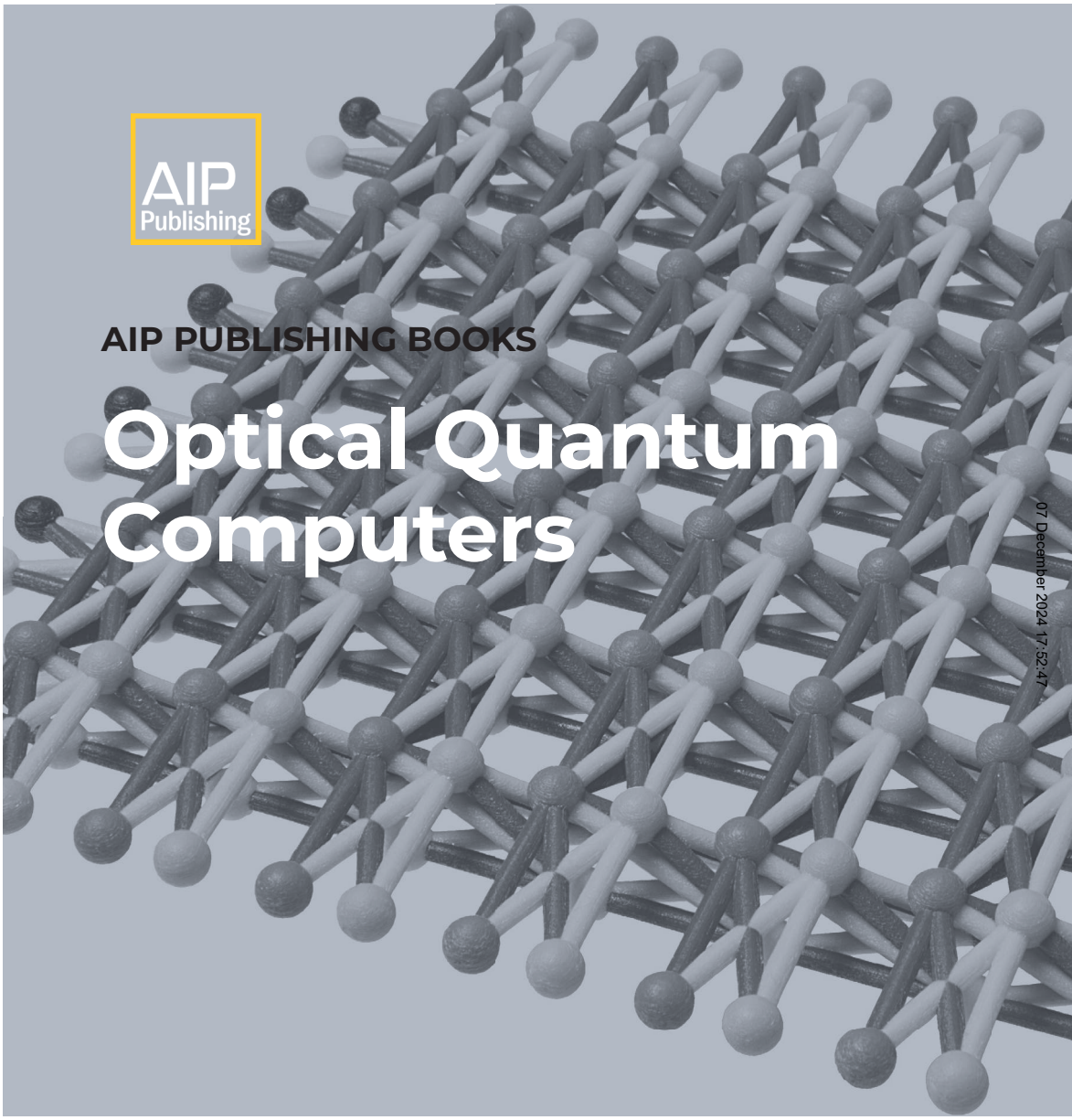

07 December 2024 17:52:47

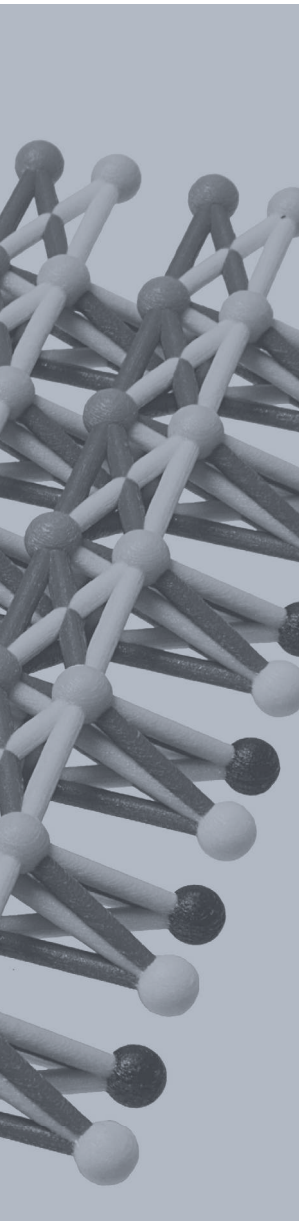

TABLE OF CONTENTS

Chapter 1 Introduction 1-1

1.1 Brief Introduction to Quantum Computation 1-1

1.2 Qubits (Discrete Variables) and Modes (Continuous Variables) 1-2

1.3 Building an Optical Quantum Computer 1-6

1.4 About this Book 1-10

References 1-11

Chapter 2 Quantum Optics 2-1

2.1 Revision of Quantum Mechanics 2-1

2.2 Brief Review of Classical Electromagnetism 2-7

2.3 Quantization of the Electromagnetic Fields 2-9

2.4 Basic Quantum States and Their Representations 2-15

2.5 Quantum Operations and Universality 2-33

2.6 Homodyne Measurement 2-44

2.7 Fock Basis Measurement 2-45

2.8 Quantum Entanglement 2-48

References 2-55

Chapter 3 Quantum Teleportation and Measurement-Based Quantum Computation 3-1

3.1 Quantum Teleportation Protocol 3-1

3.2 Measurement-Based Quantum Computation 3-7

References 3-24

Chapter 4 Quantum Computation in Time Domain 4-1

4.1 Encoding Information in a Wave Packet 4-1

4.2 Time-Domain-Multiplexed Cluster States 4-6

4.3 Loop-Based Time-Domain Quantum Computation 4-16

07 December 2024 17:52:47

4.4 Quantum Operations on the Wave Packet Mode 4-17
4.5 Other Multiplexing Methods 4-20
References 4-21

Chapter 5 Non-Gaussian Quantum States 5-1
5.1 Introduction 5-1
5.2 Heralding Generation of Non-Gaussian States 5-2
5.3 Generation of Superposition of Fock States 5-7
5.4 Photon Subtraction and Cat State 5-16
References 5-21

Chapter 6 Quantum Error Correction in Continuous-Variable System 6-1
6.1 "Analog" Quantum Computer and Fault Tolerance 6-1
6.2 Examples of Logical Qubits in the CV Optical System 6-5
6.3 Gottesman–Kitaev–Preskill Qubit 6-8
6.4 Analog Information in CV Quantum Error Correction 6-18
References 6-20

Chapter 7 Integrated Optics for Quantum Computer 7-1
7.1 Moving from Table-Top to Integrated Optics 7-1
7.2 Interferometer 7-3
7.3 Optical Delay Line 7-5
7.4 Single-Photon Source 7-5
7.5 Squeezed-Light Source 7-7
7.6 Photon Detectors 7-8
7.7 Homodyne Measurement 7-9
7.8 Feedforward Operation 7-9
References 7-11

07 December 2024 17:52:47

Chapter 8 Conclusion and Future Perspective 8-1

8.1 From Qubit to Continuous Variable to Logical Qubit 8-1

8.2 The Next Steps 8-2

8.3 Final Remarks 8-4

References 8-4

Appendix A: Miscellaneous Calculations A-1

A.1 Derivation of the Heisenberg Picture Time Evolution of $\hat{A}$ and $\hat{\Pi}$ A-1

A.2 Hamiltonian of the Monochromatic Mode A-3

A.3 Evolution of Operators and Baker–Campbell–Hausdorff Formula A-5

A.4 Proof of the Overcompleteness of the Coherent States A-6

A.5 Mathematical Treatment of an Optical Parametric Oscillator A-7

A.6 Multimode Wigner Function and Analysis of Quantum teleportation A-11

A.7 Wigner Functions of GKP Qubits A-14

References A-18

Appendix B: Experimental Methods in Quantum Optics Experiments B-1

B.1 Gaussian Beam B-1

B.2 Optical Cavity B-2

B.3 Phase Locking of the Interferometer B-8

B.4 Feedforward and Cancellation B-10

References B-11

Index I-1

07 December 2024 17:52:47

07 December 2024 17:52:47

CHAPTER

1 INTRODUCTION

1.1 BRIEF INTRODUCTION TO QUANTUM COMPUTATION

Before the beginning of the twentieth century, Newtonian mechanics and Maxwell's electromagnetic theory laid the foundations of physics and formed a perspective about how the physical world works. No one could have predicted that, now in the twenty-first century, our basic stances and understanding of the physical world have to be updated and replaced by Einstein's relativity theory and quantum mechanics. One of the reasons that both relativity theory and quantum mechanics took a while to be discovered is that their effects are barely visible in the usual daily-lives level; relativistic effects are dominant when objects move with speeds that are comparable to the speed of light, and quantum effects are visible only for microscopic objects. After its discovery, quantum mechanics has been used to predict and explain many microscopic systems. A famous example is the energy level of a hydrogen atom, which has now become a standard problem of discussion in undergraduate quantum mechanic courses.

As classical mechanics and electromagnetic theory are not only useful for describing natural phenomena, quantum mechanics also has applications beyond just describing the microscopic system. In his paper in 1982, Richard Feynman pointed out that currently used computers (which we will call classical computers) cannot be used to efficiently simulate a quantum system, and a computational system based on quantum mechanics (a quantum computer) might perform such tasks (Feynman, 1982). Quantum computers gained even more attention when Peter Shor showed that factorization, a task that could not be efficiently solved with a classical computer, could be easily solved with a quantum computer (Shor, 1999). Since then, research studies in quantum computation have been increasing more than ever before, and there are already many impressive results such as Google's demonstration of the so-called quantum supremacy (Arute *et al.*, 2019). There is no doubt that we are now progressing from describing a quantum object to controling and engineering a quantum system. We can expect that the developments in quantum technologies will change the landscape of the world as we know it, similar to how classical physics brought about the Industrial Revolution.

Quantum computers are fundamentally different from classical computers. Although this statement might seem like a tautology as these two computers operate using different physics, their differences are much deeper and irreconcilable as these two theories are based on different frameworks. In classical physics, we assume that with or without measurements, the objects of our interest possess all physical quantities (such as positions, velocities, and so on) and that physical laws dictate changes in those

07 December 2024 17:52:47

https://doi.org/10.1063/9780735424074_001 1-1

Optical Quantum Computers: A Route to Practical Continuous Variable Quantum Information Processing, W. Asavanant and A. Furusawa
© 2022 AIP Publishing, published by AIP Publishing

quantities. As such, if we know the physical quantities of all particles in the universe, classical physics would be able to completely predict the time evolution of the whole universe. This argument, famously known as Laplace's demon, stresses the determinacy of classical physics. In quantum mechanics, however, prior to measurements, one cannot assume the values of the physical quantities. This is not a mere lack of knowledge but is fundamental to quantum mechanics; quantum mechanics can only predict the probability of the outcome when the physical quantities are measured (this interpretation is also known as the Copenhagen interpretation), and even then, there are limitations to how "certain" physical quantities can be (the famous Heisenberg uncertainty principle). Moreover, quantum mechanics also predict a type of correlation between physical quantities, which seems to defy locality, a principle on which classical physics is based. This correlation is called quantum entanglement. Currently, quantum mechanics is widely accepted as a standard physics theory that forms our view of the world, and quantum technologies and computations are being developed by combining quantum mechanics with engineering techniques. In the past, however, quantum mechanics was controversial as it contradicted with classical physics, which was a well-established and widely accepted theory. There were also many famous quotes (Einstein's "God does not play with dice") and papers (Einstein's paper trying to refute quantum mechanics based on the existence of entanglement; Einstein *et al.*, 1935) trying to disprove quantum mechanics. An irony is that one of the most important types of quantum entanglement, Einstein–Podolsky–Rosen (EPR) states, is named after the authors of the paper who tried to claim that quantum mechanics is incomplete.

Nevertheless, our understanding of quantum mechanics and quantum systems is far from complete, and research studies in quantum information and computation can help deepen and broaden our perspective in addition to the prospective real-world applications. Although the ultimate goal, the realization of a quantum computer, is an important objective, we must not forget that the journey itself is also equally important. In that sense, quantum computation is a unique field of research where both experiments and theories are being simultaneously developed and contribute to each others' developments. Another important feature is that there are so many physical systems that are being developed as physical platforms for quantum computation: superconducting systems, trapped-ion systems, optical systems, silicon-based systems, to name a few. Each system has its own pros and cons and takes very different approaches toward the same goal of realizing a full-fledged quantum computer. As such, although we now do have some rough ideas on the requirements of the actual quantum computer, it is still too early to say what the actual quantum computer would look like.

1.2 QUBITS (DISCRETE VARIABLES) AND MODES (CONTINUOUS VARIABLES)

In classical information processing, information is encoded using binary bits (or simply bits) that take the value 0 or 1. The computations are then implemented by doing gates on these bits. Figure 1.1 shows a NOT gate and a NAND gate, which are elementary gates for classical computation. A NOT

07 December 2024 17:52:47

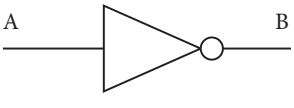

A	B
0	1
1	0

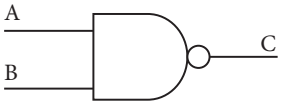

A	B	C
0	0	1
1	0	1
0	1	1
1	1	0

FIG. 1.1
Basic logic gates in a classical digital computer: NOT gate (left) and NAND gate (right).

gate simply flips the bit values from 0 to 1 and vice versa. A NAND gate gives 0 when both bits are 1, otherwise it gives 1 as outputs. These kinds of gates are also called logical gates or Boolean gates, as 0 and 1 can also be considered as "true" and "false" in logical operations. Note that for a classical digital computer, with only NAND gates, all logical operations can be implemented, which means that the NAND gate is a *universal gate* for classical digital computers. Computers are now inseparable parts of our daily life to the point that we do not think much about it, but from the information processing point of view, using binary bits is not a trivial decision; why not use decimal numbers? The reason behind this lies in a rather physical point of view. The development of transistors, which is in a way a binary switch, and their capability for large-scale integration indeed make binary bit a compelling approach. Moreover, when we consider errors and noises, classical binary bits are very robust as we can easily "digitize" information by looking at whether the signals (usually voltage of the transistors) are above a certain threshold.

In quantum computation, we can also adopt a similar approach. We can consider a system with two levels $|0\rangle$ and $|1\rangle$ and encode information in quantum states that has the form

$$|\psi\rangle = \alpha\,|0\rangle + \beta\,|1\rangle, \tag{1.1}$$

where the coefficients α and β are complex numbers and $|\psi\rangle$ is called a qubit. Then, quantum information processing is just simply how we transform these coefficients. Note, however, that although $|\psi\rangle$ is in general a superposition of $|0\rangle$ and $|1\rangle$, when we do the measurement, we would get either 0 or 1 as the measurement result. Quantum computation deals with how we manipulate the probability distributions so that we can easily and quickly obtain the calculation results. Quantum information processing using the approach explained here is called *qubit-based* or *discrete-variable (DV)* quantum computation. Qubit-based quantum computation is currently the mainstream method used by almost everyone, such as Google and IBM, and the notable physical platform for this method is superconducting qubits and trapped-ion systems.

Although qubits are the major approach to quantum computation, when we think about it, it is actually quite peculiar. Unlike the widely celebrated transistor in classical computation, most of the naturally occurring atomic or matter-based systems are not two-level systems, and we actually have to engineer

07 December 2024 17:52:47

and somehow isolate their energy levels to use them as qubits. For the photonic system, many degrees of freedom such as polarization can be used as qubits as they are genuinely two-level systems, but they entail different problems, which we will see in Sec. 1.3. Moreover, although the measurement results, which are classical information, are binary in nature, the "actual" quantum parts that are encoded in α and β are continuous, which means that it is not certain how analogous can DV quantum computation be to the classical digital computation.

Quantum mechanics is originally formulated using the wave function $\psi(x)$ of a continuous-value parameter x. This means that, instead of qubits, we can consider encoding the information in the form

$$|\psi\rangle = \int_{-\infty}^{\infty} \mathrm{d}x\, \psi(x)\, |x\rangle. \tag{1.2}$$

This x could be a parameter such as the position of a particle or, as we will see in this book, an amplitude of a component of the electromagnetic field. Then, instead of qubit-based quantum computation, we can also think of quantum computation where our physical quantities take continuous values instead of binary values. This paradigm is called *continuous-variable* quantum computation, and the smallest unit of the information is called *mode* or *qumode*. CV quantum computation, in a sense, encompasses DV quantum computation, as the Hilbert space of DV quantum computation is a subspace of CV quantum computation. In CV quantum computation, instead of the two parameters α and β, we manipulate the wave function $\psi(x)$. Unlike DV quantum computation, the measurement results in CV quantum computation take continuous values.

Another interesting aspect of CV quantum computation is that in addition to the continuous-valued parameter x, the quantum state can be equivalently written as

$$|\psi\rangle = \sum_{n=0}^{\infty} c_n\, |n\rangle, \tag{1.3}$$

where n are integers. As a physical example, in optical systems, this n can be considered a photon number. Therefore, in the CV system, we can think of quantum states and measurements using either continuous parameters x or discrete (but not binary) values n. This interplay between continuous and discrete aspect is the strength of CV quantum computation, allowing us to take advantage of both approaches (this methodology in CV quantum computation is sometimes also called "hybrid quantum computation"). The relationship between DV and CV quantum computation is somewhat analogous to the wave-particle duality. For the optical system, depending on how we approach the system, we can describe and measure quantum states using either amplitude of the electric fields x (wave picture) or photon number n (particle picture), and these two pictures are complementary to each other.

Figure 1.2 shows an olden-day classical digital and analog computer. When we consider the modern-day classical computer, all are digital; we do not see any analog computer around. However, when we think about all the physical quantities such as electrical current, voltage, temperature, mass, etc., almost every one of these are analog in nature. Therefore, it is quite an interesting question why computations

07 December 2024 17:52:47

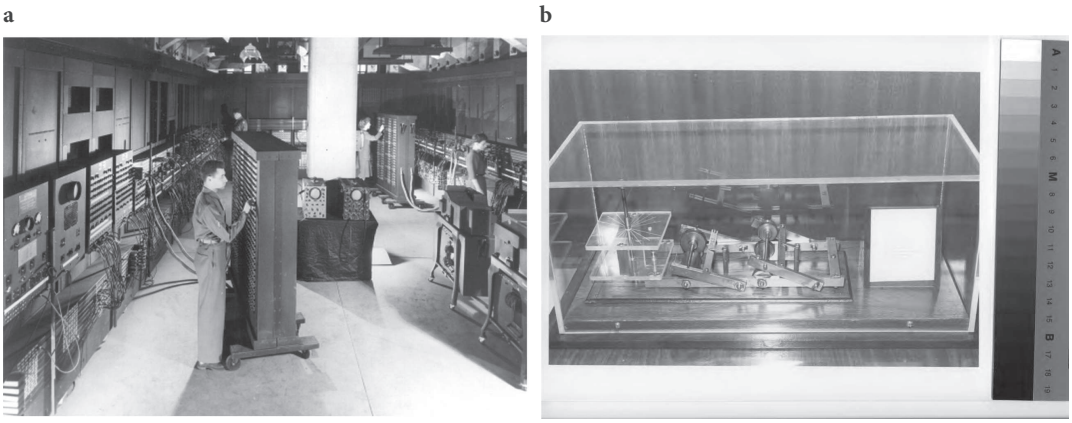

FIG. 1.2
Early classical digital computer and analog computer. (a) ENIAC, an electronic digital computer developed in 1946. From https://library.artstor.org/public/SS7732016_7732016_12329971). (b) FERMIAC, a type of analog computer. Courtesy of the Computer History Museum.

07 December 2024 17:52:47

are digital. Historically, computers using an analog system have also been developed. Then, when and why did the analog computer become obsolete? Compared with digital information, it is very difficult to faithfully copy and process analog information due to the fact that infinite precisions are required for extracting analog information. Moreover, due to the birth of the transistor, the integration of the digital classical computer became possible, which greatly accelerated the development of the digital computer and rendered the analog computer obsolete.

At this point, some readers may already become skeptical that, if the analog classical computers are, eventually, obsolete, then is there any point in studying the CV quantum computer whose measurement results are analog? We do ensure the reader, however, that the CV quantum computer is an important approach toward information processing. This is because by using a quantum system, we can "digitize" CV quantum information and achieve fault tolerance. By the end of this book, we believe that the readers would be convinced that CV quantum computation is promising and has several advantages over DV quantum computation in many aspects.

We need to emphasize again that the readers should never directly associate DV quantum computation with the classical digital computer and CV quantum computation with the classical analog computer, as this analogy is inaccurate. Although the measurement results in DV and CV are discrete and continuous values, respectively, the parameters that govern the quantum states [α and β for DV and $\psi(x)$ for CV] in both approaches take continuous values. In this sense, manipulations of quantum states, and thus quantum computations, in both DV and CV resemble the classical analog computer more than the digital computer. As such, unless one changes the quantum states slowly and adiabatically, the realisitic

quantum computer will always involve errors, making quantum error corrections necessary, regardless of whether the measurement results are digital or analog.

Another important point that we should mention here is regarding the fluctuation of the physical quantities. In the CV system, the physical quantity x and its conjugate p (for example, a position and a momentum of a particle) satisfy the Heisenberg uncertainty principle and always have finite fluctuations. This property also appears in the phase space representations of CV quantum states (called Wigner functions, which we will go into detail in the next chapter) that always have a finite width and are not infinitely sharp. When CV systems are compared with DV systems, there are sometimes misconceptions that this uncertainty is unique to CV systems as the measurement results in DV systems are binary. We have to stress that this is not true and that the uncertainty principle also holds for the observables in DV as well. The source of this misconception might stem from the fact that the visualization of the quantum states of qubits are points on the Bloch sphere that do not explicitly show fluctuations in the observables. Nevertheless, quantum fluctuations are the fundamental properties of both CV and DV quantum systems, and we ask the readers not to get confused between the concepts of quantum fluctuations, quantum error corrections, and the analog and digital nature of the measurement results when comparing CV and DV quantum computations.

07 December 2024 17:52:47

1.3 BUILDING AN OPTICAL QUANTUM COMPUTER

1.3.1 Optical classical computer

Before research studies in quantum computation can flourish, there is now a situation where optical classical computers are being widely researched and are expected to be a next generation computer, surpassing classical computers based on transistors. As we all know, research studies have not yet achieved any breakthrough, and we are now still using transistor-based computers. Reminiscing the difficulties related to the optical classical computer is important if we are to realize optical quantum computers.

As the digital computer uses transistors as its main components, we could think of trying to make an optical transistor, a component that, depending on the injected optical power, gives out a beam with different, ideally digital, optical power. Such components, however, would require very high nonlinearity, which is currently not available. While it is possible to increase the nonlinearity by using a very short pulse, the propagation of such a pulse is greatly affected by the dispersion of the optical fiber, making the option not so viable. The requirements of high nonlinearity and the dispersion of the fiber would eventually limit the speed of the optical classical computer.

Another implementation of the optical classical computer is based on the imaging technique. We can consider an optical image on a two-dimensional plane. By passing this image through filters and optical components such as lenses, we can transform the image and, thus, implement computation. This allows computation on bivariate functions and is expected to be useful for applications such as pattern

recognition. This kind of computation utilizes Fourier transform and is an interplay between the spatial domain and the spatial frequency domain. From certain aspects, this is relatable to CV quantum computation where computations also take place in the phase space.

The main limitation of the optical classical computer (and the analog classical computer in general) is that faithful copying of the analog information and error corrections is highly difficult, if at all possible. However, as we will see in this book, for CV optical quantum computation, it is possible to digitize the phase space that allows fault-tolerant quantum computation.

1.3.2 Photonic qubits and optical modes

There are two main approaches in the research of the quantum computer using the optical system: photonic qubits (DV) and optical modes (CV). Optical systems in general have many distinctive features; thanks to their large energy scale, optical quantum computation can be implemented at room temperature and atmospheric pressure. Moreover, the optical quantum system is highly compatible with telecommunication, making it currently the only promising candidate when considering applications such as quantum communication and quantum network. Although both photonic qubits and optical modes share these properties, we shall see that they have many physical differences. Do note that throughout this textbook when we consider the optical quantum computer, we are considering propagating electromagnetic waves. They are also candidates for quantum computers that are based on the standing wave such as the cavity quantum electrodynamics system or microwave cavity. Although these systems have high nonlinearity that can be used for quantum computation, we will see that the propagating wave system is more suitable when considering scalability.

In the photonic-qubit approach, single photons are used as qubits and information is encoded using certain degrees of freedom of the photon. As one example, we can consider a state where there is a photon as $|1\rangle$ and the state without a photon as $|0\rangle$. We can also consider using the polarization degree of freedom to encode the information: P-polarization as $|0\rangle$ and S-polarization as $|1\rangle$. There are also many other methods such as encoding using the arrival time of the single photon (time-bin qubits), encoding with the spatial mode (dual-rail qubits), and encoding with the frequency mode. Although there are subtle differences between each encoding, all photonic qubits suffer from a similar limitation: many operations and measurements are probabilistic in nature.

As an example of quantum protocols using photonic qubits, let us consider quantum teleportation, a protocol to send an unknown quantum state using quantum entanglements and classical communications. Quantum teleportation was realized in the photonic system by Zeilinger's group in 1997 (Bouwmeester *et al.*, 1997). However, in that experiment, quantum teleportation had a success probability of only 1/4. This success probability means that three out of four times, we would fail to send the quantum state using the photonic teleportation system. Moreover, as the physical process used in generating the quantum entanglement generally generates multiple photons outside of the photonic qubit space (this process is called parametric down conversion and is also an important process in

07 December 2024 17:52:47

CV quantum computation), the detection of the output state is necessary to eliminate the possibility of multiple photons. Braunstein and Kimble pointed this out in their correspondence to Zeilinger's work, calling this teleportation *a posteriori* teleportation, a quantum teleportation, in which certain measurement results of the output states are required to show the success of the teleportation (Braunstein and Kimble, 1998).

Later, it was shown by Knill *et al.* that even with the probabilistic overhead, single photon sources, linear optics (such as beamsplitters that are basically just coated plates of glass), and single photon detectors, universal quantum computation can be realized with the photonic system (Knill *et al.*, 2001). This scheme is called the KLM scheme and is one of the main approaches for quantum computation with photonic qubits. Although the KLM scheme does remove the theoretical hurdles regarding the probabilistic overhead, it does not in any way remove the experimental hurdle. Let us say if a certain operation has a success probability of p ($p < 1$), then if we try to repeat it n times, the total success rate would be p^n, which decreases exponentially. As the generation of a single photon is mostly probabilistic, the success rates and, subsequently, the event rates of quantum computation using photonic qubits are very low. Although there are efforts to increase these rates, with regard to technology, it is very challenging. Thus, while there are various advantages, photonic systems are still far from producing realistic success rates and clock frequencies for actual quantum computing.

One might be tempted to argue that for quantum algorithms that give an exponential speed up, a quantum computer with a very slow clock frequency might still provide some uses since clock frequency affects only the scaling factors when considering the total computational time. This, however, is not true from both an experimental and realistic point of view. For many real-life problems, not only should the quantum algorithms be better than, or at least equal to, the classical ones but also they should be able to do computation within a realistic and necessary time frame. A good example of this is if we want to use the quantum computer to optimize the flow of traffic on city streets, just being able to overpower classical machines at the large-scale asymptotic limit is not enough; we need to do the optimization and get the results quickly enough so that the computation results can actually be used.

For CV optical quantum computation, instead of photonic qubits, the smallest unit is an optical mode, also simply called mode. Mode is one of the central and important concepts in CV optical quantum computers and will be explained in detail in Chap. 2. For readers who are familiar with the classical coupled harmonic oscillator, the optical mode in quantum computation is similar to that of the eigenmode of the classical system. This picture, however, might be confusing for those with a basic background in quantum mechanics. The standard quantum mechanics courses refer to photon as a particle, and the oscillatory mode of a single particle does not seem to make any sense. We will see in this book, however, that if we do not consider light as a photon but as a radiation field, the concept of mode, in fact, becomes a natural concept. The amplitudes of the optical modes (also called quadrature), which take continuous values, are then used to encode information in CV optical quantum computation.

07 December 2024 17:52:47

In the CV system, quantum computation works when the distributions of the values of the quadratures are changed. These transformations can be separated into two types: linear (Gaussian) transformations and nonlinear (non-Gaussian) transformations. Although we will go into the details in the next chapter, linear transformations can be implemented deterministically and all of them have already been demonstrated. On the other hand, the nonlinear transformation or the non-Gaussian transformation has not yet been realized. A direct realization of the non-Gaussian transformation requires very high nonlinearity, which is not available in the conventional optical medium. We will see in this book, however, that by applying the CV quantum teleportation technique, even such a non-Gaussian transformation can be realized in a deterministic fashion. This determinism of the operations is one of the distinct advantages of the CV system over that of the photonic qubits. As an example of this, the CV quantum teleportation is deterministic and always succeeds. This has been first demonstrated by Kimble's group (Furusawa *et al.*, 1998) and since then have been researched extensively. Therefore, CV optical quantum computation can utilize all advantages of the optical systems over other physical systems without having to resort to probabilistic operations.

In the previous paragraph, we briefly mentioned CV quantum teleportation. Many readers might already be familiar with the term quantum teleportation and imagine it as a process where quantum states are transferred. Here, we will briefly explain quantum teleportation and how it forms the heart of CV quantum computation. Figure 1.3 shows a conceptual diagram of quantum teleportation, which consists of three components: sharing of quantum entanglement (red), bell measurement (green), and feedforward operations (blue). At the beginning of quantum teleportation, quantum entanglement is shared between two parties (we will follow the tradition and call them Alice and Bob). Then, Alice takes a quantum state to be delivered to Bob, combines it with one of the parties of the quantum entanglement, and performs a measurement, which is called the Bell measurement, on it. The results of the measurement will be random, and the quantum states of the other party of the entanglement at Bob will depend on the measurement results. However, by conveying the measurement results to Bob and implementing operations (called feedforward operations) on another party, this randomness can be removed and the quantum state of Bob is the same as the input state of Alice. At a first glance, quantum teleportation seems to be a boring protocol that can only send the input state. However, by modifying the quantum entanglement and Bell measurement, it is possible to realize quantum computation. This approach is called measurement-based quantum computation (MBQC) (Raussendorf and Briegel, 2001; and Menicucci *et al.*, 2006).

In addition to the deterministic operations, CV optical quantum teleportation has many advantages over most of the physical systems. In the CV optical system, quantum entanglement can be easily and deterministically generated and CV Bell measurements can be implemented with high efficiency. Therefore, rather than the conventional gate model/circuit model that matter-based qubits use, it is more natural to consider CV quantum computation using quantum teleportation. In other words, it is not an exaggeration to say that quantum teleportation is the foundation of CV quantum computation.

07 December 2024 17:52:47

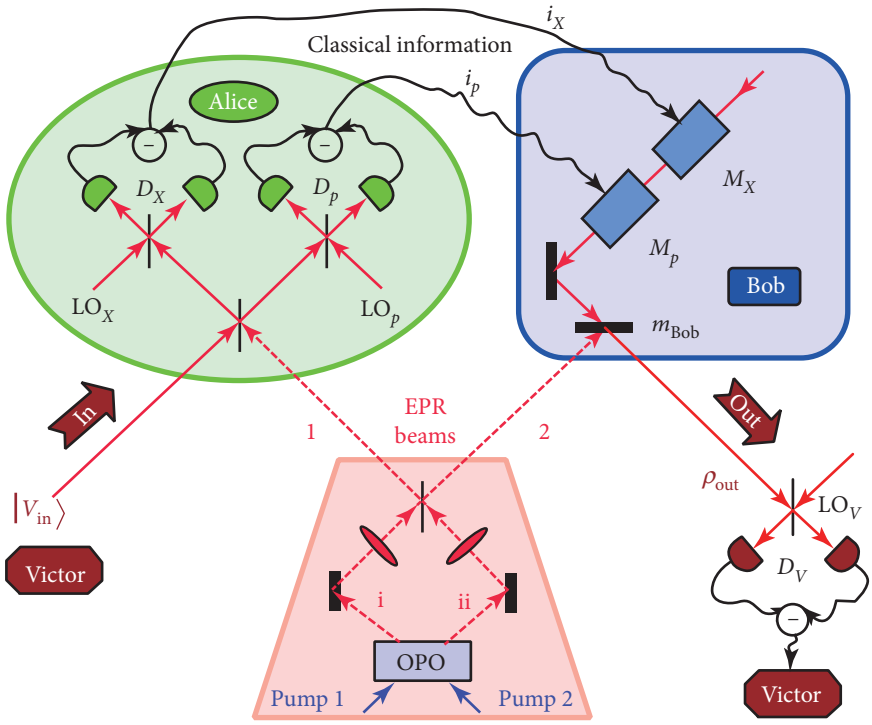

FIG. 1.3
Schematic diagram of CV quantum teleportation. Reprinted with permission from Furusawa, A. *et al.*, Sciences **282**(5389), 706–709 (1998). Copyright 1998 Journal Science.

1.4 ABOUT THIS BOOK

This book explains CV quantum computation based on optical systems. While the subject itself is very broad, making it difficult to cover in a single book, we place two main areas of focus in this book. First, rather than a standard model of quantum computation using the circuit model, we focus on the computational model called measurement-based quantum computation (MBQC). Although the circuit model and MBQC are theoretically equivalent, as we will see throughout this book, MBQC provides many advantages over the circuit model, especially in CV systems. One of the ways to think about this is that MBQC is actually an application of quantum teleportation protocol that can be efficiently implemented on CV optical systems. The second focus is the time domain methodology. As the optical system is rich in its degrees of freedom, there are many different ways to encode and process the

07 December 2024 17:52:47

information. Here, we will be focusing on the time-domain multiplexing methodology, whose many components have been experimentally demonstrated by our group. Time-domain multiplexing is a promising route toward large-scale CV optical quantum computation, and we believe that many of its concepts will be useful for physical systems, such as CV and DV.

This book is oriented toward university students and researchers with a background in physics. Although we try to keep this book a self-contained one, we do expect that the readers have a basic knowledge in undergraduate-level mathematics and quantum mechanics. However, basic knowledge in conventional DV quantum computation usually covered in an undergraduate quantum information course is not assumed, although readers with an understanding of DV quantum information might appreciate the differences between CV and DV quantum information more. Many parts of the book are dedicated to showcase the experimental CV quantum computation experiment in optical systems, and some basic experimental techniques are also covered in more detail in the Appendix for readers who want to research on CV optical quantum computation.

For further reading in quantum optics, we recommend U. Leonhardt's *Essential Quantum Optics* and W. P. Schleich's *Quantum Optics in Phase Space for Quantum Optics*. For readers with interest in quantum optic experiments, H.-A. Bachor and T. C. Ralph's *A Guide to Experiments in Quantum Optics* and A. Furusawa and P. van Loock's *Quantum Teleportation and Entanglement* might be good choices. R. Ukai's *Multi-Step Multi-Input One-Way Quantum Information Processing with Spatial and Temporal Modes of Light* might also be of interest as an additional reading for those who are interested in CV measurement-based quantum computation and the time-domain multiplexing method. For a background in DV quantum computation, the standard *Quantum Computation and Quantum Information* by M. A. Nielsen and I. L. Chuang would be a good choice.

07 December 2024 17:52:47

REFERENCES

Arute, F., Arya, K., Babbush, R., Bacon, D., Bardin, J. C., and Barends, R., "Quantum supremacy using a programmable superconducting processor," Nature **574**(7779), 505–510 (2019).

Bouwmeester, D., Pan, J. W., Mattle, K., Eibl, M., Weinfurter, H., and Zeilinger, A., "Experimental quantum teleportation," Nature **390**(6660), 575–579 (1997).

Braunstein, S. L. and Kimble, H. J., "*A posteriori* teleportation," Nature **394**(6696), 840–841 (1998).

Einstein, A., Podolsky, B., and Rosen, N., "Can quantum-mechanical description of physical reality be considered complete?," Phys. Rev. **47**, 777–780 (1935).

Feynman, R. P., "Simulating physics with computers," Int. J. Theor. Phys. **21**(6), 467–488 (1982).

Furusawa, A., Sørensen, J. L., Braunstein, S. L., Fuchs, C. A., Kimble, H. J., and Polzik, E. S., "Unconditional quantum teleportation," Sciences **282**(5389), 706–709 (1998).

Knill, E., Laflamme, R., and Milburn, G. J., "A scheme for efficient quantum computation with linear optics," Nature **409**(6816), 46–52 (2001).

Menicucci, N. C., van Loock, P., Gu, M., Weedbrook, C., Ralph, T. C., and Nielsen, M. A., "Universal quantum computation with continuous-variable cluster states," Phys. Rev. Lett. **97**, 110501 (2006).

Raussendorf, R. and Briegel, H. J., "A one-way quantum computer," Phys. Rev. Lett. **86**, 5188–5191 (2001).

Shor, P. W., "Polynomial-time algorithms for prime factorization and discrete logarithms on a quantum computer," SIAM Rev. **41**(2), 303–332 (1999).

07 December 2024 17:52:47

CHAPTER

2 QUANTUM OPTICS

2.1 REVISION OF QUANTUM MECHANICS

2.1.1 Schrödinger picture and Heisenberg picture

In basic quantum mechanics, we always start from Schrödinger's equation,

$$i\hbar\frac{\mathrm{d}}{\mathrm{d}t}|\psi\rangle = \hat{H}|\psi\rangle, \tag{2.1}$$

where $\hat{H}$ is the Hamiltonian of the system. From this equation, we can determine the state vector (or ket vector) $|\psi(t)\rangle$ as a function of time. The basic postulations of quantum mechanics then let us calculate the probability of the measurement results on the physical quantities from this ket vector.

In a special case where $\hat{H}$ is time independent, $|\psi(t)\rangle$ can be written as

$$|\psi(t)\rangle = \hat{U}(t)|\psi(t=0)\rangle, \tag{2.2}$$

$$\hat{U}(t) = \exp\left(-i\frac{\hat{H}}{\hbar}t\right). \tag{2.3}$$

A physical quantity can be expressed using a Hermite operator $\hat{A}$. For a Hermite operator $\hat{A}$ with discrete eigenvalues whose eigenvalues and corresponding eigenvectors are $\{a\}$ and $\{|a\rangle\}$, the probability of obtaining the measurement results a when $\hat{A}$ is measured and the expectation value of $\hat{A}$ is given by

$$\Pr(a) = |\langle a|\psi\rangle|^2 \tag{2.4}$$

and

$$\left\langle\hat{A}\right\rangle = \left\langle\psi\middle|\hat{A}\middle|\psi\right\rangle, \tag{2.5}$$

respectively. Note that for a Hermite operator with continuous values, the above formulas change into an integral. For example, if we consider a Hermite operator $\hat{x}$ whose eigenvalues run from $-\infty$ to ∞ and the corresponding eigenvectors are $\{|x\rangle\}$, the probability and the expectation values of $\hat{x}$ become

$$\Pr(x_0 < x < x_1) = \int_{x_0}^{x_1}\mathrm{d}x\,|\psi(x)|^2, \tag{2.6}$$

$$\langle\hat{x}\rangle = \int_{-\infty}^{\infty}\mathrm{d}x\,x\,|\psi(x)|^2, \tag{2.7}$$

where $\psi(x)$ is a wave function of $|\psi\rangle$ given by

$$\psi(x) = \langle x|\psi\rangle. \tag{2.8}$$

07 December 2024 17:52:47

https://doi.org/10.1063/9780735424074_002

Optical Quantum Computers: A Route to Practical Continuous Variable Quantum Information Processing, W. Asavanant and A. Furusawa
© 2022 AIP Publishing, published by AIP Publishing

The formulation of quantum mechanics that starts from Schrödinger's equation and deriving the changes of quantum states (ket vectors) is called the *Schrödinger picture*. It is also possible to formulate quantum mechanics where the quantum states remain constant and the physical quantity go through the time evolution. This picture is called the *Heisenberg picture*. To describe the Heisenberg picture, we return to Eq. (2.5) and rewrite it as

$$\left\langle \hat{A} \right\rangle = \left\langle \psi(t=0) \middle| \hat{U}^\dagger \hat{A} \hat{U} \middle| \psi(t=0) \right\rangle. \tag{2.9}$$

Then, instead of the time evolution of ket vectors, we can consider the time evolution of the Hermite operator $\hat{A}$ and its eigenvector $|a\rangle$ as

$$\hat{A}(t) = \hat{U}^\dagger(t) \hat{A} \hat{U}(t), \tag{2.10}$$

$$|a(t)\rangle = \hat{U}^\dagger(t) \, |a\rangle. \tag{2.11}$$

Note that the eigenvalues remain the same. In the same spirit to Schrödinger's equation, we can also write down a differential equation governing the time evolution of operators in the Heisenberg picture as

$$\frac{\mathrm{d}}{\mathrm{d}t} \hat{A} = \frac{i}{\hbar} \left[\hat{H}, \hat{A} \right] + \frac{\partial}{\partial t} \hat{A}, \tag{2.12}$$

where the partial derivative is taken on the explicit time dependence of the initial operators.

In quantum information using qubits, the calculations are done mostly with the Schrödinger picture. In CV quantum computation and quantum optics, however, both the Heisenberg picture and the Schrödinger picture are used, depending on the situation. When we want to calculate the expectation values such as variances of physical quantities or derive the input–output relations of quantum operations, the Heisenberg picture is much clearer. On the other hand, when we talk about state generations, their measurements, and their estimations, the Schrödinger picture tends to be more suitable. Also, in many calculations in this book, we will be talking about quantum states but using the Heisenberg picture in the calculations. For some readers, this might take a while to get used to this.

2.1.2 Mixed states and density matrices

Quantum states are usually represented using ket vectors and their evolutions are unitary, meaning that they are reversible. In the actual experiments, however, not all time evolutions are reversible. For example, scattering of lights in the optical systems (i.e., optical losses) or decoherence of the atomic systems due to the coupling with the environment occurs in an irreversible fashion. Quantum states that involve irreversible processes are called mixed states to distinguish them from the quantum states that can be represented with ket vectors, which are called pure states. The mathematical descriptions of mixed states are very important in experimental physics as experiments always have imperfections and we can never assume pure states.

Let us consider the following situation: we have a source of quantum states that randomly emits a quantum state from a set $\{|\psi_k\rangle\}$ with a probability distribution $\{p_k\}$ whose constraint is $\sum p_k = 1$.

07 December 2024 17:52:47

The emitted quantum states arrive to Alice who measure the physical quantity $\hat{A}$. Then, the probability distribution of the measurement results and the expectation values of $\hat{A}$ is given by

$$\Pr(a) = \sum_k p_k \, |\langle a|\psi_k\rangle|^2, \tag{2.13}$$

$$\left\langle \hat{A} \right\rangle = \sum_k p_k \left\langle \psi_k \middle| \hat{A} \middle| \psi_k \right\rangle. \tag{2.14}$$

From the above equations, instead of the ket vector, we can define a *density matrix* or *density operator* $\hat{\rho}$ to describe a mixed state as

$$\hat{\rho} = \sum_k p_k \, |\psi_k\rangle \, \langle\psi_k|. \tag{2.15}$$

Equations (2.13) and (2.14) can be written using the density matrix $\hat{\rho}$ as

$$\Pr(a) = \left\langle a \middle| \hat{\rho} \middle| a \right\rangle, \tag{2.16}$$

$$\left\langle \hat{A} \right\rangle = \mathrm{Tr}(\hat{\rho}\hat{A}), \tag{2.17}$$

where $\mathrm{Tr}(\cdot)$ is a trace of an operator. Therefore, for mixed states, if we know the density matrix $\hat{\rho}$, then we can calculate all the properties of the quantum states. There are a few points that have to be noted here. First, for the sake of simplicity, we used the set of state $\{|\psi_k\rangle\}$ and the probability distribution $\{p_k\}$ to describe the density matrix but, in fact, this information is not at all accessible to the observer (in our case, Alice). There are many possible sets of quantum states and probability distributions that would give the same $\hat{\rho}$, which, in turn, give the same probability distributions and expectation values for all physical quantities. Thus, there is no point in considering $\{|\psi_k\rangle\}$ and $\{p_k\}$, and we need to consider only $\hat{\rho}$. On the other hand, we might want to know how close a density matrix $\hat{\rho}$ is to a pure state. There is a figure of merit called *purity* P, which is defined as

$$P \equiv \mathrm{Tr}(\hat{\rho}^2). \tag{2.18}$$

For a pure state $|\psi\rangle$, the density matrix is given by $\hat{\rho}_{|\psi\rangle} = |\psi\rangle \, \langle\psi|$ and the purity P is unity. On the other hand, for mixed states, $P < 1$, and the further P is from unity, the more mixed the state is.

Next, let us consider physical constraints on the density matrix $\hat{\rho}$. These are constraints that a matrix has to satisfy for it to be a physically allowed density matrix,

$$\hat{\rho} = \hat{\rho}^\dagger, \tag{2.19}$$

$$\hat{\rho} \geq 0, \tag{2.20}$$

$$\mathrm{Tr}(\hat{\rho}) = 1. \tag{2.21}$$

The first and the second conditions ensure that the eigenvalue of the density matrix is a positive real number, which is required as the eigenvalues correspond to probability. The third condition is the normalization of the probability. As such, if we have a matrix that satisfies both of the three conditions above, then that matrix is valid as a density matrix and corresponds to a certain physical quantum state.

07 December 2024 17:52:47

Similar to Schrödinger's equation, we can also write down a differential equation governing the time evolution of a density matrix $\hat{\rho}$ given the Hamiltonian $\hat{H}$. This differential equation is called *von Neumann equation* and is given by

$$\frac{\mathrm{d}}{\mathrm{d}t}\hat{\rho} = -\frac{i}{\hbar}\left[\hat{H}, \hat{\rho}\right]. \tag{2.22}$$

For a more general non-unitary time evolution, we can resort to master equation or quantum Langevin equation. But as these formalisms are somewhat out of the scope of this book. We will not go into details here and invoke their results only when necessary.

Note that it might also be interesting to consider how we can describe mixed states using the transformation of operators. At the beginning of this section, we use the classical mixture of the quantum states as a starting point in the formulation of the density matrix. Equivalently, we can also consider mixed states as states that arise due to the unknown entanglement to the environment,

$$|\Psi\rangle = \sum_k c_k |\psi_k\rangle \otimes |E_k\rangle, \tag{2.23}$$

where $\{|E_k\rangle\}$ are the ket vectors of the states of the environment, which we assume them to be orthonormal basis. Then, if the environment was projected to $|E_k\rangle$, our quantum state will be $|\psi_k\rangle$. However, as we do not know which state the environment is projected to, the resultant quantum states are mixed states with the probability distribution $p_k = |c_k|^2$. Mathematically, we can represent our lack of knowledge of the environment by tracing out the environment from $|\Psi\rangle$. This procedure is called *partial trace*. From a density matrix $\hat{\rho}_{AB}$ of two subsystems A and B, the density matrix of the only subsystem A can be found by tracing out B,

$$\hat{\rho}_A = \mathrm{Tr}_B(\hat{\rho}_{AB}). \tag{2.24}$$

As mixed states can be considered as the results of the entanglement due to an additional mode, one of the ways to deal with mixed states in a Heisenberg picture style is that we add ancillary modes that give rise to the mixed states. With the ancillary modes, the whole states can be treated as pure states and we can simply use the Heisenberg picture transformations. At the end of the calculation, however, as the ancillary modes are not actually there, we have to trace them out. This kind of method is actually widely used in the calculations of CV quantum computation protocol. A simple example of this is the calculation regarding optical losses or the quantum teleportation with imperfect resource states.

2.1.3 Measurements

In the basic quantum mechanics course, we usually first consider projective measurement. When we measure a physical quantity that is represented with a Hermitian operator $\hat{A}$, the basic postulate in quantum mechanics states that the measurement results will be one of the eigenvalues of $\hat{A}$. The probability of obtaining the measurement results a when $\hat{A}$ is measured and the post-measurement state is given by

$$\Pr(a) = \mathrm{Tr}(\hat{\Pi}_a \hat{\rho}) \tag{2.25}$$

07 December 2024 17:52:47

and

$$\hat{\rho}_a = \frac{1}{\Pr(a)} \hat{\Pi}_a \hat{\rho} \hat{\Pi}_a^\dagger, \tag{2.26}$$

respectively. $\hat{\Pi}_a$ is a projection operator and is given by

$$\hat{\Pi}_a = |a\rangle \langle a|, \tag{2.27}$$

where $|a\rangle$ is an eigenvector of $\hat{A}$. There are two important properties of projection operator

$$\hat{\Pi}_a \hat{\Pi}_{a'} = \delta_{aa'} \hat{\Pi}_a, \tag{2.28}$$

$$\sum_a \hat{\Pi}_a = \hat{I}. \tag{2.29}$$

The first property ensures that when the projective measurement of $\hat{A}$ is done consecutively, the result of the second measurement is the same as the result of the first measurement (hence the name projective measurement). The second condition ensures that the measurement results are one of the eigenvalues a.

We can also consider a Hermitian operator whose eigenvalues are continuous. For a Hermitian operator $\hat{x}$ whose eigenvalues are continuous, we can take eigenvectors $|x\rangle$ with the following normalization condition:

$$\langle x | x' \rangle = \delta(x - x'). \tag{2.30}$$

Then, the projection operator and its property become

$$\hat{\Pi}_x = |x\rangle \langle x|, \tag{2.31}$$

$$\hat{\Pi}_x \hat{\Pi}_{x'} = \delta(x - x') \hat{\Pi}_x, \tag{2.32}$$

$$\int_{-\infty}^{\infty} \mathrm{d}x \, |x\rangle \langle x| = \hat{I}. \tag{2.33}$$

Note, however, that projection measurement alone cannot account for all kinds of measurement; actual measurements have inefficiency and some measurements do not allow consecutive measurements as was discussed for the projective measurements. Below, we explain a more general type of measurement called positive operator-valued measure (POVM) (Nielsen and Chuang, 2000).

Definition 2.1. Let us assume a set of positive-definite operator $\{\hat{P}_k\}$ that satisfies

$$\sum_k \hat{P}_k = \hat{I}. \tag{2.34}$$

Then, these $\{\hat{P}_k\}$ correspond to measurements and the probability of obtaining the result k corresponded to $\hat{P}_k$ is

$$\Pr(a) = \mathrm{Tr}\left(\hat{P}_k \hat{\rho}\right). \tag{2.35}$$

Note that this definition of $\hat{P}_k$ is almost the same as the projection operator without the constraint in Eq. (2.28) and is called POVM.

07 December 2024 17:52:47

The post-measurement states of the certain POVM are not determined by $\hat{P}_k$ but by another operator, which we will call $\hat{K}_k$. For a set of operator $\{\hat{K}_k\}$ that satisfies

$$\sum_k \hat{K}_k^\dagger \hat{K}_k = \hat{I}, \tag{2.36}$$

$$\hat{K}_k^\dagger \hat{K}_k = \hat{P}_k, \tag{2.37}$$

the post-measurement quantum state will be given by

$$\hat{\rho}_k = \frac{1}{\mathrm{Tr}(\hat{K}_k \hat{\rho} \hat{K}_k^\dagger)} \hat{K}_k \hat{\rho} \hat{K}_k^\dagger. \tag{2.38}$$

Note that the above relation takes a general form of the Kraus operator. Interestingly, rather than $\hat{P}_k$, the post-measurement states depend on $\hat{K}_k$ as for any $\hat{K}_k$ with the form

$$\hat{K}_k = \hat{U}\sqrt{\hat{P}_k}, \tag{2.39}$$

where $\hat{U}$ is an arbitrary unitary operator will satisfy Eqs. (2.36) and (2.37). Note that we can take square root of $\hat{P}_k$ as it is a positive-definite operator. We will not go into the details regarding Kraus operators here and the readers who are interested should consult any basic quantum mechanics textbook.

07 December 2024 17:52:47

2.1.4 Uncertainty principle

In quantum mechanics, we can only predict the probability distributions of the outcome when physical quantities are measured. In the same system, there could be many physical quantities; for example, if we consider a moving particle, we can measure its position or its momentum. Then, it is natural to consider whether quantum mechanics allows us to freely engineer the distributions of all physical quantities of a quantum system or not. The answer, as everyone with a basic background in quantum mechanics knows, is no; distributions of physical quantities are constrained by the Heisenberg uncertainty principle and physical quantities that are non-commutative must abide by this principle. The Heisenberg uncertainty principle is a fundamental property of quantum mechanics that determines quantum states that are physically allowed. This principle is sometimes wrongly interpreted as "we cannot measure position and momentum simultaneously." This is wrong as this can be done experimentally but entails back-action. Back-action of the quantum measurement is out of the scope of this book and when we refer to the uncertainty principle, we will exclusively mean the Heisenberg uncertainty principle.

Let us consider a quantum state $\hat{\rho}$ and two Hermitian operators $\hat{A}$ and $\hat{B}$. From these two operators, we define

$$\Delta\hat{A} \equiv \hat{A} - \left\langle \hat{A} \right\rangle_{\hat{\rho}}, \tag{2.40}$$

$$\Delta\hat{B} \equiv \hat{B} - \left\langle \hat{B} \right\rangle_{\hat{\rho}}. \tag{2.41}$$

Then, the square of the above operators are variances of $\hat{A}$ and $\hat{B}$ of the state $\hat{\rho}$ and we will denote that as $\Delta^2\hat{A}$ and $\Delta^2\hat{B}$. The uncertainty principle gives the lower bound of the products of the variances of these two operators as

$$\left\langle \Delta^2\hat{A} \right\rangle_{\hat{\rho}} \left\langle \Delta^2\hat{B} \right\rangle_{\hat{\rho}} \geq \frac{1}{4} \left| \left\langle [\hat{A}, \hat{B}] \right\rangle_{\hat{\rho}} \right|^2, \tag{2.42}$$

whose proof is given below.

Proof. We can also prove the following identity:

$$[\Delta\hat{A}, \Delta\hat{B}] = [\hat{A}, \hat{B}]. \tag{2.43}$$

Then, we consider the following quantities $\left\langle (\Delta\hat{A} - i\lambda\Delta\hat{B})(\Delta\hat{A} + i\lambda\Delta\hat{B}) \right\rangle_{\hat{\rho}}$ with $\lambda \in \mathbb{R}$, which can be expanded as

$$\left\langle (\Delta\hat{A} - i\lambda\Delta\hat{B})(\Delta\hat{A} + i\lambda\Delta\hat{B}) \right\rangle_{\hat{\rho}} = \left\langle \Delta^2\hat{A} \right\rangle_{\hat{\rho}} + i\lambda \left\langle [\hat{A}, \hat{B}] \right\rangle_{\hat{\rho}} + \lambda^2 \left\langle \Delta^2\hat{B} \right\rangle_{\hat{\rho}}. \tag{2.44}$$

As the left-hand side of the above equation is obviously positive for all λ, using our knowledge of the quadratic polynomial and the fact that for Hermitian operators $\hat{A}$ and $\hat{B}$, the commutation relation is anti-Hermitian, we arrive at Eq. (2.42). □

The product of the variances of the two physical quantities is above a certain threshold determined by the commutation relation. For operators that commute, there exist simultaneous eigenvectors and the lower limit becomes 0. Equation (2.42) has a dependence on $\hat{\rho}$ except for the case where $[\hat{A}, \hat{B}]$ is a purely imaginary number. In such a case, the dependence on $\hat{\rho}$ can be dropped and the lower bound becomes state independent. Using the relation between arithmetic mean and geometrical mean, Eq. (2.42) can be reformulated in terms of the sums of variances as

$$\left\langle \Delta^2\hat{A} \right\rangle_{\hat{\rho}} + \left\langle \Delta^2\hat{B} \right\rangle_{\hat{\rho}} \geq \left| \left\langle [\hat{A}, \hat{B}] \right\rangle_{\hat{\rho}} \right|. \tag{2.45}$$

2.2 BRIEF REVIEW OF CLASSICAL ELECTROMAGNETISM

In classical electromagnetism, the electric field **E** and the magnetic field **B** are uniquely determined by Maxwell's equations

$$\nabla \cdot \mathbf{E} = \frac{\rho}{\varepsilon_0}, \tag{2.46}$$

$$\nabla \times \mathbf{E} = -\frac{\partial}{\partial t}\mathbf{B}, \tag{2.47}$$

07 December 2024 17:52:47

$$\nabla \cdot \mathbf{B} = 0, \tag{2.48}$$

$$\nabla \times \mathbf{B} = \mu_0 \mathbf{J} + \mu_0 \varepsilon_0 \frac{\partial}{\partial t} \mathbf{E}, \tag{2.49}$$

where ρ is the charge density, $\mathbf{J}$ is the current density, ε_0 is the permittivity, and μ_0 is the permeability of vacuum. If the charge density ρ and the current density $\mathbf{J}$ are given along with the appropriate boundary conditions, the above differential equations uniquely determine $\mathbf{E}$ and $\mathbf{B}$ as functions of time and space.

For most cases of our interests, $\rho = 0$ and $\mathbf{J} = \mathbf{0}$, i.e., no charges and currents in the region of interest. In such cases, $\mathbf{E}$ and $\mathbf{B}$ follow the following equations:

$$\nabla^2 \mathbf{E} - \frac{1}{c^2} \frac{\partial^2}{\partial t^2} \mathbf{E} = 0, \tag{2.50}$$

$$\nabla^2 \mathbf{B} - \frac{1}{c^2} \frac{\partial^2}{\partial t^2} \mathbf{B} = 0, \tag{2.51}$$

where $c = 1/\sqrt{\varepsilon_0 \mu_0}$ is the speed of light in vacuum. In the above equations, $\mathbf{E}$ and $\mathbf{B}$ are decoupled, and each field follows the wave equation. Although they can be decoupled, electric fields and magnetic fields are not completely independent as they must satisfy the original Maxwell's equations, which determine the boundary conditions.

Rather than solving directly for $\mathbf{E}$ and $\mathbf{B}$, solving for the potentials tends to be easier. From Eqs. (2.47) and (2.28), we can write down a solution of Maxwell's equations in the form of

$$\mathbf{E} = -\nabla \phi - \frac{\partial}{\partial t} \mathbf{A}, \tag{2.52}$$

$$\mathbf{B} = \nabla \times \mathbf{A}, \tag{2.53}$$

where ϕ is called scalar potential and $\mathbf{A}$ is called vector potential. Inserting these two equations into the remaining Maxwell's equations, we get

$$\nabla^2 \phi + \frac{\partial}{\partial t} \nabla \cdot \mathbf{A} = -\frac{\rho}{\varepsilon_0}, \tag{2.54}$$

$$\nabla^2 \mathbf{A} - \frac{1}{c^2} \frac{\partial^2}{\partial t^2} \mathbf{A} = -\mu_0 \mathbf{J} + \nabla \left(\nabla \cdot \mathbf{A} + \frac{1}{c^2} \frac{\partial}{\partial t} \phi \right). \tag{2.55}$$

To solve for the scalar potential and vector potential, we note that both potentials can be modified as long as they give the same electric fields and magnetic fields. This property is called *gauge invariant*. There are two widely used gauges: Coulomb gauge and Lorenz gauge. We will only consider Coulomb gauge in this book. Coulomb gauge corresponds to the potentials that satisfy

$$\nabla \cdot \mathbf{A} = 0. \tag{2.56}$$

In such a condition, Eqs. (2.54) and (2.55) transform to

$$\nabla^2 \phi = -\frac{\rho}{\varepsilon_0}, \tag{2.57}$$

$$\nabla^2 \mathbf{A} - \frac{1}{c^2} \frac{\partial^2}{\partial t^2} \mathbf{A} = -\mu_0 \mathbf{J} + \frac{1}{c^2} \frac{\partial}{\partial t} \nabla \phi. \tag{2.58}$$

07 December 2024 17:52:47

Equation (2.57) is simply the Poisson equation for the electrostatic potential. Therefore, the solution of ϕ has the same form as the electrostatic potential in the Coulomb gauge. In the particular case where $\rho = 0$ and $\mathbf{J} = \mathbf{0}$, the Poisson equation reduces to the Laplace equation $\nabla^2\phi = 0$. If $\mathbf{E}$ approaches 0 at the infinity, we can take $\phi = 0$ in the whole region and the electromagnetic field is determined only by the vector potential $\mathbf{A}$ that follows:

$$\nabla^2\mathbf{A} - \frac{1}{c^2}\frac{\partial^2}{\partial t^2}\mathbf{A} = 0. \tag{2.59}$$

In summary, for the region without electric charges and currents, if we take Coulomb gauge, then we can put the scalar potential $\phi = 0$ and the vector potential $\mathbf{A}$ follows wave equation and determines the electromagnetic fields.

2.3 QUANTIZATION OF THE ELECTROMAGNETIC FIELDS

Now, we consider the quantization of the electromagnetic fields. We will restrict ourselves to the case where there are no charges and currents. In the quantization of the electromagnetic field, we replace $\mathbf{E}$ and $\mathbf{B}$ with some Hermitian operators $\hat{\mathbf{E}}$ and $\hat{\mathbf{B}}$. As the uncertainty principle is an underlying principle of quantum mechanics, we expect some operators to be noncommutative, thus resulting in the uncertainty principle.

There are two aspects that we have to consider. First, as classical electromagnetic fields satisfy Maxwell's equations, we would expect that the expectation values of $\hat{\mathbf{E}}$ and $\hat{\mathbf{B}}$ should also satisfy Maxwell's equation for all quantum states of light. This property is automatically achieved if $\hat{\mathbf{E}}$ and $\hat{\mathbf{B}}$ satisfy Maxwell's equations.

Second, in the canonical quantization procedure, we usually start from the Lagrangian of the system and derive the Hamiltonian in the form of the coordinates and their conjugated momentum. To move from the classical to quantum, we then assign non-zero commutation relation between the coordinate and the momentum. For electromagnetic fields, we use Lagrangian and Hamiltonian density as fields are distributed in space. We will not go into details here but we can treat the vector potential $\mathbf{A}$ in the same way as the coordinate in the Hamiltonian mechanics. Assuming Coulomb gauge, the classical Hamiltonian density $\mathcal{H}$ and the conjugate momentum can be written as (Kok and Lovett, 2010)

$$\mathcal{H} = \frac{1}{2\varepsilon_0}\mathbf{\Pi}^2 + \frac{1}{2\mu_0}(\nabla \times \mathbf{A})^2, \tag{2.60}$$

$$\mathbf{\Pi} = \varepsilon_0\dot{\mathbf{A}}. \tag{2.61}$$

Similarly, the Hamiltonian operator $\hat{\mathcal{H}}$ in the term of vector potential operator $\hat{\mathbf{A}}$ and its conjugate momentum $\hat{\mathbf{\Pi}}$ become

$$\hat{\mathcal{H}} = \frac{1}{2\varepsilon_0}\hat{\mathbf{\Pi}}^2 + \frac{1}{2\mu_0}(\nabla \times \hat{\mathbf{A}})^2. \tag{2.62}$$

07 December 2024 17:52:47

The commutation relation between $\hat{\mathbf{A}}$ and $\hat{\mathbf{\Pi}}$ is given by

$$[\hat{A}_j(\mathbf{r},t),\hat{\Pi}_k(\mathbf{r}',t)] = i\hbar\delta_{jk}\delta^{\perp}(\mathbf{r}-\mathbf{r}'), \tag{2.63}$$

$$[\hat{A}_j(\mathbf{r},t),\hat{A}_k(\mathbf{r}',t)] = [\hat{\Pi}_j(\mathbf{r},t),\hat{\Pi}_k(\mathbf{r}',t)] = 0. \tag{2.64}$$

Note that the function $\delta^{\perp}(\mathbf{r}-\mathbf{r}')$ is called a *transversal delta function*. This function acts as a normal delta function inside the integral but has zero divergence, so that the Coulomb gauge is satisfied.

By imposing the commutation relation, we can show that the Heisenberg picture time evolutions of $\hat{\mathbf{A}}$ and $\hat{\mathbf{\Pi}}$ are (see Appendix A for detailed calculations),

$$\frac{\mathrm{d}}{\mathrm{d}t}\hat{\mathbf{A}} = \frac{i}{\hbar}[\hat{H},\hat{\mathbf{A}}] = \frac{1}{\varepsilon_0}\hat{\mathbf{\Pi}}, \tag{2.65}$$

$$\frac{\mathrm{d}}{\mathrm{d}t}\hat{\mathbf{\Pi}} = \frac{i}{\hbar}[\hat{H},\hat{\mathbf{\Pi}}] = \frac{1}{\mu_0}\nabla^2\hat{\mathbf{A}}. \tag{2.66}$$

The first equation is the definition of the conjugated momentum $\hat{\mathbf{\Pi}}$, while the second equation corresponds to the wave equation (2.59). Note that the Hamiltonian $\hat{H}$ is the integral of the Hamiltonian density $\hat{\mathcal{H}}$ over the space, i.e.,

$$\hat{H} = \int \mathrm{d}^3\mathbf{r}\,\hat{\mathcal{H}}. \tag{2.67}$$

07 December 2024 17:52:47

2.3.1 Modes

Classical vector potential in Coulomb gauge follows Eq. (2.59), which is a linear differential equation. Therefore, if we can find a set of solutions that is complete, arbitrary vector potentials can be written as linear combinations of those solutions. In a similar manner, vector potential operator can be expanded using classical vector potentials in a form

$$\hat{\mathbf{A}} = \sum_k \hat{a}_k\mathbf{A}_k(\mathbf{r},t) + \hat{a}_k^{\dagger}\mathbf{A}_k^*(\mathbf{r},t). \tag{2.68}$$

For each $\mathbf{A}_k(\mathbf{r},t)$, there are operators $\hat{a}_k$ and $\hat{a}_k^{\dagger}$ associated with it. In the language of quantum optics, each of this k is called *mode* and the function $A_k(\mathbf{r},t)$ is called *mode function*. Modes represent the oscillations that the electromagnetic waves are in. When we manipulate the electric fields in optical quantum computation, we have to consider which mode we are manipulating.

As with the usual linear algebra, it would be convenient to select a set of solutions that form a complete orthonormal basis. To define the orthonormality, we have to properly define the inner product first.

Definition 2.2. The inner product of the vector potential is defined as (Leonhardt, 2010)

$$(\mathbf{A}_j,\mathbf{A}_k) = i\frac{\varepsilon_0}{\hbar}\int \mathrm{d}^3\mathbf{r}\left(\mathbf{A}_j^*\cdot\frac{\partial\mathbf{A}_k}{\partial t} - \frac{\partial\mathbf{A}_j^*}{\partial t}\cdot\mathbf{A}_k\right). \tag{2.69}$$

The above inner product is invariant under the time evolution due to Maxwell's equations. The operator $\hat{a}_k$ and $\hat{a}_k^\dagger$ can be represented using the inner product as

$$\hat{a}_k = (\mathbf{A}_k, \hat{\mathbf{A}}), \tag{2.70}$$

$$\hat{a}_k^\dagger = -(\mathbf{A}_k^*, \hat{\mathbf{A}}). \tag{2.71}$$

Under the orthonormalized condition, by using the definition of the inner product, we can find the commutation relation as

$$[\hat{a}_k, \hat{a}_{k'}^\dagger] = \delta_{kk'}, \tag{2.72}$$

$$[\hat{a}_k, \hat{a}_{k'}] = 0. \tag{2.73}$$

This commutation relation has a form of the Bosonic commutation relation. Therefore, we can also consider electromagnetic wave as Bosonic particle, known as a *photon*, and $\hat{a}_k$ and $\hat{a}_k^\dagger$ are annihilation and creation operators for an electromagnetic wave in mode k, respectively. This, in a way, seems like the wave-particle duality in quantum mechanics. However, as with the quote by Lamb (1995):

> It is high time to give up the use of the word "photon," and of a bad concept, which will shortly be a century old. Radiation does not consist of particles, and the classical, i.e., non-quantum, limit of QTR is described by Maxwell's equations for the electromagnetic fields, which do not involve particles. Talking about radiation in terms of particles is like using such ubiquitous phrases as "You know" or "I mean" which are very much to be heard in some cultures. For a friend of Charlie Brown, it might serve as a kind of security blanket.

we do advise the readers against considering the quantized electromagnetic wave as an actual stream of photons as such physical image sometimes hinders the comprehension of CV optical quantum computation which uses the wave aspect, i.e., the actual electromagnetic fields.

07 December 2024 17:52:47

2.3.2 Transformation of modes

There are many possible sets of the complete orthonormal basis, which we can use in the expansion of the vector potential operator $\hat{\mathbf{A}}$. It would be convenient to look at how different sets of bases are related. In addition to the expansion in Eq. (2.68), let us also expand the operator $\hat{\mathbf{A}}$ using a different basis $\mathbf{B}_k(\mathbf{r}, t)$,

$$\hat{\mathbf{A}} = \sum_l \hat{b}_l \mathbf{B}_l(\mathbf{r}, t) + \hat{b}_l^\dagger \mathbf{B}_k^*(\mathbf{r}, t). \tag{2.74}$$

Using Eq. (2.68) and the definition of the inner product, the operators $\hat{b}_k$ and $\hat{b}_k^\dagger$ can be expressed using $\hat{a}_k$ and $\hat{a}_k^\dagger$ as

$$\hat{b}_l = (\mathbf{B}_l, \hat{\mathbf{A}}) = \sum_k (\mathbf{B}_l, \mathbf{A}_k)\hat{a}_k + (\mathbf{B}_l, \mathbf{A}_k^*)\hat{a}_k^\dagger, \tag{2.75}$$

$$\hat{b}_l^\dagger = -(\mathbf{B}_l^*, \hat{\mathbf{A}}) = \sum_k (\mathbf{A}_k^*, \mathbf{B}_l)\hat{a}_k + (\mathbf{A}_k, \mathbf{B}_l)\hat{a}_k^\dagger. \tag{2.76}$$

Because $(\mathbf{B}_l, \mathbf{A}_k^*) \neq 0$ in general, an annihilation operator in a certain mode could be a linear combination of both annihilation operators and creation operators in different modes. This is highly

counterintuitive in the particle picture, where this result makes it seems that, depending on the basis, there might be or might not be any photon. On the other hand, linear combinations of annihilation and creation operators are completely acceptable as interference is a fundamental property of the wave.

To depict more clearly the constraints of the transformation of modes, we simplify Eqs. (2.75) and (2.76) into

$$\begin{pmatrix} \hat{\mathbf{b}} \\ \hat{\mathbf{b}}^\dagger \end{pmatrix} = \begin{pmatrix} C & D \\ D^* & C^* \end{pmatrix} \begin{pmatrix} \hat{\mathbf{a}} \\ \hat{\mathbf{a}}^\dagger \end{pmatrix}, \tag{2.77}$$

where

$$\hat{\mathbf{a}} = \begin{pmatrix} \hat{a}_1 \\ \hat{a}_2 \\ \vdots \\ \hat{a}_n \end{pmatrix}, \quad \hat{\mathbf{b}} = \begin{pmatrix} \hat{b}_1 \\ \hat{b}_2 \\ \vdots \\ \hat{b}_n \end{pmatrix}. \tag{2.78}$$

C and D are $n \times n$ matrices corresponding to the coefficients in the mode transformations and the Hermite conjugate $\cdot^\dagger$ does not transpose the vertical vectors. The constraints due to the Bosonic commutation relation can be compactly written as

$$\begin{pmatrix} 0_n & I_n \\ -I_n & 0_n \end{pmatrix} = \begin{pmatrix} C & D \\ D^* & C^* \end{pmatrix} \begin{pmatrix} 0_n & I_n \\ -I_n & 0_n \end{pmatrix} \begin{pmatrix} C & D \\ D^* & C^* \end{pmatrix}^{\mathrm{T}}, \tag{2.79}$$

where 0_n and I_n are $n \times n$ zero matrix and identity matrix. This type of transformation is called the Bogoliubov transformation and the coefficient matrix is a symplectic matrix as Eq. (2.79) is a definition of a symplectic matrix. Conversely, any quantum operation in the aforementioned form can be interpreted as a mode transformation.

2.3.3 Quadrature

Although vector potentials and annihilation operators can be used to describe quantum optics, they are not physical quantities that are usually measured; in the experiments, we measure electric fields or magnetic fields. In this section, we will introduce the concept of *quadrature*, which will be the main physical quantity that is measured and used for the CV optical quantum computation.

First, let us return to Eqs. (2.52) and (2.53). Using that equation in conjunction with the expansion of the vector potential, we can write down the electric field operator $\hat{E}$ and the magnetic field operator $\hat{B}$ as

$$\hat{\mathbf{E}} = -\sum_k \left[\hat{a}_k \dot{\mathbf{A}}_k(\mathbf{r}, t) + \hat{a}_k^\dagger \dot{\mathbf{A}}_k^*(\mathbf{r}, t) \right], \tag{2.80}$$

$$\hat{\mathbf{B}} = \sum_k \left[\hat{a}_k \nabla \times \mathbf{A}_k(\mathbf{r}, t) + \hat{a}_k^\dagger \nabla \times \mathbf{A}_k^*(\mathbf{r}, t) \right]. \tag{2.81}$$

07 December 2024 17:52:47

To be more explicit, let us consider the case where $\mathbf{A}_k(\mathbf{r}, t)$ is monochromatic, i.e.,

$$\mathbf{A}_k(\mathbf{r}, t) = \mathbf{A}_k(\mathbf{r}) \exp(-i\Omega_k t), \tag{2.82}$$

where Ω_k is the carrier frequency of the beam. Inserting this equation into Eq. (2.59), we get

$$\left(\nabla^2 + \frac{\Omega_k^2}{c^2}\right) \mathbf{A}_k(\mathbf{r}) = 0, \tag{2.83}$$

which shows that the spatial part of the monochromatic mode follows Helmholtz equation. Now, let us return to Eqs. (2.80) and (2.81), and write down the electric field and the magnetic field as

$$\hat{\mathbf{E}} = i \sum_k \Omega_k \left[\hat{a}_k \mathbf{A}_k(\mathbf{r}) e^{-i\Omega_k t} - \hat{a}_k^\dagger \mathbf{A}_k^*(\mathbf{r}) e^{i\Omega_k t}\right], \tag{2.84}$$

$$\hat{\mathbf{B}} = \sum_k \left[\hat{a}_k \nabla \times \mathbf{A}_k(\mathbf{r}) e^{-i\Omega_k t} + \hat{a}_k^\dagger \nabla \times \mathbf{A}_k^*(\mathbf{r}) e^{i\Omega_k t}\right]. \tag{2.85}$$

Plugging the above equation into the Hamiltonian density and doing some math, we arrive at the Hamiltonian (see Appendix A for calculations)

$$\hat{H} = \sum_k \hbar\Omega_k \left(\hat{a}_k^\dagger \hat{a}_k + \frac{1}{2}\right). \tag{2.86}$$

This Hamiltonian is obviously the quantum harmonic oscillator Hamiltonian, which suggests that the monochromatic CV system is an assembly of independent harmonic oscillators with frequency Ω_k. In the mechanical harmonic oscillator, the position and the momentum are usually the physical quantities that we are interested in. The situation is also the same for an optical harmonic oscillator, but instead of position and momentum, we can define *quadrature* as

Definition 2.3. The quadrature operators of the mode that can be represented using the annihilation operator $\hat{a}_k$ are

$$\hat{x}_k \equiv \sqrt{\frac{\hbar}{2\Omega_k}} (\hat{a}_k + \hat{a}_k^\dagger), \tag{2.87}$$

$$\hat{p}_k \equiv -i\sqrt{\frac{\hbar\Omega_k}{2}} (\hat{a}_k - \hat{a}_k^\dagger). \tag{2.88}$$

Quadrature operators are Hermitian operators and can be physically measured using *homodyne measurement* (Sec. 2.6). Using the definition of the quadrature, their commutation relation and the Hamiltonian become

$$[\hat{x}_k, \hat{p}_l] = i\hbar\delta_{kl}, \tag{2.89}$$

$$\hat{H} = \sum_k \left(\frac{1}{2}\Omega_k^2 \hat{x}_k^2 + \frac{\hat{p}_k^2}{2}\right), \tag{2.90}$$

07 December 2024 17:52:47

which has the same commutation relation as position and momentum of the particle in quantum mechanics. From the commutation relation, the uncertainty principle of the quadrature operators is

$$\langle \Delta^2 \hat{x} \rangle \langle \Delta^2 \hat{p} \rangle \geq \frac{\hbar^2}{4}. \tag{2.91}$$

Next, we consider the time evolution of the quadrature operators. However, so far, there is no explicit time dependence on either quadrature operators or the annihilation operators, and the time dependence in the vector potential operators appears in the mode function $\mathbf{A}_k(\mathbf{r}, t)$. However, if we define the time-dependent operators as

Definition 2.4. Time-dependent annihilation operators and quadrature operators are

$$\hat{a}_k(t) \equiv \hat{a}_k \exp(-i\Omega_k t), \tag{2.92}$$

$$\hat{x}_k(t) \equiv \sqrt{\frac{\hbar}{2\Omega_k}} [\hat{a}_k(t) + \hat{a}_k^\dagger(t)], \tag{2.93}$$

$$\hat{p}_k(t) \equiv -i\sqrt{\frac{\hbar\Omega_k}{2}} [\hat{a}_k(t) - \hat{a}_k^\dagger(t)], \tag{2.94}$$

then the electric field operator and the magnetic field operator become

$$\hat{\mathbf{E}} = -\sum_k \sqrt{\frac{2\Omega_k}{\hbar}} \left\{ \Omega_k \hat{x}_k(t) \Im[\mathbf{A}_k(\mathbf{r})] + \hat{p}_k(t) \Re[\mathbf{A}_k(\mathbf{r})] \right\}, \tag{2.95}$$

$$\hat{\mathbf{B}} = \sum_k \sqrt{\frac{2}{\hbar\Omega_k}} \left\{ \Omega_k \hat{x}_k(t) \Re[\nabla \times \mathbf{A}_k(\mathbf{r})] - \hat{p}_k(t) \Im[\nabla \times \mathbf{A}_k(\mathbf{r})] \right\}, \tag{2.96}$$

where $\Re[\cdot]$ and $\Im[\cdot]$ denote the real part and the imaginary part, respectively. Thus, the quadrature operators can be intuitively understood as a real part or an imaginary part of the complex electric (magnetic) field amplitude. In classical optics, both components of the electric fields can be determined arbitrarily, but as the commutation relation in Eq. (2.89) shows, the quadrature must satisfy the Heisenberg uncertainty principle.

As a more concrete example, consider a single-mode plane wave, which corresponds to

$$\mathbf{A}(\mathbf{r}) \propto \exp(i\mathbf{k} \cdot \mathbf{r})\hat{e}, \tag{2.97}$$

where $\mathbf{k}$ is a wave vector and $\hat{e}$ is a unit vector representing the polarization. In this case, the electric fields and the magnetic fields become

$$\hat{\mathbf{E}} \propto \left(\Omega \hat{x}(t) \sin \mathbf{k} \cdot \mathbf{r} + \hat{p}(t) \cos \mathbf{k} \cdot \mathbf{r} \right) \hat{e}, \tag{2.98}$$

$$\hat{\mathbf{B}} \propto \left(\Omega \hat{x}(t) \sin \mathbf{k} \cdot \mathbf{r} + \hat{p}(t) \cos \mathbf{k} \cdot \mathbf{r} \right) \hat{k} \times \hat{e}, \tag{2.99}$$

where $\hat{k}$ is a unit vector in the direction of $\mathbf{k}$. In the plane wave expansion, the quadrature operators $\hat{x}$ and $\hat{p}$ correspond to the sine component and the cosine component of the electric and magnetic fields.

07 December 2024 17:52:47

Since we will be dealing mainly with the quadrature operators, for readers who are not interested in the details of the quantization of the electromagnetic field, it might be sufficient to familiarize with the quadrature and understand its physical correspondence. Unless stated otherwise, we will assume single-mode monochromatic light throughout this chapter. Note that in the actual quantum states, modes are not monochromatic and possess finite frequency bandwidth. However, as the frequency bandwidths are usually small compared to Ω_k, the results in the monochromatic case hold. Also, we will be assuming a unit system where $\Omega = 1$. It is also customary in quantum optics to use the units where $\hbar$ is a constant number. But as there are many variants (mostly $\hbar = 1$ or 1/2 or 2), we will write out $\hbar$ explicitly.

When defining the quadrature operators in phase space, we can freely choose any two orthogonal directions. Let suppose we first define quadrature operators $\hat{x}$ and $\hat{p}$. Then, we denote the quadrature operators in other direction as $\hat{x}_\theta$ and $\hat{p}_\theta$ which are related via a rotation matrix as

$$\begin{pmatrix} \hat{x}_\theta \\ \hat{p}_\theta \end{pmatrix} = \begin{pmatrix} \cos\theta & \sin\theta \\ -\sin\theta & \cos\theta \end{pmatrix} \begin{pmatrix} \hat{x} \\ \hat{p} \end{pmatrix}. \tag{2.100}$$

Note that the commutation relation is preserved in the above transformation, i.e., $[\hat{x}_\theta, \hat{p}_\theta] = i\hbar$.

2.4 BASIC QUANTUM STATES AND THEIR REPRESENTATIONS

2.4.1 Review of Bloch sphere of the qubit system

Although the ket vectors $|\psi\rangle$ (or density matrices $\hat{\rho}$ in case of mixed states) contain all information regarding the states, it would be convenient if we could visualize the quantum states. For the qubit system, the most convenient method is via the Bloch sphere. For a single qubit whose density matrix $\hat{\rho}_{\text{qubit}}$ is a 2×2 matrix, its matrix can be expanded as

$$\hat{\rho}_{\text{qubit}} = \frac{1}{2}(\hat{I} + a\hat{\sigma}_x + b\hat{\sigma}_y + c\hat{\sigma}_z), \tag{2.101}$$

where all matrices are 2×2 and $\hat{\sigma}_i$ are Pauli operators given by

$$\hat{\sigma}_x = \begin{pmatrix} 0 & 1 \\ 1 & 0 \end{pmatrix}, \tag{2.102}$$

$$\hat{\sigma}_y = \begin{pmatrix} 0 & -i \\ i & 0 \end{pmatrix}, \tag{2.103}$$

$$\hat{\sigma}_z = \begin{pmatrix} 1 & 0 \\ 0 & -1 \end{pmatrix}. \tag{2.104}$$

By representing the quantum state using the parameters (a, b, c), we can write down the quantum states of the qubits as points in three-dimensional space, which is what usually called as Bloch

07 December 2024 17:52:47

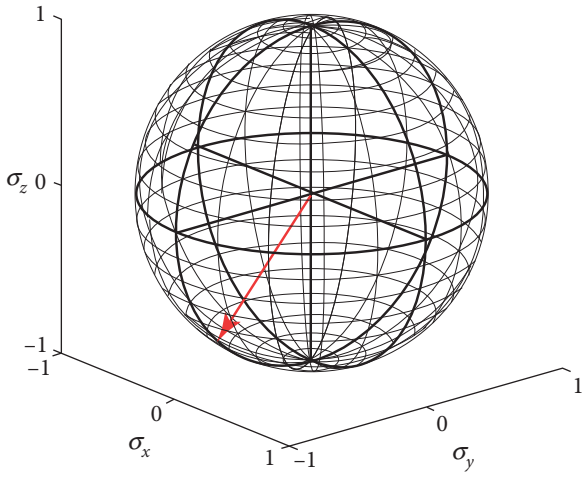

FIG. 2.1
Image of a Bloch sphere. The red vector represents a qubit quantum state.

sphere (Fig. 2.1). If we calculate the purity, we can show that $\sqrt{a^2 + b^2 + c^2} \leq 1$, meaning that physical qubit quantum states are inside a unit sphere and pure states are on the surface of the sphere (hence the term Bloch sphere). The quantum operations in qubit systems can then be visualized as moving points inside the Bloch sphere. Do note that although quantum states are represented as points, the actual measurement results do follow the uncertainty principle and there are quantum fluctuations in the measurement results.

2.4.2 Wigner function

In the CV quantum system, if we limit ourselves to pure states, the wave functions $\psi(x)$ can be used to easily represent the quantum states and the quantum operations are simply transformations of wave functions. There are, however, two disadvantages. First, the wave function does not include mixed states. Second, the representation using wave functions $\psi(x)$ does not visualize the distributions of the conjugated variable $\hat{p}$. In qubit's Bloch sphere, the probability distributions of each Pauli operators are visualized by the projection of the vector representing quantum states to the axes of the Bloch sphere. Therefore, we need a method to visualize states in quantum optics in the phase space.

If we recall from the basic classical mechanics, the states of the particles are often represented on the phase space of position x and momentum p, and time evolutions are shown as phase space trajectories. In classical optics, electric fields are also often represented on a phase space where the two axes correspond to the real part and the imaginary part. Therefore, it is natural to try and represent CV quantum states in phase space where the axes correspond to $\hat{x}$ and $\hat{p}$. There is, however, a small difference: since $\hat{x}$ and $\hat{p}$ must satisfy uncertainty principle, the visualization of quantum states cannot be directly considered as the joint probability distribution of $\hat{x}$ and $\hat{p}$. Nevertheless, since they shared many similar traits to the probability distributions, the visualization of quantum states in phase space is usually called *quasiprobability distributions*.

There are many types of quasiprobability distributions but we will mainly consider a quasiprobability distribution called the *Wigner function*. The Wigner function was originally studied in the context of statistical mechanics (Wigner, 1932) and now is an important tool in quantum optics. Without formal prove, we give the formula to calculate Wigner function $W(x, p)$ from a density matrix $\hat{\rho}$ below.

07 December 2024 17:52:47

Definition 2.5. The Wigner function $W(x, p)$ of a density matrix $\hat{\rho}$ is given by

$$W(x,p) = \frac{1}{2\pi\hbar}\int_{-\infty}^{\infty} \mathrm{d}\zeta \left\langle x + \frac{1}{2}\zeta \middle| \hat{\rho} \middle| x - \frac{1}{2}\zeta \right\rangle \exp\left(-\frac{i}{\hbar}\zeta p\right). \tag{2.105}$$

Below, we give a few properties regarding the Wigner function.

Theorem 2.1. *The marginal distributions of $\hat{x}$ and $\hat{p}$, denoted as $\mathrm{Pr}_x(x)$ and $\mathrm{Pr}_p(p)$, is related to the Wigner function via*

$$\mathrm{Pr}_x(x) = \int_{-\infty}^{\infty} \mathrm{d}p\, W(x,p), \tag{2.106}$$

$$\mathrm{Pr}_p(p) = \int_{-\infty}^{\infty} \mathrm{d}x\, W(x,p). \tag{2.107}$$

By integrating the quadrature in the orthogonal direction, we can find the marginal distribution of the quadrature in any direction, meaning that the Wigner function contains complete information regarding the CV quantum states. From the marginal distribution, the normalization condition of the Wigner function is

$$\int_{-\infty}^{\infty}\int_{-\infty}^{\infty} \mathrm{d}x\,\mathrm{d}p\, W(x,p) = 1. \tag{2.108}$$

Another useful property of the Wigner function is called the *overlap formula*.

Theorem 2.2. *The overlap between two operators, i.e., $\mathrm{Tr}(\hat{A}\hat{B})$, is given by*

$$\mathrm{Tr}(\hat{A}\hat{B}) = 2\pi\hbar\int_{-\infty}^{\infty}\int_{-\infty}^{\infty} \mathrm{d}x\,\mathrm{d}p\, W_A(x,p)\, W_B(x,p), \tag{2.109}$$

where $W_A(x, p)$ and $W_B(x, p)$ are Wigner functions of operators $\hat{A}$ and $\hat{B}$ calculated by replacing the density matrices in Eq. (2.105) with the operators $\hat{A}$ and $\hat{B}$, respectively.

One of the important consequences of the overlap formula is that, similar to how purity limits the lengths of the vector representing quantum states in the qubit Bloch sphere, by calculating the purity, we can show that

$$\int_{-\infty}^{\infty}\int_{-\infty}^{\infty} \mathrm{d}x\,\mathrm{d}p\, \left|W(x,p)\right|^2 \leq \frac{1}{2\pi\hbar}, \tag{2.110}$$

which limits the square integrals of the Wigner functions to be below $1/(2\pi\hbar)$. Another constraint on the Wigner function is that the absolute values of the Wigner functions at any point are bound (Leonhardt, 2010),

$$\left|W(x,p)\right| \leq \frac{1}{\pi\hbar}. \tag{2.111}$$

This boundary is a manifestation of the Heisenberg uncertainty principle, which prevents us from having Wigner functions with infinitely sharp peaks. The extension to the multimode cases is rather trivial and will be omitted here.

07 December 2024 17:52:47

2.4.3 Quadrature eigenstates

Quantum states can be expanded using a basis with the continuous spectrum. In quantum optics, such basis are eigenstates of quadrature operator, which we shall denote as $|x\rangle$ and $|p\rangle$, and they satisfy

$$\hat{x}\,|x\rangle = x\,|x\rangle, \tag{2.112}$$
$$\hat{p}\,|p\rangle = p\,|p\rangle. \tag{2.113}$$

Rather than the usual normalization condition, the quadrature eigenstates have the delta function normalization conditions

$$\langle x|x'\rangle = \delta(x - x'), \tag{2.114}$$
$$\langle p|p'\rangle = \delta(p - p'). \tag{2.115}$$

These normalization conditions are unphysical, which stems from the fact that the quadrature eigenstates have fixed quadrature values, violating the Heisenberg uncertainty principle. Rather than considering these states as actual physical states, it might be better to consider them as useful mathematical tools. Quadrature eigenstates provide a complete orthonormal basis, which satisfies

$$\int_{-\infty}^{\infty} \mathrm{d}x\ |x\rangle\langle x| = \int_{-\infty}^{\infty} \mathrm{d}p\ |p\rangle\langle p| = \hat{I}. \tag{2.116}$$

One of the useful relations of the quadrature eigenstates is the inner product between $|x\rangle$ and $|p\rangle$,

$$\langle x|p\rangle = \frac{1}{\sqrt{2\pi\hbar}} \exp\left(\frac{i}{\hbar}xp\right). \tag{2.117}$$

This inner product allows us to easily change the basis of the wave function. Readers who are well versed in the signal analysis might already notice from this relation that the wave function $\psi(x)$ in x basis and $\tilde{\psi}(p)$ in p basis are related via a Fourier transform.

2.4.4 Vacuum states

As we have already shown in Sec. 2.3.3, the electromagnetic wave can be considered as the quantum harmonic oscillator. In harmonic oscillators, energy eigenstates have non-negative eigenvalues and there exists an eigenstate with least energy, a ground state. For electromagnetic fields, the ground state is called a *vacuum state*, which will be denoted by $|0\rangle$[1]. Given an annihilation operator $\hat{a}$, we can define a vacuum state:

Definition 2.6. A vacuum state $|0\rangle$ of a mode represented by $\hat{a}$ is a state that satisfies

$$\hat{a}\,|0\rangle = 0. \tag{2.118}$$

[1] This is not equivalent to the $|0\rangle$ state of the qubit as qubit requires two bases that are orthogonal to each other but do not impose any requirement that one of them must be the ground state.

07 December 2024 17:52:47

Using the definition in Eq. (2.87) and (2.88), we can write down the differential equation for the wave function $\psi_0(x)$ of the vacuum state as

$$\left(x + \hbar\frac{\mathrm{d}}{\mathrm{d}x}\right)\psi_0(x) = 0. \tag{2.119}$$

Solving the above equation and considering the normalization condition, we arrive at

$$\psi_0(x) = \frac{1}{(\pi\hbar)^{1/4}}\exp\left(-\frac{x^2}{2\hbar}\right). \tag{2.120}$$

Even for the vacuum state, which seems to correspond to the case where there is no light, the quadrature is not completely zero but has a Gaussian distribution centered at zero. This finite variance corresponds to what usually referred to as zero point oscillation. The wave function in p basis, $\tilde{\psi}_0(p)$, can also be calculated as

$$\tilde{\psi}_0(p) = \frac{1}{(\pi\hbar)^{1/4}}\exp\left(-\frac{p^2}{2\hbar}\right). \tag{2.121}$$

Both x and p have the same Gaussian distributions and their variances are

$$\langle\Delta^2\hat{x}\rangle_0 = \frac{\hbar}{2}, \tag{2.122}$$

$$\langle\Delta^2\hat{p}\rangle_0 = \frac{\hbar}{2}. \tag{2.123}$$

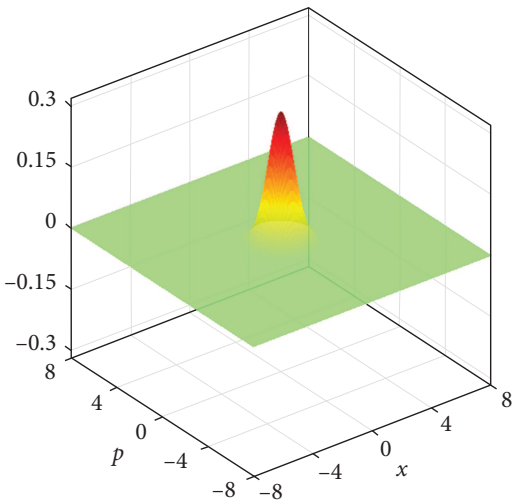

FIG. 2.2
Wigner function of a vacuum state. Note that we use $\hbar = 1$ for all plots in this chapter.

Variances of the vacuum state minimize the product of the variances in the uncertainty inequality in Eq. (2.91). Such quantum states are called minimum uncertainty states. We will see later on that all pure states whose wave functions are Gaussian are minimum uncertainty states.

The Wigner function of the vacuum state $W_0(x, p)$ can also be calculated using the definition in Eq. (2.105). As the calculation involves only simple Gaussian integrals, we will omit the derivation and give only the final result,

$$W_0(x,p) = \frac{1}{\pi\hbar}\exp\left(-\frac{x^2+p^2}{\hbar}\right), \tag{2.124}$$

which is a bivariate Gaussian function and is shown in Fig. 2.2. This Wigner function is positive in all regions and has a rotational invariance. Quantum states whose Wigner functions are invariant with respect to phase rotations are sometimes called phase-insensitive quantum states. In CV quantum optics experiments, the difficulties

07 December 2024 17:52:47

of the experiments drastically change depending on whether the quantum states we want to measure and manipulate are phase sensitive or not.

2.4.5 Fock states

Next, let us consider the energy eigenstates that are not vacuum states. If we go back to Eq. (2.86), the Hamiltonian of the electromagnetic wave in free space is given by[2]

$$\hat{H} = \hbar\left(\hat{a}^\dagger\hat{a} + \frac{1}{2}\right). \tag{2.125}$$

The energy eigenstates then correspond to the eigenstate of $\hat{n} \equiv \hat{a}^\dagger\hat{a}$ and we shall denote an eigenstate whose eigenvalue is n with $|n\rangle$. It can be easily shown that n is a non-negative integer and the effects of the annihilation operator $\hat{a}$ and creation operator $\hat{a}^\dagger$ are

$$\hat{a}\,|n\rangle = \sqrt{n}\,|n-1\rangle, \tag{2.126}$$

$$\hat{a}^\dagger\,|n\rangle = \sqrt{n+1}\,|n+1\rangle. \tag{2.127}$$

Therefore, if we know the wave function of $|n-1\rangle$ [denoted as $\psi_{n-1}(x)$], it is a simple matter of finding $\psi_n(x)$. Thus, the relationship between vacuum state $|0\rangle$ and Fock state $|n\rangle$ and the recursive formula connecting ψ_n and ψ_{n-1} are

$$|n\rangle = \frac{1}{\sqrt{n!}}(\hat{a}^\dagger)^n\,|0\rangle, \tag{2.128}$$

$$x\psi_n(x) + \hbar\frac{\mathrm{d}}{\mathrm{d}x}\psi_n(x) = \sqrt{2\hbar n}\psi_{n-1}(x). \tag{2.129}$$

The above equation can be analytically solved and the solution is

$$\psi_n(x) = \frac{1}{\sqrt{2^n n!\sqrt{\pi\hbar}}}H_n\left(\frac{x}{\sqrt{\hbar}}\right)\exp\left(-\frac{x^2}{2\hbar}\right), \tag{2.130}$$

where $H_n(\,\cdot\,)$ is a Hermite polynomial defined by

$$H_n(x) \equiv (-1)^n\exp(x^2)\frac{\mathrm{d}^n}{\mathrm{d}x^n}\exp(-x^2). \tag{2.131}$$

We can also calculate and write down the Wigner function of the Fock state as

$$W_n(x,p) = \frac{(-1)^n}{\pi\hbar}\exp\left(-\frac{x^2+p^2}{\hbar}\right)L_n\left(2\frac{x^2+p^2}{\hbar}\right), \tag{2.132}$$

where $L_n(x)$ is a Laguerre polynomial, which is given by

$$L_n(x) \equiv \sum_{k=0}^{n}\binom{n}{k}\frac{(-1)^k}{k!}x^k. \tag{2.133}$$

Now that we have worked out all the maths, let us look at some of the properties of the Fock states. Figure 2.3 shows the Wigner functions of some of the Fock states. As nth order Hermite polynomials

[2] Remember that we are using a system with $\Omega = 1$.

07 December 2024 17:52:47

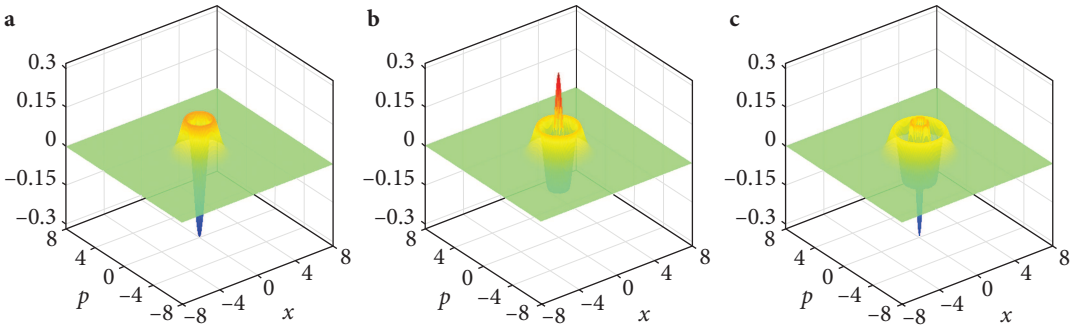

FIG. 2.3
Wigner functions of various Fock states: (a) $|1\rangle$, (b) $|2\rangle$, and (c) $|3\rangle$.

have n roots, when we measure the quadrature, there are places where the probabilities of the measurements become zero. On the other hand, if we look at the Wigner functions, we observe that, similar to the vacuum states, the Wigner functions are invariant with respect to arbitrary phase rotations. This rotational invariance is because Fock states are the energy eigenstates, which cannot be phase sensitive.

Another important property of the Fock states is that the values of their Wigner function at the origin are $\pm 1/(\pi\hbar)$, depending on whether n is odd or even. This property stems from the parity of the wave function $\psi_n(x)$ [Hermite polynomials $H_n(x)$ are odd functions when n are odd and even functions when n are even]. We can also generalize this result regarding the values of the Wigner functions at the origin to arbitrary quantum states $\hat{\rho}$:

Theorem 2.3. *The values at the origin of the Wigner function, $W(0,0)$, of a quantum state represented with a density matrix $\hat{\rho}$ is determined by its diagonal components as*

$$W(0,0) = \frac{1}{\pi\hbar}(P_{\text{even}} - P_{\text{odd}}), \tag{2.134}$$

where P_{even} and P_{odd} are the probability to get even and odd values when photon number n is measured.

Fock states play an important role in quantum optics as they are the orthonormal complete basis, i.e.,

$$\langle n|m\rangle = \delta_{nm}, \tag{2.135}$$

$$\sum_{n=0}^{\infty} |n\rangle\langle n| = \hat{I}. \tag{2.136}$$

Therefore, arbitrary pure states $|\psi\rangle$ and mixed states $\hat{\rho}$ can be expanded using Fock basis as

$$|\psi\rangle = \sum_{n=0}^{\infty} c_n |n\rangle, \tag{2.137}$$

07 December 2024 17:52:47

$$\hat{\rho} = \sum_{n,m=0}^{\infty} \rho_{nm} |n\rangle \langle m|. \tag{2.138}$$

In CV quantum computation, it is sometimes convenient to represent quantum states in the Fock basis rather than the wave function in the quadrature basis. One of the particular examples is quantum state engineering, which usually involves the generation of two-mode entangled states and projection measurement on a Fock basis $|n\rangle$, also called photon number detection (see Chap. 5 for more details on non-Gaussian state generation).

Fock states are also called photon number states and $|1\rangle$, $|2\rangle$, and $|3\rangle$ are called single-photon state, two-photon state, three-photon state, and so forth. In Chap. 4, we will be considering quantum states and their manipulations in the time domain, where the modes are temporal wave packets localized in time. When trying to explain the concept of time-domain quantum computation, one of the problems that the authors often encounter is that many people tend to wonder how could photons exist as a wave packet and this is even more problematic when discussing multi-photon states. This discrepancy would not at all occur if we consider lights as electromagnetic waves and Fock states with larger n simply corresponded to oscillations with higher energy, rather than states of more particles. Even so, since the word "photon" has become a standard terminology when discussing quantum optics, we will follow such tradition when deemed appropriate. We do again advise the readers to consider Fock state $|n\rangle$ as simply energy eigenstate rather than having n photons flying around.

07 December 2024 17:52:47

2.4.6 Coherent states

In the classical harmonic oscillator, the position x and the momentum p follow sinusoidal time evolution with $\pi/2$ phase difference. Since lights are quantum harmonic oscillator, it is then of our interest to consider quantum states whose expectation values of the quadrature $\hat{x}$ and $\hat{p}$ follow the same time evolution. Note that although the expectation values follow the classical trajectory, the quadrature $\hat{x}$ and $\hat{p}$ possess uncertainties and fluctuations. Such quantum states are sometimes referred to as classical or semi-classical states, and in quantum optics, they are usually called *coherent states*. A representative example of the coherent states is a laser light.

Coherent states are usually defined in two ways that are equivalent. The first definition is as follows:

Definition 2.7. A coherent state $|\alpha\rangle$ where $\alpha \in \mathbb{C}$ is an eigenstate of an annihilation operator,

$$\hat{a} |\alpha\rangle = \alpha |\alpha\rangle. \tag{2.139}$$

Using the definition of $\hat{x}(t)$ and $\hat{p}(t)$ in Eqs. (2.93) and (2.94), we can calculate the expectation values as

$$\langle \hat{x}(t) \rangle_\alpha = \sqrt{\frac{2\hbar}{\Omega}} [\Re(\alpha) \cos \Omega t + \Im(\alpha) \sin \Omega t], \tag{2.140}$$

$$\langle \hat{p}(t) \rangle_\alpha = \sqrt{2\hbar\Omega} [-\Re(\alpha) \sin \Omega t + \Im(\alpha) \cos \Omega t]. \tag{2.141}$$

Note that we explicitly wrote Ω here to show the frequency dependence. The expectation values of $\hat{x}(t)$ and $\hat{p}(t)$ indeed have a phase difference of $\pi/2$. Moreover, the real part and the imaginary part of α correspond to $\langle\hat{x}(t=0)\rangle_\alpha$ and $\langle\hat{p}(t=0)\rangle_\alpha$, respectively. In that sense, α can be regarded as a complex amplitude. We can also calculate the variances of the quadrature,

$$\langle\Delta^2\hat{x}(t)\rangle_\alpha = \langle\Delta^2\hat{p}(t)\rangle_\alpha = \frac{\hbar}{2}. \tag{2.142}$$

Regardless of the values of the α, the variances of the coherent states are the same as that of the vacuum state. This suggests that we should be able to consider coherent states as vacuum states that have been *displaced* in the phase space. This is the second way to define the coherent states and we will come back to this later.

Returning to Eq. (2.139), we can find the expansion of $|\alpha\rangle$ using Fock basis as

$$|\alpha\rangle = \exp\left(-\frac{|\alpha|^2}{2}\right)\sum_{n=0}^{\infty}\frac{\alpha^n}{\sqrt{n!}}|n\rangle. \tag{2.143}$$

A notable feature of the coherent state when expanded in Fock basis is that the probability distribution of n, denoted by p_n, becomes

$$p_n = \frac{|\alpha|^{2n}}{n!}\exp\left(-|\alpha|^2\right), \tag{2.144}$$

which is a Poisson distribution with average $\langle n\rangle = |\alpha|^2$. Because the coherent state is a semi-classical state, it is not surprising that the measurement results in the Fock basis are Poissonian, which is a signature of the discrete classical randomness.

The second definition of the coherent state is via a *displacement operator* $\hat{D}(\alpha)$,

Definition 2.8. If we define a displacement operator $\hat{D}(\alpha)$,

$$\hat{D}(\alpha) \equiv \exp(\alpha\hat{a}^\dagger - \alpha^*\hat{a}), \tag{2.145}$$

this operator transforms the annihilation operator in the Heisenberg picture as

$$\hat{D}^\dagger(\alpha)\hat{a}\hat{D}(\alpha) = \hat{a} + \alpha. \tag{2.146}$$

Note that in the derivation, we use the formula

$$e^{\hat{A}}\hat{B}e^{-\hat{A}} = \hat{B} + [\hat{A},\hat{B}] + \frac{1}{2}[\hat{A},[\hat{A},\hat{B}]] + \cdots + \frac{1}{n!}[\underbrace{\hat{A},[\hat{A},\ldots,[\hat{A}}_{\text{n terms}},\hat{B}]\ldots] + \cdots, \tag{2.147}$$

whose proof is given in Appendix A. Then, the coherent state can be written as

$$|\alpha\rangle = \hat{D}(\alpha)\,|0\rangle. \tag{2.148}$$

We can calculate the Heisenberg transformation of the quadrature operator $\hat{x}$ and $\hat{p}$ due to the displacement operator. The results are

$$\hat{D}^\dagger(\alpha)\hat{x}\hat{D}(\alpha) = \hat{x} + \sqrt{2\hbar}\Re(\alpha), \tag{2.149}$$

$$\hat{D}^\dagger(\alpha)\hat{p}\hat{D}(\alpha) = \hat{p} + \sqrt{2\hbar}\Im(\alpha). \tag{2.150}$$

07 December 2024 17:52:47

These results indeed show that the displacement operator corresponds to the phase space displacement. To explicitly show the amount of the displacement in the phase space, α is sometimes written using x_0 and p_0 as

$$\alpha = \frac{1}{\sqrt{2\hbar}}(x_0 + ip_0). \tag{2.151}$$

We can also define operators that displace only either $\hat{x}$ or $\hat{p}$. Such cases correspond when α are either purely real or purely imaginary and the operators are

$$\hat{D}_x(x_0) = \exp\left(-\frac{i}{\hbar}x_0\hat{p}\right), \tag{2.152}$$

$$\hat{D}_p(p_0) = \exp\left(\frac{i}{\hbar}p_0\hat{x}\right). \tag{2.153}$$

However, note that, $\hat{D}(\alpha)$ cannot be broken down into a simple product of $\hat{D}_x(x_0)$ and $\hat{D}_p(p_0)$ as these two are not commutative. If we use the Baker–Campbell–Hausdorff formula (see Appendix A for proof), we get

$$\hat{D}(\alpha) = \exp\left(-\frac{ip_0x_0}{2\hbar}\right)\hat{D}_p(p_0)\hat{D}_x(x_0) = \exp\left(\frac{i}{2\hbar}x_0p_0\right)\hat{D}_x(x_0)\hat{D}_p(p_0), \tag{2.154}$$

which has an additional phase factor.

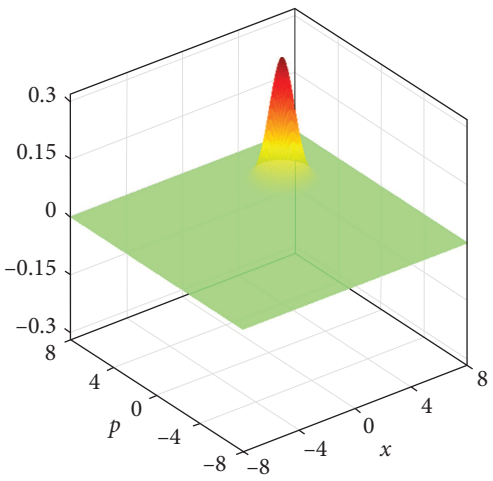

FIG. 2.4
Wigner function of a coherent state with $\alpha = (4 + 4i)/\sqrt{2\hbar}$.

Using Eq. (2.148), we can easily write down the wave function in both x and p as

$$\psi_\alpha(x) = \frac{1}{(\pi\hbar)^{1/4}}\exp\left(-\frac{(x-x_0)^2}{2\hbar} + \frac{i}{\hbar}p_0x - \frac{i}{2\hbar}x_0p_0\right), \tag{2.155}$$

$$\tilde{\psi}_\alpha(p) = \frac{1}{(\pi\hbar)^{1/4}}\exp\left(-\frac{(p-p_0)^2}{2\hbar} - \frac{i}{\hbar}x_0p + \frac{i}{2\hbar}x_0p_0\right), \tag{2.156}$$

which are simply the displaced vacuum state wave functions. We can also calculate the Wigner function of the coherent state using the definition of the displacement operator. The result is

$$W_\alpha(x,p) = \frac{1}{\pi\hbar}\exp\left(-\frac{(x-x_0)^2 + (p-p_0)^2}{\hbar}\right), \tag{2.157}$$

which is plotted in Fig. 2.4. In the same manner as the wave function, the Wigner function of the coherent state can also be simply obtained by displacing Wigner function of the vacuum state by x_0 and p_0.

07 December 2024 17:52:47

In the last part of this section, we will mention some of the properties of the coherent states. Any two coherent states are non-orthogonal to each other. This can be calculated by using Eq. (2.143), which results in

$$\langle\alpha|\beta\rangle = \exp\left(-\frac{|\alpha|^2 + |\beta|^2 - 2\alpha^*\beta}{2}\right), \tag{2.158}$$

$$|\langle\alpha|\beta\rangle|^2 = \exp(-|\alpha - \beta|^2). \tag{2.159}$$

Therefore, although coherent states are approximately orthogonal to each other when the differences in the complex amplitudes are large, they will never be truly orthogonal. Another property of coherent states is that they form an overcomplete basis, which is shown by the following equation (see proof in Appendix A):

$$\int \mathbf{d}\alpha \; |\alpha\rangle \langle\alpha| = \pi \hat{I}, \tag{2.160}$$

where integration is calculated over a complex plane. It is possible to expand any arbitrary quantum states using the coherent state basis but this is not done so often as the basis is overcomplete and non-orthogonal. Instead, we can consider whether we can write a quantum state as *classical mixture* of coherent state,

$$\hat{\rho} = \int \mathbf{d}\alpha P(\alpha) \, |\alpha\rangle \langle\alpha|. \tag{2.161}$$

Quantum states that can be written in a form of Eq. (2.161) with a positive and well-behaved $P(\alpha)$ are considered classical states. This is because a positive $P(\alpha)$ can be considered as a probability distribution, which means that $\hat{\rho}$ becomes simply a classical mixture of coherent states. On the other hand, quantum states whose $P(\alpha)$ are negative or ill-behaved are considered as nonclassical states. This is a formal definition of nonclassicality in quantum optics and the function $P(\alpha)$ is a type of quasiprobabilistic function called P-function or Glauber–Sudarshan representation after Glauber and Sudarshan who first studied this function (Glauber, 1963; and Sudarshan, 1963).

2.4.7 Squeezed vacuum states

The variances of both vacuum states and coherent states are equal for both quadrature $\hat{x}$ and $\hat{p}$ and saturate the uncertainty principle in Eq. (2.91). For the Fock states, their Wigner functions are rotational invariant and the variances are again equal for both quadratures, although they do not minimize Eq. (2.91). In general, variances of quadratures do not have to be isotropic; they can possess different values in different directions as long as the uncertainty principle and the constraints on the physicality are satisfied. In this section, we will consider one of the most important classes of the quantum states in quantum optics and CV quantum computation: *squeezed vacuum states*.

Squeezed vacuum states (sometimes simply called squeezed states) are quantum states that corresponded to vacuum states whose variances in one of the quadratures are reduced (squeezed). Due to the uncertainty principle, the variances of the other quadrature will increase (antisqueezed). However, the

07 December 2024 17:52:47

product of the variances will still minimize the uncertainty principle inequality, making the squeezed states minimum uncertainty states.

Squeezed states have been extensively studied for over 30 years [see Andersen *et al.* (2016) for a nice review] and have found a broad spectrum of applications: quantum metrology [such as those in the gravitational wave detector (Aasi *et al.*, 2013)], quantum state engineering (most of the generations of CV quantum states start from squeezed states), quantum communications and quantum key distributions, and quantum computation. Squeezed states are irreplaceable resources in CV quantum computation and it is not an exaggeration to say that almost all CV experimental systems start with sources of squeezed states.

Squeezed states $|0_r\rangle$ can be defined as follows:

Definition 2.9. If we define a squeezing operator $\hat{S}(r)$ where $r \in \mathbb{C}$ as

$$\hat{S}(r) \equiv \exp\left[\frac{1}{2}(r\hat{a}^2 - r^*\hat{a}^{\dagger 2})\right]. \tag{2.162}$$

The squeezed state is defined by

$$|0_r\rangle = \hat{S}(r)\,|0\rangle. \tag{2.163}$$

Using Eq. (2.147), we can write down the transformation of the annihilation and creation operator in the Heisenberg picture,

$$\hat{S}^\dagger(r)\hat{a}\hat{S}(r) = \cosh|r|\,\hat{a} - \exp(-i\phi)\sinh|r|\,\hat{a}^\dagger, \tag{2.164}$$

$$\hat{S}^\dagger(r)\hat{a}^\dagger\hat{S}(r) = -\exp(i\phi)\sinh|r|\,\hat{a} + \cosh|r|\,\hat{a}^\dagger, \tag{2.165}$$

where $\phi = \arg(r)$. The above transformations are Bogoliubov transformations we mentioned in Sec. 2.3.2. Therefore, it is also possible to define a new mode $\hat{\beta} = \cosh|r|\,\hat{a} - \exp(-i\phi)\sinh|r|\,\hat{a}^\dagger$ and consider quantum states such as Fock states and coherent states based on this mode. Historically, squeezed states were called two-photon coherent states by Yuen, who first theoretically studied the squeezed states (Yuen, 1976).

The transformations of the quadrature operators can also be written as

$$\hat{S}^\dagger(r)\hat{x}\hat{S}(r) = (\cosh|r| - \cos\phi\sinh|r|)\hat{x} + \sin\phi\sinh|r|\,\hat{p}, \tag{2.166}$$

$$\hat{S}^\dagger(r)\hat{p}\hat{S}(r) = (\cosh|r| + \cos\phi\sinh|r|)\hat{p} + \sin\phi\sinh|r|\,\hat{x}. \tag{2.167}$$

If we use Eq. (2.100) and consider the quadrature in the direction of $\phi/2$, we have

$$\hat{S}^\dagger(r)\hat{x}_{\phi/2}\hat{S}(r) = \exp(-|r|)\hat{x}_{\phi/2}, \tag{2.168}$$

$$\hat{S}^\dagger(r)\hat{p}_{\phi/2}\hat{S}(r) = \exp(|r|)\hat{p}_{\phi/2}. \tag{2.169}$$

Therefore, the squeezing operator squeezes one of the quadratures by a factor $\exp(-|r|)$ and anti-squeezes the other quadrature by factor $\exp(|r|)$. The parameter r is usually called *squeezing parameter*

07 December 2024 17:52:47

and the value of $10\log_{10}[\exp(-2|r|)]$ is often called *squeezing level*. The squeezing level shows how small the variances of the squeezed states are compared to the vacuum states in a decibel scale. For the sake of simplicity, unless stated otherwise, we will assume $r \in \mathbb{R}$. In such a case, $r > 0$ corresponded to squeezing in $\hat{x}$, while $r < 0$ corresponded to squeezing in $\hat{p}$.

Next, let us consider the Fock basis representation of squeezed states. To do so, we notice the following relation:

$$\hat{S}(r)\hat{a}\hat{S}^{\dagger}(r)\hat{S}(r)\,|0\rangle = 0. \tag{2.170}$$

The above equation shows that the squeezed states $\hat{S}(r)\,|0\rangle$ are eigenstates of the operator $\hat{S}(r)\hat{a}\hat{S}^{\dagger}(r)$. Then, if we let $\hat{S}(r)\,|0\rangle = \sum_n c_n\,|n\rangle$, we get

$$(\cosh r\hat{a} + \sinh r\hat{a}^{\dagger})\sum_{n=0}^{\infty} c_n\,|n\rangle = 0. \tag{2.171}$$

Solving the recursive equation of the coefficient c_n and considering the normalization condition, we arrive at

$$|0_r\rangle = \frac{1}{\sqrt{\cosh r}}\sum_{m=0}^{\infty}\left(-\frac{\tanh r}{2}\right)^m \frac{\sqrt{(2m)!}}{m!}\,|2m\rangle. \tag{2.172}$$

A remarkable thing about the squeezed states is that they consist of only the even Fock state components. A physical reason behind this lies in the parity of the wave function. Experimentally, the even parity property of the squeezed states is connected to the fact that squeezed states can be generated from the parametric down-conversion process, a process that produces coherent photon pairs.

We can also write down the wave function $\psi_r(x)$ and $\tilde{\psi}_r(p)$ and Wigner function $W_r(x,p)$ of the squeezed states as

$$\psi_r(x) = \frac{1}{(\pi\hbar e^{-2r})^{1/4}}\exp\left(-\frac{x^2}{2\hbar e^{-2r}}\right), \tag{2.173}$$

$$\tilde{\psi}_r(p) = \frac{1}{(\pi\hbar e^{2r})^{1/4}}\exp\left(-\frac{p^2}{2\hbar e^{2r}}\right), \tag{2.174}$$

$$W_r(x,p) = \frac{1}{\pi\hbar}\exp\left(-\frac{x^2}{\hbar e^{-2r}} - \frac{p^2}{\hbar e^{2r}}\right). \tag{2.175}$$

As expected, both wave functions and Wigner functions of the squeezed states are Gaussian functions, similar to the vacuum states. Moreover, their forms correspond to scaling from the vacuum states as $x \to xe^r$ and $p \to pe^{-r}$. The Wigner function of the squeezed state is plotted in Fig. 2.5. Also, note that because the wave functions of the squeezed states are even functions, their Fock basis representations consist only of even components.

In many ideal CV quantum information protocols, quadrature eigenstates are used as the physical resources. However, as they are unphysical, they are usually approximated with the squeezed states.

07 December 2024 17:52:47

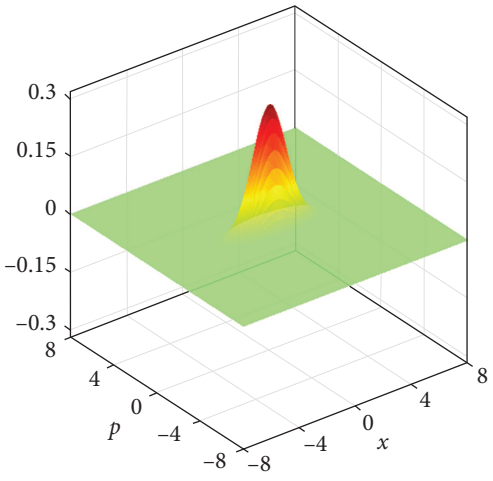

FIG. 2.5
Wigner function of a squeezed state with $r = 0.5$.

This is a valid approximation as squeezed states approach quadrature eigenstates in the infinite squeezing limit. For example, x-squeezed states, $\hat{S}(r)\,|0\rangle$ with $r > 0$, approach $|x = 0\rangle$ as $r \to \infty$. We should, however, be wary that continuous-variable algorithms or protocols that work in the ideal limits (usually called infinite squeezing limits) do not necessarily work in the actual physical setting (usually called finite squeezing limits). We urge the readers to be skeptical about any CV quantum computation papers that do not discuss situations in the finite squeezing limits as the infinite squeezing limits are unattainable and unphysical.

2.4.7.1 Experimental generation of squeezed lights

As squeezed lights are fundamental resources in almost all experiments and protocols in quantum optics, we will briefly introduce the experimental generation of squeezed lights. The first experimental realizations of squeezed light sources were realized almost simultaneously by Slusher *et al.* (1985) and Wu *et al.* (1986). Their experimental setups are shown in Fig. 2.6. Interestingly, these two experiments utilize different nonlinear optical processes, namely, four wave mixing (FWM) and spontaneous parametric down conversion (SPDC).

When we pass electromagnetic wave through mediums such as crystals, electrical polarization **P** is induced and affects the electric fields. Although it is often taken that **P** is proportional to the electric fields **E**, in general, i-component ($i = x, y, z$) of **P** is related to the electric field via

$$P_i = \chi_{ij}^{(1)} E_j + \chi_{ijk}^{(2)} E_j E_k + \chi_{ijkl}^{(3)} E_j E_k E_l + \cdots. \tag{2.176}$$

Note that we use Einstein's summation notation here. A medium whose $\chi^{(1)}$ is dominant is usually called linear optical medium. The optical medium that involves the optical effect with $\chi^{(n)}$, where $n \geq 2$ is called the nonlinear optical medium and the optical process involved is called nth order nonlinear effect. SPDC and FWM are a type of second-order and third-order nonlinear optical effect, respectively.

For the sake of physical intuitions, we will try to intuitively explain how SPDC and FWM process can generate squeezed lights. Fock basis representation in Eq. (2.172) suggests that squeezed lights should be generated from the optical process that creates coherent photon pairs. If we solve classical Maxwell equations with electric polarization included, it can be shown that second-order nonlinear optical process involves three electric fields and third-order nonlinear optical process involves four electric fields. In SPDC, nonlinear crystal is pumped with an electric field of angular frequency 2ω and the pump beam is converted into two frequency components ω_1 and ω_2, which satisfy $2\omega = \omega_1 + \omega_2$

07 December 2024 17:52:47

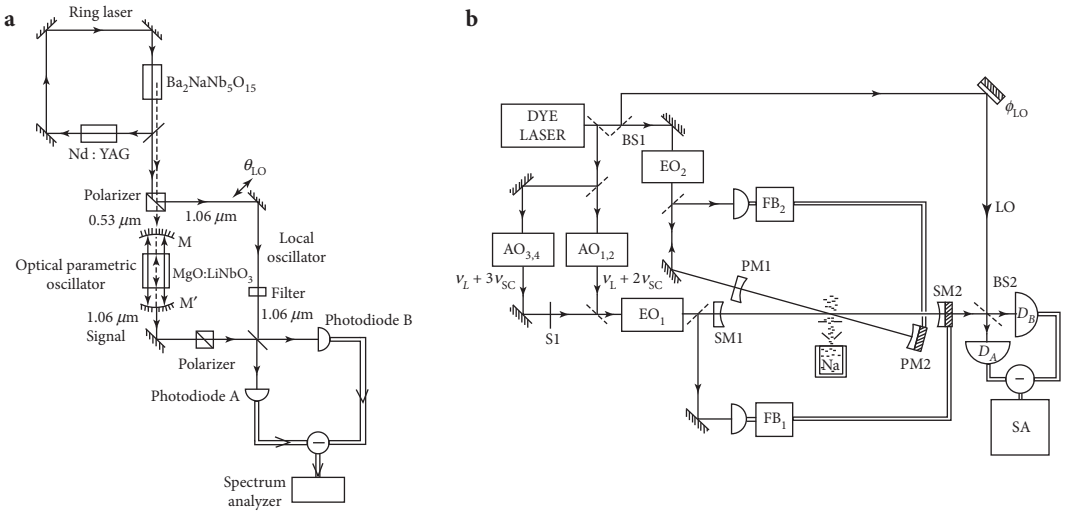

FIG. 2.6
Setup of one of the first squeeze light generation experiments based on (a) spontaneous parametric down conversion (Wu *et al.*, 1986) (http://dx.doi.org/10.1103/PhysRevLett.57.2520) and (b) four wave mixing (Slusher *et al.*, 1985) (http://dx.doi.org/10.1103/PhysRevLett.55.2409).

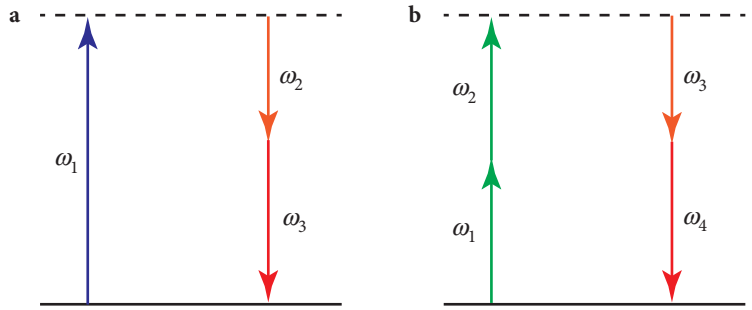

FIG. 2.7
Conceptual diagram of nonlinear optical process. (a) Spontaneous parametric down conversion. (b) Four wave mixing.

[Fig. 2.7(a)]. In a special case where $\omega_1 = \omega_2 = \omega$, this process is called degenerate parametric down conversion (DPDC). In the quantum regime, the DPDC process is equivalent to the generation of photon pairs and if we consider the 2ω pump beam as classical light, we can write down the Hamiltonian as

$$\hat{H}_{\mathrm{DPCP}} = i(\epsilon \hat{a}^2 - \epsilon^* \hat{a}^{\dagger 2}), \tag{2.177}$$

07 December 2024 17:52:47

where ϵ is a parameter that includes the pump power and the strength of the nonlinearity of the crystal. The form of the Hamiltonian is exactly that of the squeezing operator in Eq. (2.162). In FWM case, the situation is also similar but instead two photons of the pump beams are absorbed before coherent photon pairs are emitted [Fig. 2.7(b)]. The condition regarding the angular frequency is equivalent to the conservation of energy. In addition to this, *the phase-matching condition* must also be satisfied. Phase-matching condition corresponded to momentum conservation and for SPDC, it can be written as

$$\mathbf{k}_{2\omega} = \mathbf{k}_{\omega_1} + \mathbf{k}_{\omega_2}, \tag{2.178}$$

where $\mathbf{k}$ are the wave vectors. In the DPDC case, if we want these wave vectors to be collinear, then it can be shown that the refractive index n of the nonlinear crystal must satisfy

$$n(2\omega) = n(\omega). \tag{2.179}$$

For most optical medium, this condition is not satisfied as there are dispersions, making the refractive index at ω and 2ω different. To satisfy the phase-matching condition, various techniques such as birefringence or *quasi-phase matching*. In the latter, the polarity of the nonlinear crystal is periodically switched so that the phase-matching condition is satisfied. For more information regarding nonlinear optics, we recommend Ref. Yariv and Yeh (2006).

After the first two SPDC and FWM experiments, it turns out that these two methods work well so that despite many technological developments, squeezed light generations are, in principle, based on either of these methods, depending on the nature of the physical systems used.

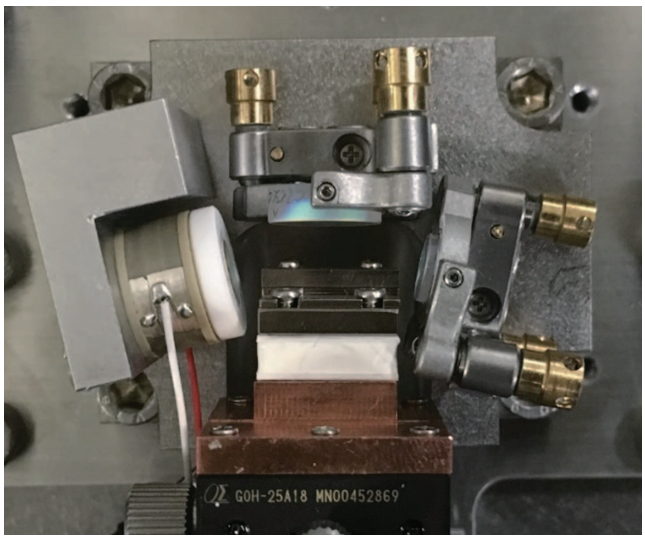

FIG. 2.8
Picture of an OPO that was used in the generation of two-dimensional cluster states (Asavanant *et al.*, 2019).

Optical experiments can be roughly categorized into two groups, depending on the light sources: continuous-wave (CW) experiments and pulsed-laser experiments. In the CW experiments, because the nonlinearities are often weak, the nonlinear crystal is often accompanied by an optical cavity to increase the effective nonlinearity. This kind of setup is called *optical parametric oscillator (OPO)* and is a de facto standard for the generation of squeezed light in CW experiments (see Fig. 2.8 for an example of actual OPO). Strictly speaking, the Hamiltonian of the OPO is not so simple and has to be treated as an open quantum system in which the fields outside of the OPO interact with the intracavity mode. Analysis of the OPO was done by Collett and Gardiner (1984) and we show some of the mathematical treatments in

07 December 2024 17:52:47

the Appendix. On the other hand, although squeezed lights can be generated simply by pumping the nonlinear crystal in pulsed-laser experiments, there are some other technical difficulties. In particular, measuring squeezed lights generated in pulse setup tends to be difficult as the spatial modes of the squeezed lights are not completely determined and there are also dispersions that change the mode of the squeezed lights. This is in contrast with CW experiments, where the spatial modes are completely determined by the cavity of the OPO. The current world record of the squeezing level of 15 dB in the optical system is achieved by CW setup at the wavelength of 1064 nm (Vahlbruch *et al.*, 2016).

There are also research studies aiming to integrate squeezed light sources onto waveguide chips. These types of sources, while still somewhat lossy, hold a promising potential as components for a large-scale optical quantum computer. One of the advantages over the free space OPO and the usual nonlinear crystals is that a broadband squeezed light can be generated from the waveguide system. Recently, there was a report of a THz-order wave guide squeezed light source where the squeezed light of about −6 dB was observed (Kashiwazaki *et al.*, 2020).

2.4.8 Schrödinger's cat states

Anyone who studies quantum mechanics would have heard of the infamous Schrödinger's cat paradox. This paradox was used to point out the possibility of the quantum superposition, which is sometimes (wrongly) said as until we open the box, Schrödinger's cat is alive and dead at the same time. It also raises another open question about whether we can have macroscopic objects in the state of superposition or not (i.e., being alive or dead is macroscopic).

In quantum optics, the most "classical" states are coherent states. Thus, we can consider the superposition of coherent states. Such superpositions of coherent states are called *Schrödinger's cat states* (or simply cat states) and here we will consider two types of cat states,

$$|\mathrm{Cat}(\alpha,\pm)\rangle = N_{\alpha,\pm}(|\alpha\rangle \pm |-\alpha\rangle), \tag{2.180}$$

where the $\pm$ signs tell us the phase of the superposition and each corresponding cat state is called plus cat state and minus cat state, respectively. The normalization factor is also given by

$$N_{\alpha,\pm} = \frac{1}{\sqrt{2\left[1 \pm \exp\left(-2\,|\alpha|^2\right)\right]}}. \tag{2.181}$$

Note that at the limit of $|\alpha| \to \infty$, the normalization factor approaches $1/\sqrt{2}$, which is expected as $|\alpha\rangle$ and $|-\alpha\rangle$ are orthogonal at such limit.

With Eq. (2.143), we write down the Fock representation of cat states as

$$|\mathrm{Cat}(\alpha,+)\rangle = \frac{1}{\sqrt{\cosh|\alpha|^2}} \sum_{m=0}^{\infty} \frac{\alpha^{2m}}{\sqrt{(2m)!}} |2m\rangle, \tag{2.182}$$

$$|\mathrm{Cat}(\alpha,-)\rangle = \frac{1}{\sqrt{\sinh|\alpha|^2}} \sum_{m=0}^{\infty} \frac{\alpha^{2m+1}}{\sqrt{(2m+1)!}} |2m+1\rangle. \tag{2.183}$$

07 December 2024 17:52:47

Depending on the phase of the superposition, cat states contain only even or odd Fock basis. In addition to the Fock basis, we can find the wave functions and the Wigner functions. For the sake of simplicity, let us assume that $\alpha = x_0/\sqrt{2\hbar}$ with $x_0 \in \mathbb{R}$. Then, the wave functions are

$$\psi_{\alpha,+}(x) = \frac{N_{\alpha,+}}{(\pi\hbar)^{1/4}}\left[\exp\left(-\frac{(x-x_0)^2}{2\hbar}\right) + \exp\left(-\frac{(x-x_0)^2}{2\hbar}\right)\right], \tag{2.184}$$

$$\tilde{\psi}_{\alpha,+}(p) = \frac{2N_{\alpha,+}}{(\pi\hbar)^{1/4}}\exp\left(-\frac{p^2}{2\hbar}\right)\cos\left(\frac{1}{\hbar}x_0 p\right), \tag{2.185}$$

$$\psi_{\alpha,-}(x) = \frac{N_{\alpha,-}}{(\pi\hbar)^{1/4}}\left[\exp\left(-\frac{(x-x_0)^2}{2\hbar}\right) - \exp\left(-\frac{(x-x_0)^2}{2\hbar}\right)\right], \tag{2.186}$$

$$\tilde{\psi}_{\alpha,-}(p) = -\frac{2iN_{\alpha,-}}{(\pi\hbar)^{1/4}}\exp\left(-\frac{p^2}{2\hbar}\right)\sin\left(\frac{1}{\hbar}x_0 p\right). \tag{2.187}$$

These wave functions have many distinctive characteristics. First, for $\psi_{\alpha,\pm}(x)$, despite the difference near $x = 0$, both $\psi_{\alpha,+}(x)$ and $\psi_{\alpha,-}(x)$ have two Gaussian peaks at $x \approx \pm x_0$ due to the amplitudes of the coherent states. On the other hand, for $\tilde{\psi}_{\alpha,\pm}(p)$, there are oscillatory structures due to the quantum interference and reflect the interference phase. This is different from the coherent states whose amplitudes are in only the x basis, whose wave functions in p basis will be just Gaussian distributions centered at $p = 0$. As the physical quantities we measure are quadratures, the plus cat and the minus cat will have almost the same distributions of x quadrature and the measurement of the quadrature p, i.e., the interference fringes, is required to distinguish them.

We can also look at the Wigner functions. It is actually very educative to compare the Wigner functions of mixed coherent states $\hat{\rho}_{\text{mixed}} = (|\alpha\rangle\langle\alpha| + |-\alpha\rangle\langle-\alpha|)/2$ to that of the cat states. First, the Wigner function of the mixed coherent states can be easily written down as

$$W_{\text{mixed}}(x,p) = \frac{1}{2}[W_\alpha(x,p) + W_{-\alpha}(x,p)]. \tag{2.188}$$

The Wigner function of the mixed coherent states is simply two Gaussian peaks without any distinctive features and is positive throughout the whole phase space. On the other hand, the Wigner function of the cat states $W_{\alpha,\pm}(x,p)$ can be calculated as

$$W_{\alpha,\pm}(x,p) = 2N_{\alpha,\pm}^2\left[W_{\text{mixed}}(x,p) \pm \frac{1}{\pi\hbar}\exp\left(-\frac{x^2+p^2}{\hbar}\right)\cos\left(\frac{2}{\hbar}x_0 p\right)\right] \tag{2.189}$$

and is plotted in Fig. 2.9. There is an additional interference term, which contributes to the interference fringes and the negative part of the Wigner functions. The quantum interference between quantum states whose Wigner functions have no negative regions can result in a Wigner function with negativity. The negativity of the Wigner function is an important evidence of nonclassicality, as quantum states whose Wigner functions have negative regions are without a doubt nonclassical states. Do note that the converse, i.e., positive Wigner functions, is the sign of classical states, is not necessarily true. An example of this is the squeezed vacuum states that are nonclassical states but do not possess negative regions.

07 December 2024 17:52:47

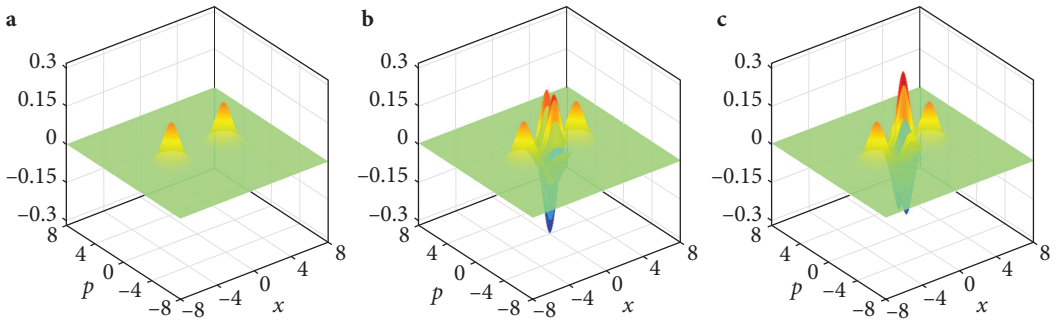

FIG. 2.9
Wigner functions of mixed coherent states and cat states for $\alpha = 2$. (a) $\frac{1}{2}(|\alpha\rangle\langle\alpha| + |-\alpha\rangle\langle-\alpha|)$, (b) $|\mathrm{Cat}(\alpha, -)\rangle$, (c) $|\mathrm{Cat}(\alpha, +)\rangle$.

2.5 QUANTUM OPERATIONS AND UNIVERSALITY

In this section, we will discuss how to implement quantum operations, thus doing the quantum computation using the CV system. Some of the operators such as displacement operator and squeezing operator will be the operators we have already encountered. However, rather than acting these operators on certain states (namely, vacuum state) to define some particular quantum states, we consider what happens to arbitrary quantum states when these operations are implemented. But first, let us briefly review the quantum operations in the qubit system.

2.5.1 A brief review on operations on qubits systems

As we have mentioned in Sec. 2.4.1, single-qubit quantum states $\hat{\rho}_{\mathrm{qubit}}$ can be represented as vectors inside the Bloch sphere. Then, qubit operations can be considered as rotations on Bloch sphere. In Sec. 2.4.1, we have introduced Pauli matrices. In fact, we can consider unitary operations $\hat{\sigma}_x$, $\hat{\sigma}_y$, and $\hat{\sigma}_z$. These Pauli operators corresponded to 180° rotation on the Bloch sphere with respect to each corresponding axis. Pauli operators satisfy the following relation:

$$\hat{\sigma}_z\hat{\sigma}_x = i\hat{\sigma}_y. \tag{2.190}$$

The above relation also holds for the cyclic permutations. In addition to the Pauli operations, there are also two other important operations called Hadamard gate and phase gate. Hadamard gate $\hat{H}$ transform the eigenvector of $\hat{\sigma}_z$, $|0\rangle$, and $|1\rangle$, as

$$|0\rangle \to \frac{1}{\sqrt{2}}(|0\rangle + |1\rangle), \tag{2.191}$$

$$|1\rangle \to \frac{1}{\sqrt{2}}(|0\rangle - |1\rangle). \tag{2.192}$$

07 December 2024 17:52:47

From the above equation, it can be easily shown that $\hat{H}^2 = \hat{I}$, meaning that implementing the Hadamard gate twice returns the quantum states to the original states. Moreover, we can look at how the Hadamard gate transforms the Pauli operator: using the Heisenberg picture transformation and the fact that the inverse of the Hadamard gate is itself, we get

$$\hat{H}\hat{\sigma}_z\hat{H} = \hat{\sigma}_x, \tag{2.193}$$
$$\hat{H}\hat{\sigma}_x\hat{H} = \hat{\sigma}_z, \tag{2.194}$$
$$\hat{H}\hat{\sigma}_y\hat{H} = -\hat{\sigma}_y. \tag{2.195}$$

Thus, the Hadamard gate swaps the Pauli-x and Pauli-z operator, while adding the minus sign to the Pauli-y operator. It can be shown more rigorously that the Hadamard gate corresponds to the 180° rotation along $(a, b, c) = (1/\sqrt{2}, 0, 1/\sqrt{2})$ axis of the Bloch sphere.

On the other hand, the phase gate $\hat{P}$ simply adds an additional phase to the eigenvector $|1\rangle$ of the $\hat{\sigma}_z$,

$$|0\rangle \rightarrow |0\rangle, \tag{2.196}$$
$$|1\rangle \rightarrow i\,|1\rangle. \tag{2.197}$$

As phase gate leaves eigenvectors of $\hat{\sigma}_z$ unchanged (up to the global phase), this gate corresponded to 90° rotation along the z axis. This is even clearer if we look at how the phase gate transforms the Pauli operators:

$$\hat{P}^\dagger\hat{\sigma}_z\hat{P} = \hat{\sigma}_z, \tag{2.198}$$
$$\hat{P}^\dagger\hat{\sigma}_x\hat{P} = -\hat{\sigma}_y, \tag{2.199}$$
$$\hat{P}^\dagger\hat{\sigma}_y\hat{P} = \hat{\sigma}_x. \tag{2.200}$$

The Hadamard gate and the phase gate are examples of what are called *Clifford gates*. Clifford gates are gates that (roughly speaking) take eigenstates of the Pauli operators to other eigenstates. In a more rigorous formulation, Clifford operations or Clifford group are unitary operations that take a Pauli operator to another Pauli operator[3]. Obviously, however, that with only eigenstates of the Pauli operators, Pauli operators, and Clifford operations, we cannot realize arbitrary quantum states on the single-qubit Bloch sphere. As such, we need to add at least one operation outside of the Clifford operations, which are called *non-Clifford operations*.

As an example of non-Clifford operations, we consider a quantum gate called $\pi/8$ gate. The effects of the $\pi/8$ gate on the qubit $a|0\rangle + b|1\rangle$ can be written as

$$a\,|0\rangle + b\,|1\rangle \rightarrow a\exp\left(-i\frac{\pi}{8}\right)|0\rangle + b\exp\left(i\frac{\pi}{8}\right)|1\rangle. \tag{2.201}$$

If we ignore the global phase, then the matrix T corresponding to this transformation is

$$T = \begin{pmatrix} 1 & 0 \\ 0 & \exp\left(i\frac{\pi}{4}\right) \end{pmatrix}. \tag{2.202}$$

[3] In a more rigorous mathematical term, the Clifford group preserves Pauli operation under conjugation.

07 December 2024 17:52:47

This matrix corresponded to 45° rotation along the z axis. As $T^4 = \sigma_z$, this operation is sometimes also called $\sqrt[4]{Z}$ gate. With single-qubit Clifford gates and non-Clifford gates, arbitrary single-qubit operations can be realized. Therefore, to realize *universality* for single-qubit operations, we need arbitrary Clifford gates and any single non-Clifford gate (Nielsen and Chuang, 2000).

In addition to the single-qubit universality, when we consider multi-qubit operations, we also need multi-qubit gates. In the qubit system, there are two representative two-qubit gates: controlled-not (CNOT) gate and controlled-Z (CZ) gate. If we have two qubits whose combined basis can be written as $|i\rangle \otimes |j\rangle$ $(i, j = 0, 1)$ and we take the first qubit as a control qubit, then CNOT gate transforms the basis as

$$|i\rangle \otimes \left|j\right\rangle \rightarrow |i\rangle \otimes \left|(i+j) \bmod 2\right\rangle. \tag{2.203}$$

In a way, CNOT gate corresponds to a binary addition. On the other hand, CZ gate changes the basis as

$$|i\rangle \otimes \left|j\right\rangle \rightarrow (-1)^{ij} |i\rangle \otimes \left|j\right\rangle. \tag{2.204}$$

It can be easily shown that CNOT gate and CZ gate are related via local Clifford operation and either one of them is sufficient for multi-qubit operations. CNOT gate and CZ gate both have analogous gates in CV setting as we will in Sec. 2.5.4.

2.5.2 Universality and classical simulatability

In CV systems, although it is possible to categorize the quantum gates similarly to the qubit systems, let us first look at how universality is defined in the CV system. The term *universality* usually means the capability to implement arbitrary operations on the system of our interest. In reality, however, it is not so feasible to have a physical system that can directly implement arbitrary operations. Instead, we usually consider and try to realize a finite number of operations that can be used to generate arbitrary operations. This set of operation is usually called the universal gate set. The concept of the universal gate set is similar to the classical digital computer where any multi-input logic gate can be constructed using only NAND gate.

To consider the classification of CV quantum operations, let us again use a very useful Eq. (2.147). If we let our Hamiltonian $\hat{H}$ be a polynomial in $\hat{x}$ and $\hat{p}$, then Eq. (2.147) shows that the transformations of the quadrature operators due to this Hamiltonian depend on the commutation relation between the quadrature operators and $\hat{H}$. If we note the following relations:

$$[\hat{x}, \hat{p}^n] = in\hbar\hat{p}^{n-1}, \tag{2.205}$$

$$[\hat{p}, \hat{x}^n] = -in\hbar\hat{x}^{n-1}, \tag{2.206}$$

then it is evident that if the Hamiltonian $\hat{H}$ is at most quadratic polynomial (i.e., $n \leq 2$), the Heisenberg picture transformation of the quadrature operator is linear transformations. These linear transformations are also called *Gaussian operations* as these operations transform quantum states whose Wigner

07 December 2024 17:52:47

functions are Gaussian (also called Gaussian states) into other Gaussian states. To realize a nonlinear transform of the quadrature operators, we need a Hamiltonian that has $n \geq 3$. This kind of operation is called *non-Gaussian operations* as they can change Gaussian states into non-Gaussian states, i.e., quantum states whose Wigner functions are non-Gaussian.

There are two important theorems regarding quantum operations in the CV system. The first result is about classical simulatability, which was found by Bartlett *et al.* (2002). The second is regarding the universal gate set by Lloyd and Braunstein (1999).

Theorem 2.4. *Any quantum algorithms that start from vacuum states (or any Gaussian state), followed by Gaussian operations, measurements of the quadrature operators, and Gaussian operations depending on such measurement results, can be "efficiently" simulated by the classical computer. Here, "efficiently" means that the simulation on the classical computer can be done on the time scale that scales polynomially with the size of the computation.*

Theorem 2.5. *Arbitrary CV unitary operations can be realized if we can implement arbitrary multi-mode Gaussian operations and at least one non-Gaussian operation.*

For some readers, these two theorems might seem redundant. We note, however, that the first theorem only states the condition for classical simulatability, meaning that the assumptions must at very least be broken to achieve useful quantum computation that is beyond the classical computer. Although we can simply add non-Gaussian operation and achieve universality, it is also possible to consider a setup or algorithm where the input states or the measurements are non-Gaussian, not the operations. For readers who are familiar with qubits, this theorem is an extension of the Gottesman–Knill theorem in the qubit system (Nielsen and Chuang, 2000).

The theorem about the universality in the CV system is the reason why the term "Gaussian" in the CV system is usually associated with the term "Clifford" in the qubit system. Although there are some correspondences, there exist subtle differences. Clifford operations are defined through the Pauli operators, meaning that they are defined related to the logical-level operations rather than the physical-level phenomena. On the other hand, the term Gaussian operations are defined via the actual physical Hamiltonian, i.e., operations whose Hamiltonian is the polynomial that is at most quadratic in the quadrature operator. In that sense, the definition of the Gaussian operations is not directly associated with any particular logical-level encoding of the quantum information. Figure 2.10 shows the classification of the CV quantum operation.

2.5.3 Weyl–Heisenberg group

Now, let us look at some basic quantum operations in the CV system. First, we will look at the displacement operations that constitute a group called *Weyl–Heisenberg group*, a group that is analogous to the Pauli group in the qubit system.

07 December 2024 17:52:47

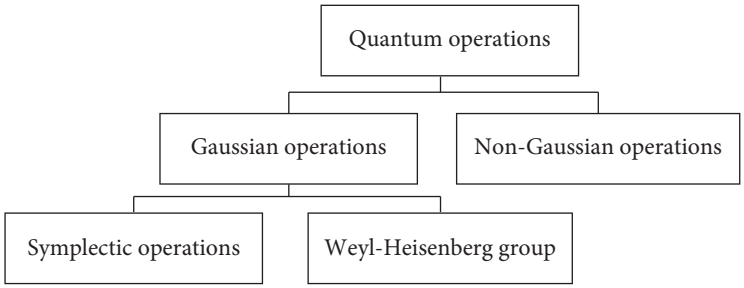

FIG. 2.10
Classification of quantum operation in CV system.

We can extend the displacement operators on single-mode quantum states [Eqs. (2.152) and (2.153)] to the N-mode quantum states as

$$\hat{D}_{\mathbf{x}}(\mathbf{m}_x) = \exp\left(-\frac{i}{\hbar}\mathbf{m}_x^{\mathrm{T}}\hat{\mathbf{p}}\right), \tag{2.207}$$

$$\hat{D}_{\mathbf{p}}(\mathbf{m}_p) = \exp\left(\frac{i}{\hbar}\mathbf{m}_p^{\mathrm{T}}\hat{\mathbf{x}}\right), \tag{2.208}$$

where $\hat{\mathbf{x}} = (\hat{x}_1 \quad \hat{x}_2 \quad \ldots \quad \hat{x}_N)^{\mathrm{T}}$, $\mathbf{m}_x = (m_{x,1} \quad m_{x,2} \quad \ldots \quad m_{x,N})^{\mathrm{T}}$, and so on. Displacement operators transform quadrature operators in the Heisenberg picture as

$$\hat{D}_{\mathbf{x}}^{\dagger}(\mathbf{m}_x)\hat{\mathbf{x}}\hat{D}_{\mathbf{x}}(\mathbf{m}_x) = \hat{\mathbf{x}} + \mathbf{m}_x, \tag{2.209}$$

$$\hat{D}_{\mathbf{p}}^{\dagger}(\mathbf{m}_p)\hat{\mathbf{p}}\hat{D}_{\mathbf{p}}(\mathbf{m}_p) = \hat{\mathbf{p}} + \mathbf{m}_p. \tag{2.210}$$

Using the definition of the Wigner function in Eq. (2.105), we can also show that the Wigner function of the quantum states that have been displaced $W_{\mathbf{m}_x,\mathbf{m}_p}(\mathbf{x},\mathbf{p})$ is related to the original Wigner function $W_{\text{initial}}(\mathbf{x},\mathbf{p})$ as

$$W_{\mathbf{m}_x,\mathbf{m}_p}(\mathbf{x},\mathbf{p}) = W_{\text{initial}}(\mathbf{x}-\mathbf{m}_x, \mathbf{p}-\mathbf{m}_p), \tag{2.211}$$

which corresponds to simply displacing the original Wigner function.

2.5.4 Symplectic transformations

Gaussian operations correspond to the linear transformations of the quadrature operators. Arbitrary linear transformation of the quadrature operators of N-mode quantum states is given by

$$\hat{\mathbf{q}}' = \mathbf{S}\hat{\mathbf{q}} + \mathbf{c}, \tag{2.212}$$

where $\hat{\mathbf{q}} = (\hat{\mathbf{x}} \quad \hat{\mathbf{p}})^{\mathrm{T}}$, $\mathbf{S}$ is a $2N \times 2N$ matrix, and $\mathbf{c}$ is a $2N \times 1$ scalar vector. Note that when taking the transpose, we are not taking the transpose of the operator but only of the elements of the vectors or the matrices. Since $\mathbf{c}$ corresponds to the displacement operations, let us consider only the $\mathbf{S}$ part. We can

07 December 2024 17:52:47

show that for physically realizable operation, $\mathbf{S}$ is a symplectic matrix and the corresponding operation is called *symplectic operations*. Therefore, we can state the following regarding arbitrary multimode Gaussian operations,

Theorem 2.6. *Arbitrary multimode Gaussian operations can be realized with the combination of the symplectic transformations and displacement operations.*

This can be proved by considering the commutation relation of the quadrature operators and the proof is given below.

Proof. The commutation relation of the quadrature operators can be compactly written using $\hat{\mathbf{q}}$ as

$$\hat{\mathbf{q}}\hat{\mathbf{q}}^{\mathrm{T}} - \left(\hat{\mathbf{q}}\hat{\mathbf{q}}^{\mathrm{T}}\right)^{\mathrm{T}} = i\hbar\boldsymbol{\Omega}, \tag{2.213}$$

where the matrix $\boldsymbol{\Omega}$ is defined as

$$\boldsymbol{\Omega} \equiv \begin{pmatrix} \mathbf{0}_N & \mathbf{I}_N \\ -\mathbf{I}_N & \mathbf{0}_N \end{pmatrix}, \tag{2.214}$$

with $\mathbf{0}_N$ and $\mathbf{I}_N$ being the $N \times N$ zero matrix and identity matrix, respectively. After the linear transformation, the new quadrature operators $\hat{\mathbf{q}}'$ must also satisfy the commutation relation in Eq. (2.89). Therefore, we arrive at the constraint of the matrix $\mathbf{S}$ as

$$\mathbf{S}\boldsymbol{\Omega}\mathbf{S}^{\mathrm{T}} = \boldsymbol{\Omega}. \tag{2.215}$$

The above equation is the equation defining symplectic matrix, meaning that we can conclude that $\mathbf{S}$ is symplectic. □

Next, let us consider how to construct arbitrary symplectic matrix $\mathbf{S}$. From our knowledge in basic linear algebra, matrix decompositions are usually not unique and there are usually multiple ways to decompose the same matrix. Let us consider a decomposition method called *Bloch–Messiah decomposition*, which is closely related to the singular value decomposition. In Bloch–Messiah decomposition, any symplectic matrix $\mathbf{S}$ can be expressed as

$$\mathbf{S} = \mathbf{U}' \begin{pmatrix} \boldsymbol{\Lambda} & \mathbf{0}_N \\ \mathbf{0}_N & \boldsymbol{\Lambda}^{-1} \end{pmatrix} \mathbf{U}. \tag{2.216}$$

$\mathbf{U}$ and $\mathbf{U}'$ are $2N \times 2N$ orthogonal matrices, $\boldsymbol{\Lambda} = \mathrm{Diag}(\lambda_1, \lambda_2, \ldots, \lambda_N)$ with $\lambda_i > 0$. If we could realize operations that correspond to the orthogonal matrices and the matrix between them, an arbitrary symplectic matrix can be realized. If we recall the section about the squeezed vacuum states, it is obvious that the $\boldsymbol{\Lambda}$ part corresponds to the single-mode squeezing operation. For $r \in \mathbb{R}$, the squeezing operator on a single-mode state $\hat{S}(r)$ is

$$\hat{S}(r) = \exp\left[\frac{r}{2}(\hat{a}^2 - \hat{a}^{\dagger 2})\right]. \tag{2.217}$$

07 December 2024 17:52:47

Then, the transformation of the quadrature operator due to the squeezing operator is

$$\hat{S}^{\dagger}(r)\hat{x}\hat{S}(r) = \hat{x}e^{-r}, \tag{2.218}$$

$$\hat{S}^{\dagger}(r)\hat{p}\hat{S}(r) = \hat{p}e^{r}, \tag{2.219}$$

which, indeed, correspond to the $\mathbf{\Lambda}$ part in Eq. (2.216).

Next, let us move to the orthogonal matrix part. For the sake of simplicity, let us first consider the single-mode case where $N = 1$. In such a case, an orthogonal matrix $\mathbf{R}(\theta)$ can be parameterized as

$$\mathbf{R}(\theta) = \begin{pmatrix} \cos\theta & \sin\theta \\ -\sin\theta & \cos\theta \end{pmatrix}. \tag{2.220}$$

The above matrix is obviously a rotation matrix, which means that for a single-mode state, the necessary orthogonal matrix part can be realized via rotation in phase space. This operation is called phase shifting operation or phase rotation operation and we will denote this operation with $\hat{R}(\theta)$ which can be written down as

$$\hat{R}(\theta) = \exp(-i\theta\hat{a}^{\dagger}\hat{a}). \tag{2.221}$$

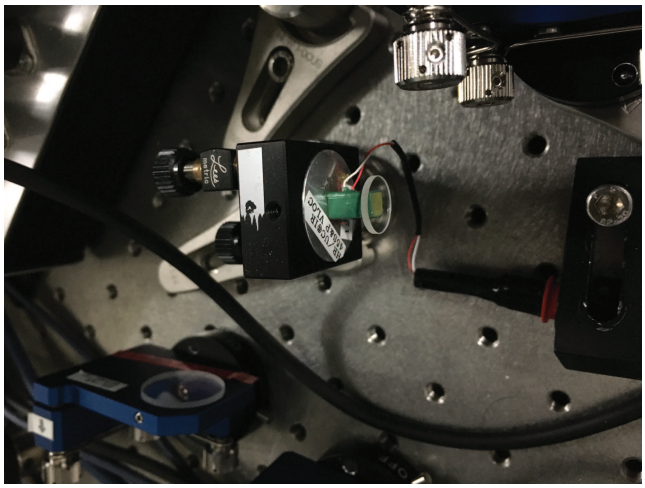

FIG. 2.11
Picture of a mirror with a piezoelectric which is used for adjusting the path length, thus implementing phase rotation operation.

If we look at the form of $\hat{R}(\theta)$, we can see that it simply corresponds to the free evolution of the electromagnetic wave. Therefore, the phase rotation operation is relatively easy to realize experimentally; one simply changes the distance or the time duration that the electromagnetic wave propagates (Fig. 2.11).

For the multi-mode orthogonal matrix, it can be shown that such transformations can be realized using passive linear optics. The word "passive" here means no energy is added to the system. In contrast to this, the squeezing operations change the total energy of the system as it is obvious that squeezed vacuum states have more energy than the vacuum states. For a symplectic transformation that consists of only the orthogonal matrix part, i.e., $\hat{\mathbf{q}}' = \mathbf{U}\hat{\mathbf{q}}$, the Hamiltonian after the transformation is

$$\hat{H} = \frac{1}{2}\hat{\mathbf{q}}'^{\mathrm{T}}\hat{\mathbf{q}}' = \frac{1}{2}\hat{\mathbf{q}}^{\mathrm{T}}\mathbf{U}^{\mathrm{T}}\mathbf{U}\hat{\mathbf{q}} = \frac{1}{2}\hat{\mathbf{q}}^{\mathrm{T}}\hat{\mathbf{q}}, \tag{2.222}$$

07 December 2024 17:52:47

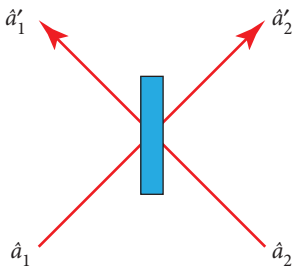

FIG. 2.12
Image of the beamsplitter operation.

which shows that this part of the symplectic transformation preserves the total energy. The most basic passive optical instrument that is used for interacting between two beams is called a *beamsplitter* (Fig. 2.12). A beamsplitter is usually a plate of glass that is coated so that the incident lights are partially reflected and transmitted. When two light beams interfered on the beamsplitter, the lights at the two output ports are the combinations of the original incident lights. In such a sense, a beamsplitter is a two-input two-output optical instrument. Although in some classical optics applications, we use a beamsplitter to split an incident laser light into two beams which makes it seems like an one-input two-output instrument, in quantum optics, a beamsplitter always have two inputs. Even when we do not inject any light into one of the ports, there is still a vacuum state there. This effect of the interference with the vacuum state exists and can be observed experimentally.

The model of a beamsplitter is usually represented using the annihilation operator. Let us consider interference between mode 1 and mode 2. Then, the interference due to the beamsplitter can be written as

$$\begin{pmatrix} \hat{a}_1' \\ \hat{a}_2' \end{pmatrix} = \mathbf{B} \begin{pmatrix} \hat{a}_1 \\ \hat{a}_2 \end{pmatrix}. \tag{2.223}$$

This 2×2 matrix $\mathbf{B}$ is in general complex, and from the passivity of the beamsplitter, it is easy to show that this matrix is a unitary matrix. We can also relate this matrix $\mathbf{B}$ to the transformation of the quadrature as

$$\begin{pmatrix} \hat{x}_1' \\ \hat{x}_2' \\ \hat{p}_1' \\ \hat{p}_2' \end{pmatrix} = \begin{pmatrix} \Re[\mathbf{B}] & -\Im[\mathbf{B}] \\ \Im[\mathbf{B}] & \Re[\mathbf{B}] \end{pmatrix} \begin{pmatrix} \hat{x}_1 \\ \hat{x}_2 \\ \hat{p}_1 \\ \hat{p}_2 \end{pmatrix}. \tag{2.224}$$

From the fact that $\mathbf{B}$ is unitary, it is also trivial to show that the matrix connecting the quadrature is orthogonal. Also, an arbitrary unitary matrix $\mathbf{B}$ can be decomposed into

$$\mathbf{B} = e^{i\Phi} \begin{pmatrix} e^{i\phi_2} & 0 \\ 0 & e^{-i\phi_2} \end{pmatrix} \begin{pmatrix} \cos\theta & -\sin\theta \\ \sin\theta & \cos\theta \end{pmatrix} \begin{pmatrix} e^{i\phi_1} & 0 \\ 0 & e^{-i\phi_1} \end{pmatrix}, \tag{2.225}$$

which shows that the beamsplitter interaction consists of a local phase rotation, the interaction between two beams, followed by another local phase rotation. For most cases, we will ignore the phase rotation part and consider the case where $\mathbf{B}$ is a real matrix. In such a case, we can parameterize $\mathbf{B}$ as

$$\mathbf{B}(\theta) = \begin{pmatrix} \cos\theta & -\sin\theta \\ \sin\theta & \cos\theta \end{pmatrix}. \tag{2.226}$$

From Eq. (2.224), we can see that in the case where $\mathbf{B}$ is real, the beamsplitter transformation does not mix $\hat{x}$ and $\hat{p}$. In the actual experiment, when we buy or design a beamsplitter, rather than the parameter θ, the beamsplitter is characterized by the energy reflectivity R and energy transmittance T.

07 December 2024 17:52:47

In such a case, Eq. (2.226) can be written as

$$\mathbf{B} = \begin{pmatrix} \sqrt{R} & -\sqrt{T} \\ \sqrt{T} & \sqrt{R} \end{pmatrix}. \tag{2.227}$$

At this point, some of the readers might wonder how do we determine which term in Eq. (2.227) has the minus sign as no matter where we put the minus sign, the matrix **B** is unitary. Experimentally, the sign of the beamsplitter can be controlled by controlling the relative phase of the two beams that interfere at the beamsplitter. As such, although the phase term in Eq. (2.225) is important for beamsplitter interaction, they are not so relevant when we consider a beamsplitter as an optical instrument. The unitary operator, which corresponds to the beamsplitter interaction in Eq. (2.226), is

$$\hat{B}(\theta) = \exp\left[-i\frac{\theta}{\hbar}\left(\hat{x}_1 \otimes \hat{p}_2 - \hat{x}_2 \otimes \hat{p}_1\right)\right]. \tag{2.228}$$

Now that we have shown that **U** and **U**′ for the two-mode quantum states can be realized using phase rotation $\hat{R}$ and beamsplitter interaction $\hat{B}$, let us consider how to do this in arbitrary multimode cases. There is a known result that the unitary matrix **U** and **U**′ can be constructed using only beamsplitters (and phase rotations) (Reck *et al.*, 1994). The number of beamsplitters that are needed to realize any orthogonal transformations of the quadrature operators for N-mode quantum states scales on the order of $\approx N^2/2$.

From the above results, we can state one of a possible gate set to realize arbitrary multimode Gaussian operations.

Theorem 2.7. *With single-mode squeezing $\hat{S}(r)$, phase rotation $\hat{R}(\theta)$, and beamsplitter interaction $\hat{B}(\phi)$, arbitrary multimode symplectic operations can be realized. Adding the displacement operations to this, we can realize arbitrary multimode Gaussian operations.*

Although these operations, in addition to non-Gaussian operations, are already sufficient in achieving the universality, for theoretical purpose, we will also consider Shear operation and CV controlled-Z gate. First, let us consider shear operation $\hat{P}(\gamma)$ given by

$$\hat{P}(\gamma) = \exp\left(i\frac{\gamma}{2\hbar}\hat{x}^2\right). \tag{2.229}$$

This operation transforms the quadrature operator as

$$\begin{pmatrix} \hat{x}' \\ \hat{p}' \end{pmatrix} = \begin{pmatrix} 1 & 0 \\ \gamma & 1 \end{pmatrix} \begin{pmatrix} \hat{x} \\ \hat{p} \end{pmatrix}. \tag{2.230}$$

The shear operation leaves the quadrature $\hat{x}$ unchanged, while adding some information regarding $\hat{x}$ quadrature to the $\hat{p}$ quadrature. In some analogy, we can treat the qubit Pauli operator $\hat{\sigma}_z$ and $\hat{\sigma}_x$ on a similar footing to the quadrature operator $\hat{x}$ and $\hat{p}$. In such analogy, the shear operation can be considered as rotation along the z axis of the qubit Bloch sphere. This analogy will be even clearer when we consider GKP qubits in Chap. 6 for which the Shear operation becomes logical-qubit phase gate.

07 December 2024 17:52:47

We can also consider a CV version of the controlled-Z gate $\hat{C}_z(g)$, which is given by a unitary operator

$$\hat{C}_z(g) = \exp\left(i\frac{g}{\hbar}\hat{x}_1 \otimes \hat{x}_2\right). \tag{2.231}$$

Unlike the qubit version of the controlled-Z gate, CV controlled-Z gate has a parameter g which controls the strength of the interaction. The transformation of the quadrature operators due to the controlled-Z gate is

$$\begin{pmatrix} \hat{x}_1' \\ \hat{x}_2' \\ \hat{p}_1' \\ \hat{p}_2' \end{pmatrix} = \begin{pmatrix} 1 & 0 & 0 & 0 \\ 0 & 1 & 0 & 0 \\ 0 & g & 1 & 0 \\ g & 0 & 0 & 1 \end{pmatrix} \begin{pmatrix} \hat{x}_1 \\ \hat{x}_2 \\ \hat{p}_1 \\ \hat{p}_2 \end{pmatrix}. \tag{2.232}$$

The CV controlled-Z gate leaves the quadrature operator $\hat{x}$ unchanged while adding the quadrature $\hat{x}$ of the other mode to the quadrature $\hat{p}$. If we return to the analogy between the qubit and the CV system mentioned in the section about shear operations, we can see that the reason that this operation is called controlled-Z gate is because it leaves the quadrature $\hat{x}$ unchanged similar to how the qubit controlled-Z gate does not change the statistics regarding $\hat{\sigma}_z$.

Here, we state another possible gate set to realize arbitrary Gaussian operation.

Theorem 2.8. *By using the p-quadrature displacement $\hat{D}_p(m_p)$, shear operation $\hat{P}(\gamma)$, controlled-Z gate $\hat{C}_z(g)$, and Fourier transform (which is a 90° rotation in phase space) $\hat{F} \equiv \hat{R}(-\pi/2)$, multimode Gaussian operation can be realized.*

This gate set for multimode Gaussian operations is somewhat closer to the qubit version where the p-displacement corresponds to the Pauli-Z operator, the shear operation corresponds to the phase gate, and the Fourier transform corresponds to the Hadamard gate.

In fact, as we will see in Chap. 3, the original CV one-way quantum computation used these gates in the theoretical formulation and not the beamsplitter interactions and the squeezing operations. Although shear operation and controlled-Z gate are somewhat theoretically nicer as they change only the quadrature $\hat{p}$ and not both, the optical realization of the squeezing operations and the beamsplitter interactions are much easier. Experimentally, shear operations and controlled-Z gates are realized via squeezed vacuum states, beamsplitter interactions in combination with measurements and feedforward operations.

Finally, we briefly state how Gaussian operation transform the Wigner function of the input states.

Theorem 2.9. *For the Gaussian operations that can be represented using the Heisenberg picture in the form of Eq. (2.212), if the initial Wigner function is $W_{\text{initial}}(\mathbf{q})$, then the output Wigner function $W_{\text{out}}(\mathbf{q})$ is given by*

$$W_{\text{out}}(\mathbf{q}) = W_{\text{initial}}(\mathbf{S}^{-1}(\mathbf{q} - \mathbf{c})). \tag{2.233}$$

This means that for the Wigner functions, Gaussian operations are simply linear geometrical transformations.

07 December 2024 17:52:47

2.5.5 Non-Gaussian operations

In addition to arbitrary multimode Gaussian operation, we need at least one non-Gaussian operation to realize universality. Here, we will introduce two operations: cubic phase gate $\hat{U}_{CPG}(\gamma)$ and controlled-controlled-Z (CCZ) gate $\hat{C}_{CZ}(g)$.

In the same spirit as the shear operation, the cubic phase gate is defined as

$$\hat{U}_{CPG}(\gamma) = \exp\left(\frac{i}{3\hbar}\gamma\hat{x}^3\right). \tag{2.234}$$

This operation transforms the quadrature operators in the Heisenberg picture as

$$\begin{pmatrix}\hat{x}'\\ \hat{p}'\end{pmatrix} = \begin{pmatrix}\hat{x}\\ \hat{p}+\gamma\hat{x}^2\end{pmatrix}. \tag{2.235}$$

We observe that the transformation due to the cubic phase gate is nonlinear transformation of the quadrature operator, a signature of the non-Gaussian operations. Cubic phase gate is studied as it is a lowest order of the non-Gaussian gate. Optically, this gate can be realized directly if we have third-order optical nonlinearity.

Another notable non-Gaussian gate is a CCZ gate, which generates entanglement between three parties and is given by the unitary operator,

$$\hat{C}_{CZ}(g) = \exp\left(\frac{i}{\hbar}g\hat{x}_1\otimes\hat{x}_2\otimes\hat{x}_3\right). \tag{2.236}$$

This gate transforms the quadrature operators as

$$\begin{pmatrix}\hat{x}_1'\\ \hat{x}_2'\\ \hat{x}_3'\\ \hat{p}_1'\\ \hat{p}_2'\\ \hat{p}_3'\end{pmatrix} = \begin{pmatrix}\hat{x}_1\\ \hat{x}_2\\ \hat{x}_3\\ \hat{p}_1+g\hat{x}_2\hat{x}_3\\ \hat{p}_2+g\hat{x}_3\hat{x}_1\\ \hat{p}_3+g\hat{x}_1\hat{x}_2\end{pmatrix}. \tag{2.237}$$

Unlike the Gaussian operations, we can see that the product of the quadrature operator is also presented. For those who have knowledge in the quantum information processing using the qubit system, this CCZ gate is reminiscent of the Toffoli gate in the qubit system. A Toffoli gate is a three-input three-output gate that transforms the qubit quantum state as

$$|i\rangle\otimes|j\rangle\otimes|k\rangle \rightarrow |i\rangle\otimes|j\rangle\otimes|(k+ij) \bmod 2\rangle. \tag{2.238}$$

which in a way is similar to the CZZ gate where the modulo 2 sum is replaced by a usual summation. In the qubit setup, Hadamard gate, phase gate, controlled-Z gate, and toffoli gate are one of the possible universal gate sets.

07 December 2024 17:52:47

2.6 HOMODYNE MEASUREMENT

Here, we will discuss measurements on the quantum states of the electromagnetic fields. In quantum optics, we usually expand quantum states using either the quadrature eigenvector basis $|x\rangle$ or the Fock basis $|n\rangle$. We will first discuss the measurement of the quadrature, which is called *balanced homodyne measurement* or simply *homodyne measurement*.

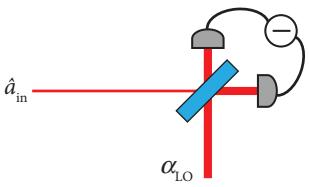

FIG. 2.13
Schematic diagram of the homodyne measurement.

Figure 2.13 depicts the schematic of the homodyne measurement. First, the quantum state we want to measure interfered with a strong laser beam at a 50:50 beamsplitter [i.e., a beamsplitter corresponded to $\mathbf{B}(\pi/4)$]. This strong laser light is called *local oscillator*. In Sec. 2.3.3, we have discussed that the quadrature operators are defined with respect to some phase reference ($\hat{x}$, $\hat{p}$, or somewhere in between); thus, it is expected that the measurement of the quadrature operator should be phase sensitive. In that sense, the local oscillator provides a phase reference as to which direction of the quadrature are we measuring.

Since the amplitude of the local oscillator is usually very large compared to the vacuum fluctuation, the annihilation operator of the local oscillator $\hat{a}_{\text{LO}}$ can be replaced with a complex electric field amplitude α_{LO}. This is justified as follows. If we start from a vacuum state whose annihilation operator is $\hat{a}_{\text{vac}}$, then the annihilation operator of the local oscillator becomes $\hat{a}_{\text{LO}} = \alpha_{\text{LO}} + \hat{a}_{\text{vac}}$. When the amplitude α_{LO} is much larger than the vacuum variances, the contribution due to the vacuum variances can be neglected and we can replace the annihilation operator with a complex number. Then, the annihilation operator at each output of the 50:50 beamsplitter is

$$\hat{a}_1' = \frac{1}{\sqrt{2}}(\hat{a} - \alpha_{\text{LO}}), \tag{2.239}$$

$$\hat{a}_2' = \frac{1}{\sqrt{2}}(\hat{a} + \alpha_{\text{LO}}). \tag{2.240}$$

After the quantum state and the local oscillator interfered at the beamsplitter, they are detected by the photodiodes and the difference between the photocurrent is calculated. If we assume that the photocurrents are proportional to the incident energy, the difference in the photocurrent will be proportional to

$$\hat{a}_2'^{\dagger}\hat{a}_2' - \hat{a}_1'^{\dagger}\hat{a}_1' = \sqrt{2\hbar}\,|\alpha_{\text{LO}}|\,(\hat{x}\cos\phi + \hat{p}\sin\phi), \tag{2.241}$$

where we put $\alpha_{\text{LO}} = |\alpha_{\text{LO}}|\exp(i\phi)$. There are two important points here. First, by changing the phase of the local oscillator, we can select the component of the quadrature we wish to measure. Second, although the quadrature themselves are very small as they are components of the electric fields of the quantum states, by using the strong classical lights as the local oscillators, the measurement signals are amplified, which let us observe the quantum level electric fields.

07 December 2024 17:52:47

In the actual homodyne detectors, after the lights are absorbed by the photodiodes, the photocurrents are usually converted to voltages as voltages are much easier to deal with. As the proportional factor between the measured electrical signals and the actual values of the quadratures is affected by various components, it has to be determined experimentally. This is usually done by measuring vacuum states and then by calculating the variances of the electrical signals and using them as the normalization factors.

Because quantum states are susceptible to optical losses, the efficiency of the photodiode (called quantum efficiency) needed to be as high as possible. One of the ways to realize this is by using a photodiode whose surface is relatively large and has a big thickness. However, this increases the capacitance of the photodiode, which then limits the frequency bandwidth of the homodyne detectors. For applications where the modes of the quantum states are wave packets, the frequency bandwidth of the homodyne detectors is crucial in ensuring that we can measure the quadrature of that mode correctly.

As the photodiodes for each wavelength are limited by the properties of the materials, ultimately the bandwidth of the homodyne measurement will be limited by the photodiode, even if we could make ideal circuitry. Recently, there have also been research studies in what is called *all-optical homodyne measurement*, which does not resort to photodiodes for homodyne measurement (Shaked *et al.*, 2018). This method could prove to be a way to achieve broadband homodyne measurements as the bandwidth of the optical system are usually much broader (THz order) compared to the photodiode and the circuitry (GHz order).

07 December 2024 17:52:47

2.7 FOCK BASIS MEASUREMENT

In addition to measurements in quadrature basis, we can also consider the measurement in Fock basis, also called photon counting and the detectors used for this are called *photon number resolving detector*. In Sec. 2.5.2, universality was discussed on the quadrature basis and quadrature measurements are adequate for measuring the outcome of the CV quantum computation. Even so, photon counting is usually useful in the state generation and can sometimes provide the source of non-Gaussianity required to realize the universality. There is, however, one downfall with Fock basis measurement: unlike the homodyne measurement, the measurements tend to be probabilistic. This is because unlike homodyne measurement, which is sensitive to vacuum fluctuation, when photon counting detects 0 photons, it is not evident if this is due to inefficiency or there really is no photon at that timing. This is extremely problematic in the continuous-wave experiments where the lights are continuously emitted. As such, photon counting are usually used only for the probabilistic (but heralded) state generations in continuous-wave experiments. For pulsed-laser experiments, although we can use the timing of the pulses to synchronize the detection of the photon counting, as the efficiency of the photon counting with sufficient speed is still relatively low, photon counting is mainly used for the state generation in pulse experiments as well.

Another aspect that we have to be careful regarding the photon counting is that the realistic photon countings are most of the time not projection measurements. An ideal photon counting is the measurement that can be written using the projection operator

$$\hat{\Pi}_n = |n\rangle \langle n|, \tag{2.242}$$

where $|n\rangle$ is the Fock state. As the energy of a single photon is very small, we usually have to amplify the signals or find the way to detect the small signals from the detection of the single photon that is not noisy. One of the widely used detectors to detect photons is called avalanche photodetector (APD). In APD, when a photon is detected at the photodiode and the electron–hole pair is generated, the electron–hole pair further induces more pairs resulting in a large amount of current, thus the term avalanche. APD is indeed sensitive to the energy on the single photon level. The resolution of the APD, however, is rather problematic; the amplification of the APD is so large that it is not possible to distinguish the actual energy; thus, the photon number of the incident lights. This type of detector is usually called *ON/OFF detector* or *bucket detector* to distinguish it from the ideal photon counting detector. The POVM of the ON/OFF detector is given by

$$\hat{\Pi}_{\text{off}} = |0\rangle \langle 0|, \tag{2.243}$$

$$\hat{\Pi}_{\text{on}} = \hat{I} - |0\rangle \langle 0|. \tag{2.244}$$

One of the intuitive interpretations of the ON/OFF detector is that rather than detecting the photon number, the on signals of this type of detector eliminate the possibility that the incident lights are vacuum states.

Another type of the widely used single photon detector is called *superconducting nanostrip photon detectors* (SNSPD), which is shown in Fig. 2.14(a). SNSPD uses the fact that when the photon incident on the superconducting nanowire, the nanowire will no longer be superconducting and we can detect the resistance (or the voltage) across the SNSPD. The main features of the SNSPD over the APD are that SNSPD is faster and has a lower dark count (fake counts when there are no input photons). Although SNSPD is still a type of ON/OFF detector, there are some recent research studies that show that the rise time of the SNSPD can be used to count photons up to a few photons (about three to four photons) [Fig. 2.14(b)]. This is highly impressive as it provides a fast and low-noise method to count a few photons.

Regarding the detectors that can count photons, a transition-edge sensor (TES) is one of the promising detectors [Fig. 2.14(c)]. TES uses the breakdown of the superconducting similar to SNSPD. However, instead of the complete breakdown, TES operates near the transition between superconducting and normal conducting states and the changes in the resistances depend on the energy of the absorbed photons, allowing photon number measurements up to a certain photon number [Fig. 2.14(d)]. The maximum photon number that TES can distinguish depends on the resistance gap and the energy of the incident photons.

07 December 2024 17:52:47

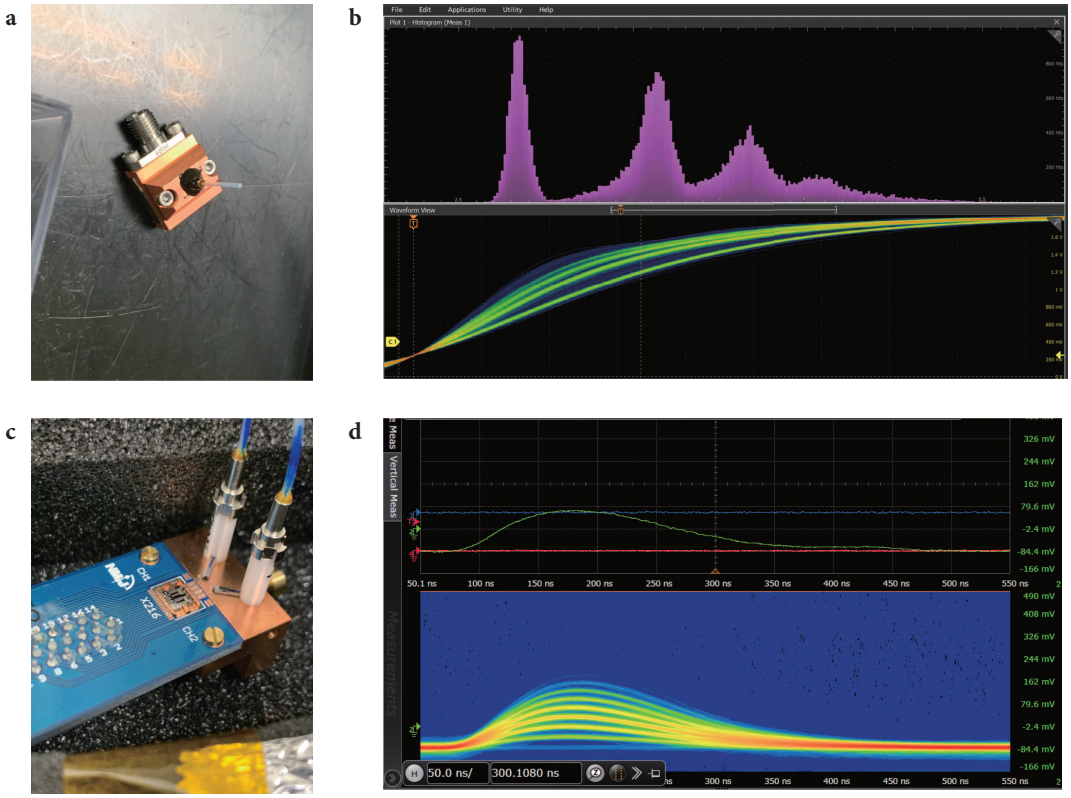

FIG. 2.14
Photon number detectors. (a) Picture SNSPD. (b) Signals of SNSPD for photon counting. (c) Picture of TES. (d) Signals of TES for photon counting. This SNSPD was provided by Dr. Shigehito Miki and Dr. Hirotaka Terai (NICT). These TES chips and the module were provided by Dr. Daiji Fukuda (AIST). Figures and data provided by Mamoru Endo.

There is one noteworthy point about photon number detections. Until recent years, it has been widely believed that even if we do not have photon number resolving detector, by using arrays of ON/OFF detectors (Fig. 2.15), we can effectively build a photon number resolving detectors. Although this might be true theoretically, this approach has been shown to be experimentally unfeasible. For example, Jönsson and Björk (2019) showed that to distinguish ten photons at the accuracy that is better than guessing (more than 50%), we need about 50 ON/OFF detectors. Therefore, a detector that can resolve photon number is essential in CV quantum computation.

07 December 2024 17:52:47

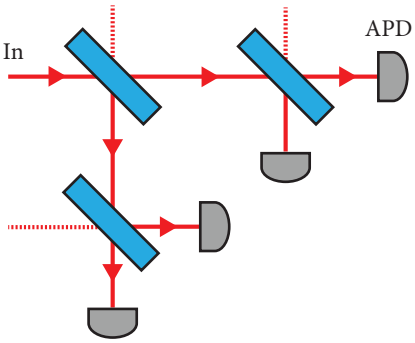

FIG. 2.15
An example of APD array with four APDs. The dotted lines represent vacuum states.

2.8 QUANTUM ENTANGLEMENT

We will end this chapter with a discussion about the quantum entanglements. Among many interesting features of quantum theory, entanglement is a peculiar property that even Einstein dubbed "spooky action at a distance." When talking about entanglement in CV system, one "paradox" that must be mentioned is the famous Einstein–Podolsky–Rosen paradox.

2.8.1 Einstein–Podolsky–Rosen paradox

In 1935, Einstein, Podolsky, and Rosen published a paper titled "Can quantum-mechanical description of physical reality be considered complete?" (Einstein *et al.*, 1935), which claims that quantum mechanics is incomplete. To illustrate their claim, they introduce a very interesting quantum state. Let us consider a quantum system consisting of two particles, labeled "1" and "2." From the commutation relation, we know that $[\hat{x}_1, \hat{p}_1] = [\hat{x}_2, \hat{p}_2] = i\hbar \neq 0$, meaning that we cannot have a quantum state that both $\hat{x}$ and $\hat{p}$ are determined. However, we can construct a linear combination of quadrature operators such that

$$[\hat{x}_1 - \hat{x}_2, \hat{p}_1 + \hat{p}_2] = 0. \tag{2.245}$$

Since the above commutation relation is 0, there exists a quantum state that is a simultaneous eigenstate of $\hat{x}_1 - \hat{x}_2$ and $\hat{p}_1 + \hat{p}_2$. In their paper, they consider the prediction of such a state as an evidence of the incompleteness of the quantum mechanics. Their arguments are as follows. Let us suppose that we measure $\hat{x}_1$ of the particle 1 of such quantum states. Then, the quadrature $\hat{x}_2$ of the particle 2 will be exactly the same and the state of the particle 2 will be position eigenstate. On the other hand, if the observer measure $\hat{p}_1$, depending on its measurement results, the quantum state of the particle 2 will be a momentum eigenstate whose eigenvalues is a minus of the measurement result of $\hat{p}_1$. As the position eigenstate and the momentum eigenstate are supposed to be incompatible in quantum mechanics, Einstein, Podolsky, and Rosen argue that the fact that such incompatible states can be selectively

07 December 2024 17:52:47

induced by the choice of the measurement basis ("spooky action at a distance") is paradoxical and is the evidence of the incompleteness of the quantum mechanics.

Although not so many people now would consider the above setting paradoxical, this *EPR paradox* shows many different concepts between classical physics and quantum physics such as nonlocality and contextuality (i.e., whether the values of the physical quantities are predetermined or are determined when the measurements are made). Interestingly enough, the quantum state that was considered in the EPR paradox later becomes one of the most basic and widely used quantum entanglements in the CV system, analogous to the Bell states in the qubit systems. This entanglement is called *EPR state*, which is quite an irony when one considers that the purpose of their paper was to show the incompleteness of the quantum mechanics.

Similar to how quadrature eigenstates are unnormalizable and cannot be physically realized, EPR states are also unphysical. We can, however, generate quantum states that approximate EPR states. These states are called *two-mode squeezed states*. It is possible to generate these states with the nondegenerate parametric down-conversion process whose Hamiltonian has the form of

$$\hat{H}_{\mathrm{NPDC}} = i(r\hat{a}_1\hat{a}_2 - r^*\hat{a}_1^\dagger\hat{a}_2^\dagger). \tag{2.246}$$

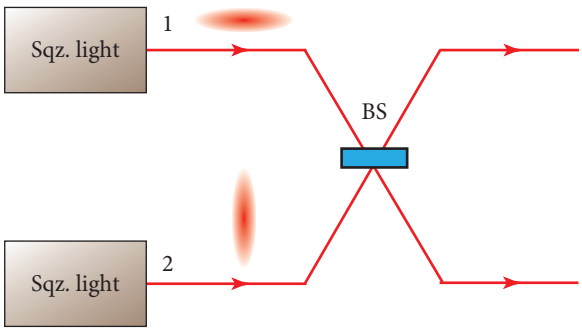

FIG. 2.16
Setup for generation of two-mode squeezed states using two squeezed vacuum states.

Experimentally, however, two-mode squeezed states are usually generated by combining two squeezed vacuum states on a 50:50 beamsplitter (Fig. 2.16). Let us show that this setup indeed generates two-mode squeezed states by using the Heisenberg picture evolution. First, we can represent the quadrature operators of the squeezed lights as

$$\begin{pmatrix}\hat{x}_1\\ \hat{x}_2\\ \hat{p}_1\\ \hat{p}_2\end{pmatrix} = \begin{pmatrix}\hat{x}_{1,\mathrm{vac}}e^{r}\\ \hat{x}_{2,\mathrm{vac}}e^{-r}\\ \hat{p}_{1,\mathrm{vac}}e^{-r}\\ \hat{p}_{2,\mathrm{vac}}e^{r}\end{pmatrix}, \tag{2.247}$$

where $\hat{x}_{i,\mathrm{vac}}$ is a quadrature operator of the vacuum state in mode i. Then, after the 50:50 beamsplitter, the quadrature operators are transformed as

$$\begin{pmatrix}\hat{x}_1'\\ \hat{x}_2'\\ \hat{p}_1'\\ \hat{p}_2'\end{pmatrix} = \frac{1}{\sqrt{2}}\begin{pmatrix}1 & -1 & 0 & 0\\ 1 & 1 & 0 & 0\\ 0 & 0 & 1 & -1\\ 0 & 0 & 1 & 1\end{pmatrix}\begin{pmatrix}\hat{x}_{1,\mathrm{vac}}e^{r},\\ \hat{x}_{2,\mathrm{vac}}e^{-r},\\ \hat{p}_{1,\mathrm{vac}}e^{-r},\\ \hat{p}_{2,\mathrm{vac}}e^{r}\end{pmatrix}. \tag{2.248}$$

From the above equation, we can calculate the linear combinations of the quadrature operators as

$$\hat{x}_1' - \hat{x}_2' = -\sqrt{2}\hat{x}_{2,\mathrm{vac}}e^{-r}, \tag{2.249}$$

$$\hat{x}_1' + \hat{x}_2' = \sqrt{2}\hat{x}_{1,\mathrm{vac}}e^{r}, \tag{2.250}$$

07 December 2024 17:52:47

$$\hat{p}'_1 - \hat{p}'_2 = -\sqrt{2}\hat{p}_{2,\mathrm{vac}}e^{r}, \tag{2.251}$$
$$\hat{p}'_1 + \hat{p}'_2 = \sqrt{2}\hat{p}_{1,\mathrm{vac}}e^{-r}. \tag{2.252}$$

In the limit of $r \to \infty$, i.e., the infinite squeezing limit, the correlations $\hat{x}'_1 - \hat{x}'_2$ and $\hat{p}'_1 + \hat{p}'_2$ approach 0, meaning that the generated states approach ideal EPR states as the squeezing level increase. These correlations of the quadrature operators are sometimes called *EPR correlations* and the smaller the variances of the EPR correlations are, the closer the state is to the ideal EPR states.

2.8.2 Quantum entanglement and inseparability

EPR states are one of the examples of the quantum entanglement. In Sec. 2.8.1, we take the correlations between quadrature as the signs of the quantum entanglement. Strictly speaking, this is inaccurate and we need a more precise mathematical definition. Moreover, the discussion regarding EPR states and the two-mode squeezed states are based on pure states; experimentally generated quantum states are generally mixed states; thus, we need a definition that can be related to actual experimental results.

To define entanglement, let us consider a quantum state $\hat{\rho}$ of a system that is composed of several subsystems. We can then separate these subsystems into two sets A and B. Then, we can define *separability* of subsystems A and B as follows.

Definition 2.10. We say that the quantum state $\hat{\rho}$ is *separable* with respect to A and B if and only if there exist a set of quantum states $\{\hat{\rho}_i^A\}$ and $\{\hat{\rho}_i^B\}$ on the sets A and B, and a probability distribution $\{p_i\}$ that allows us to write $\hat{\rho}$ as

$$\hat{\rho} = \sum_i p_i \hat{\rho}_i^A \otimes \hat{\rho}_i^B. \tag{2.253}$$

On the other hand, we say that the quantum states ρ is *inseparable* or *entangled* with respect to A and B if we cannot find any $\{\hat{\rho}_i^A\}$, $\{\hat{\rho}_i^B\}$, and $\{p_i\}$ that satisfy Eq. (2.253).

Interestingly, the formal definition of quantum entanglement does not directly involve measurements and correlations but is defined through the separability of the quantum states. Even if the inseparability of the quantum states most of the time consequentially results in the correlations between physical quantities, we have to be careful not to mix them together. It is possible to have quantum states that show correlations of physical quantities between different modes, but do not have any quantum entanglement.

As an example, if we split a coherent state with random amplitude using a 50:50 beamsplitter, the resulting quantum state $\hat{\rho}_{\mathrm{sep}}$ is

$$\hat{\rho}_{\mathrm{sep}} = \int \mathrm{d}^2\alpha\, p(\alpha) \left|\alpha\right\rangle \left\langle\alpha\right| \otimes \left|\alpha\right\rangle \left\langle\alpha\right|, \tag{2.254}$$

where $p(\alpha)$ is the probability distribution of the complex amplitude. When we measure the quadrature operator $\hat{x}_\theta$ in any direction, there will be some correlations between two modes as the complex amplitudes are always the same. This simple example shows that we cannot determine whether there is entanglement in the system or not simply by looking at the correlations of the physical quantities.

07 December 2024 17:52:47

Some readers might argue that for the state in this example, since the correlations are not perfect due to the vacuum variances, we can distinguish them from quantum entanglement such as EPR states where the quadrature operators are perfectly correlated. This argument is actually very problematic when we consider actual experiments where everything could be imperfect. It is crucial that we carefully formulate an experimental methodology to verify the existence of the quantum entanglement even when the quantum states are mixed states.

We can also consider quantum entanglement between more than two parties (multipartite quantum entanglement). The definition, classification, and verification of the multipartite entanglement in CV system is a very complex and broad field, which is out of the scope of this book. Nevertheless, we will introduce some of the very basic concepts.

Definition 2.11. A quantum state is fully multipartite inseparable if and only if for any bipartition A and B, the quantum states cannot be written using Eq. (2.253).

Definition 2.12. A quantum state has genuine multipartite entanglement if and only if its density matrix cannot be written as a convex sum of any biseparable states.

To illustrate the difference between the above two definitions, let us consider tripartite quantum states whose quantum state can be written as

$$\hat{\rho}_{\text{tri}} = \sum_i p_i^{AB,C} \hat{\rho}_i^{AB} \otimes \hat{\rho}_i^{C} + p_i^{BC,A} \hat{\rho}_i^{BC} \otimes \hat{\rho}_i^{A} + p_i^{CA,B} \hat{\rho}_i^{CA} \otimes \hat{\rho}_i^{B}. \tag{2.255}$$

In the above state, even though it is full multipartite inseparable, only quantum states with bipartite entanglements are involved. Thus, it does not have genuine multipartite entanglement. In addition to entanglement, there are other two quantum correlations, *quantum steering* and *nonlocality*, which are stronger than entanglement. For the readers who are interested in quantum entanglement in the CV system, we recommend consulting a textbook that is dedicated to the discussion about quantum entanglement.

2.8.3 PPT criteria

Experimental verification of quantum entanglement using the definition in Eq. (2.253) is an experimentalists' nightmare for multiple reasons. First, the definition of quantum entanglement requires the knowledge of the quantum states $\hat{\rho}$. In experiments, we measure physical quantities such as quadrature $\hat{x}$ and $\hat{p}$ and not $\hat{\rho}$. Although there are methods to estimate $\hat{\rho}$ from the measurement results of the quadrature operators, the amount of the measurements required for such estimations usually scales poorly with the number of the modes, making the estimation of $\hat{\rho}$ for multimode quantum states not so experimentally feasible. Second, even if we could somehow estimate $\hat{\rho}$, direct verification using the definition of the quantum entanglement is still very difficult. We have to show the nonexistence of the choices of the basis that can split the density matrix into the separable form. Moreover, this procedure must be done on a density matrix that is estimated, meaning that the precision of the estimation will be crucial.

07 December 2024 17:52:47

Therefore, it is more desirable if we could find a criterion that does not require proving of the nonexistence of the basis. This type of criterion is sometimes called *entanglement witness* and when the witnesses are satisfied, we can say that there are quantum entanglement in the system. These witnesses, although there are sufficient criteria, they are rarely sufficient and necessary criteria, except for some special cases. For experimentalists, this does not pose much problem as long as the sufficient criteria for the quantum entanglement are easy to use and can be satisfied in the actual experimental setting. Moreover, if we just want to verify the existence of the quantum entanglements, tailoring sufficient criteria to a certain type of quantum entanglement is a good strategy.

Here, we will introduce one of the sufficient criteria for showing quantum entanglement. This criterion was formulated by Peres (1996) and Horodecki (1997) and is also called *positive partial transpose (PPT) criteria*. Note that many other criteria widely used in CV quantum computation can actually be traced back to be equivalent to these PPT criteria making understanding of PTT criteria a crucial step in understanding CV quantum entanglement. PPT criteria are based on a very simple idea. When we consider a mapping between a density matrix $\hat{\rho} \to \hat{\rho}'$ on a composite system, for this map to be physical, this map has to be a *completely positive trace-preserving (CPTP) map*. While the term "trace preserving" is self-evident, many readers might not be familiar with the term "completely positive." In linear algebra, the positive map is a mapping that maps a matrix with non-negative eigenvalues to another matrix whose eigenvalues are also non-negative. This is crucial for the density matrix as the eigenvalues of the density matrix are interpreted as a probability. On the other hand, the term completely positive means that even if we expand the system into a composite system, implementing the same map only on the subsystem still take the density matrix of the whole system to a matrix with non-negative eigenvalues.

The idea of the PPT criteria is based on the fact that transpose is a positive but not completely positive map. Let us consider a biseparable state that can be written as

$$\hat{\rho} = \sum_i p_i \hat{\rho}_i^A \otimes \hat{\rho}_i^B. \tag{2.256}$$

Then, if we perform transpose operation on only subsystem A (partial transpose), the output state denoted as $\hat{\rho}^{\mathrm{T}_A}$ is

$$\hat{\rho}^{\mathrm{T}_A} = \sum_i p_i (\hat{\rho}_i^A)^{\mathrm{T}} \otimes \hat{\rho}_i^B. \tag{2.257}$$

As the transposed density matrix satisfies the constraints on the density matrix [Eqs. (2.19)–(2.21)]; if $\hat{\rho}$ is separable, then the partially transposed density matrix $\hat{\rho}^{\mathrm{T}_A}$ is a physical density matrix. We can take a contraposition of this statement and states, our sufficient condition for detecting inseparability as follows.

Theorem 2.10. *For a quantum state $\hat{\rho}$ of a composite system with a bipartition A and B, if the partial transposed density matrix $\hat{\rho}^{T_A}$ is an unphysical density matrix, then $\hat{\rho}$ is inseparable with respect to the bipartition A and B.*

07 December 2024 17:52:47

This criterion provides an easy test for inseparability without having to show the impossibility to find the basis that can express the density matrix in a separable form. Note, however, that as this criterion is a sufficient criterion, the tests become inconclusive when the partially transposed density matrices are physical.

As an example, let us consider a Bell state given by

$$\hat{\rho}_{\text{Bell}} = \frac{1}{2}\left(|0\rangle_A|1\rangle_B + |1\rangle_A|0\rangle_B\right)\left(\langle 0|_A\langle 1|_B + \langle 1|_A\langle 0|_B\right). \tag{2.258}$$

If we use the basis $\{|0\rangle_A|0\rangle_B, |1\rangle_A|0\rangle_B, |0\rangle_A|1\rangle_B, |1\rangle_A|1\rangle_B\}$ to write down the density matrix, we get

$$\hat{\rho}_{\text{Bell}} = \frac{1}{2}\begin{pmatrix} 0 & 0 & 0 & 0 \\ 0 & 1 & 1 & 0 \\ 0 & 1 & 1 & 0 \\ 0 & 0 & 0 & 0 \end{pmatrix}. \tag{2.259}$$

The eigenvalues of the above matrix are obviously 0, 0, 0, and 1, which are all non-negative. If we take a partial transpose on mode A, the resultant matrix is

$$\hat{\rho}_{\text{Bell}}^{\text{T}_A} = \frac{1}{2}\begin{pmatrix} 0 & 0 & 0 & 1 \\ 0 & 1 & 0 & 0 \\ 0 & 0 & 1 & 0 \\ 1 & 0 & 0 & 0 \end{pmatrix}. \tag{2.260}$$

The eigenvalues of the above matrix can be easily calculated as 1/2, 1/2, 1/2, and $-1/2$. As the partial transposed density matrix has a negative eigenvalue, this matrix is unphysical. Using the PPT criteria, it is shown that there is entanglement between modes A and B. Although this example is a very simple example as we know that Bell state is a quantum entangled state, it illustrates how to use PPT criteria for simple verification of the quantum entanglement.

2.8.4 van Loock–Furusawa criteria

Although PPT criteria are relatively easy to use, they still require the knowledge of the density matrix $\hat{\rho}$ of the quantum states. In CV experiments, the physical quantities that are easy to measure are the quadratures. Therefore, it is desirable to have criteria to verify quantum entanglement that uses only the measurement results of the physical quantities and not the density matrices which can only be accessed by estimations via various measurements.

In 2000, Duan *et al.* (2000) and Simon (2000) independently construct sufficient and necessary criteria to verify two-mode CV quantum entanglement that uses only the knowledge of the quadrature operators. Their criteria are mathematically equivalent and require only measurements of the variances of the quadrature operators and comparing them with a threshold. If the variances are below the threshold, the quantum states possess quantum entanglement.

07 December 2024 17:52:47

In the same spirit as Duan and Simon, van Loock and Furusawa derive sufficient criteria for detecting full multipartite inseparability of the quantum states with more than two modes (van Loock and Furusawa, 2003). Their criteria are also based on the measurements of the quadrature operators and have been utilized in the verifications of various types of quantum entanglements. In particular, the van Loock–Furusawa criteria have been extensively used in the verifications of the CV cluster states, the computational resources of the one-way quantum computation. van Loock–Furusawa criteria are stated as follows:

Theorem 2.11. *van Loock–Furusawa criteria: On N-mode quantum states, we can consider operators $\hat{X}$ and $\hat{P}$, which are linear combinations of the quadrature operators,*

$$\hat{X} = \sum_{j=1}^{N} g_j \hat{x}_j, \tag{2.261}$$

$$\hat{P} = \sum_{j=1}^{N} h_j \hat{p}_j. \tag{2.262}$$

If we group the modes of the quantum states into two sets, A and B, with $A \cap B = \phi$ and the quantum state $\hat{\rho}$ of our interest is separable with respect to A and B, i.e., $\hat{\rho}$ can be written as

$$\hat{\rho} = \sum_{j} p_j \hat{\rho}_j^A \otimes \hat{\rho}_j^B, \tag{2.263}$$

then the sum of the variances satisfies the following inequality:

$$\left\langle \Delta^2 \hat{X} \right\rangle + \left\langle \Delta^2 \hat{P} \right\rangle \geq \hbar \left(\sum_{j \in A} |g_j h_j| + \sum_{k \in B} |g_k h_k| \right). \tag{2.264}$$

By taking a contraposition of the above criteria, we can see that if we measure the variances of the linear combination of the quadrature operators and find that it is below a certain threshold, we can conclude that the quantum state of our interest is inseparable with respect to a certain bipartition. By applying the van Loock–Furusawa criteria to all bipartitions, we can show the full multipartite inseparability. Note that we do not need to use the same linear combination to negate different biparitions. van Loock Furusawa criteria can be easily proved using the uncertainty principle and the Cauchy–Schwartz inequality.

Proof. For the $\hat{\rho}$ in Eq. (2.263), the left-hand side of Eq. (2.264) can be calculated as

$$\begin{aligned} &\left\langle \Delta^2 \hat{X} \right\rangle_{\hat{\rho}} + \left\langle \Delta^2 \hat{P} \right\rangle_{\hat{\rho}} \\ &= \sum_j p_j \left[\left\langle \Delta^2 \hat{X}^A \right\rangle_{\hat{\rho}_j^A} + \left\langle \Delta^2 \hat{P}^A \right\rangle_{\hat{\rho}_j^A} + \left\langle \Delta^2 \hat{X}^B \right\rangle_{\hat{\rho}_j^B} + \left\langle \Delta^2 \hat{P}^B \right\rangle_{\hat{\rho}_j^B} \right] \end{aligned}$$

07 December 2024 17:52:47

$$+\sum_j p_j\left(\left\langle\hat{X}^A\right\rangle_{\hat{\rho}_j^A}+\left\langle\hat{P}^A\right\rangle_{\hat{\rho}_j^A}\right)^2-\left[\sum_j p_j\left(\left\langle\hat{X}^A\right\rangle_{\hat{\rho}_j^A}+\left\langle\hat{P}^A\right\rangle_{\hat{\rho}_j^A}\right)\right]^2$$
$$+\sum_j p_j\left(\left\langle\hat{X}^B\right\rangle_{\hat{\rho}_j^B}+\left\langle\hat{P}^B\right\rangle_{\hat{\rho}_j^B}\right)^2-\left[\sum_j p_j\left(\left\langle\hat{X}^B\right\rangle_{\hat{\rho}_j^B}+\left\langle\hat{P}^B\right\rangle_{\hat{\rho}_j^B}\right)\right]^2, \tag{2.265}$$

where we define $\hat{X}^A=\sum_{j\in A} g_j\hat{x}_j$ and so on. The first line of the Eq. (2.265) is bound from below by the uncertainty principle in Eq. (2.91). The second and third lines are bounded to be greater or equal to 0 by the Cauchy–Schwartz inequality, i.e.,

$$\left|\sum_j a_j b_j\right|^2\le\left(\sum_j a_j^2\right)\left(\sum_j b_j^2\right), \tag{2.266}$$

where the two vectors are, for example,

$$a_j=\sqrt{p_j}, \tag{2.267}$$
$$b_j=\sqrt{p_j}\left(\left\langle\hat{X}^A\right\rangle_{\hat{\rho}_j^A}+\left\langle\hat{P}^A\right\rangle_{\hat{\rho}_j^A}\right). \tag{2.268}$$

Then, as the lower bound of the right-hand side does not depend on the details of $\hat{\rho}$, we drop the state dependency and arrive at Eq. (2.264). □

Experimentally, the van Loock–Furusawa criteria are relatively easy to use because the linear combination of the quadrature operators can be determined simply by measuring the quadrature values of each mode and then numerically calculating the linear combination. Moreover, for some particular set of states, such as cluster states, there are sets of operators whose variances approach 0. Such a type of state has good compatibility with the van Loock–Furusawa criteria as the left-hand side of Eq. (2.264) can easily approach 0.

REFERENCES

Aasi, J., Abadie, J., Abbott, B. P., Abbott, R., Abbott, T. D., and Abernathy, M. R., "Enhanced sensitivity of the LIGO gravitational wave detector by using squeezed states of light," Nat. Photon. **7**(8), 613–619 (2013).

Andersen, U. L., Gehring, T., Marquardt, C., and Leuchs, G., "30 years of squeezed light generation," Phys. Scripta **91**(5), 053001 (2016).

Asavanant, W., Shiozawa, Y., Yokoyama, S., Charoensombutamon, B., Emura, H., and Alexander, R. N., "Generation of time-domain-multiplexed two-dimensional cluster state," Science **366**(6463), 373–376 (2019).

07 December 2024 17:52:47

Bartlett, S. D., Sanders, B. C., Braunstein, S. L., and Nemoto, K., "Efficient classical simulation of continuous variable quantum information processes," Phys. Rev. Lett. **88**, 097904 (2002).

Collett, M. J. and Gardiner, C. W., "Squeezing of intracavity and traveling-wave light fields produced in parametric amplification," Phys. Rev. A **30**, 1386–1391 (1984).

Duan, L. M., Giedke, G., Cirac, J. I., and Zoller, P., "Inseparability criterion for continuous variable systems," Phys. Rev. Lett. **84**, 2722–2725 (2000).

Einstein, A., Podolsky, B., and Rosen, N., "Can quantum-mechanical description of physical reality be considered complete?," Phys. Rev. **47**, 777–780 (1935).

Glauber, R. J., "Coherent and incoherent states of the radiation field," Phys. Rev. **131**, 2766–2788 (1963).

Horodecki, P., "Separability criterion and inseparable mixed states with positive partial transposition," Phys. Lett. A **232**(5), 333–339 (1997).

Jönsson, M. and Björk, G., "Evaluating the performance of photon-number-resolving detectors," Phys. Rev. A **99**, 043822 (2019).

Kashiwazaki, T., Takanashi, N., Yamashima, T., Kazama, T., Enbutsu, K., and Kasahara, R., "Continuous-wave 6-dB-squeezed light with 2.5-THz-bandwidth from single-mode PPLN waveguide," APL Photon. **5**(3), 036104 (2020).

Kok, P. and Lovett, B. W., *Introduction to Optical Quantum Information Processing* (Cambridge University Press, Cambridge, 2010).

Lamb, W. E., "Anti-photon," Appl. Phys. B **60**(2), 77–84 (1995).

Leonhardt, U., *Essential Quantum Optics: From Quantum Measurements to Black Holes* (Cambridge University Press, Cambridge, 2010).

Lloyd, S. and Braunstein, S. L., "Quantum computation over continuous variables," Phys. Rev. Lett. **82**, 1784–1787 (1999).

van Loock, P. and Furusawa, A., "Detecting genuine multipartite continuous-variable entanglement," Phys. Rev. A **67**, 052315 (2003).

Nielsen, M. A. and Chuang, I. L., *Quantum Computation and Quantum Information* (Cambridge University Press, Cambridge, 2000).

Peres, A., "Separability criterion for density matrices," Phys. Rev. Lett. **77**, 1413–1415 (1996).

Reck, M., Zeilinger, A., Bernstein, H. J., and Bertani, P., "Experimental realization of any discrete unitary operator," Phys. Rev. Lett. **73**, 58–61 (1994).

Shaked, Y., Michael, Y., Vered, R. Z., Bello, L., Rosenbluh, M., and Pe'er, A., "Lifting the bandwidth limit of optical homodyne measurement with broadband parametric amplification," Nat. Commun. **9**(1), 609 (2018).

Simon, R., "Peres-Horodecki separability criterion for continuous variable systems," Phys. Rev. Lett. **84**, 2726–2729 (2000).

Slusher, R. E., Hollberg, L. W., Yurke, B., Mertz, J. C., and Valley, J. F., "Observation of squeezed states generated by four-wave mixing in an optical cavity," Phys. Rev. Lett. **55**, 2409–2412 (1985).

07 December 2024 17:52:47

Sudarshan, E. C. G., "Equivalence of semiclassical and quantum mechanical descriptions of statistical light beams," Phys. Rev. Lett. **10**, 277–279 (1963).

Vahlbruch, H., Mehmet, M., Danzmann, K., and Schnabel, R., "Detection of 15 dB squeezed states of light and their application for the absolute calibration of photoelectric quantum efficiency," Phys. Rev. Lett. **117**, 110801 (2016).

Yariv, A. and Yeh, P., in Photonics: Optical Electronics in Modern Communications, The Oxford Series in Electrical and Computer Engineering (Oxford University Press Inc, 2006).

Yuen, H. P., "Two-photon coherent states of the radiation field," Phys. Rev. A **13**, 2226–2243 (1976).

Wigner, E., "On the quantum correction for thermodynamic equilibrium," Phys. Rev. **40**, 749–759 (1932).

Wu, L. A., Kimble, H. J., Hall, J. L., and Wu, H., "Generation of squeezed states by parametric down conversion," Phys. Rev. Lett. **57**, 2520–2523 (1986).

07 December 2024 17:52:47

07 December 2024 17:52:47

CHAPTER

3 QUANTUM TELEPORTATION AND MEASUREMENT-BASED QUANTUM COMPUTATION

3.1 QUANTUM TELEPORTATION PROTOCOL

The term continuous-variable (CV) quantum teleportation could point to one of the two protocols, which we will call *half teleportation* and *full teleportation*. Historically, the CV version of measurement-based quantum computation (MBQC) was analyzed based on the half-teleportation circuit (Menicucci *et al.*, 2006). This CV half-teleportation circuit is, in a way, a direct generalization from the qubit-based MBQC (Raussendorf and Briegel, 2001). Most quantum teleportation experiments, however, are based on the full-teleportation circuit, rather than the half-teleportation circuit. For optical systems, this is particularly the case as the formulation of the half-teleportation circuit was based on the controlled-Z gates, while the full-teleportation circuit was based on the beamsplitter interactions, which are much easier to realize optically.

07 December 2024 17:52:47

3.1.1 Half-teleportation circuit

Figure 3.1 shows the half-teleportation circuit. We will analyze this circuit using the Heisenberg picture. Let "in" and "anc" represent the input mode and the ancillary mode. Then, after the controlled-Z gate, the quadrature operators at (i) become

$$\hat{x}_{\text{in}}^{(i)} = \hat{x}_{\text{in}}, \tag{3.1}$$

$$\hat{p}_{\text{in}}^{(i)} = \hat{p}_{\text{in}} + \hat{x}_{\text{anc}}, \tag{3.2}$$

$$\hat{x}_{\text{anc}}^{(i)} = \hat{x}_{\text{anc}}, \tag{3.3}$$

$$\hat{p}_{\text{anc}}^{(i)} = \hat{p}_{\text{anc}} + \hat{x}_{\text{in}}. \tag{3.4}$$

After the controlled-Z gate, we measure $\hat{p}_{\text{in}}^{(i)}$. One of the convenient methods in quantum optics is that in the Heisenberg picture, when we do the measurement, we replace an operator with a scalar representing the measurement result. In our case, let us denote m_p as the measurement result. Then,

$$m_p = \hat{p}_{\text{in}} + \hat{x}_{\text{anc}}. \tag{3.5}$$

https://doi.org/10.1063/9780735424074_003

Optical Quantum Computers: A Route to Practical Continuous Variable Quantum Information Processing, W. Asavanant and A. Furusawa
© 2022 AIP Publishing, published by AIP Publishing

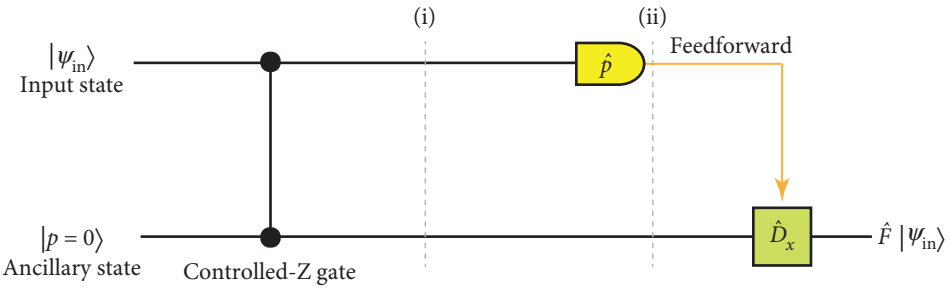

FIG. 3.1
Half-teleportation circuit.

Inserting Eq. (3.5) into Eq. (3.3), we can write down the quadrature operator of the ancillary mode after the measurement of the input mode as

$$\hat{x}_{anc}^{(ii)} = -\hat{p}_{in} + m_p, \tag{3.6}$$

$$\hat{p}_{anc}^{(ii)} = \hat{x}_{in} + \hat{p}_{anc}. \tag{3.7}$$

To make sure that the readers do not make any mistake here, we want to emphasize that the values of m_p in Eq. (3.6) will differ from each implementation of the circuit in Fig. 3.1. The probability distribution of m_p will be highly dependent on the input state and the ancillary state. However, if for every implementation, we perform displacement operation depending on this m_p on the ancillary mode and erase the m_p in Eq. (3.6), the output mode will become

$$\hat{x}_{out} = -\hat{p}_{in}, \tag{3.8}$$

$$\hat{p}_{out} = \hat{x}_{in} + \hat{p}_{anc}. \tag{3.9}$$

In the case that we use the p-quadrature eigenstate $|p = 0\rangle$ as the ancillary state, $\hat{p}_{anc}$ will always be 0 and the input–output relation of the half-teleportation circuit is simply the Fourier transform of the input mode. The quadrature eigenstates are, however, unphysical and are usually replaced with squeezed states in the actual implementation. If we use a squeezed state with a squeezing parameter r as our ancillary state, we can write down the input–output relation compactly as

$$\begin{pmatrix} \hat{x}_{out} \\ \hat{p}_{out} \end{pmatrix} = \begin{pmatrix} 0 & -1 \\ 1 & 0 \end{pmatrix} \begin{pmatrix} \hat{x}_{in} \\ \hat{p}_{in} \end{pmatrix} + \begin{pmatrix} 0 \\ \hat{p}_{anc,0} e^{-r} \end{pmatrix}. \tag{3.10}$$

There are a few interesting points that we should note. First, we observe that regardless of what we use as an ancillary state, the effect of the ancillary state only appears in the p quadrature and not in the x quadrature. This is due to the fact that the effect of the ancillary state in the x quadrature is "erased" via the feedforward operation. Second, if we use a squeezed state as an ancillary state, then only the squeezing of the squeezed state affects the output. The role of the antisqueezing component is, in a sense, to make sure that the measurement of $\hat{p}_{in}^{(i)}$ does not reveal the information about $\hat{p}_{in}$, which would

07 December 2024 17:52:47

collapse the wave function of the input state. As the effect of the antisqueezing is completely erased due to the feedforward operations, this property can be generalized to the case where the ancillary state is a mixed state. In other words, only the amount of the squeezing in the ancillary state is important when we consider the operation due to the half-teleportation circuit. Adjustment of the feedforward operations via erasure of the contribution of the antisqueezing components is a basic experimental methodology, and has been rigorously pointed out in the context of MBQC recently (Walshe *et al.*, 2019).

3.1.2 Full-teleportation circuit

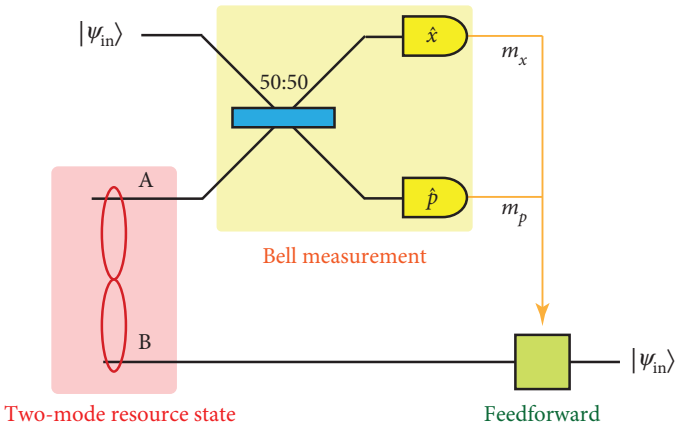

FIG. 3.2
Full-teleportation circuit.

The reason the circuit in Fig. 3.1 is called a half-teleportation circuit is that by repeating the same circuit twice, we get an identity operation, i.e., quantum teleportation, because $\hat{F}^2 = -\hat{I}$, where $\hat{F}$ is a Fourier transform. In the optical system, however, repeating a half-teleportation circuit twice is not how quantum teleportation is implemented. Figure 3.2 shows the circuit that we will call the full-teleportation circuit. This circuit implements identity operation. The main difference between this circuit and the half-teleportation circuit is that this circuit uses beamsplitter interaction instead of the controlled-Z gate. As explained in Chap. 2, beamsplitter interaction is much easier to realize than the controlled-Z gate in the optical setting.

We will now analyze the input–output relation of the full-teleportation circuit. We will denote "in," "A," and "B" as the input mode, mode A of the two-mode resource state, and mode B of the resource state, respectively. The input mode and mode A are first interfered on a beamsplitter, and the quadrature operators of each mode are measured afterward. This joint measurement is called the *Bell measurement*. If we let the measurement results of each homodyne detector be m_x and m_p, then we get

$$\sqrt{2}m_x = \hat{x}_{\text{in}} - \hat{x}_A, \tag{3.11}$$

$$\sqrt{2}m_p = \hat{p}_{\text{in}} + \hat{p}_A. \tag{3.12}$$

It is obvious that the CV Bell measurement corresponded to the projection measurement of the input mode and mode A onto the displaced Einstein–Podolsky–Rosen (EPR) state (projection to the EPR

07 December 2024 17:52:47

state corresponds to the case where $m_x = m_p = 0$). This is in parallel to the qubit-based quantum teleportation where the Bell measurements are projective measurements onto one of the four possible Bell states. Using m_x and m_p, we can write down mode B of the ancillary state as

$$\hat{x}_B = \hat{x}_{\text{in}} - \sqrt{2}m_x + (\hat{x}_B - \hat{x}_A), \tag{3.13}$$

$$\hat{p}_B = \hat{p}_{\text{in}} - \sqrt{2}m_p + (\hat{p}_B + \hat{p}_A). \tag{3.14}$$

Therefore, if we implement displacement operations depending on the measurement results m_x and m_p, we arrive at the output

$$\hat{x}_{\text{out}} = \hat{x}_{\text{in}} + (\hat{x}_B - \hat{x}_A), \tag{3.15}$$

$$\hat{p}_{\text{out}} = \hat{p}_{\text{in}} + (\hat{p}_B + \hat{p}_A). \tag{3.16}$$

If we select our two-mode resource state so that

$$\hat{x}_A - \hat{x}_B = 0, \tag{3.17}$$

$$\hat{p}_A + \hat{p}_B = 0, \tag{3.18}$$

the quadrature operator of the output mode is the same as that of the input mode, meaning that we successfully transfer the quantum state of the input mode to the output mode. The ideal ancillary state for the full-teleportation circuit is a quantum entanglement called the EPR state. As it is not possible to achieve ideal EPR states, quantum teleportation protocol will always involve some kind of noise determined by the distribution of $\hat{x}_A - \hat{x}_B$ and $\hat{p}_A + \hat{p}_B$. If we approximate the ideal EPR states using the two-mode squeezed states, then the variances $\langle \Delta^2(\hat{x}_A - \hat{x}_B) \rangle$ and $\langle \Delta^2(\hat{p}_A + \hat{p}_B) \rangle$ determine the amount of noise in the system. This is also true in the actual experiments where all quantum states must be considered mixed states. The fact that only two types of correlations matter is similar to how only the squeezing (not the antisqueezing) of the ancillary squeezed state matters in the half-teleportation circuit.

Let us look a little bit more into the details of the full-teleportation circuit. If we consider a two-mode squeezed state as an ancillary state, when we look at only mode A (i.e., if we trace out mode B), its quantum state is a thermal state that is simply a large random quantum fluctuation. By doing the joint measurement of this mode with the input mode, we do not reveal the information regarding the quadratures of the input mode as such information is covered by the noise of mode A. This noise, however, is correlated to mode B, which means that by doing the feedforward operation, we can reconstruct the information regarding the input mode. Note that even if we do not use the EPR state, i.e., we do simultaneous measurement of $\hat{x}$ and $\hat{p}$ on the input state and then displace a vacuum state, we do get some information regarding the input mode as shown in Eqs. (3.15) and (3.16). There is, however, a penalty due to the simultaneous measurement of the quadrature ($\hat{x}_A$ and $\hat{p}_A$) and the original variances of the vacuum state ($\hat{x}_B$ and $\hat{p}_B$).

One of the interesting facts about CV quantum computation is the feedforward process. In qubit-based quantum computation, the feedforward operations are Pauli operations, and as the measurement results are either 0 or 1, the measurement results only determine whether to do the Pauli operations or

07 December 2024 17:52:47

not. On the other hand, the feedforward gains in the CV teleportation can be tuned. There are some studies regarding this feedforward gain, and gain tuning has also been utilized in the teleportation of photonic qubits using a CV quantum teleporter (Takeda *et al.*, 2013).

We also consider the Wigner function of the output state. If we let $W_{\text{in}}(x_{\text{in}}, p_{\text{in}})$ and $W_{AB}(x_A, p_A, x_B, p_B)$ be the Wigner function of the input state and the two-mode resource state, respectively, we can write the Wigner function of the output as (see Appendix A for derivation)

$$W_{\text{out}}(x_{\text{out}}, p_{\text{out}}) = \int\int \mathrm{d}x\mathrm{d}p\, W_{\text{in}}(x, p)\Phi(x_{\text{out}} - x, p_{\text{out}} - p), \tag{3.19}$$

where

$$\Phi(x_{\text{out}} - x, p_{\text{out}} - p) \equiv \int\int \mathrm{d}x'\mathrm{d}p'\, W_{AB}(x', p', x_{\text{out}} - x + x', p_{\text{out}} - p - p'). \tag{3.20}$$

Equation (3.19) shows that the output Wigner function is the convolution between the input Wigner function and the function $\Phi(x, p)$. In the case where the resource state is an ideal EPR state, we can easily show that $\Phi_{\text{EPR}}(x_{\text{out}} - x, p_{\text{out}} - p) \propto \delta(x_{\text{out}} - x)\delta(p_{\text{out}} - p)$ and the input state is faithfully transmitted. For the two-mode squeezed state that is generated with a two squeezed state and a 50:50 beamsplitter, we have

$$\Phi_{\text{TMSS}}(x_{\text{out}} - x, p_{\text{out}} - p) \propto \exp\left[-\frac{(x_{\text{out}} - x)^2 + (p_{\text{out}} - p)^2}{2\hbar e^{-2r}}\right]. \tag{3.21}$$

In this situation, the output Wigner function is a convolution between the input function and a Gaussian function.

3.1.3 Experimental realization of CV quantum teleportation

Historically, quantum teleportation was first theoretically proposed in a qubit system by Bennett *et al.* (1993) and was later extended to a CV system by Vaidman (1994) and Braunstein and Kimble (1998). Experimentally, in the photonic qubit system, the quantum teleportation protocol was demonstrated by Zeilinger's group (Bouwmeester *et al.*, 1997). It was pointed out by Braunstein and Kimble (1998), however, that the Zeilinger experiment is *a posteriori* teleportation: complete destruction of the output state to eliminate the possibility of multiphoton components and ensure the success of the protocol [see Fig. 3.3(a)].

Subsequently, a CV quantum teleportation experiment was realized in the optical system by Furusawa *et al.* (1998), whose schematic is shown in Fig. 3.3(b). Optical CV quantum teleportation has many advantages over its qubit counterpart. First, the necessary entanglement, i.e., two-mode squeezed states, can be generated deterministically. Second, unlike photon counting that is currently limited to a non-ideal ON/OFF detector, homodyne measurement has a relatively higher efficiency.

Two main experimental leaps that are important in the realization of CV quantum teleportation are the phase-locking technology and the feedforward technology. Unlike the Bell state in the photonic

07 December 2024 17:52:47

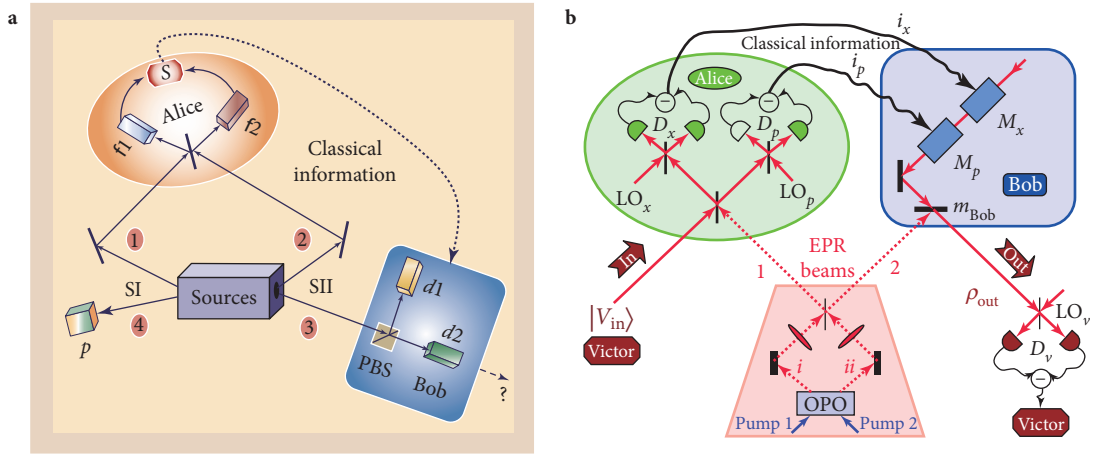

FIG. 3.3
Quantum teleportation setups. (a) Photonic qubit system (Braunstein and Kimble, 1998). Reprinted with permission from Braunstein, S. L. & Kimble, H. J., Nature **394**(6696), 840–841 (1998). Copyright 2009 Springer Nature Customer Service Centre GmbH, Springer Nature. (b) CV optical system (Furusawa *et al.*, 1998).

system, the squeezed lights used in the generation of the two-mode squeezed states are phase sensitive. Therefore, at every beamsplitter, the relative phases must be locked. This is realized by injection of classical probe beams into the systems, tapping these beams, and using their signals for feedback controls. Regarding the feedforward operations, when we perform homodyne measurement, we change the optical signals to electrical signals. To implement feedforward displacement operations, we need to again convert these electrical signals faithfully back to the optical signals. A methodology to realize this, which is called *cancellation*, was developed and has remained a basic tool in subsequent quantum teleportation experiments. To briefly explain, cancellation uses classical beams with phase modulation, which is split into two paths: one to the homodyne detector and the other to the path where feedforward operation is done. If the feedforward gain is properly adjusted, the phase modulation on the second path can be completely erased, which can be easily verified.

After the experiment by Furusawa *et al.*, there are many developments related to quantum teleportation. Technologically, most of the experiments can be summed up to improvement regarding the phase-locking technique or the feedforward channel. For example, by the improvement of the phase-locking technology, a more complex entanglement called cluster states has been realized (Yukawa *et al.*, 2008). On the other hand, by increasing the frequency bandwidth of both the homodyne detector and the feedforward channel, it becomes possible to teleport a quantum state that exists in a localized temporal wave packet. This leads to realization of the quantum teleportation of the cat state (Lee *et al.*, 2011) (Fig. 3.4). Recently, there has also been a research that extends the feedforward operation

07 December 2024 17:52:47

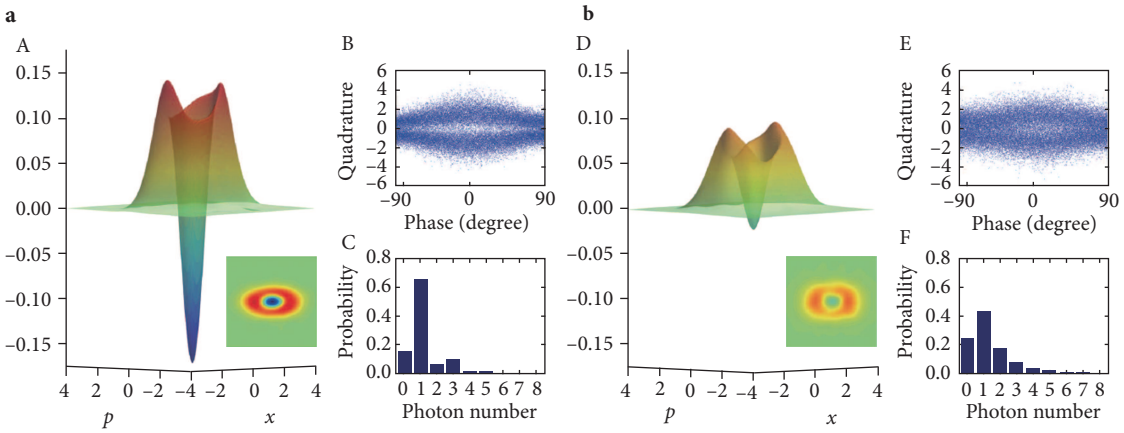

FIG. 3.4
Cat state teleportation in Lee *et al.* (2011). (a) Initial cat state. (b) Cat state after teleportation.

for quantum teleportation into nonlinear feedforward operation (Sakaguchi *et al.*, 2018) necessary to realize gate teleportation and measurement-based non-Gaussian quantum operations. Experiments on quantum teleportation are also not limited to the optical system but are implemented across various physical platforms. For a concise review on the quantum teleportation, we refer the readers to Andersen *et al.* (2015).

3.2 MEASUREMENT-BASED QUANTUM COMPUTATION

3.2.1 Quantum operations with half- and full-teleportation

Let us consider a circuit in Fig. 3.5. In this circuit, we implement a unitary operator $\hat{U}(\hat{p})$ that is only a function of the quadrature operator $\hat{p}$ after the half-teleportation circuit. Then, if our ancillary state is ideal, the output of this circuit in the Schrödinger picture is

$$|\psi_{\text{out}}\rangle = \hat{U}(\hat{p})\hat{F}\,|\psi_{\text{in}}\rangle = \hat{F}\hat{U}(\hat{x})\,|\psi_{\text{in}}\rangle, \tag{3.22}$$

which is equivalent to if we use $\hat{U}(\hat{x})\,|\psi_{\text{in}}\rangle$ as an input for the half-teleportation circuit. The unitary operator of the controlled-Z gate contains only the quadrature operator $\hat{x}$, meaning that it is commutative with $\hat{U}(\hat{x})$. Therefore, we can conclude that if we want to implement $\hat{F}\hat{U}(\hat{x})$ on the input state, what we have to do is we can use the half-teleportation circuit, but instead of just measuring $\hat{p}$, we implement $\hat{U}(\hat{x})$ before measuring $\hat{p}$.

07 December 2024 17:52:47

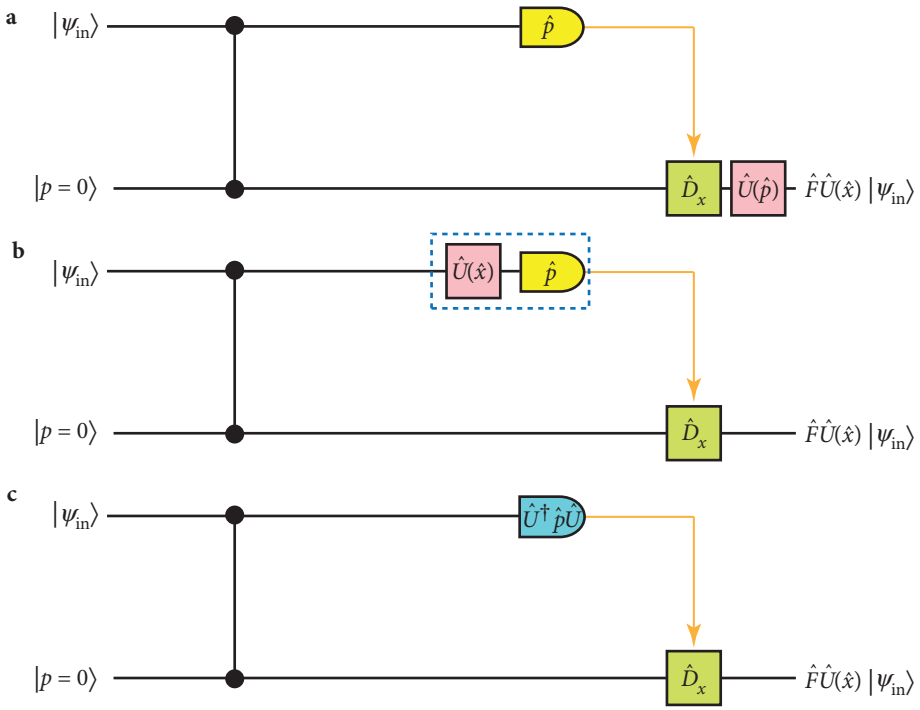

FIG. 3.5
Modification of the half-teleportation circuit. (a) Adding the operation $\hat{U}(\hat{p})$. (b) Moving $\hat{U}(\hat{x})$ to the measurement. (c) New measurement basis.

We can also show further that implementing $\hat{U}(\hat{x})$ before measuring $\hat{p}$ is equivalent to changing the measurement basis. This can be shown by noting that

$$m_p\hat{U}^\dagger(\hat{x})\,|\hat{p}=m_p\rangle=\left[\hat{U}^\dagger(\hat{x})\hat{p}\hat{U}(\hat{x})\right]\hat{U}^\dagger(\hat{x})\,|\hat{p}=m_p\rangle. \tag{3.23}$$

This means that implementation of the projection operator after the unitary $\hat{U}(\hat{x})$, i.e., $|\hat{p}=m_p\rangle\langle\hat{p}=m_p|\,\hat{U}(\hat{x})$, is equivalent to simply measuring $\hat{U}^\dagger(\hat{x})\hat{p}\hat{U}(\hat{x})$. Below, we show how this can be used to implement arbitrary quantum operation.

To realize universality on a single mode, one of the possible gate sets consists of p-displacement $\hat{D}_p(m_p)$, shear operation $\hat{P}(\gamma)$, cubic-phase gate $\hat{U}_{\mathrm{CPG}}(\gamma)$, and Fourier transform $\hat{F}$. As we have already shown that the half-teleportation circuit can be used to implement Fourier transform, we show that other operations can be implemented as well.

07 December 2024 17:52:47

Proof.

1. For $\hat{U}(x) = \hat{D}_p(m_p) = \exp\left(\frac{i}{\hbar} m_p \hat{x}\right)$, we get

$$\hat{U}^\dagger(\hat{x})\hat{p}\hat{U}(\hat{x}) = \hat{p} + m_p, \tag{3.24}$$

which is simply measurement of $\hat{p}$, added by the amount of displacement we wish to implement.

2. For $\hat{U}(x) = \hat{P}(\gamma) = \exp\left(\frac{i}{2\hbar}\gamma\hat{x}^2\right)$, we get

$$\hat{U}^\dagger(\hat{x})\hat{p}\hat{U}(\hat{x}) = \hat{p} + \gamma\hat{x} = \sqrt{1+\gamma^2}(\hat{p}\cos\theta + \hat{x}\sin\theta), \tag{3.25}$$

where $\tan\theta = \gamma$. Therefore, to implement shear operation, we simply have to do the homodyne measurement on a different basis and rescale the measurement results.

3. For $\hat{U}(x) = \hat{U}_{\text{CPG}}(\gamma) = \exp\left(\frac{i}{3\hbar}\gamma\hat{x}^3\right)$, we get

$$\hat{U}^\dagger(\hat{x})\hat{p}\hat{U}(\hat{x}) = \hat{p} + \gamma\hat{x}^2, \tag{3.26}$$

which is a nonlinear measurement of the quadrature operator. □

From the above proof, we can see that if we restrict ourselves to the homodyne measurement, we can only implement Gaussian operations using the half-teleportation circuit. This is expected as the homodyne measurement themselves cannot introduce non-Gaussianity. We will come back to how to implement the nonlinear measurement in Sec. 3.2.3. In addition to the single-mode quantum operations, we also need the two-mode operations such as a controlled-Z gate. Some readers might argue that since we already use the controlled-Z gate in the half-teleportation circuit, we should be able to use that for our two-mode operations, which should complete the proof of the universality with the half-teleportation circuit. While this might be the case, we might not want to implement the controlled-Z gate directly on the input modes. For example, in some systems, entangling gates are either probabilistic or difficult to implement.

Next, let us consider what kind of quantum operation we can implement when we change the measurement basis of the full-teleportation circuit from the Bell measurement basis. Although we consider implementation of the unitary operator $\hat{U}(\hat{p})$ in the case of the half-teleportation circuit, in the derivation of the input–output relation of the quantum teleportation circuit, we will consider what happens when the measurement basis is changed.

Theorem 3.1. *Let the measurement basis of each homodyne detector in Fig. 3.6 be $\hat{x}_1(\theta_1)$ and $\hat{x}_2(\theta_2)$, where $\hat{x}(\theta) \equiv \hat{x}\cos\theta + \hat{p}\sin\theta$ and $\theta_1 \neq \theta_2$. Then, we can write down the input–output relation of the quantum teleportation circuit as*

$$\hat{\mathbf{q}}_{\text{out}} = \mathbf{V}(\theta_+, \theta_-)\hat{\mathbf{q}}_{\text{in}} + \begin{pmatrix} \hat{x}_B - \hat{x}_A \\ \hat{p}_B + \hat{p}_A \end{pmatrix}, \tag{3.27}$$

where $\hat{\mathbf{q}} = (\hat{x} \quad \hat{p})^T$, and the matrix $\mathbf{V}(\theta_+, \theta_-)$ is defined as

$$\mathbf{V}(\theta_+, \theta_-) \equiv \mathbf{R}\left(\theta_+ - \frac{\pi}{2}\right)\mathbf{S}(\ln\tan\theta_-)\mathbf{R}(\theta_+), \tag{3.28}$$

07 December 2024 17:52:47

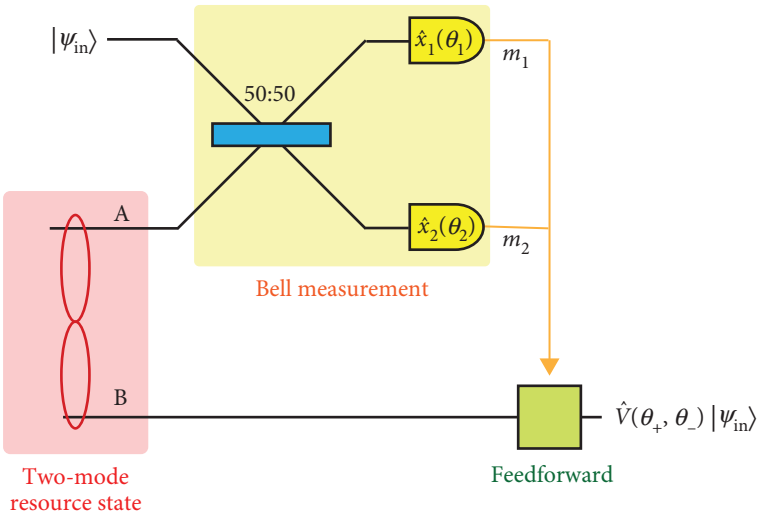

FIG. 3.6
Modified full-teleportation circuit.

with $\theta_\pm = (\theta_2 \pm \theta_1)/2$ *and the rotation matrix* $\mathbf{R}(\theta)$ *and the squeezing matrix* $\mathbf{S}(r)$ *defined by*

$$\mathbf{R}(\theta) = \begin{pmatrix} \cos\theta & \sin\theta \\ -\sin\theta & \cos\theta \end{pmatrix}, \tag{3.29}$$

$$\mathbf{S}(r) = \begin{pmatrix} e^{-r} & 0 \\ 0 & e^{r} \end{pmatrix}. \tag{3.30}$$

The above result can be proved as follows.

Proof. We first notice that if we let the measurement results at each homodyne detector be m_1 and m_2, we can compactly represent it using the original quadrature operator as

$$\sqrt{2}\mathbf{m} = \begin{pmatrix} \cos\theta_1 & \sin\theta_1 \\ \cos\theta_2 & \sin\theta_2 \end{pmatrix} \begin{pmatrix} \hat{x}_{\text{in}} \\ \hat{p}_{\text{in}} \end{pmatrix} + \begin{pmatrix} -\cos\theta_1 & -\sin\theta_1 \\ \cos\theta_2 & \sin\theta_2 \end{pmatrix} \begin{pmatrix} \hat{x}_A \\ \hat{p}_A \end{pmatrix}, \tag{3.31}$$

where $\mathbf{m} = (m_1 \quad m_2)^{\mathrm{T}}$. Then, similar to Eqs. (3.13) and (3.14), we can invert Eq. (3.31) and use the quadrature of mode A to get

$$\begin{aligned} \begin{pmatrix} \hat{x}_{\text{out}} \\ \hat{p}_{\text{out}} \end{pmatrix} = {} & \frac{1}{\sin(\theta_2 - \theta_1)} \begin{pmatrix} \sin\theta_2 & \sin\theta_1 \\ \cos\theta_2 & \cos\theta_1 \end{pmatrix} \begin{pmatrix} \cos\theta_1 & \sin\theta_1 \\ \cos\theta_2 & \sin\theta_2 \end{pmatrix} \begin{pmatrix} \hat{x}_{\text{in}} \\ \hat{p}_{\text{out}} \end{pmatrix} \\ & - \frac{\sqrt{2}}{\sin(\theta_2 - \theta_1)} \begin{pmatrix} \sin\theta_2 & \sin\theta_1 \\ \cos\theta_2 & \cos\theta_1 \end{pmatrix} \mathbf{m} + \begin{pmatrix} \hat{x}_B - \hat{x}_A \\ \hat{p}_B + \hat{p}_A \end{pmatrix}. \end{aligned} \tag{3.32}$$

07 December 2024 17:52:47

The second term is the feedforward term that can be erased if we do appropriate feedforward operation. The third term is a term due to the imperfection of our two-mode resource state. The coefficient in front of the first term determines $V(\theta_+, \theta_-)$ in Eq. (3.28), which can be obtained via a straightforward algebra. □

Therefore, by changing the measurement basis of the two homodyne measurements in the full-teleportation circuit, it is possible to implement various quantum operations. Notably, if we set $\theta_- = \pi/4$, i.e., if we set the measurement bases to be orthogonal, the matrix $\mathbf{V}(\theta_+, \theta_-)$ has only the rotational part. This is intuitively expected as by doing so, it should be equivalent to the identity operation in a rotated reference frame of the quadrature operator. On the other hand, if the bases of the two homodyne detectors are non-orthogonal, then effectively, we obtain more information of the certain quadrature of the input mode, which results in the squeezing operation in the output mode.

We have restricted ourselves to the case where $\theta_1 \neq \theta_2$. If we do not put this restriction, for example, let $\theta_1 = \theta_2 = 0$, then we have

$$\sqrt{2}m_1 = \hat{x}_{\text{in}} - \hat{x}_A, \tag{3.33}$$

$$\sqrt{2}m_2 = \hat{x}_{\text{in}} + \hat{x}_A, \tag{3.34}$$

which can be inverted into

$$\hat{x}_{\text{in}} = \frac{1}{\sqrt{2}}(m_2 + m_1), \tag{3.35}$$

$$\hat{x}_A = \frac{1}{\sqrt{2}}(m_2 - m_1). \tag{3.36}$$

This means that when the measurement bases are the same, we are simply measuring the input mode and mode A, which means that no operations can be done on the input mode. Note that this property is very useful for output readout in the MBQC.

3.2.2 Cluster state quantum computation

We have shown how the modification of the measurement bases allows both half-teleportation and full-teleportation circuits to be used in the implementation of the quantum operations. In this section, by extending such a concept, we will introduce a type of multipartite entanglement called cluster states. Cluster states can be considered extensions of the resource states for the teleportation circuit, which naturally arise if we consider multi-step multi-input quantum operations using the teleportation circuit.

3.2.2.1 Definition of canonical cluster states

To appropriately define the cluster state, let us consider sequential half-teleportation shown in Fig. 3.7(a). As displacement operation can be switched with the controlled-Z gate, which are Gaussian operations, at the cost of the displacement operations having a different amplitude, we arrive at

07 December 2024 17:52:47

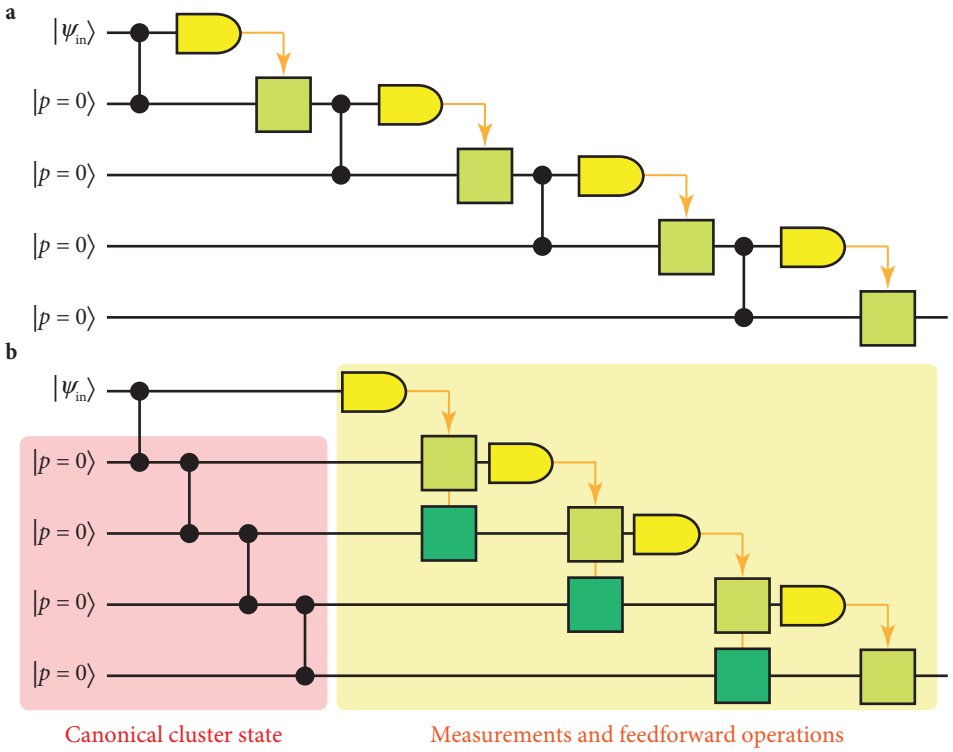

FIG. 3.7
Canonical cluster state and half-teleportation. (a) Sequential half-teleportation. (b) Equivalence to the computation using the canonical cluster state. The light green and the dark green blocks are displacements in x quadrature and p quadrature, respectively.

the circuit in Fig. 3.7(b). This circuit shows that multi-step quantum operations can be implemented using three steps:

1. generation of a multi-mode quantum entanglement,
2. coupling of the input mode to the quantum entanglement, and
3. measurements and feedforward operations.

This removes the necessity of having multiple half-teleportation circuits and replaces it with a quantum entanglement. If we want to implement two-mode operations, we can also construct a similar circuit but with two inputs instead. Also, note that in the case where the measurements are restricted to the homodyne measurements, the displacements operations can be further absorbed into the homodyne

07 December 2024 17:52:47

measurements and implemented only at the end of the operation, a property called *Gaussian parallelism* (Menicucci *et al.*, 2006). Therefore, if we start from the half-teleportation circuit, we are then interested in the quantum entanglements that are represented by controlled-Z gates connecting the quadrature eigenstates $|\hat{p} = 0\rangle$. This state is a type of cluster states, which is called a *canonical cluster state* to distinguish them from other types of cluster states. Mathematically, as controlled-Z gates between arbitrary modes commute with each other, we can properly define a canonical cluster state.

Definition 3.1. For a given adjacency matrix $\mathcal{A}$, i.e., a real matrix whose diagonal elements are zero and $\mathcal{A}^{\mathrm{T}} = \mathcal{A}$, a N-mode ideal canonical cluster state $|\mathcal{A}\rangle$ associated with this matrix $\mathcal{A}$ is given by

$$|\mathcal{A}\rangle = \hat{C}_Z[\mathcal{A}]\,|\hat{p} = 0\rangle^{\otimes N}, \tag{3.37}$$

where $\hat{C}_Z[\mathcal{A}]$ is a generalized version of the controlled-Z gate given by

$$\hat{C}_Z[\mathcal{A}] \equiv \exp\left(\frac{i}{\hbar}\hat{\mathbf{x}}^{\mathrm{T}}\mathcal{A}\hat{\mathbf{x}}\right), \tag{3.38}$$

where $\hat{\mathbf{x}} = (\hat{x}_1 \quad \hat{x}_2, \ldots, \hat{x}_N)^{\mathrm{T}}$.

As the ordering of the controlled-Z gates does not matter, we can visualize the ideal canonical cluster state using its adjacency matrix $\mathcal{A}$ (see Fig. 3.8 for an example). Although Fig. 3.7(b) shows the case where the generated cluster state is a four-mode linear cluster state, to implement universal MBQC, a cluster state whose structure graph is a two-dimensional grid, also called a *two-dimensional cluster state*, is required as one needs the two-mode operation in the realization of universality.

Ideal canonical cluster states, however, possess various problems. First, the generation of the ideal canonical cluster states required $|\hat{p} = 0\rangle$, which is unphysical. The best thing we can do is substitute the quadrature eigenstates with the squeezed states. Then, we need to quantify how close the

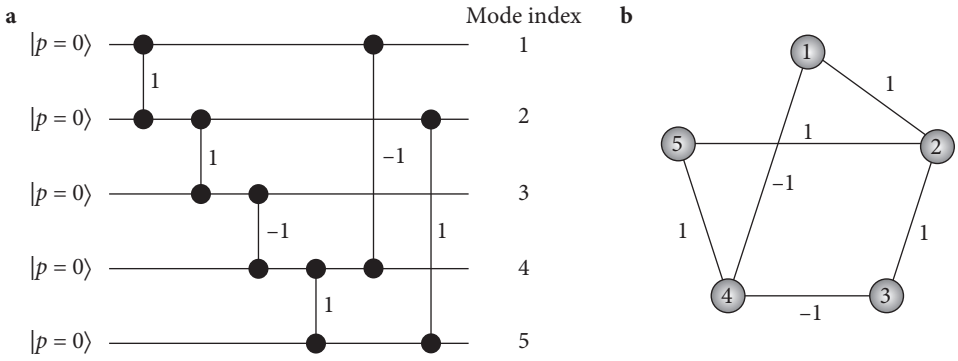

FIG. 3.8
An example of a canonical cluster state (a) and its corresponding graph (b).

07 December 2024 17:52:47

approximated state is to the ideal state. Second, the definition in Eq. (3.37) uses controlled-Z gates. In general, beamsplitter interactions are much easier to realize in the optical setup. Moreover, when we consider finite squeezing, it is likely that there are multiple possible setups that would result in the same ideal canonical cluster states in the infinite squeezing limit. We will address these issues in Sec. 3.2.2.2.

3.2.2.2 Canonical cluster states with offline squeezing and linear optics

First, we define nullifiers of pure Gaussian states.

Definition 3.2. For an N-mode pure Gaussian state $|\psi_G\rangle$, there are N independent operators $\hat{\delta}$ such as

$$\hat{\delta}\,|\psi_G\rangle = 0. \tag{3.39}$$

These operators are called *nullifiers*, and they uniquely define $|\psi_G\rangle$.

When the pure Gaussian states are transformed via Gaussian operations, we can track the quantum states simply by looking at the transformation of $\hat{\delta}$. There are two important properties regarding the nullifiers.

Theorem 3.2. *If $\hat{\delta}_1$ and $\hat{\delta}_2$ are the nullifiers of the pure Gaussian states $|\psi_G\rangle$, then for arbitrary $a, b \in \mathbb{C}$, the following holds:*

$$(a\hat{\delta}_1 + b\hat{\delta}_2)\,|\psi_G\rangle = 0. \tag{3.40}$$

Theorem 3.3. *If $\hat{\delta}$ is a nullifier of the pure Gaussian state $|\psi_G\rangle$, then the nullifier $\hat{\delta}'$ of the quantum state $\hat{U}\,|\psi_G\rangle$ is related to $\hat{\delta}$ by*

$$\hat{\delta}' = \hat{U}\hat{\delta}\hat{U}^{\dagger}. \tag{3.41}$$

Interestingly, the evolution of the nullifiers is the inverse of the Heisenberg picture evolution of the operators. This is due to the fact that when we represent the pure Gaussian states using nullifiers, we are actually using the Schrödinger picture where the quantum states are transformed. The nullifier is also a convenient representation from an experimental point as N-mode Gaussian pure states can be characterized by measuring only N independent nullifiers.

For the ideal canonical cluster states, we can calculate the nullifiers by using the fact that the nullifiers of the initial momentum eigenstates are $\hat{p}$ and Eq. (3.41). We arrive at

Theorem 3.4. *For an N-mode ideal canonical cluster state represented with an adjacency matrix $\mathcal{A}$, its nullifiers are*

$$\hat{\boldsymbol{\delta}}[\mathcal{A}] = \hat{\mathbf{p}} - \mathcal{A}\hat{\mathbf{x}}, \tag{3.42}$$

where $\hat{\boldsymbol{\delta}}$ is an $N \times 1$ vector of the nullifiers.

07 December 2024 17:52:47

In such a sense, the matrix $\mathcal{A}$ is a single matrix that defines the ideal canonical cluster state as it defines the nullifiers.

To generate a physical state that approximates an ideal canonical cluster state, we could think of generating a quantum state that takes the ideal nullifiers in Eq. (3.42) to zero in the infinite squeezing limit. Then, we can consider the variance of the nullifier as a quantity that tells us how good is the generated state. This idea is used in various experimental generations of the cluster states (Yukawa *et al.*, 2008; Yoshikawa *et al.*, 2016; Yokoyama *et al.*, 2013; Chen *et al.*, 2014; Asavanant *et al.*, 2019; and Larsen *et al.*, 2019) where the nullifiers are measured and the variances are calculated. In addition, as the cluster states are multipartite entangled states, the measurements of the nullifiers are also used in the verification of multipartite inseparability using the van Loock–Furusawa criteria described in Chap. 2.

For a given adjacency matrix $\mathcal{A}$, we want to derive a setup to generate a state that can approximate the ideal canonical cluster state well. This can be done by noticing the following

Theorem 3.5. *Any zero-mean Gaussian pure state $|\psi_G\rangle$ can be generated using offline squeezed vacuum states and linear optics.*

This comes from the fact that zero-mean Gaussian pure states can be generated using symplectic transformations on the vacuum state, which can be decomposed as Fig. 3.9(a). However, as the linear optics on a vacuum state results in a vacuum state, we are left with only the offline squeezed vacuum states and the linear optics in Fig. 3.9(b). As cluster states are also the Gaussian states, they can also be generated using only offline squeezed states and linear optics (van Loock *et al.*, 2007). The idea is that the

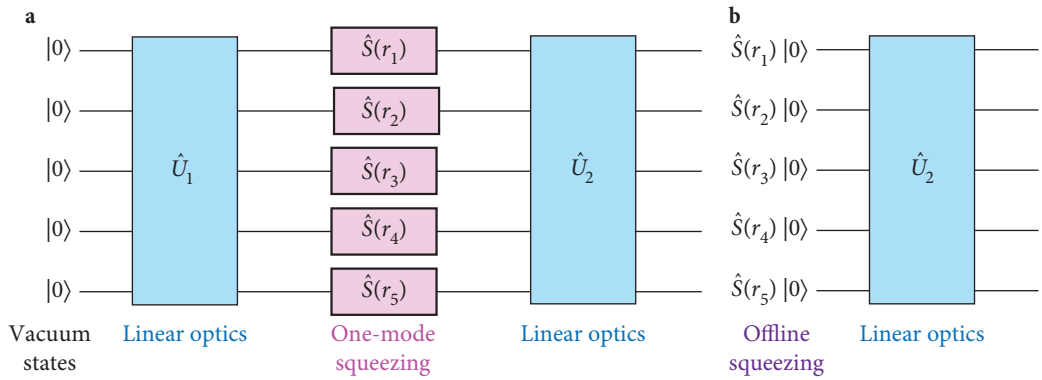

FIG. 3.9
Generation of zero-mean Gaussian pure states. (a) Bloch–Messiah decomposition. (b) Equivalence to offline squeezing and linear optics.

07 December 2024 17:52:47

desired linear optics should have the property that when the nullifiers in Eq. (3.42) are calculated, only the squeezing components of the initial squeezed states are left and the antisqueezing components all cancel out. This leads to the ideal nullifiers in the infinite squeezing limit.

3.2.2.3 Graphical calculus

In the visualization of an ideal canonical cluster state, we can simply draw an undirected graph from the adjacency matrix $\mathcal{A}$ where each mode is denoted with a node and $\mathcal{A}_{ij}$ is the weight of the edge between the node i and j. For physical cluster states, this visualization is not sufficient as it does not incorporate the effects of finite squeezing. Moreover, other types of entanglement such as two-mode squeezed states, which are obviously resource states for a full-quantum teleportation circuit, are not included in this visualization. In this section, we will introduce a methodology called a *graphical calculus* (Menicucci *et al.*, 2011), which is a convenient method to visualize multi-mode pure Gaussian states, which include approximated canonical cluster states and other resource states such as the two-mode squeezed state. First, we properly define a pure Gaussian state.

Definition 3.3. A N-mode pure Gaussian state is a quantum state that can be generated from a N-mode vacuum state $|0\rangle^{\otimes N}$ and Gaussian operations. A zero-mean pure Gaussian state can be uniquely determined from its second-order moment of the quadrature operators, i.e., its covariance matrix $\operatorname{cov}\hat{\mathbf{q}}$, which is defined as

$$\operatorname{cov}\hat{\mathbf{q}} \equiv \frac{1}{2}\left\langle \hat{\mathbf{q}}\hat{\mathbf{q}}^{\mathrm{T}} + \left(\hat{\mathbf{q}}\hat{\mathbf{q}}^{\mathrm{T}}\right)^{\mathrm{T}} \right\rangle, \tag{3.43}$$

where $\hat{\mathbf{q}} = (\hat{\mathbf{x}} \quad \hat{\mathbf{p}})^{\mathrm{T}}$.

It is possible to write down the covariance matrix, the wave function, and the Wigner function of the pure Gaussian state. Let us assume that the state of our interest has zero mean, and the symplectic matrix $\mathbf{S}$ required to generate the N-mode pure Gaussian state from the vacuum state is uniquely decomposed in the form (Simon *et al.*, 1988)

$$\mathbf{S} = \begin{pmatrix} \mathbf{I} & \mathbf{0} \\ \mathbf{V} & \mathbf{I} \end{pmatrix} \begin{pmatrix} \mathbf{U}^{-1/2} & \mathbf{0} \\ \mathbf{0} & \mathbf{U}^{1/2} \end{pmatrix} \begin{pmatrix} \mathbf{X} & -\mathbf{Y} \\ \mathbf{Y} & \mathbf{X} \end{pmatrix}. \tag{3.44}$$

$\mathbf{U}$ is symmetric and positive definite, $\mathbf{V}$ is symmetric, and the third matrix on the right in Eq. (3.44) is orthogonal. From this decomposition, we have

Theorem 3.6. *The covariance matrix* $\operatorname{cov}\hat{\mathbf{q}}$ *of a state generated with* $\mathbf{S}$ *in Eq. (3.44) is given by*

$$\operatorname{cov}\hat{\mathbf{q}} = \frac{\hbar}{2}\mathbf{S}\mathbf{S}^{\mathrm{T}}. \tag{3.45}$$

Theorem 3.7. *The wave function* $\psi_{\mathbf{S}}(\mathbf{x})$ *of the quantum state generated with* $\mathbf{S}$ *in Eq. (3.44) is given by*

$$\psi_{\mathbf{S}}(\mathbf{x}) = \left(\frac{\det \mathbf{U}}{\pi^N \hbar^N}\right)^{\frac{1}{4}} \exp\left[-\frac{1}{2\hbar}\mathbf{x}^{\mathrm{T}}(\mathbf{U} - i\mathbf{V})\mathbf{x}\right]. \tag{3.46}$$

07 December 2024 17:52:47

Similarly, the Wigner function $W_{\mathbf{S}}(\mathbf{q})$ *is given by*

$$W_{\mathbf{S}}(\mathbf{q}) = \frac{1}{(\pi\hbar)^N} \exp\left[-\frac{1}{\hbar}\left(\mathbf{S}^{-1}\mathbf{q}\right)^{\mathrm{T}}\left(\mathbf{S}^{-1}\mathbf{q}\right)\right]. \tag{3.47}$$

There are a few interesting things about the above results. First, rather than $\mathbf{S}$ itself, the covariance matrix and the Wigner function that uniquely specifies the pure Gaussian states are determined by the product $\mathbf{S}\mathbf{S}^{\mathrm{T}}$. This is, in a way, somewhat expected as the symplectic matrix $\mathbf{S}$ to generate a pure Gaussian state from the vacuum state is not unique [for example, we can add arbitrary linear optics at the beginning, corresponding to the third matrix in Eq. (3.44)]. Second, the factor $\mathbf{U} - i\mathbf{V}$ suggests that this combination might provide a way to visualize an arbitrary Gaussian state. In the ideal canonical cluster state, although the wave function is unnormalizable, it is somewhat equivalent to the case where $\mathbf{U} = \mathbf{0}$ and $\mathbf{V} = \mathcal{A}$. From this, a graph of the pure Gaussian states is defined as

Definition 3.4. A graph of a pure Gaussian state generated with the symplectic matrix in Eq. (3.44) is represented with a complex, symmetric matrix $\mathbf{Z}$, which is defined as

$$\mathbf{Z} \equiv \mathbf{V} + i\mathbf{U}. \tag{3.48}$$

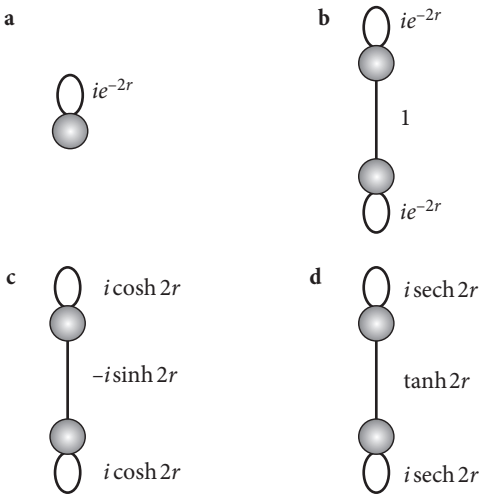

FIG. 3.10
Examples of graphs of various Gaussian states: (a) p-squeezed state. (b) Two p-squeezed states joined with a controlled-Z gate. (c) A two-mode squeezed state. (d) A two-mode squeezed state with Fourier transform on one of the modes.

Each element $(\mathbf{Z})_{ij}$ determines the complex weights of the edges between the nodes representing modes i and j.

The reason that this is how the graphs of the pure Gaussian states are defined is because of the following property.

Theorem 3.8. *If an initial Gaussian state with a graph* $\mathbf{Z}$ *undergoes a symplectic transformation, which can be written in a form*

$$\mathbf{S} = \begin{pmatrix} \mathbf{A} & \mathbf{B} \\ \mathbf{C} & \mathbf{D} \end{pmatrix}, \tag{3.49}$$

then the resulting state will have a graph $\mathbf{Z}'$*, which is given by*

$$\mathbf{Z}' = (\mathbf{C} + \mathbf{D}\mathbf{Z})(\mathbf{A} + \mathbf{B}\mathbf{Z})^{-1}. \tag{3.50}$$

The transformation in Eq. (3.50) resembles a linear fractional transformation. We will not go further into details and urge the readers who are interested in the derivations to consult Menicucci *et al.* (2011).

Figure 3.10 shows examples of the graphs of various states. First, we observe that for a two-mode canonical cluster state generated by joining two p-squeezed states with a controlled-Z gate, the graph is almost the same with an ideal canonical

07 December 2024 17:52:47

cluster state except for the self-loops with complex weights, which represented finite squeezing as these loops vanish in the limit of $r \to \infty$. On the other hand, the two-mode squeezed state, which is an approximation of the EPR state, has complex edge weight and self-loops, all of which go to the infinity in the infinite squeezing limit. Now, what is interesting is that if we perform a Fourier transform on one of the modes of the two-mode squeezed state, we get the graph in Fig. 3.10(d). Although it looks different from the graph in Fig. 3.10(b), in the infinite squeezing limit, both graphs become ideal canonical cluster states. This suggests that the two-mode squeezed state, up to the local phase rotation, can also be considered an approximated state to an ideal canonical cluster state. However, as their graphs differ, their properties are different in the finite squeezing limit. This simple example illustrates how graphical calculus allows us to deal with physical cluster states and quantify the cluster states. Nevertheless, it is important that for the cluster states, their graphs are their mathematical descriptions.

3.2.2.4 Experiments on optical canonical cluster states

In this section, we will briefly discuss the generation of the canonical cluster states. Note that in this section, we will restrict ourselves to the setup where no multiplexing is used. Discussions regarding multiplexing will be given in Chap. 4.

Based on the methodology discussed in Sec. 3.2.2.2, generation of four-mode CV cluster state with different architecture have been realized (Fig. 3.11), and up to six-mode CV cluster state has also been achieved (Su *et al.*, 2013). In addition to the generation of the cluster states, there are also some experiments that utilize them for implementation of some basic operations. The three-mode cluster state has been used to demonstrate the gain-tunable entangling gate (Yokoyama *et al.*, 2015), and implementation of single-mode Gaussian states using the four-mode linear cluster state has also been demonstrated (Ukai *et al.*, 2011). There is also an experiment that uses a six-mode cluster state to implement quantum operation (Su *et al.*, 2013). In these experiments, what they have in common is that they can choose the measurement bases of the homodyne freely and they can also implement the necessary feedforward displacement operations. These technologies are the same basic technologies required in the quantum teleportation experiments.

To realize universal MBQC, the cluster states should at least have a two-dimensional structure; for example, a cluster state whose graph is a two-dimensional square lattice would allow multi-input multi-output MBQC. For most of the system, although there exists various theoretical proposals, the experimental realizations have been limited to a very small scale cluster state. Such scaling up to the two-dimensional cluster states has only been recently realized using the time-domain-multiplexing method (Menicucci, 2011; Asavanant *et al.*, 2019; and Larsen *et al.*, 2019), which we will discuss in Chap. 4. Note, however, that the two-dimensional cluster states generated in those experiments are not canonical cluster states as their ideal nullifiers do not have the form in Eq. (3.42).

07 December 2024 17:52:47

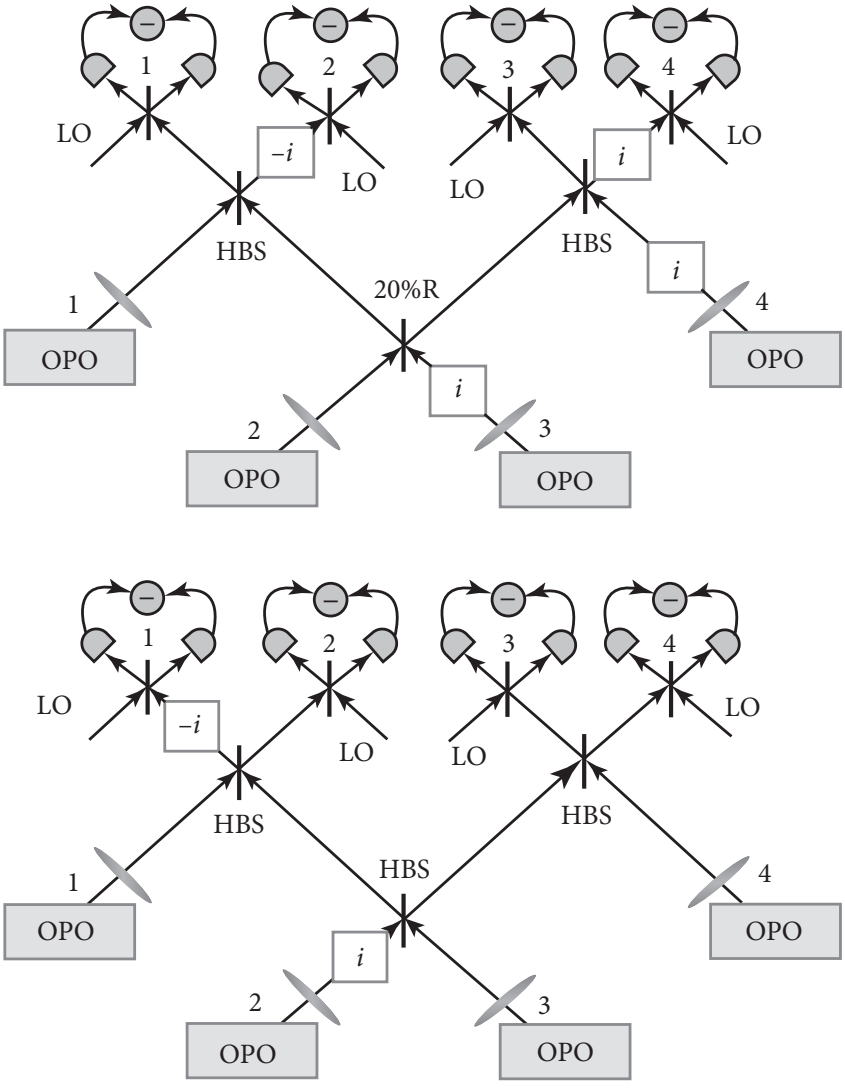

FIG. 3.11
An example of the experimental systems for four-mode cluster state generation with different graphical structures. [Yukawa *et al.*, Phys. Rev. A **78**, 012301 (2008).]

07 December 2024 17:52:47

3.2.2.5 "Non"-canonical cluster state

We have seen that the two-mode squeezed states are related to the canonical cluster states via local phase rotations. When we consider the measurements on such resource states, as the local phase rotations corresponds to simply the change on the basis of the homodyne measurement, their capability in MBQC should be the same. Mathematically, they are different states as the ideal EPR state nullifiers have only an $\hat{x}$ or a $\hat{p}$ operator, while the canonical cluster state has both operators as in Eq. (3.42). In recent years, many of the cluster states generated have nullifiers that, similar to the EPR states, are linear combinations of either an $\hat{x}$ or a $\hat{p}$ operator. This type of cluster states is in fact called *$\mathcal{H}$-graph states* (Menicucci *et al.*, 2011). It is known that $\mathcal{H}$-graph states can also be generated using a single optical parametric oscillator (OPO).

3.2.2.6 Single-mode Gaussian universality of the cluster state

When considering the quantum computation using the cluster state, it is interesting to think of how large we need the cluster state to be. For arbitrary operations, this is not so trivial. For a single-mode Gaussian operation, however, it has been theoretically shown that we only need a four-mode linear canonical cluster state to realize arbitrary single-mode Gaussian universality (Ukai *et al.*, 2010) despite the fact that a 2×2 symplectic matrix has three degrees of freedom.

For the cluster states based on the full-teleportation circuit, we prove below that we need two steps of full teleportation to realize arbitrary symplectic operations.

Proof. Arbitrary single-mode symplectic transformation $\mathcal{S}$ has a form of

$$\mathcal{S} = \mathbf{R}(\psi)\mathbf{S}(r)\mathbf{R}(\phi), \tag{3.51}$$

where $\mathbf{R}(\psi)$ and $\mathbf{S}(r)$ are the rotational matrix and the squeezing matrix, respectively. From Eq. (3.28), it is clear that a single step of the full-teleportation circuit does not possess sufficient degree of freedom to realize Eq. (3.51). If we, however, implement the full teleportation twice, we get

$$\mathbf{V}_{\text{resultant}} = \mathbf{V}(\theta'_+, \theta'_-)\mathbf{V}(\theta_+, \theta_-). \tag{3.52}$$

If we select, for example,

$$\theta'_+ + \theta_+ + \frac{\pi}{2} = \psi, \tag{3.53}$$

$$\theta'_- = 0, \tag{3.54}$$

$$\theta_+ = \phi, \tag{3.55}$$

$$\ln \tan \theta_- = r, \tag{3.56}$$

which definitely has a solution, we can realize arbitrary symplectic transformation. □

07 December 2024 17:52:47

3.2.2.7 Comparison with the qubit cluster state

As a comparison, we will briefly compare the CV cluster states to the qubit cluster states. In CV systems, cluster states are mathematically defined by its nullifiers. For a qubit system, however, instead of the nullifiers, *stabilizers* are usually used.

Definition 3.5. A stabilizer $\hat{S}$ of a quantum state $|\psi\rangle$ is an operator that is defined as

$$\hat{S}|\psi\rangle = |\psi\rangle. \tag{3.57}$$

Similar to how N-mode cluster states can be specified with N nullifiers, N-qubit cluster states can be specified using N independent stabilizers. To be more precise, the stabilizers of the qubit cluster state and its corresponding graph are defined as follows.

Definition 3.6. In N-qubit cluster states with an arbitrary (unweighted) graph, its stabilizer is given by

$$\hat{S}_j = \hat{\sigma}_{x,j} \otimes_k \hat{\sigma}_{z,k}, \tag{3.58}$$

where $\hat{\sigma}_{x,j}$ and $\hat{\sigma}_{z,j}$ are the Pauli-x and Pauli-z operator associated with qubit j. The tensor product $\otimes_k$ is taken with respect to the nodes that are adjacent to node j.

From the above definition, we can see the parallelism between the nullifiers in CV cluster states and the stabilizer in the qubit cluster states. In qubit cluster states, the stabilizer is made up of the Pauli operators, which are observables. While it is also possible to formulate the stabilizer in the CV cluster states, the stabilizer will become a unitary operator, which is not an observable.

In a qubit system, MBQC can be done by appropriate measurements on the qubits of the cluster states. Similar to the CV cluster states, in addition to the Pauli measurements, the non-Pauli measurement is also necessary to achieve universality.

3.2.3 Gate teleportation

In the cluster state computation, the idea is to replace the resource states in the quantum teleportation protocol with appropriate cluster states and change the measurement bases. However, one of the difficulties in the cluster state computation is that it requires a nonlinear or non-Gaussian measurement to realize a non-Gaussian operation. Here, we will consider one of the methods to realize non-Gaussian operations such that instead of a non-Gaussian measurement, we use a non-Gaussian ancillary state. This method is known as *gate teleportation.* One of the merits of the gate teleportation in the optical system is that preparation of a particular non-Gaussian state is usually much easier than direct implementation of non-Gaussian operation that works on arbitrary quantum states. Moreover, as non-Gaussian ancillary states are not required inline, i.e., they can be injected from outside of the circuit, the state generation process can be probabilistic without making the computation probabilistic. See Chap. 5 for more details on non-Gaussian state generation in the optical system.

07 December 2024 17:52:47

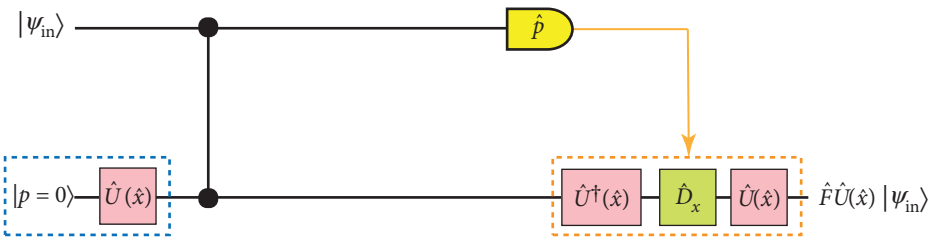

FIG. 3.12
Gate teleportation circuit.

3.2.3.1 Circuit diagram

Figure 3.12 shows a diagram of the gate teleportation (Gottesman and Chuang, 1999; and Bartlett and Munro, 2003). Note that this circuit is also based from the half-teleportation circuit. Instead of moving the unitary operation $\hat{U}(\hat{x})$ to the homodyne detector, we move it to the quadrature eigenstate $|p=0\rangle$. Therefore, if we could generate an ancillary state $\hat{U}(\hat{x})\left|p=0\right\rangle$ and use it in the half-teleportation circuit, we could realize non-Gaussian operation $\hat{U}(\hat{x})$ with only homodyne detection. Note that as a cost of this, the feedforward operation is changed from the displacement in x quadrature $\hat{D}_x(m_p)$ to $\hat{U}(\hat{x})\hat{D}_x(m_p)\hat{U}^{\dagger}(\hat{x})$. In general, this feedforward operation could become a very difficult operation that rendering gate teleportation is not experimentally feasible. We will show that, however, for a specific non-Gaussian operation $\hat{U}(\hat{x})$ called a cubic-phase gate, the feedforward operation is doable.

3.2.3.2 Cubic-phase gate with gate teleportation

Let us consider the case where the unitary operator $\hat{U}(\hat{x})$ in Fig. 3.12 is a cubic-phase gate whose unitary operator is given by

$$\hat{U}_{\mathrm{CPG}}(\gamma)=\exp\left(\frac{i}{3\hbar}\gamma\hat{x}^3\right). \tag{3.59}$$

Then, the necessary ancillary state, which is called cubic-phase state |CPS⟩, is given by

$$|\mathrm{CPS}\rangle=\hat{U}_{\mathrm{CPG}}(\gamma)\left|p=0\right\rangle. \tag{3.60}$$

Note that as this state is unnormalizable, we have to actually make an approximated version of this state. One of the ways to do so is we can notice that |CPS⟩ is a zero-eigenstate of an operator

$$\hat{U}_{\mathrm{CPG}}(\gamma)\hat{p}\hat{U}_{\mathrm{CPG}}^{\dagger}(\gamma)=\hat{p}-\gamma\hat{x}^2. \tag{3.61}$$

Therefore, in a similar manner to the nullifiers of the cluster state, we can try generating quantum states that minimize $\hat{p}-\gamma\hat{x}^2$, and there has been a recent experimental demonstration of this (Konno *et al.*, 2021).

07 December 2024 17:52:47

Regarding the feedforward operation, we can show that it is transformed to

$$\hat{U}_{\mathrm{CPG}}(\gamma)\hat{D}_x(m_p)\hat{U}^{\dagger}_{\mathrm{CPG}}(\hat{x}) = \exp\left[-\frac{i}{\hbar}m_p(\hat{p}-\gamma\hat{x}^2)\right]. \tag{3.62}$$

The operation in Eq. (3.62) is no longer a displacement operation but is a Gaussian operation whose "gain" depends on the measurement results m_p. If we use the convenient Baker–Campbell–Hausdorff (BCH), Eq. (3.62) can be decomposed into displacement operations and shear operations. Therefore, although a cubic-phase gate allows feedforward operations that are still Gaussian operations, it requires the implementation of shear operations whose strength can be dynamically changed. Experimentally, this type of dynamical shear operation has been experimentally demonstrated (Miyata *et al.*, 2014) using the analog circuits, and there are also research studies using digital circuits for this type of feedforward (Sakaguchi *et al.*, 2018).

3.2.3.3 Qubit-based gate teleportation

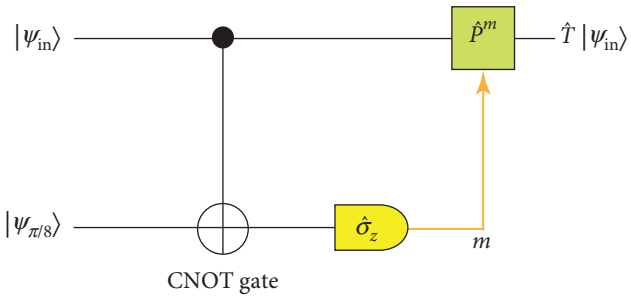

FIG. 3.13
Qubit gate teleportation circuit.

As a comparison, let us briefly introduce the qubit-based gate teleportation. One of the non-clifford single-qubit gates is a T gate $\hat{T}$ (or a $\pi/8$ gate), which transforms the initial qubit $|\psi_{\mathrm{in}}\rangle = a|0\rangle + b|1\rangle$ as

$$\hat{T} : a|0\rangle + b|1\rangle \rightarrow a|0\rangle + be^{i\frac{\pi}{4}}|1\rangle. \tag{3.63}$$

Figure 3.13 shows the circuit diagram for the qubit-based gate teleportation. We can notice the similarity to the CV gate teleportation, only that the resource state is changed to $|\psi_{\pi/8}\rangle$, which is the state obtained when $\pi/8$ is implemented on the $|+\rangle = (|0\rangle + |1\rangle)/\sqrt{2}$, similar to how the resource state for the cubic-phase gate is $\hat{U}_{\mathrm{CPS}}(\gamma)\,|p=0\rangle$.

Prior to the measurement, the quantum state $|\psi'\rangle$ is given by

$$|\psi'\rangle = \frac{1}{\sqrt{2}}\left[(a\,|0\rangle + be^{i\frac{\pi}{4}}\,|1\rangle)\otimes|0\rangle + e^{i\frac{\pi}{4}}(a\,|0\rangle + be^{-i\frac{\pi}{4}}\,|1\rangle)\otimes|1\rangle\right]. \tag{3.64}$$

Then, by measuring the second qubit with the Pauli-Z basis, we get $\hat{T}\,|\psi_{\mathrm{in}}\rangle$ if the measurement result is $|0\rangle$ and $\hat{P}^{-1}\hat{T}\,|\psi_{\mathrm{in}}\rangle$ if the measurement result is $|1\rangle$, where $\hat{P}$ is the phase gate, which is a Clifford gate. By implementing $\hat{P}$ depending on the measurement results, we can implement the T gate on the input state.

07 December 2024 17:52:47

3.2.4 Non-Gaussian measurement using ancillary states

We have shown that by using the gate teleportation protocol, we can use the non-Gaussian ancillary state to realize non-Gaussian operations on an arbitrary quantum state. The idea of the gate teleportation is, in a way, the quantum teleportation of the non-Gaussian operation on the ancillary state to the input state. On the other hand, we have discussed in Sec. 3.2.2 that if we can implement non-Gaussian measurements on the cluster state, then we can realize non-Gaussian operation. In this section, we will introduce an idea similar to the gate teleportation but is somewhat qualitatively different. Instead of teleporting the non-Gaussianity of the ancillary state to the input state, we can use the non-Gaussian ancillary state, in combination with homodyne measurement and appropriate feedforward operation, to realize non-Gaussian measurement.

The idea of using ancillary states for non-Gaussian measurement has much higher affinity with the MBQC based on cluster states than the gate teleportation scheme in a sense that rather than changing the resource state, we are simply changing our measurement gadget. Figure 3.14 shows the concepts of using a non-Gaussian ancillary state for non-Gaussian measurements (Marek *et al.*, 2018). We can see that this scheme requires dynamic changes of the interaction strength (beamsplitter or a controlled-Z gate) and the measurement basis. As a concrete example, there is a scheme for the cubic-phase-gate measurement using a non-Gaussian ancillary state and nonlinear feedforward (Miyata *et al.*, 2016). If we could realize this scheme, then we could use this measurement system to measure the modes of the cluster states instead of the homodyne measurements and realize universal quantum computation.

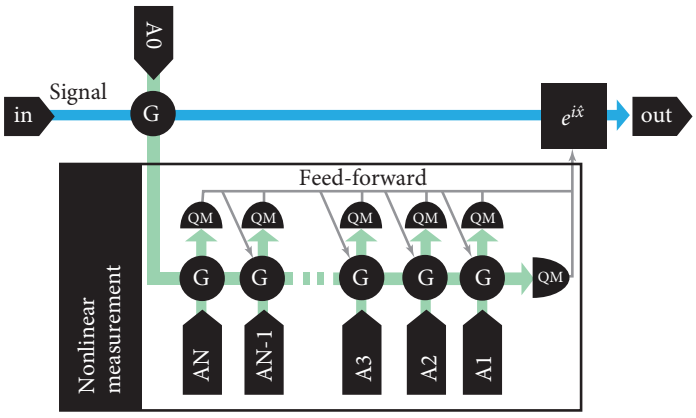

FIG. 3.14
Non-Gaussian (nonlinear) measurement using non-Gaussian ancillary states (A1 to AN), beamsplitter interactions, or quantum nondemolition interactions (G), and feedforward (Marek *et al.*, 2018).

REFERENCES

Andersen, U. L., Neergaard-Nielsen, J. S., van Loock, P., and Furusawa, A., "Hybrid discrete- and continuous-variable quantum information," Nat. Phys. **11**(9), 713–719 (2015).

Asavanant, W., Shiozawa, Y., Yokoyama, S., Charoensombutamon, B., Emura, H., Alexander, R. N., "Generation of time-domain-multiplexed two-dimensional cluster state," Science **366**(6463), 373–376 (2019).

07 December 2024 17:52:47

Bartlett, S. D. and Munro, W. J., "Quantum teleportation of optical quantum gates," Phys. Rev. Lett. **90**, 117901 (2003).

Bennett, C. H., Brassard, G., Crépeau, C., Jozsa, R., Peres, A., and Wootters, W. K., "Teleporting an unknown quantum state via dual classical and Einstein-Podolsky-Rosen channels," Phys. Rev. Lett. **70**, 1895–1899 (1993).

Bouwmeester, D., Pan, J. W., Mattle, K., Eibl, M., Weinfurter, H., and Zeilinger, A., "Experimental quantum teleportation," Nature **390**(6660), 575–579 (1997).

Braunstein, S. L. and Kimble, H. J., "*A posteriori* teleportation," Nature **394**(6696), 840–841 (1998).

Braunstein, S. L. and Kimble, H. J., "Teleportation of continuous quantum variables," Phys. Rev. Lett. **80**, 869–872 (1998).

Chen, M., Menicucci, N. C., and Pfister, O., "Experimental realization of multipartite entanglement of 60 modes of a quantum optical frequency comb," Phys. Rev. Lett. **112**, 120505 (2014).

Furusawa, A., Sørensen, J. L., Braunstein, S. L., Fuchs, C. A., Kimble, H. J., and Polzik, E. S., "Unconditional quantum teleportation," Science **282**(5389), 706–709 (1998).

Gottesman, D. and Chuang, I. L., "Demonstrating the viability of universal quantum computation using teleportation and single-qubit operations," Nature **402**(6760), 390–393 (1999).

Konno, S., Sakaguchi, A., Asavanant, W., Ogawa, H., Kobayashi, M., Marek, P., "Nonlinear squeezing for measurement-based non-Gaussian operations in time domain," Phys. Rev. Appl. **15**, 024024 (2021).

Larsen, M. V., Guo, X., Breum, C. R., Neergaard-Nielsen, J. S., and Andersen, U. L., "Deterministic generation of a two-dimensional cluster state," Science **366**(6463), 369–372 (2019).

Lee, N., Benichi, H., Takeno, Y., Takeda, S., Webb, J., Huntington, E., "Teleportation of nonclassical wave packets of light," Science **332**(6027), 330–333 (2011).

Marek, P., Filip, R., Ogawa, H., Sakaguchi, A., Takeda, S., Yoshikawa, J., "General implementation of arbitrary nonlinear quadrature phase gates," Phys. Rev. A **97**, 022329 (2018).

Menicucci, N. C., "Temporal-mode continuous-variable cluster states using linear optics," Phys. Rev. A **83**, 062314 (2011).

Menicucci, N. C., Flammia, S. T., and van Loock, P., "Graphical calculus for Gaussian pure states," Phys. Rev. A **83**, 042335 (2011).

Menicucci, N. C., van Loock, P., Gu, M., Weedbrook, C., Ralph, T. C., and Nielsen, M. A., "Universal quantum computation with continuous-variable cluster states," Phys. Rev. Lett. **97**, 110501 (2006).

Miyata, K., Ogawa, H., Marek, P., Filip, R., Yonezawa, H., Yoshikawa, J., "Experimental realization of a dynamic squeezing gate," Phys. Rev. A **90**, 060302 (2014).

Miyata, K., Ogawa, H., Marek, P., Filip, R., Yonezawa, H., Yoshikawa, J., "Implementation of a quantum cubic gate by an adaptive non-Gaussian measurement," **Phys. Rev. A 93**, 022301 (2016).

Raussendorf, R. and Briegel, H. J., "A one-way quantum computer," Phys. Rev. Lett. **86**, 5188–5191 (2001).

07 December 2024 17:52:47

Sakaguchi, A., Ogawa, H., Kobayashi, M., Suzuki, S., Yonezawa, H., Huntington, E., "Low-latency digital feedforward for universal continuous-variable quantum computation in time domain," in *Conference on Lasers and Electro-Optics* (Optical Society of America, 2018), p. FTu4G.3.

Simon, R., Sudarshan, E. C. G., and Mukunda, N., "Gaussian pure states in quantum mechanics and the symplectic group," Phys. Rev. A **37**, 3028–3038 (1988).

Su, X., Hao, S., Deng, X., Ma, L., Wang, M., Jia, X., "Gate sequence for continuous variable one-way quantum computation," Nat. Commun. **4**(1), 2828 (2013).

Takeda, S., Mizuta, T., Fuwa, M., van Loock, P., and Furusawa, A., "Deterministic quantum teleportation of photonic quantum bits by a hybrid technique," Nature **500**(7462), 315–318 (2013).

Ukai, R., Iwata, N., Shimokawa, Y., Armstrong, S. C., Politi, A., Yoshikawa, J., "Demonstration of unconditional one-way quantum computations for continuous variables," Phys. Rev. Lett. **106**, 240504 (2011).

Ukai, R., Yoshikawa, J., Iwata, N., van Loock, P., and Furusawa, A., "Universal linear Bogoliubov transformations through one-way quantum computation," Phys. Rev. A **81**, 032315 (2010).

van Loock, P., Weedbrook, C., and Gu, M., "Building Gaussian cluster states by linear optics," Phys. Rev. A **76**, 032321 (2007).

Vaidman, L., "Teleportation of quantum states," Phys. Rev. A **49**, 1473–1476 (1994).

Yokoyama, S., Ukai, R., Armstrong, S. C., Sornphiphatphong, C., Kaji, T., Suzuki, S., "Ultra-large-scale continuous-variable cluster states multiplexed in the time domain," Nat. Photonics **7**(12), 982–986 (2013).

Yokoyama, S., Ukai, R., Armstrong, S. C., Yoshikawa, J., van Loock, P., and Furusawa, A., "Demonstration of a fully tunable entangling gate for continuous-variable one-way quantum computation," Phys. Rev. A **92**, 032304 (2015).

Yoshikawa, J., Yokoyama, S., Kaji, T., Sornphiphatphong, C., Shiozawa, Y., Makino, K., "Invited article: Generation of one-million-mode continuous-variable cluster state by unlimited time-domain multiplexing," APL Photonics **1**(6), 060801 (2016).

Yukawa, M., Ukai, R., van Loock, P., and Furusawa, A., "Experimental generation of four-mode continuous-variable cluster states," Phys. Rev. A **78**, 012301 (2008).

Walshe, B. W., Mensen, L. J., Baragiola, B. Q., and Menicucci, N. C., "Robust fault tolerance for continuous-variable cluster states with excess antisqueezing," Phys. Rev. A **100**, 010301 (2019).

07 December 2024 17:52:47

CHAPTER

4 QUANTUM COMPUTATION IN TIME DOMAIN

4.1 ENCODING INFORMATION IN A WAVE PACKET

First, we will describe how to treat wave packets in the continuous-variable (CV) optical system. In Secs. 4.1.1 and 4.1.2, the mathematical formulation of a wave packet in both the time domain and the frequency domain is given. Understanding of the wave packet mode from both aspects is crucial, similar to how the Fourier transformation can help understand time-domain signals. Then, we show how to treat squeezing in the temporal wave packet in Sec. 4.1.3. This is substantially different from the treatment of the squeezed state in this book so far where we have assumed a single-mode state.

4.1.1 Treatment of wave packet in the time domain

In Chap. 2, we have discussed that when we quantize the electromagnetic fields, we can represent the electromagnetic wave using the vector potentials and the annihilation (and creation) operators corresponding to each mode. Here, let us consider an annihilation operator $\hat{a}(t)$ that corresponds to an electromagnetic field at time t.[1] The annihilation and creation operator will have the following commutation relation:

$$[\hat{a}(t), \hat{a}^\dagger(t')] = \delta(t - t'). \tag{4.1}$$

The above commutation relation is not a Bosonic commutation relation as the right-hand side is a delta function and not a Kronecker delta. This is expected as a temporal mode with infinitesimal width is unphysical. Nevertheless, we can define an annihilation operator $\hat{a}_f$ associated with a function $f(t)$ as

$$\hat{a}_f \equiv \int_{-\infty}^{\infty} \mathrm{d}t\, f(t)\hat{a}(t), \tag{4.2}$$

[1] In this section, we will define the annihilation operator $\hat{a}(t)$ in a rotating reference frame of the angular frequency Ω of the carrier frequency, i.e., if the original annihilation operator is $\hat{A}(t)$, then we have $\hat{A}(t) = \hat{a}(t)\exp(-i\Omega t)$. In this definition, the component of $\hat{A}(t)$ that is oscillating with the term $\exp(-i\Omega t)$ will have no time dependence when considered as $\hat{a}(t)$. When we do the homodyne measurement with the local oscillator with the same carrier frequency, we will be measuring $\hat{a}(t)$. Also, note the difference between the Definition 2.4 ($\hat{a}_k(t)$) in Chap. 2, which is not the operator in the rotating reference frame, but corresponds to moving the time dependence to the annihilation operator.

07 December 2024 17:52:47

https://doi.org/10.1063/9780735424074_004

Optical Quantum Computers: A Route to Practical Continuous Variable Quantum Information Processing, W. Asavanant and A. Furusawa
© 2022 AIP Publishing, published by AIP Publishing

and we call this $\hat{a}_f$ our wave packet mode and $f(t)$ a mode function. If we expand our system using a set of a mode function $\{f_k(t)\}$, then using Eq. (4.1), we can calculate the commutation relation as

$$[\hat{a}_{f_k}, \hat{a}^\dagger_{f_l}] = \int_{-\infty}^{\infty} \mathrm{d}t\, f_k(t) f_l^*(t). \tag{4.3}$$

Therefore, if we select a set of mode functions so that they form an orthonormal basis, our wave packet modes will satisfy the Bosonic commutation relation.

Next, we show how to measure the quadrature operators of the wave packet mode. Let $\hat{x}_{f,\theta}$ be a quadrature operator associated with $\hat{a}_f$ in the θ direction where $\theta = 0$ corresponds to the $\hat{x}$ quadrature and $\theta = \pi/2$ corresponds to $\hat{p}$ quadrature. Then, from the definition of the quadrature operator, we have

$$\hat{x}_{f,\theta} = \sqrt{\frac{\hbar}{2}} \left[\hat{a}_f e^{-i\theta} + \hat{a}_f^\dagger e^{i\theta} \right]. \tag{4.4}$$

Note that we assume that the frequency bandwidth of the wave packet is much smaller than the carrier angular frequency, which holds for almost every case. Using the definition of $\hat{a}_f$, we have

$$\hat{x}_{f,\theta} = \int_{-\infty}^{\infty} \mathrm{d}t\, \left\{ \Re[f(t)] \hat{x}_\theta(t) - \Im[f(t)] \hat{p}_\theta(t) \right\}, \tag{4.5}$$

where $\hat{x}_\theta(t)$ are the quadrature operators associated with each time t, and $\Re[\cdot]$ and $\Im[\cdot]$ denote the real and the imaginary part. Interestingly, for a general mode function $f(t)$, measuring $\hat{x}_{f,\theta}$ requires measuring different quadrature at each timing t depending on the argument of $f(t)$. For the case of our interest where $f(t)$ is a real function, we have

$$\hat{x}_{f,\theta} = \int_{-\infty}^{\infty} \mathrm{d}t\, f(t) \hat{x}_\theta(t). \tag{4.6}$$

In this case, measuring the quadrature operator $\hat{x}_{f,\theta}$ of a wave packet mode simply requires the measurement of only the quadrature operator $\hat{x}_\theta(t)$ at each timing and then post-processing, i.e., integration with the shape of the mode function $f(t)$. This shows that the quadrature operators of the wave packet modes can be easily accessed; we only have to do the usual homodyne measurement and then to the digital integration afterward.

4.1.2 Frequency-domain treatment of the wave packet

In the signal processing theory, it is often advantageous to consider and analyze the time-domain signals in the frequency domain. In the time-domain quantum computation, the same also holds and we will consider how to represent the wave packet mode in the frequency domain.

If we let the carrier angular frequency of our system be Ω, we can write down the annihilation operator in the frequency domain $\hat{\tilde{a}}(\omega)$ in the rotating reference frame of Ω as[2]

$$\hat{a}(t) = \frac{1}{\sqrt{2\pi}} \int_{-\infty}^{\infty} \mathrm{d}\omega\, \hat{\tilde{a}}(\omega) e^{-i\omega t}, \tag{4.7}$$

[2] In the Fourier transform in Eq. (4.7), there are no $e^{-i\Omega t}$ terms on the right as we are using the rotating reference frame.

07 December 2024 17:52:47

$$\hat{\tilde{a}}(\omega) = \frac{1}{\sqrt{2\pi}} \int_{-\infty}^{\infty} \mathrm{d}t\, \hat{a}(t) e^{i\omega t}. \tag{4.8}$$

Note that $\omega = 0$ corresponds to the carrier frequency Ω. Using the commutation relation in Eq. (4.1), we can show that

$$[\hat{\tilde{a}}(\omega), \hat{\tilde{a}}^{\dagger}(\omega')] = \delta(\omega - \omega'). \tag{4.9}$$

The mode function can also be reformulated in the frequency domain. Using Eqs. (4.2) and (4.7), we can write down $\hat{a}_f$ using the frequency domain $\hat{\tilde{a}}(\omega)$ as

$$\hat{a}_f = \int_{-\infty}^{\infty} \mathrm{d}\omega \tilde{f}(\omega) \hat{\tilde{a}}(\omega), \tag{4.10}$$

with

$$\tilde{f}(\omega) \equiv \frac{1}{\sqrt{2\pi}} \int_{-\infty}^{\infty} \mathrm{d}t f(t) e^{-i\omega t}. \tag{4.11}$$

We do observe that the signs in front of ω in Eqs. (4.8) and (4.11) are opposite so that they cancel out.

Similar to the treatment of the homodyne measurement of the wave packet mode in Eq. (4.5), we consider the mathematical treatment of the homodyne measurement in the frequency domain. We consider the case where the local oscillator has a single frequency Ω and its complex amplitude is given by $\alpha_{\mathrm{LO}} = |\alpha_{\mathrm{LO}}| e^{i\theta}$. Instead of assuming that the input state is also monochromatic, however, we assume that it has finite frequency bandwidth. Then, using the Fourier transform in Eq. (4.7), the temporal signal from the homodyne detector $\hat{I}_\theta(t)$ can be expanded in the frequency domain as

$$\hat{I}_\theta(t) \propto \int_{-\infty}^{\infty} \mathrm{d}\omega \left[\hat{\tilde{a}}(\omega) e^{-i\theta} + \hat{\tilde{a}}^{\dagger}(-\omega) e^{i\theta} \right] e^{-i\omega t}. \tag{4.12}$$

The frequency component of the signal of the homodyne measurement highly resembles the definition of the quadrature operator, with a difference being that the component $\pm\omega$ are mixed together. Let us define

$$\hat{X}_\theta(\omega) \equiv \sqrt{\frac{\hbar}{2}} \left[\hat{\tilde{a}}(\omega) e^{-i\theta} + \hat{\tilde{a}}^{\dagger}(-\omega) e^{i\theta} \right], \tag{4.13}$$

then for the real mode function $f(t)$, we have

$$\hat{x}_{f,\theta} = \int_{-\infty}^{\infty} \mathrm{d}\omega \tilde{f}(\omega) \hat{X}_\theta(\omega), \tag{4.14}$$

where we used the fact that for a real $f(t)$, $\tilde{f}^*(\omega) = \tilde{f}(-\omega)$. We observe the parallelism between $\hat{x}_\theta(t)$ and $\hat{X}_\theta(\omega)$ in Eqs. (4.6) and (4.14). Note, however, that as $\hat{X}_\theta(\omega)$ in not Hermitian, i.e., $\hat{X}_\theta^{\dagger}(\omega) = \hat{X}_\theta(-\omega)$, this operator does not correspond to an observable and cannot be directly observed.

We can write Eqs. (4.12) and (4.14) in a more constructive form as

$$\hat{I}_\theta(t) \propto \int_{0}^{\infty} \mathrm{d}\omega \left[\hat{X}_\theta(\omega) + \hat{X}_\theta^{\dagger}(\omega) \right] \cos\omega t + \left[-i(\hat{X}_\theta(\omega) - \hat{X}_\theta^{\dagger}(\omega)) \right] \sin\omega t, \tag{4.15}$$

07 December 2024 17:52:47

$$\hat{x}_{f,\theta} = \int_0^\infty \mathrm{d}\omega\, \Re[\tilde{f}(\omega)] \left[\hat{X}_\theta(\omega) + \hat{X}_\theta^\dagger(\omega)\right] - \Im[\tilde{f}(\omega)] \left[-i(\hat{X}_\theta(\omega) - \hat{X}_\theta^\dagger(\omega))\right]. \tag{4.16}$$

Unlike $\hat{X}_\theta(\omega)$, the linear combinations $\hat{X}_\theta(\omega) + \hat{X}_\theta^\dagger(\omega)$ and $-i(\hat{X}_\theta(\omega) - \hat{X}_\theta^\dagger(\omega))$ are Hermitian and they are also commutative, which means that they can be simultaneously measured. This is evident from Eq. (4.15), as it shows that by splitting the electrical signal of the homodyne detector and demodulates it with $\cos \omega t$ or $\sin \omega t$, we can select the linear combination we wish to measure. These linear combinations are called *sidebands* and are important concepts when discussing the homodyne measurement and the temporal wave packet in the frequency domain. As such, in the frequency domain, rather than measuring single frequency components, the homodyne measurements measure the sideband components, which are the combination of $+\omega$ and $-\omega$ components.

4.1.3 Squeezed vacuum state in the temporal wave packet

In Sec. 4.2, we will be discussing various experimental generations of the time-domain-multiplexed cluster states. As a preparation, let us use the methodology in Sec. 4.1.2 to first analyze the squeezed vacuum state in the temporal wave packet.

For a squeezed vacuum state on a beam, a squeezing operator has a form (Yoshikawa *et al.*, 2017)

$$\hat{S}_r = \exp\left[\frac{1}{2}\left(\hat{P}_r^\dagger - \hat{P}_r\right)\right], \tag{4.17}$$

where $\hat{P}_r^\dagger$ is a photon-pair creation operator, which, in general, has a form

$$\hat{P}_r^\dagger = \int\int \mathrm{d}t_1 \mathrm{d}t_2\, r(t_1, t_2)\hat{a}^\dagger(t_1)\hat{a}^\dagger(t_2). \tag{4.18}$$

The function $r(t_1, t_2)$ can be interpreted as a correlation function, i.e., the probability that when a photon at time t_1 is created, there will also be a photon at time t_2. If we further restrict ourselves to the continuous-wave experiment, the correlation function will be time-translational invariant, i.e. $r(t_1, t_2) = r(t_1 - t_2)$. Thus, we can write Eq. (4.18) in the frequency domain as

$$\hat{P}_r^\dagger = \int \mathrm{d}\omega\, \tilde{r}(\omega)\hat{a}^\dagger(\omega)\hat{a}^\dagger(-\omega), \tag{4.19}$$

where the Fourier transform of the correlation function $\tilde{r}(\omega)$ is given by

$$\tilde{r}(\omega) = \int_{-\infty}^\infty \mathrm{d}t\, r(t)e^{i\omega t}. \tag{4.20}$$

We observe that, regardless of the details of $r(t)$, the squeezing operator in the continuous-wave regime always involves the generation of photon pairs in sidebands; note also that as $r(t) = r(-t)$, we have $\tilde{r}(\omega) = \tilde{r}(-\omega)$.

07 December 2024 17:52:47

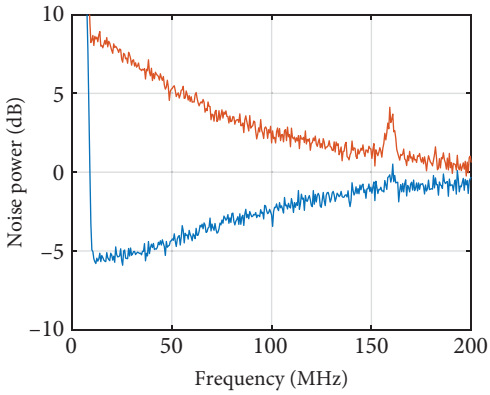

FIG. 4.1
Experimental measurements of the squeezing (blue) and antisqueezing (orange) spectral in sidebands using homodyne detector. The data here are normalized with respect to the vacuum state (0 dB) (Data: Baramee Charoensombutamon and Tatsuki Sonoyama).

Assume $\tilde{r}(\omega) \in \mathbb{R}$ for the sake of the simplicity, we can calculate the squeezing of the sideband components in the Heisenberg picture as

$$\hat{S}_r^\dagger \left[\hat{X}(\omega) + \hat{X}^\dagger(\omega)\right] \hat{S}_r = \left[\hat{X}(\omega) + \hat{X}^\dagger(\omega)\right] \exp\left(\left|\tilde{r}(\omega)\right|\right), \tag{4.21}$$

$$\hat{S}_r^\dagger \left[\hat{P}(\omega) + \hat{P}^\dagger(\omega)\right] \hat{S}_r = \left[\hat{P}(\omega) + \hat{P}^\dagger(\omega)\right] \exp\left(-\left|\tilde{r}(\omega)\right|\right), \tag{4.22}$$

where $\hat{X}(\omega) \equiv \hat{X}_{\theta=0}(\omega)$ and $\hat{P}(\omega) \equiv \hat{X}_{\theta=\pi/2}(\omega)$. At each sideband, the squeezing is pure as the product of the squeezing and the antisqueezing component satisfy the minimum uncertainty principle. As an example of the squeezing in the sideband, Fig. 4.1 shows the experimental data of the frequency spectral of the squeezed vacuum state measured from the optical parametric oscillator (OPO). We can see that there is frequency dependence, which is due to the fact that $\tilde{r}(\omega)$ is not flat (see Appendix A for the mathematical treatment of the OPO). Note also that the product of the squeezing and the antisqueezing component does not satisfy the minimum uncertainty as there are optical losses in the actual experiments.

Next, let us calculate the squeezing in a temporal wave packet. If we denote $\tilde{S}_+(\omega)$ and $\tilde{S}_-(\omega)$ as the antisqueezing and the squeezing at each sideband (this corresponds to each frequency component in Fig. 4.1), the variances of a temporal wave packet with a real mode function $f(t)$ are given by

$$\left\langle \Delta^2 \hat{x}_f \right\rangle = \int_{-\infty}^{\infty} \mathrm{d}\omega \left|\tilde{f}(\omega)\right|^2 \tilde{S}_+(\omega), \tag{4.23}$$

$$\left\langle \Delta^2 \hat{p}_f \right\rangle = \int_{-\infty}^{\infty} \mathrm{d}\omega \left|\tilde{f}(\omega)\right|^2 \tilde{S}_-(\omega). \tag{4.24}$$

Therefore, if we can measure the squeezing spectral at each sideband, we can predict the squeezing of the squeezed vacuum state when we consider a wave packet mode in Eq. (4.2). Equations (4.23) and (4.24) also show the relation between the wave packet shape, the squeezing spectral of the squeezed light source, and the squeezing level in the wave packet mode. The squeezing level of the wave packet mode is determined mainly by the frequency component of $\tilde{S}_\pm(\omega)$ that is in the region where the value of $\tilde{f}(\omega)$ is substantial. As $\tilde{f}(\omega)$ becomes broad as $f(t)$ becomes narrow, a broadband squeezed light source is essential if we want to have a short temporal mode with sufficient squeezing level. Another interesting property about the squeezing in the wave packet mode is that even though the squeezing is

07 December 2024 17:52:47

pure in each sideband component, the variances of the wave packet mode do not satisfy the minimum uncertainty, which can be easily proved as follows:

Proof. Using the Cauchy–Schwarz inequality, we have

$$\left\langle \Delta^2 \hat{x}_f \right\rangle \left\langle \Delta^2 \hat{p}_f \right\rangle \geq \left| \int_{-\infty}^{\infty} \mathrm{d}\omega \left| \tilde{f}(\omega) \right|^2 \sqrt{\tilde{S}_+(\omega)\tilde{S}_-(\omega)} \right|^2 = \frac{\hbar^2}{4}. \tag{4.25}$$

The equal sign is satisfied only when the squeezing spectra are flat in the region where $\tilde{f}(\omega)$ are nonzero. □

This intrinsic impurity in the wave packet mode affects the quality of the computation. When squeezed lights are used as the computational resources, only the squeezing component affects the quality of the computation; thus, the aforementioned impurity does not matter as long as the variances of the squeezing components are sufficiently small. On the other hand, this impurity affects applications that do not only utilize the squeezing component. One such example is the generation of the non-Gaussian states from the squeezed state (Yoshikawa *et al.*, 2017).

4.2 TIME-DOMAIN-MULTIPLEXED CLUSTER STATES

In Chap. 3, we have explained that the computational resource of the measurement-based quantum computation (MBQC), the cluster state, can be generated using offline squeezed vacuum states and linear optics. Originally, spatially separated beams are used as modes of the cluster states in the optical system. Thus, when we want to increase the constituent modes of the cluster states, this involves increasing the number of the squeezed light sources and the linear optics. Although the scaling is somewhat linear, this greatly limits the size of the cluster state that can be achieved. In this section, we will discuss one of the methods to overcome such scaling, which is called *time-domain-multiplexing method*.

4.2.1 Schematic idea

Figure 4.2 shows the schematic idea of the time-domain-multiplexing method. Instead of considering a single light beam as a single mode, we consider time bins of equal width Δt on this beam. In each time bin, we define a wave packet mode. As we want to interact the wave packet modes in the different bin, we would want the shapes of the wave packets to be the same. If we denote $f_k(t)$ as the mode function of the wave packet mode in a time bin with an index k, whose center timing is $k\Delta t$, we can write down $f_k(t)$ as

$$f_k(t) = \begin{cases} f(t - k\Delta t), & |t - k\Delta t| \leq \frac{\Delta t}{2}, \\ 0, & |t - k\Delta t| > \frac{\Delta t}{2}, \end{cases} \tag{4.26}$$

07 December 2024 17:52:47

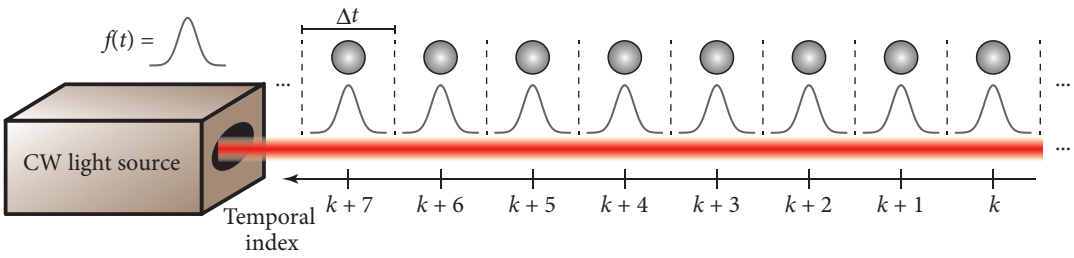

FIG. 4.2
Schematic of the idea of the time-domain-multiplexing method.

where $f(t)$ is the shape of the temporal mode. In the time-domain-multiplexing methods, by using optical delay lines, these modes can be made to interact with linear optics networks, where the number of the optical components in the network *does not* scale with the size of the cluster state we wish to generate.

We emphasize here that although we are considering a wave packet mode here, we are not necessarily considering pulsed laser; the system can use the continuous-wave laser and, in fact, most experimental realizations of the time-domain-multiplexed cluster states use continuous-wave squeezed light sources. The concept of the temporal mode function on the time bin here is simply the transformation of the mode, which is more similar to how we can choose bases for the expansion of vectors in linear algebra.

Next, let us consider a few properties of the mode in the time-domain-multiplexing method. First, we can easily show that temporal modes satisfy the Bosonic commutation relation as

$$[\hat{a}_k, \hat{a}_{k'}^\dagger] = \delta_{kk'}, \tag{4.27}$$

where we abbreviate $\hat{a}_k \equiv \hat{a}_{f_k}$ as the shape of the wave packet $f(t)$ is assumed to be the same for all k.

Although the Bosonic relation always holds for the choices of the wave packet in the time bin in Eq. (4.26), consideration regarding the shape of the wave packet is important. In the actual experiments, the optical modes are measured using a homodyne detector and signals are transformed into electrical signals, which we then do the integration to obtain the quadrature of each temporal mode. Electrical circuits, however, have finite frequency bandwidth and time response function that is not a delta function. Therefore, if we suppose that $f_{\text{post}}(t), f_{\text{opt}}(t)$, and $h(t)$ are the shape of the mode function used in the post-processing, the corresponding actual optical mode, and the impulse response function of the measurement system, respectively, they are related by

$$f_{\text{opt}}(t) = \int_{-\infty}^{\infty} \mathrm{d}\tau\, f_{\text{post}}(t-\tau) h(-\tau), \tag{4.28}$$

07 December 2024 17:52:47

where the right-hand side is a convolution between the post-processing mode and the time-reversal of the response function. This can be proved as follows:

Proof. If we let $\hat{a}_{\mathrm{elec}}(t)$ be an effective annihilation operator that corresponds to the measured electrical signals, using the impulse response function, this is related to $\hat{a}(t)$ as

$$\hat{a}_{\mathrm{elec}}(t) = \int_{-\infty}^{\infty} \mathrm{d}\tau\, h(t-\tau)\hat{a}(\tau). \tag{4.29}$$

Then, when we do the post-processing integration with $f_{\mathrm{post}}(t)$, we are effectively looking at a mode

$$\hat{a}_{f_{\mathrm{post}}} = \int_{-\infty}^{\infty} \mathrm{d}\tau \left[\int_{-\infty}^{\infty} \mathrm{d}\tau' f_{\mathrm{post}}(\tau') h(\tau'-\tau) \right] \hat{a}(\tau), \tag{4.30}$$

which gives the effective mode function of the optical mode $f_{\mathrm{out}}(t)$ in Eq. (4.28) when a proper change of variables is done. □

Therefore, even if the mode $f_{k,\mathrm{post}}(t)$ is selected in the manner of Eq. (4.26), when the actual system is considered, the mode we actually measure might not be orthogonal. As such, careful considerations have to be made regarding the mode function used in the data analysis so that the corresponding optical mode is still orthogonal.

In addition to the orthogonality, we also have to consider the occupancy of the mode function in a time bin. It is possible to select a mode $f_{k,\mathrm{post}}(t)$ such that orthogonality of the corresponding optical mode $f_{k,\mathrm{opt}}(t)$ with different indices k are satisfied, but the modes are not contained inside the time bin. This is problematic when we wish to measure each mode with different measurement bases; measurement bases are changed optically with in each time bin, which means that the optical modes must be contained in the time bin. Selection of the shape of the mode function must take these aspects into the consideration as well.

4.2.2 One-dimensional cluster state

Let us first consider how to generate cluster states for single-input single-output quantum operation. We will call this cluster state *one-dimensional cluster state*.

Figure 4.3(a) shows a sequential full-teleportation circuit. Similar to how the sequential half-teleportation circuit in Chap. 3 gives rise to the canonical cluster state, by modifying this circuit, we have Fig. 4.3(b), which shows the equivalent circuit for our one-dimensional cluster state. In this case, the one-dimensional cluster state is generated by first generating EPR states, and one of the modes of the EPR state is then interfered by a 50:50 beamsplitter with another mode of the other EPR pair.

Although it seems as if the number of the squeezed light sources and the beamsplitters scale with the number of the mode of the one-dimensional cluster state, this can be overcome with the time-domain-multiplexing method. Figure 4.4(a) shows the experimental setup for realizing the one-dimensional

07 December 2024 17:52:47

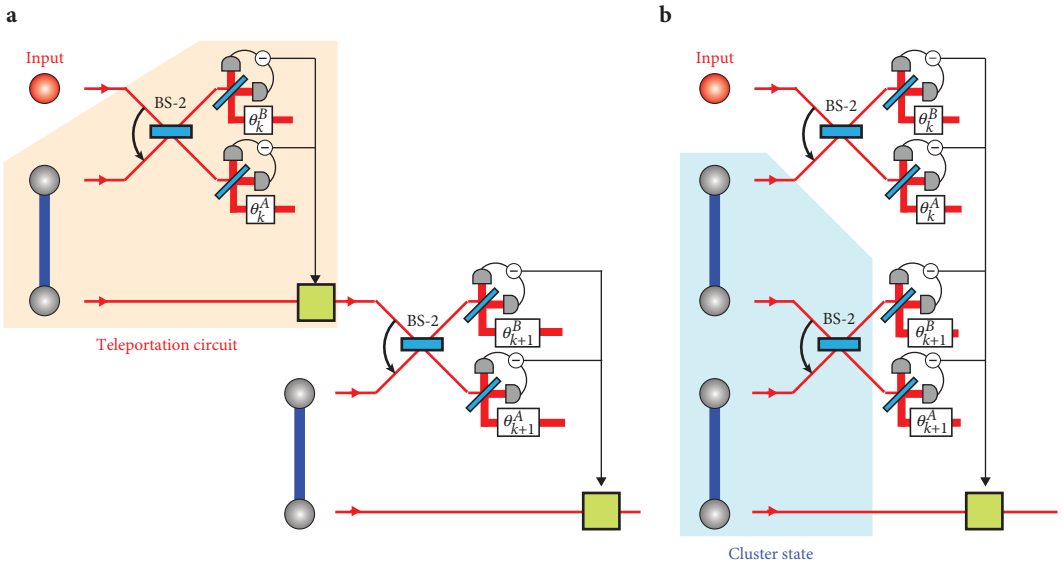

FIG. 4.3
Equivalence between sequential full-teleportation circuit and cluster state. (a) Sequential full-teleportation circuit. (b) Equivalence to the computation using the one-dimensional cluster state. This circuit shows the equivalence for two steps of full teleportation. All the beamsplitters are 50:50.

cluster state in the time domain. In this setup, we are using the continuous-wave laser but are considering our modes as a localized temporal wave packet inside a time bin of the width Δt [step (i)]. Then, the quantum state at the first beamsplitter [step (ii)] is simply a stream of the EPR states (or the two-mode squeezed states when we consider the finite squeezing limit). By delaying one of the modes by the time Δt [step (iii)] and interfering with them again using another beamsplitter [step (iv)], we arrive at the one-dimensional cluster state. Using the graphical calculus, we can write down the graph of the state in each generation step, which is also shown in Fig. 4.4. Note that this state is sometimes also called dual-rail cluster states due to its structure. In the infinite squeezing limit, the edge weight of the one-dimensional cluster state will diverge to infinity. However, if we perform appropriate Fourier transformations, we have the graph whose structure approaches that of the canonical cluster state.

The length of the one-dimensional cluster states generated using the setup in Fig. 4.4 can be literally unlimited; this is because the time-domain-multiplexing method allows us to use the same beamsplitters to implement the beamsplitter interactions between different temporal modes at a different timing. Another point that makes it is possible to generate this state using the time-domain-multiplexing method is that the generation circuit in Fig. 4.3(b) possesses a nice symmetry and has constant depth regardless of the number of the modes.

07 December 2024 17:52:47

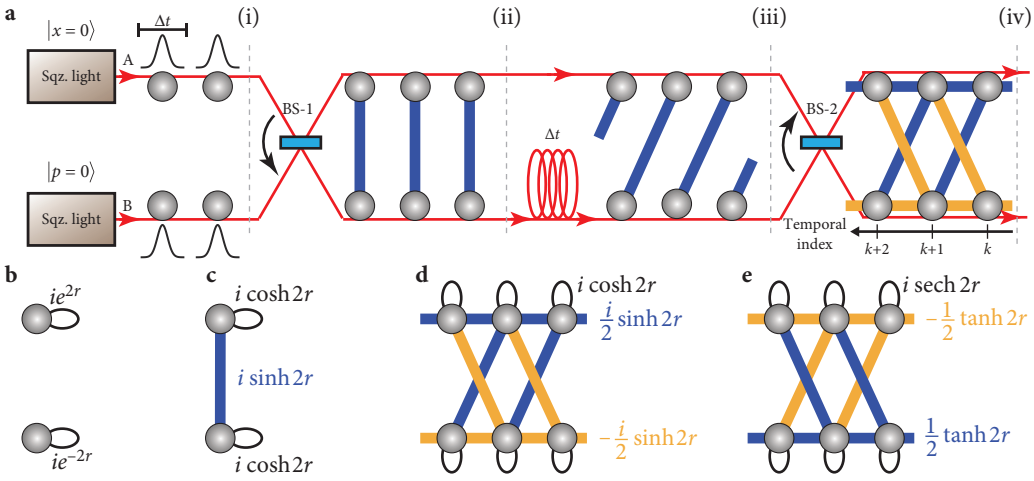

FIG. 4.4
Generation of the time-domain-multiplexed one-dimensional cluster state. (a) Generation setup. (b) Graph of the initial squeezed state. (c) Graph of the initial two-mode squeezed states. (d) Graph of the one-dimensional cluster state. (e) Equivalent graph where half of the nodes are Fourier transformed. r is the squeezing parameter of the squeezed light and is assumed to be equal for both light sources. Both beamsplitters are 50:50.

Experimentally, the setup in Fig. 4.4 was realized by Yokoyama *et al.* (2013). In their setup, they used an OPO as a squeezed light source and the wave packet width Δt was about 160 ns. This value was picked due to the consideration regarding the squeezing level of the wave packet as we have discussed in Sec. 4.1.3. In their experiment, they measure the quadrature operators and calculate the following nullifiers at each index k:

$$\hat{\delta}_k^{(x)} = \hat{x}_k^A + \hat{x}_k^B + \hat{x}_{k+1}^A - \hat{x}_{k+1}^B, \tag{4.31}$$

$$\hat{\delta}_k^{(p)} = \hat{p}_k^A + \hat{p}_k^B - \hat{p}_{k+1}^A + \hat{p}_{k+1}^B. \tag{4.32}$$

They then used the van Loock–Furusawa criteria to establish that the generated states have full multipartite inseparability up to about 10 000 modes.

The experiment by Yokoyama *et al.* (2013) stabilizes the optical system by using a method called *sample & hold*. In this method, the classical beams are injected into the system and their interference signals are used in the stabilization of the system (sample phase). During the measurements, these beams are chopped and the system is kept in the stabilized state (hold phase). As the time passes in the hold phase, however, the optical system drifts and the entanglement degrades and limits the number of the modes that the quantum entanglement can be observed. Subsequent to this experiment, Yoshikawa *et al.* (2016) use a constant stabilization method where the signals due to the classical beams are removed by

07 December 2024 17:52:47

using the electrical filtering and using the shape of the post-processing mode function that takes the influence due to the electrical filters into an account. This allows the generation of the one-dimensional cluster states with about 1×10^6 light modes.

Interestingly, the length of the cluster state in time (about 100 ms) is very long and can be, in principle, unlimited. This experiment demonstrates one of the main strengths of the time-domain-multiplexing method: *the coherence time does not limit the length (thus, the possible step of computation) of the time-domain-multiplexed cluster states*. This property is what makes the optical system, especially the CV system, different from other stationary qubit such as superconducting systems or trapped-ion systems as the coherence time in these systems usually limits the number of possible operation or the size of the cluster states that can be generated. In the optical system, however, the coherence time limits the time separation between two beams that still allow them to interfere. As such, since cluster states are generated with interferences, the coherence time limits only the size of the optical delay line that can be used (this will be more crucial in the two-dimensional cluster state in Sec. 4.2.3).

One might try to argue that we should not be able to see the entanglement between the modes that are separated beyond the coherence time. But as the homodyne measurement is also the measurement via interference, the local oscillator (LO) beam, in a sense, gives us a reference frame such that any lights whose temporal separation to the LO is well below the coherence time can be measured. Also, the strategy in the time-domain-multiplexing method is *generate and measure* in a sense that the portion of the cluster state that is generated is almost immediately measured. The capability to do so is one of the stark differences between the optical system and other matter-qubit systems. In the optical system, rather than physically making qubits or modes, we made *a source of optical modes.*

07 December 2024 17:52:47

4.2.3 Two-dimensional cluster state

As quantum computation requires multi-mode quantum operations, the one-dimensional cluster state is insufficient as it allows only single-input single-output operations. To achieve a structure required for the universal quantum computation, we need a cluster state with two-dimensional structure—*a two-dimensional cluster state*.

In the original proposal of the time-domain-multiplexing method by Menicucci (2011), methodologies for the generation of both one- and two-dimensional cluster states were given. In that paper, however, the usage of the time-domain-multiplexed cluster state was based on the half-teleportation circuit as in the canonical cluster state and most of the modes (half in one-dimension and three quarters in two-dimension) are erased to reduce the generated state to a square-lattice canonical cluster state. In Sec. 4.2.2, the dual-rail one-dimensional cluster state can be used as it is without erasing half of the modes. The main idea is that the second beamsplitter in the generation system in Fig. 4.4(a) is equivalent to the beamsplitter used in the Bell measurement in the teleportation circuit (Fig. 4.3). In a similar manner, instead of considering all of the beamsplitters as the state generation, we can consider some of the beamsplitter networks (after the gray line "logical mode" in Fig. 4.5) as a part of the measurement

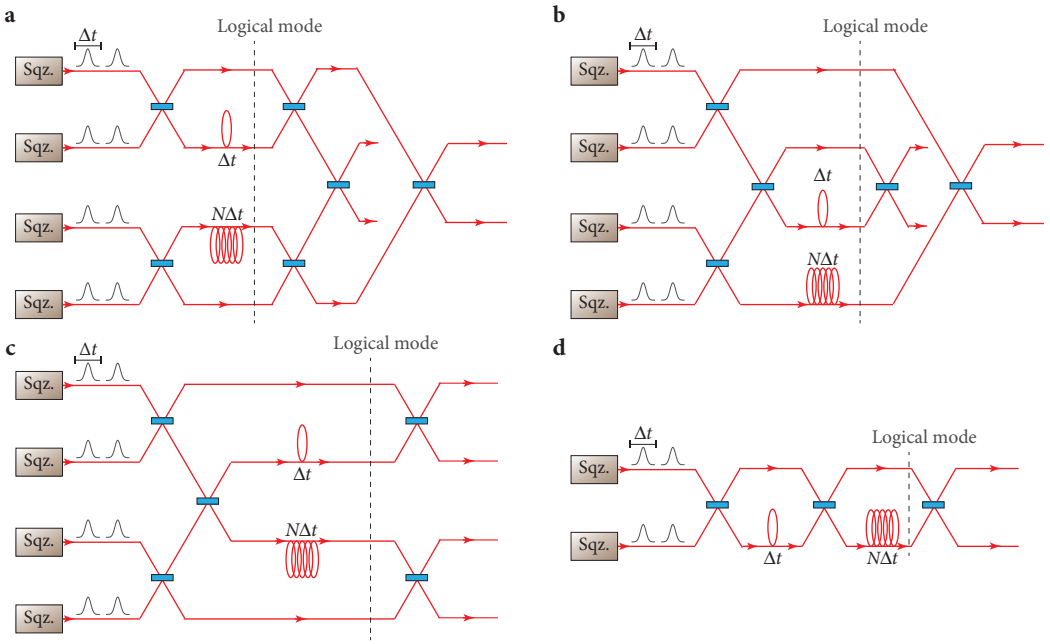

FIG. 4.5
Various generation setups for the two-dimensional cluster states. (a) Quad-rail lattice (Menicucci, 2011). (b) Bilayer square lattice (Alexander *et al.*, 2018). (c) Modified bilayer square lattice (Asavanant *et al.*, 2019). (d) Double bilayer square lattice (Larsen *et al.*, 2019). All beamsplitters are 50:50 and the phase at the first beamsplitters joining the initial squeezed light are selected so that the two-mode squeezed states are generated.

devices that result in nonlocal measurements on EPR states. This is, in a way, an extension of quantum teleportation where instead of the usual Bell measurement, a more complex measurement is used to achieve universal MBQC without erasure (Alexander and Menicucci, 2016). Note that in addition to the quad-rail lattice, a different setup to generate a universal resource with a different structure called bilayer square lattice is also proposed (Alexander *et al.*, 2018).

To be more explicit, the concept of considering a part of the beamsplitter network as a part of the measurement device can also be formulated as a mode transformation, a concept called *macronode*. Figure 4.6 shows this concept. In this concept, instead of using the localized wave packets after the units of the quantum computation, we consider modes that correspond to the linear combinations of these local wave packets. These modes are called macronode and the local homodyne measurements of the physical mode will correspond to the nonlocal measurement in the macronode basis.

07 December 2024 17:52:47

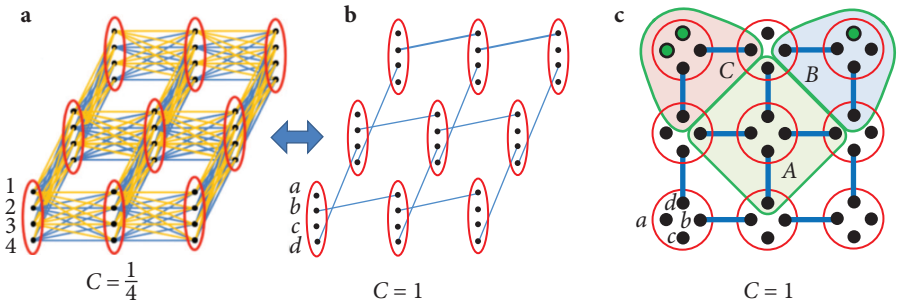

FIG. 4.6
The concept of macronode (Alexander and Menicucci, 2016). (a) Physical representation of the quad-rail lattice cluster state. (b) and (c) Macronode representation. Quantum operations are implemented via "non-local" measurements on the macronodes (Alexander and Menicucci, 2016).

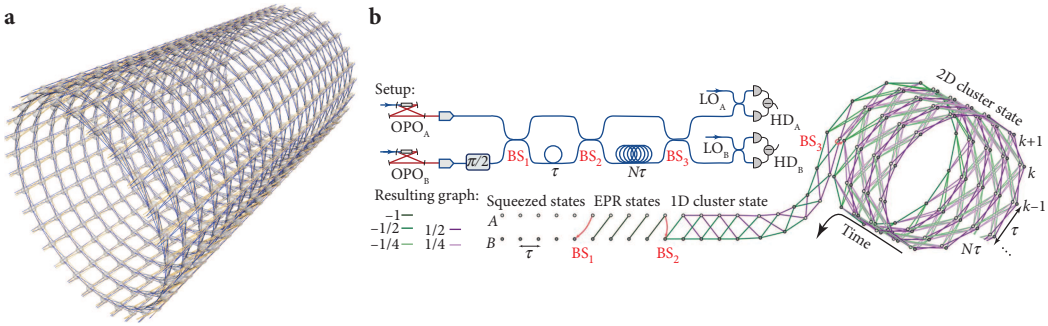

FIG. 4.7
Graphs of the two-dimensional cluster states generated in Asavanant *et al.* (2019) (a) and Larsen *et al.* (2019) (b). Reprinted with permission from Larsen *et al.*, Science **366**(6463), 369–372 (2019). Copyright 2019 AAAS.

Experimentally, two groups generate the two-dimensional cluster state using the time-domain-multiplexing method nearly at the same period (Asavanant *et al.*, 2019; and Larsen *et al.*, 2019). Interestingly, the generation setups and the structures of the generated states (Fig. 4.7) in both experiments differ from that of the precedent theoretical proposals. Figures 4.5(c) and 4.5(d) show both setups. Despite four different possible architectures, what they shared in common is that they have two optical delay lines where the length of the long delay line is an integer time of the short one. These two delay lines are used to realize the two-dimensional structure.

07 December 2024 17:52:47

As there are currently four possible setups to generate CV two-dimensional cluster states whose structures differ, one might ask how these cluster states perform in comparison to each other. Regarding Gaussian operations, as measurement-based quantum computation can be regarded as sequential teleportation, we can consider the quality of the Gaussian operations by looking at the noises in the realistic quantum teleportation protocols. Their performances have been compared (Larsen *et al.*, 2020) and, interestingly, besides the quad-rail lattice that performs significantly better than the others; the rest perform relatively the same. The main reason for this lies in the macronode representation. Macronode representation of the quad-rail lattice is simply EPR states (or two-mode squeezed states in the finite squeezing limit) that are then entangled via the "non-local" measurements consisting of four beamsplitter interactions and the homodyne measurements. Then, in a sense, this is simply a network of quantum teleportations.

Experimentally, the main difference between the one-dimensional and two-dimensional cluster states is the number of the optical delay line. In the one-dimensional cluster state setup, there is only one optical delay line, while there are two optical delay lines in all two-dimension cluster state setups. Although it might seem that adding one more delay line is not so difficult, as the length of the long delay line must be an integer time of the short delay line, this requires calibration. Also, when the lengths are not properly adjusted, the temporal mode will not be perfectly interfered, which results in the imperfection of the cluster state. For the one-dimensional cluster state, rather than adjusting the optical delay line, we can simply select Δt that matches with the setup that is actually constructed.

07 December 2024 17:52:47

4.2.4 Operations using time-domain-multiplexed cluster states

In this section, we will talk about the experimental requirements in the usage of the time-domain cluster states in the measurement-based quantum computation. We will mainly discuss the one-dimensional cluster state, as the required components in the two-dimensional cluster state are similar.

Figure 4.8 shows the additional components we would need in order to implement arbitrary (Gaussian and non-Gaussian) single-mode quantum operations on the one-dimensional cluster state. In a qubit cluster state, it is possible to use some of the qubits of the cluster states as initial input qubits. For the CV optical system, although it is also possible to do the same and achieve the universality, it is advantageous if we can inject and couple quantum states to our cluster states from the outside. This is the role of the optical switch in Fig. 4.8.

After the initial quantum states are coupled to the cluster state, to do the operations, we need to change the measurement basis. As the information is encoded in the time domain, the measurement basis must be changed dynamically in time. For the Gaussian operations that require only homodyne measurements, the measurement bases are determined by the relative phase between the mode of the cluster state and the local oscillator (LO). Note also that as there are two homodyne detectors, the timing of the switching of the measurement bases must be synchronized. The required timing precision increases as the size of the wave packet Δt becomes smaller.

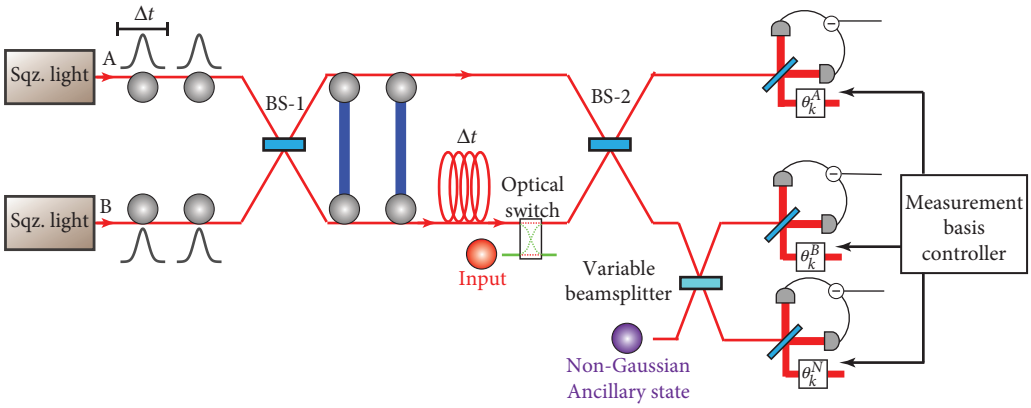

FIG. 4.8
Full setup for implementing universal one-input quantum operation with time-domain-multiplexed one-dimensional cluster state. Note that feedforward displacement is omitted here and can be implemented right after the optical switch at either path depending on the applications.

Although Gaussian operations can be implemented using only the homodyne measurements, we also need to implement non-Gaussian operations. Here, we show one of the possible configurations to implement non-Gaussian operations, where a variable beamsplitter and a non-Gaussian ancillary state are added (Alexander *et al.*, 2018). When implementing the Gaussian operation, this beamsplitter is set to be completely reflective. When we want to do the non-Gaussian operations, the variable beamsplitter is set to a 50:50 beamsplitter, and the non-Gaussian ancillary state is coupled. The non-Gaussian operations are then implemented using the measurement-based method in Chap. 3. As this implementation requires adaptive measurement, the measurement basis of the homodyne detector for the non-Gaussian operation must be calculated using the past measurement results of both homodyne-A and homodyne-B. This requires a nonlinear feedforward system, which must also be synchronized to the measurement-basis controller. Also, the feedforward displacement on the output mode must also be implemented. This can be achieved by doing the displacement after the optical switch.

Finally, after a sequence of the quantum operations is implemented, we would wish to do the readout of the final quantum state. One of the ways to do so is using the optical switch in Fig. 4.8 to deject the wave packet corresponding to the final quantum state outside and do the homodyne measurement on it. However, if we wish only to do the measurement on the wave packet, we can simply select the measurement bases of both homodyne measurements to match the basis we wish to measure and then to the appropriate linear combination of the measurement results. This eliminates the need to measure the wave packet outside of the generation system of the one-dimensional cluster states.

07 December 2024 17:52:47

All of the discussions here also hold for the two-dimensional cluster states where we need the optical switch, synchronized changes of the phase of the LOs, non-Gaussian ancillary states, and nonlinear feedforward operations to realize a complete setup for universal multimode quantum operations.

4.3 LOOP-BASED TIME-DOMAIN QUANTUM COMPUTATION

The time-domain-multiplexing method does not only apply to the measurement-based quantum computation using the cluster states but can also be used in a different type of architecture as well. Here, we will introduce one such architecture, which is called *loop-based quantum computation* (Takeda and Furusawa, 2017).

Figure 4.9 shows the schematic diagram of the loop-based quantum computation. The term "loop" comes from the fact that there are two optical delay lines of the size Δt and $N\Delta t$, where Δt is the size of the wave packet and N is an integer. The size of the optical delay line is similar to that of the two-dimensional cluster state. In addition to the optical delay line, this method uses a variable beamsplitter. The large loop acts as a quantum memory where the two optical switches determine when to inject a new wave packet into the loop or when to get the wave packet out and measure it. On the other hand, the inner loop with a variable beamsplitter is used to interact two wave packets. If we can align the wave packets of various ancillary states inside the loop along with the wave packets of the input modes, then this variable beamsplitter and the homodyne detector can be used to realize quantum operations using a measurement-based method.

Partially, the variable beamsplitter has been realized and used to synthesize many different types of quantum entanglement (Takeda *et al.*, 2019). The next obstacle in this architecture is that, unlike the cluster state based quantum computation where the non-Gaussian ancillary state can be injected offline, the wave packet of the non-Gaussian states must be injected onto the same beam at the same

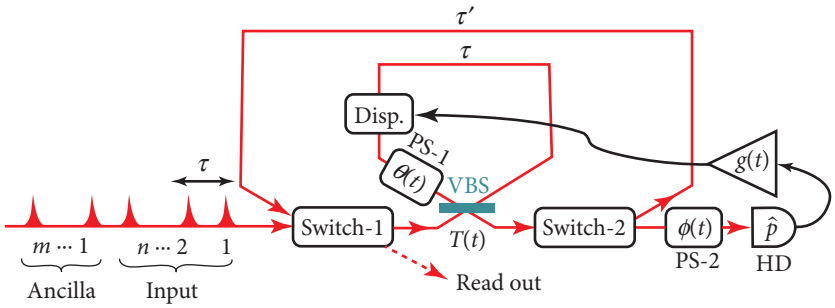

FIG. 4.9
Loop-based quantum computation architecture (Takeda and Furusawa, 2017).

07 December 2024 17:52:47

interval as the modes used in the computation. Also, as this architecture requires direct interference between various wave packet mode, the coherence time of the light source becomes an important factor; wave packets that are generated with time separation larger than the coherence time do not interfere. This is in contrast to the time-domain-multiplexed cluster state where the largest time separation is simply the long optical delay line.

4.4 QUANTUM OPERATIONS ON THE WAVE PACKET MODE

In this section, we will introduce actual experimental works that implement quantum operations on wave packet modes. As an example, we select the dynamic squeezing gate and the quantum non-demolition gate. The first experiment illustrates how to implement a nonlinear feedforward, one of the important components to realize measurement-based quantum computation in the time domain. The second experiment illustrates how to evaluate the frequency-domain response of a quantum gate, which in turn tells us the bandwidth and the size of the wave packet that a quantum gate can handle.

4.4.1 Dynamic squeezing gate

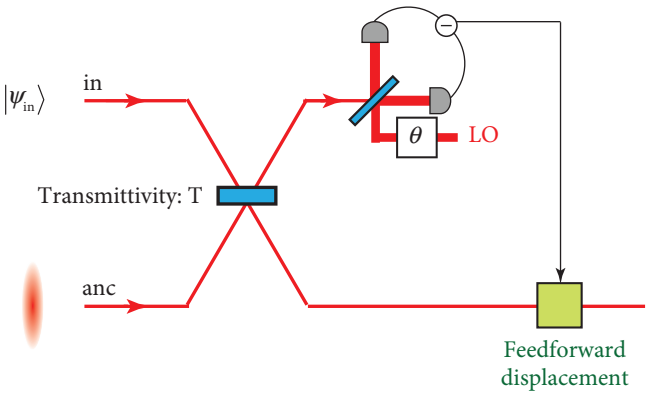

FIG. 4.10
Setup of the dynamic squeezing gate.

Figure 4.10 shows the setup for the dynamic squeezing gate. This gate is a component required to realize the cubic phase gate. If we let the measurement bases at the first homodyne detector be $\hat{p}(\theta) = \hat{p}\cos\theta + \hat{x}\sin\theta$, then the Heisenberg picture input–output relation of this gate is given by

$$\begin{pmatrix} \hat{x}_{out} \\ \hat{p}_{out} \end{pmatrix} = \begin{pmatrix} 1 & 0 \\ \frac{R}{T}\tan\theta & 1 \end{pmatrix} \begin{pmatrix} \sqrt{T} & 0 \\ 0 & \frac{1}{\sqrt{T}} \end{pmatrix} \times \begin{pmatrix} \hat{x}_{in} \\ \hat{p}_{in} \end{pmatrix} + \sqrt{R} \begin{pmatrix} \hat{x}_{anc} \\ -\tan\theta\,\hat{x}_{anc} \end{pmatrix}. \tag{4.33}$$

If we use $|x = 0\rangle$ as our ancillary state, the second term, which is the noise term, becomes zero and the output corresponds to the squeezing gate whose squeezing depends on the transmittivity of the beamsplitter and the shear operation whose parameter is tunable with the measurement basis. In the case where $\theta = 0$, this gate becomes a universal squeezer, which can be used to implement the squeezing operation on the arbitrary input state.

07 December 2024 17:52:47

When the dynamic squeezing gate is used in the realization of non-Gaussian measurement, the values θ are feedforwarded via a nonlinear function of the quadrature values measured at another homodyne detector. What is difficult about this feedforward operation is that the implementation of a nonlinear function with low latency is often difficult. In the optical system, additional latency means that an additional optical delay line is needed to synchronize the optical and electrical signals. For example, if we have an additional delay of 1 ns in the calculation of the electrical signal for the nonlinear feedforward, we will need an additional optical delay of 3 m to synchronize the wave packet to these electrical signals. There is a demonstration of the nonlinear feedforward using the analog circuit where the signal used for the feedforward is stimulated via an electrical signal source and the nonlinear feedforward is a tangent function of the electrical signals (Miyata *et al.*, 2014).

Although the analog circuits are fast, they lack programmability and stability that digital circuits can provide. Therefore, a low-latency field-programmable gate array (FPGA) has been developed to implement this nonlinear feedforward operation (Sakaguchi *et al.*, 2018) (Fig. 4.11). FPGA provides a much simpler implementation of the nonlinear feedforward and this FPGA has a low latency (about 25 ns in total). For the realization of the nonlinear feedforward in the optical system, the development of such low-latency electronics with programmability is a pressing task.

07 December 2024 17:52:47

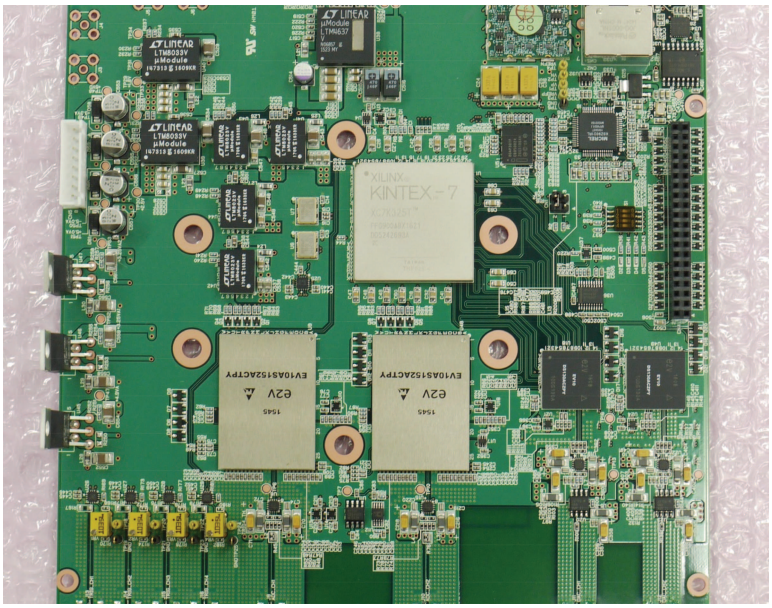

FIG. 4.11
FPGA for the nonlinear feedforward operation (Photo provided by Atsushi Sakaguchi).

4.4.2 Quantum nondemolition gate

QND gate is an important quantum gate not only in the context of quantum measurement and back-action but also in the field of quantum error correction, which we will discuss in Chap. 6. The unitary operator of the QND gate with gain g is given by

$$\hat{U}_{\mathrm{QND}}(g) = \exp\left(-i\frac{g}{\hbar}\hat{x}_1 \otimes \hat{p}_2\right). \tag{4.34}$$

In the Heisenberg picture, QND gate transforms the quadrature operator as

$$\begin{pmatrix} \hat{x}_1' \\ \hat{x}_2' \\ \hat{p}_1' \\ \hat{p}_2' \end{pmatrix} = \begin{pmatrix} 1 & 0 & 0 & 0 \\ g & 1 & 0 & 0 \\ 0 & 0 & 1 & -g \\ 0 & 0 & 0 & 1 \end{pmatrix} \begin{pmatrix} \hat{x}_1 \\ \hat{x}_2 \\ \hat{p}_1 \\ \hat{p}_2 \end{pmatrix}. \tag{4.35}$$

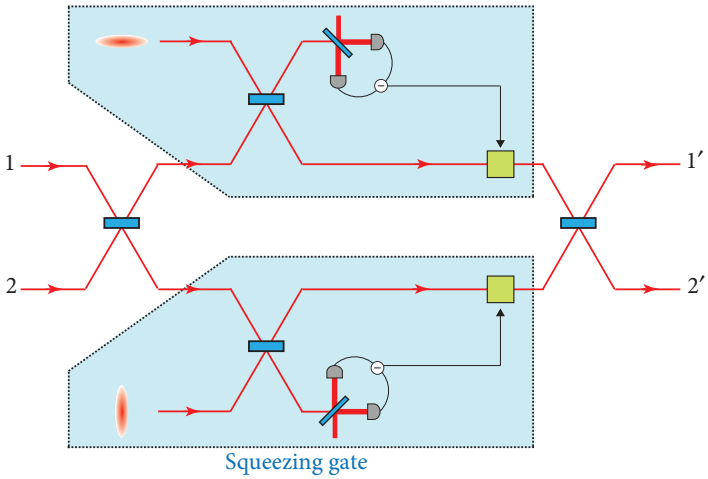

FIG. 4.12
Experimental setup for the implementation of the QND gate. The values of the splitting ratios of each beamsplitter depend on the gain of the QND gate (see, for example, Shiozawa *et al.*, 2018).

Unlike the controlled-Z gate, QND gate does not mix the two quadratures. It can be easily shown that the QND gate is related to the controlled-Z gate via a local Fourier transformation. QND gate is also called SUM gate as it takes $|x\rangle_1|x'\rangle_2$ to $|x\rangle_1|x' + gx\rangle_2$.

As with all Gaussian operations, QND gates can be decomposed using the Bloch–Messiah decomposition. This results in a system that is composed of two beamsplitters and two universal squeezers. The necessary squeezing gate can be further decomposed into the squeezed vacuum state, a beamsplitter, a homodyne detector, and a feedforward operation in the same manner as the dynamical squeezing gate.

Figure 4.12 shows the experimental setup use to realize the QND gate. The CV QND gate was first realized in the continuous-wave experiment by Yoshikawa *et al.* (2008). In their experiment, they inject coherent state at a sideband frequency of 1.25 MHz and evaluate the performance of the QND gate by looking at how much information of the other mode they can get by measuring one mode, the amount of back-action on the mode of interest, and the conditional state after the measurement (Holland *et al.*, 1990).

07 December 2024 17:52:47

For the QND gate to be useful in the time-domain quantum computation, it must operate on the wave packet mode. This means that the QND gate must be broadband in the frequency domain. Let us consider the frequency bandwidth of the components in Fig. 4.12. First, the frequency bandwidth of the linear optics such as beamsplitter is much broader than the other optical components, and thus does not limit the bandwidth of the QND gate. Next, we consider the bandwidth of the squeezed light source. As we have explained, for the light source such as OPO, the squeezing level degrades as the frequency increases. As the ancillary squeezed vacuum states determine the amount of noise in the squeezing gate, this means that if the squeezed light source is not sufficiently broadband, the high frequency component of the quantum state will become noisy, which limits the effective size of the wave packet that can be used in this gate.

In addition to the squeezed light source, the bandwidth of the homodyne detector and the feedforward system also limit the bandwidth of the whole QND gate. In addition of the bandwidth, the gain flatness of the homodyne detector is also an important factor. To implement the feedforward operation, the electrical signals from the homodyne detector need to be converted back to optical signals. If the gain of the homodyne is not flat, then such conversion is usually difficult as adjustment of the phase relation cannot be done using a simple cable. By increasing the bandwidth of the squeezed light sources, homodyne detectors, and feedforward system, a QND gate with $\approx$100-MHz frequency bandwidth has been realized (Shiozawa *et al.*, 2018).

To demonstrate that the constructed gate indeed operates up to 100 MHz, Shiozawa *et al.* (2018) utilize an idea that is usually used in the analysis of the linear time invariant system; by injecting an input coherent state whose amplitude is determined by a classical electrical signals of frequency bandwidth about 100 MHz, we can measure the input–output relation in each frequency component and determine the response of the QND gate using the frequency-domain analysis.

07 December 2024 17:52:47

4.5 OTHER MULTIPLEXING METHODS

As the time domain and the frequency domain are related via Fourier transformation, we can also consider an encoding in the frequency domain. One of the ideas of the frequency-domain multiplexing is that we can consider each frequency peak of the cavity of the OPO as a mode. Based on this idea, the generation of frequency-multiplexed one-dimensional cluster state has been demonstrated (Chen *et al.*, 2014). There is also a theoretical proposal of how to add time-domain multiplexing to the frequency-domain multiplexing and realize two-dimensional cluster state (Alexander *et al.*, 2016).

One strength of the frequency-multiplexing method over the time-multiplexing method is that it does not require an optical delay line, as modes are encoded in the frequency domain. Also, the frequency modes in the frequency multiplexing are usually generated simultaneously, whereas the modes in the time-domain multiplexing are usually generated sequentially. While this might seem to be

advantageous, this introduces experimental difficulties in accessing each mode individually and implementation of adaptive measurements that are required in the implementation of the non-Gaussian operations such as cubic phase gate. For a more thorough review on the frequency domain, see Pfister (2019).

Another notable difference in the time-domain multiplexing and the frequency-domain multiplexing is their limitations. In the time-domain multiplexing method, the factor that limits the size of the cluster state is the size of the optical delay line, which is limited by the coherence length of the light source. On the other hand, the size of the cluster state in the frequency-domain multiplexing is limited by the number of peaks we can get from the OPO, which is limited by the phase-matching bandwidth of the nonlinear medium used in the OPO.

In addition to the frequency domain, there are also some works that aim to multiplex the mode of the cluster state using the transverse modes of the optical beam (Yang *et al.*, 2016). In this method, by carefully designing the squeezed light source, the generated squeezed light contains quantum entanglement between different Laguerre–Gaussian modes, which form a set of orthonormal basis. Laguerre–Gaussian modes are usually associated with the concepts of angular momentum in the mechanical system, and we can roughly consider the generation of the entangled Laguerre–Gaussian mode as a result of the conservation of "angular momentum." Do note, however, that multiplexing with transversal mode suffers from the difficulties in the tailoring of the LO to access each individual mode.

07 December 2024 17:52:47

REFERENCES

Alexander, R. N. and Menicucci, N. C., "Flexible quantum circuits using scalable continuous-variable cluster states," Phys. Rev. A **93**, 062326 (2016).

Alexander, R. N., Wang, P., Sridhar, N., Chen, M., Pfister, O., and Menicucci, N. C., "One-way quantum computing with arbitrarily large time-frequency continuous-variable cluster states from a single optical parametric oscillator," Phys. Rev. A **94**, 032327 (2016).

Alexander, R. N., Yokoyama, S., Furusawa, A., and Menicucci, N. C., "Universal quantum computation with temporal-mode bilayer square lattices," Phys. Rev. A **97**, 032302 (2018).

Asavanant, W., Shiozawa, Y., Yokoyama, S., Charoensombutamon, B., Emura, H., and Alexander, R. N., "Generation of time-domain-multiplexed two-dimensional cluster state," Science **366**(6463), 373–376 (2019).

Chen, M., Menicucci, N. C., and Pfister, O., "Experimental realization of multipartite entanglement of 60 modes of a quantum optical frequency comb," Phys. Rev. Lett. **112**, 120505 (2014).

Holland, M. J., Collett, M. J., Walls, D. F., and Levenson, M. D., "Nonideal quantum nondemolition measurements," Phys. Rev. A **42**, 2995–3005 (1990).

Larsen, M. V., Guo, X., Breum, C. R., Neergaard-Nielsen, J. S., and Andersen, U. L., "Deterministic generation of a two-dimensional cluster state," Science **366**(6463), 369–372 (2019).

Larsen, M. V., Neergaard-Nielsen, J. S., and Andersen, U. L., "Architecture and noise analysis of continuous-variable quantum gates using two-dimensional cluster states," Phys. Rev. A **102**, 042608 (2020).

Menicucci, N. C., "Temporal-mode continuous-variable cluster states using linear optics," Phys. Rev. A **83**, 062314 (2011).

Miyata, K., Ogawa, H., Marek, P., Filip, R., Yonezawa, H., and Yoshikawa, J., "Experimental realization of a dynamic squeezing gate," Phys. Rev. A **90**, 060302 (2014).

Pfister, O., "Continuous-variable quantum computing in the quantum optical frequency comb," J. Phys. B **53**(1), 012001 (2019).

Sakaguchi, A., Ogawa, H., Kobayashi, M., Suzuki, S., Yonezawa, H., and Huntington, E., "Low-latency digital feedforward for universal continuous-variable quantum computation in time domain," in *Conference on Lasers and Electro-Optics* (Optical Society of America, 2018), p. FTu4G.3.

Shiozawa, Y., Yoshikawa, J., Yokoyama, S., Kaji, T., Makino, K., and Serikawa, T., "Quantum nondemolition gate operations and measurements in real time on fluctuating signals," Phys. Rev. A **98**, 052311 (2018).

Takeda, S. and Furusawa, A., "Universal quantum computing with measurement-induced continuous-variable gate sequence in a loop-based architecture," Phys. Rev. Lett. **119**, 120504 (2017).

Takeda, S., Takase, K., and Furusawa, A., "On-demand photonic entanglement synthesizer," Sci. Adv. **5**(5), eaaw4530 (2019).

Yoshikawa, J., Miwa, Y., Huck, A., Andersen, U. L., van Loock, P., and Furusawa, A., "Demonstration of a quantum nondemolition sum gate," Phys. Rev. Lett. **101**, 250501 (2008).

Yang, R., Wang, J., Zhang, J., Liu, K., and Gao, J., "Generation of continuous-variable spatial cluster entangled states in optical mode comb," J. Opt. Soc. Am. B **33**(12), 2424–2429 (2016).

Yoshikawa, J., Asavanant, W., and Furusawa, A., "Purification of photon subtraction from continuous squeezed light by filtering," Phys. Rev. A **96**, 052304 (2017).

Yokoyama, S., Ukai, R., Armstrong, S. C., Sornphiphatphong, C., Kaji, T., and Suzuki, S., "Ultra-large-scale continuous-variable cluster states multiplexed in the time domain," Nat. Photonics **7**(12), 982–986 (2013).

Yoshikawa, J., Yokoyama, S., Kaji, T., Sornphiphatphong, C., Shiozawa, Y., and Makino, K., "Invited article: Generation of one-million-mode continuous-variable cluster state by unlimited time-domain multiplexing," APL Photon. **1**(6), 060801 (2016).

07 December 2024 17:52:47

CHAPTER

5 NON-GAUSSIAN QUANTUM STATES

5.1 INTRODUCTION

In CV quantum computation, the resource states for various protocols can be traced back to the squeezed vacuum states. For example, the EPR state, which is a resource state for quantum teleportation, can be generated using two squeezed vacuum states and a 50:50 beamsplitter. The resource state of the measurement-based quantum computation—the cluster state—can also be generated using squeezed vacuum states and a beamsplitter network. CV quantum computations that use only Gaussian elements, however, can be efficiently simulated using classical machines (Bartlett *et al.*, 2002). Therefore, non-Gaussian elements (quantum states, operations, or measurements) are the keys to CV quantum computation.

For physical systems that possess natural high nonlinearity—for example, coupling between microwave and qubit in cavity QED systems—direct implementations of non-Gaussian operation would be the most straightforward method to introduce non-Gaussianity into the system. In the optical system, Kerr interaction is a representative optical nonlinearity that results in non-Gaussian operations. But as high-order optical nonlinearity (including Kerr interactions) tends to be either weak or lossy, utilizing them in the direct implementation of non-Gaussian operations is currently not experimentally feasible.

Measurement in the quadrature basis, i.e., the homodyne measurement, is a Gaussian element, which means that it cannot be used as a non-Gaussian element. Measurement in the photon number basis (also called Fock basis), on the other hand, is a non-Gaussian element as it can convert a Gaussian state into a non-Gaussian state. There are research studies on various types of such detectors: for example, avalanche photodiodes (APD), superconducting nanostrip photon detector (SNSPD), and transition edge sensor (TES). Therefore, even if we have an optical setup that consists of only squeezed lights and linear optics, protocols that cannot be classically simulated can be realized by replacing the homodyne detectors with the photon number measurements. Such an example is Gaussian Boson sampling, which has been demonstrated in optical systems (Wang *et al.*, 2019). For most of the CV quantum computation protocols, however, as information is encoded on the phase space, homodyne measurements that are phase-sensitive measurements (as opposed to photon number basis measurements) are preferred.

Rather than the direct introduction of non-Gaussian operations or measurements, the introduction of the non-Gaussian states is more advantageous. By using the methodology of the measurement-based

07 December 2024 17:52:47

https://doi.org/10.1063/9780735424074_005 5-1

Optical Quantum Computers: A Route to Practical Continuous Variable Quantum Information Processing, W. Asavanant and A. Furusawa
© 2022 AIP Publishing, published by AIP Publishing

quantum computation (MBQC), if we can generate appropriate non-Gaussian ancillary states, we can combine them with Gaussian elements to realize non-Gaussian measurements, which can be used in conjunction with the cluster state to realize non-Gaussian operations.

Some of the readers might be skeptical and think that if direct non-Gaussian operations are difficult, the preparation of non-Gaussian states should be difficult as well. To be more precise, it is difficult to realize "unitary" non-Gaussian operations but not "non-unitary" ones. As we will see in Sec. 5.2, by using Gaussian entanglements (such as two-mode squeezed states) and photon detectors, it is relatively simple (in principle) to convert Gaussian states into non-Gaussian states. This process, however, is non-unitary, meaning that if we directly incorporate this into the computation process, our quantum computer will become inherently probabilistic. This is where the MBQC comes in. The non-Gaussian ancillary states for non-Gaussian operations can be injected from the outside information flow (i.e., they can be offline), and by adding quantum memories to our system, we can have deterministic quantum computation even with probabilistic non-Gaussian state generations. As a cost, we require additional computational overheads (e.g., the quantum memory and the waiting time). Therefore, the generation of non-Gaussian states holds the key to the realization of the MBQC.

5.2 HERALDING GENERATION OF NON-GAUSSIAN STATES

Although there are various experimental systems for the generation of various non-Gaussian states, most of them are based on the same idea shown in Fig. 5.1: measurements and conditionings on some of the modes of the multimode quantum entanglement. As Gaussian entanglements (such as EPR states and two-mode squeezed states) are the easiest to generate optically, the measurements are usually photon number basis measurements, not homodyne measurements.

To illustrate the most basic case, let us consider the case in Fig. 5.1(b), where we have an ideal EPR state $|\mathrm{EPR}\rangle_{\mathrm{AB}}$ between mode "A" and "B" whose (unnormalized) ket vector is given by

$$|\mathrm{EPR}\rangle_{\mathrm{AB}} = \sum_{n=0}^{\infty} |n\rangle_{\mathrm{A}} \otimes |n\rangle_{\mathrm{B}}. \tag{5.1}$$

By using a beamsplitter network and photon-number-resolving detectors (PNRDs), if we can realize a measurement of mode A onto the quantum state

$$|\psi\rangle_{\mathrm{A}} = \sum_{n=0}^{\infty} c_n |n\rangle_{\mathrm{A}}, \tag{5.2}$$

then after applying this projection measurement to the EPR state, we have

$$|\psi_{\mathrm{out}}\rangle_{\mathrm{B}} \propto \left(|\psi\rangle_{\mathrm{A}}\ {}_{\mathrm{A}}\langle\psi| \otimes \hat{I}_{\mathrm{B}}\right) |\mathrm{EPR}\rangle_{\mathrm{AB}} = \sum_{n=0}^{\infty} c_n^* |n\rangle_{\mathrm{B}}. \tag{5.3}$$

07 December 2024 17:52:47

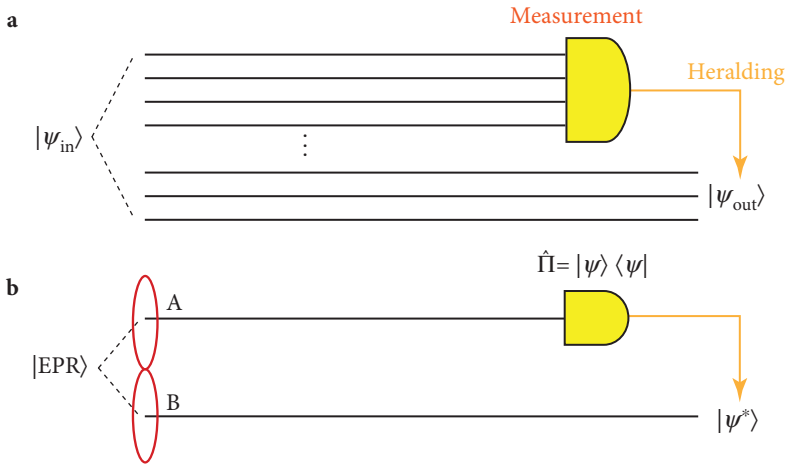

FIG. 5.1
Heralding generation of non-Gaussian states. (a) General conceptual diagram. (b) Two-mode example using an ideal EPR state and a projection measurement.

The above state is a state whose wave function is a complex conjugate of the wave function of $|\psi\rangle$, which we will denote as $|\psi^*\rangle$. Therefore, the problem of the generation of the non-Gaussian states in the optical setting reduces the problem of finding a right combination of linear optics, PNRDs, and measurement results that condition the quantum state we want to generate. As we are implementing measurement only on mode A, mode B remains unmeasured and can be used in quantum computation. This conditional method that gives desired quantum states, when successful, is called the *heralding method*.

Note that although we are restricted ourselves to the EPR state here, the initial multimode Gaussian entanglement does not have to be the EPR state as long as we can find an appropriate measurement method to herald the desired states.

5.2.1 Realistic considerations

In the previous section, we have used an ideal EPR state to illustrate the ideas of the heralding method. However, as the EPR state is unphysical, it is usually replaced with a two-mode squeezed state (TMSS), which can be generated by either combining two squeezed vacuum states on a 50:50 beamsplitter or using the non-degenerate parametric down conversion process. In any case, the TMSS can be written as

$$|\mathrm{TMSS}(\lambda)\rangle_{AB} = \sqrt{1-\lambda^2}\sum_{n=0}^{\infty}\lambda^n\,|n\rangle_A \otimes |n\rangle_B, \tag{5.4}$$

07 December 2024 17:52:47

where $|\lambda| < 1$ is a parameter determining the strength of the entanglement, which depends on various factors such as the strength of the squeezed vacuum states and the optical nonlinearity of the nonlinear crystals. If we do the projection measurement on mode A onto $|\psi\rangle_{\mathrm{A}}$, we have the output state $\left|\psi'_{\mathrm{out}}\right\rangle_{\mathrm{B}}$,

$$\left|\psi'_{\mathrm{out}}\right\rangle_{\mathrm{B}} \propto \sum_{n=0}^{\infty} \lambda^n c_n^* |n\rangle_{\mathrm{B}}. \tag{5.5}$$

Therefore, if we incorporate the effects of the coefficients $\{\lambda^n\}$ into the measurements, it is also possible to use the TMSS in a way similar to the EPR state. This, however, means that if the λ is small, we need to make our measurement so that the coefficients of the large photon number are much higher than when the ideal EPR state is used.

Another factor that has to be taken into account is the PNRD. Most of the photon counting techniques are based on the ON/OFF detector, which can only detect the presence of the photon but cannot resolve the photon number. The PNRD that is being currently developed is also not an ideal one and can resolve the photon number up to a certain maximum value. As such, when designing the system to generate the non-Gaussian states, it is crucial to consider such a factor as well. Regarding the usage of the ON/OFF detector, there are a few further considerations that must be made. First, we have to design our measurement system so that only a single photon reaches each detector at a time. Second, to realize such a situation, an approximation, usually called *weak-pump approximation*, is usually made. In this approximation, we usually consider the situation where $\lambda \ll 1$ and consider the two-mode squeezed state up to the lowest order of λ that is relevant. If we consider up to the first order, we have

$$|\mathrm{TMSS}(\lambda)\rangle_{\mathrm{AB}} \propto |0\rangle_{\mathrm{A}} \otimes |0\rangle_{\mathrm{B}} + \lambda\, |1\rangle_{\mathrm{A}} \otimes |1\rangle_{\mathrm{B}} + \mathcal{O}(|\lambda|^2). \tag{5.6}$$

Then, as we are approximating that there is utmost a single photon on mode A, even if we use an ON/OFF detector to measure mode A, we are (in the weak-pump limit) measuring a single-photon state, and the output on mode B becomes $\sim|1\rangle_{\mathrm{B}}$. Strictly speaking, as the ON/OFF detectors cannot distinguish the photon numbers, the generated states will be mixed states.

We also have to consider the generation rate as well. In principle, the generation rate will be highly dependent on how we form the measurements on mode A and the strength of the entanglement λ. As a simple example, let us consider the generation of the photon number state $|n\rangle$ from the TMSS. If we return to Fig. 5.1(b), we can replace the EPR state with the TMSS and let the measurement on mode A be an ideal PNRD whose projection operators are

$$\hat{\Pi}_n = |n\rangle\langle n|. \tag{5.7}$$

Then, we can write down the probability of heralding $|n\rangle_{\mathrm{B}}$ in mode B as a function of λ,

$$p_n(\lambda) = (1-\lambda^2)\lambda^{2n}. \tag{5.8}$$

07 December 2024 17:52:47

There are a few interesting things about Eq. (5.8). First, we observe that for each n, there exists an optimal λ (which we denote as Λ_n) that maximizes the heralding probability,

$$|\Lambda_n| = \sqrt{\frac{n}{n+1}}. \tag{5.9}$$

Second, if we take the limit where $\lambda \to 1$, i.e., the limit where the TMSS becomes an ideal EPR state, the heralding probability actually approaches 0 for all n ! Although this might seem counterintuitive as the TMSS is an approximation of the EPR state, the reason for this lies in the fact that in the EPR state, the probability of measuring n at mode A is equal for all n up to infinity.

To summarize, there are various factors that need to be considered for the realistic generation of a non-Gaussian state: what type of detectors (ON/OFF or PNRD) we have, whether we can consider the weak-pump limit and how does it affect the generated states, or whether the generation probability is high enough to actually generate and use the quantum states. Also, depending on the setup, there is also the possibility that the generation probability and the quality of the generated states have a trade-off relation, i.e., the higher the generation probability is, the lower the quality of the state becomes. In addition to some simple examples we have shown above, there are also various experimental imperfections such as optical losses, interferometric visibility, and electrical noises that also affect the generation of non-Gaussian quantum states.

07 December 2024 17:52:47

5.2.2 Modes of non-Gaussian states generated with the heralding method

We have omitted a discussion on the mode of the quantum state and assumed that the TMSS is generated between mode A and mode B. It was also assumed that the ON/OFF detector and the PNRD will detect photons in exactly the same mode as mode A. For pulsed-laser experiments, the situation might be relatively close to these assumptions as we can use the pulse timing as a trigger, and the temporal mode is relatively defined by the shape of the pulses. For the continuous-wave (CW) experiments, as the TMSS is generated continuously, we have to be more careful when we consider the generation state in the heralding method.

In Chap. 4, we have formulated the theory for the CW squeezed vacuum. Here, we can employ a similar method and consider a continuous source of the TMSS given by

$$|\text{CW-TMSS}\rangle_{\text{AB}} = \hat{S}_{\text{TM}} |\mathbf{0}\rangle_{\text{A}} \otimes |\mathbf{0}\rangle_{\text{B}}, \tag{5.10}$$

where

$$\hat{S}_{\text{TM}} = \exp\left[\frac{1}{2}\left(\hat{P}_r^\dagger - \hat{P}_r\right)\right], \tag{5.11}$$

with

$$\hat{P}_r^\dagger = \int\int \mathrm{d}t\mathrm{d}t'\, r(t-t')\hat{a}_{\text{A}}^\dagger(t)\hat{a}_{\text{B}}^\dagger(t') \tag{5.12}$$

being the photon-pair generator and $|\mathbf{0}\rangle$ being the multimode vacuum state. In the CW regime, the detection of the photon will be random. To theorize what happens when photons are detected in mode A, we need additional assumptions on the photon detectors. One of the assumptions that is usually adopted implicitly is that the response time of the photon detectors is much faster than the temporal width of $r(t, t')$. In such a case, we can approximate that when there is a click at time τ, the following projection operator is implemented

$$\hat{\Pi}_{n,\tau} = |n_\tau\rangle \langle n_\tau|, \tag{5.13}$$

where

$$|n_\tau\rangle = \frac{\hat{a}^{\dagger n}(\tau)}{\sqrt{n!}} |\mathbf{0}\rangle \tag{5.14}$$

is a Fock state with a photon number n at time τ. By measuring $\hat{\Pi}_{n,\tau}$ in mode A, we have an output state

$$|\psi_{\text{out}}\rangle \propto \left(\hat{\Pi}_{n,\tau} \otimes \hat{I}_{\text{B}}\right) \hat{S}_{\text{TM}} |\mathbf{0}\rangle_{\text{A}} \otimes |\mathbf{0}\rangle_{\text{B}}. \tag{5.15}$$

In the weak-pump limit, we can use the following approximation:

$$\hat{S}_{\text{TM}}^{\dagger} \hat{a}_A(\tau) \hat{S}_{\text{TM}} \approx \hat{a}_A(\tau) + \frac{1}{2} \int \mathrm{d}t\, r(t-\tau) \hat{a}_{\text{B}}^{\dagger}(t), \tag{5.16}$$

where we use the time-symmetry $r(t) = r(-t)$. Therefore, we can write down the output state as

$$|\psi_{\text{out}}\rangle \sim \left(|n_\tau\rangle_{\text{A}}\, {}_{\text{A}}\langle \mathbf{0}| \otimes \hat{I}_{\text{B}}\right) \hat{S}_{\text{TM}} |\mathbf{0}\rangle_{\text{A}} \otimes \hat{a}_{r,\tau}^{\dagger n} |\mathbf{0}\rangle_{\text{B}}. \tag{5.17}$$

The operator $\hat{a}_{r,\tau}^{\dagger}$ is a creation operator for a photon in a wave packet mode given by the photon-pair correlation function $r(t)$,

$$\hat{a}_{r,\tau}^{\dagger} = N_r \int \mathrm{d}t\, r(t-\tau) \hat{a}^{\dagger}(t), \tag{5.18}$$

with N_r being the normalization constant so that $\hat{a}_{r,\tau}^{\dagger}$ satisfies the bosonic commutation relation and the timing is shifted depending on the click timing τ. If we carry out the exponential expansion of the $\hat{S}_{\text{TM}}$, we can see that only the term $\hat{I}_{\text{A}} \otimes \hat{I}_{\text{B}}$ has a non-zero contribution, which means that the output state in mode B is

$$|\psi_{\text{out}}\rangle_{\text{B}} \sim \hat{a}_{r,\tau}^{\dagger n} |\mathbf{0}\rangle_{\text{B}}. \tag{5.19}$$

Therefore, we can conclude that for a PNRD with a delta-function response, in the weak-pump limit, the non-Gaussian states generated using CW TMSS will have a temporal mode with a shape determined by the photon-pair correlation function $r(t)$. This concept is highly crucial in CW quantum optics experiments and is often misunderstood; although we use a CW light source and ignore any possible response of the PNRD, the generated states are in the wave packet mode as if we are using a pulsed laser. In addition to this confusion, unlike the pulsed-laser experiment, these non-Gaussian states, although they are in wave packet modes, are measured using the CW homodyne measurement. Intuitively, the measurements by the PNRD project our states from the CW state to a wave packet mode.

07 December 2024 17:52:47

In this section, there are a few ideal assumptions that are made. Here, we will discuss what happens in the actual experiments where these assumptions might not hold. First, for the purpose of illustrating the main ideas, we have assumed a weak-pump limit and time-reversal symmetry of $r(t)$. In reality, although the weak-pump limit might not be completely satisfactory, for a modest pump level in most of the experimental work, the mode function is approximately proportional to $r(t)$ (Yoshikawa *et al.*, 2017). On the other hand, although time-reversal symmetry seems a natural property, this is not always the case for the TMSS where the two modes are non-degenerate. Such an example is the generation of a rising exponential wave packet using the non-degeneracy in the polarization (Ogawa *et al.*, 2016).

Another ideal assumption made here is regarding the response of the photon detector. When the time-response function of the photon detector is not a delta function, we have to distinguish whether the response changes at the quantum level or the classical level. An example of the quantum level is when we add an optical filter in front of an ideal PNRD. In such a case, as the process is coherent, the generated state will still be a pure state, but the resultant temporal mode will have a different shape, determined by the response function $g(t)$ of the optical filter. This technique has been leveraged to generate quantum states with various temporal modes (Asavanant *et al.*, 2017; and Takase *et al.*, 2019). On the other hand, if the response of the photon detector is distorted by a classical process such as jitter and imperfect detection processes, the resulting quantum states become mixed states and the properties are degraded.

5.3 GENERATION OF SUPERPOSITION OF FOCK STATES

In this section, we will introduce various experiments on the generation of the superposition of the photon number state, i.e., the Fock states. We will start with the generation of the single-photon state and then move to the generation of a superposition state up to a few photon numbers. Then, as an example of a generation of multimode non-Gaussian states, we will introduce a Hong–Ou–Mandel state, which appears in the Hong–Ou–Mandel effects (Hong *et al.*, 1987).

5.3.1 Herald generation of the single-photon states

Figure 5.2 shows the typical setup for the herald generation of the single-photon state in both pulsed-laser and CW experiments. In the weak-pump limit, the initial two-mode entanglements generated by pumping the second-order nonlinear crystal (labeled as OPA and OPO in Fig. 5.2) are given by

$$|\psi_{\text{initial}}\rangle \approx |0\rangle_{\text{s}} \otimes |0\rangle_{\text{i}} + \lambda\, |1\rangle_{\text{s}} \otimes |1\rangle_{\text{i}}, \tag{5.20}$$

where "i" and "s" stand for idler and signal, respectively. As a custom, the idler mode is the mode that is measured (mode A in Sec. 5.2) and the signal mode is the mode where the state is heralded (mode B in Sec. 5.2). By measuring the idler mode, we can herald the generation of the single-photon states in the signal mode without having to directly measure the signal mode. As we need to split these two modes, they are usually generated so that they are non-degenerate in either the polarization or the frequency. In the pulsed laser experiments, as we know the arriving timing of the pulse, the trigger at

07 December 2024 17:52:47

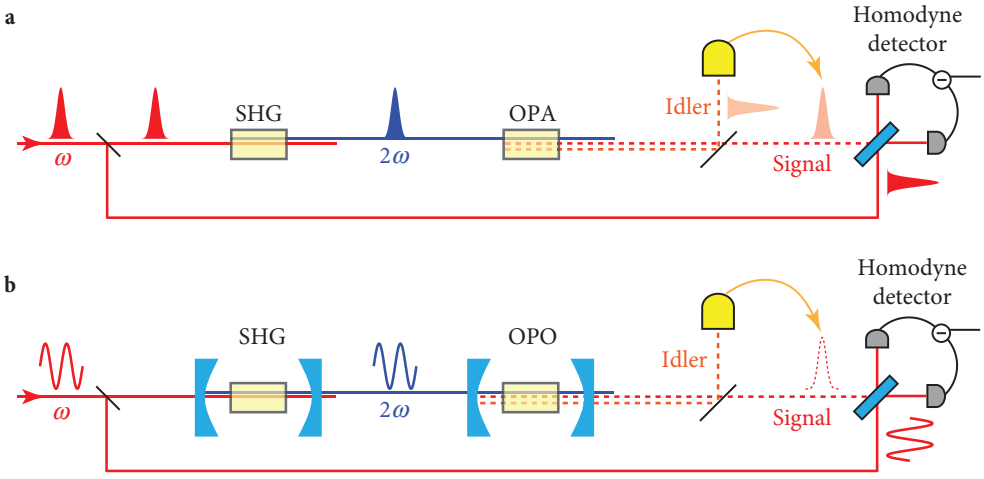

FIG. 5.2
Typical setup for the single-photon state generation and its verification with a homodyne measurement. (a) Pulsed laser. (b) Continuous-wave laser. SHG, second harmonic generator; OPA, optical parametric amplifier; OPO, optical parametric oscillator. Dashed lines are the nonclassical lights, while the solid lines are the classical lights.

the idler mode is also conditioned by the pulse timing. On the other hand, in the CW laser experiments, although the generation is completely random, unlike the pulsed-laser experiments, the generation rate is not limited by the pulsed-laser repetition rate. Also, since we are considering a weak-pump limit, our photodetector can simply be the ON/OFF detector since most of the time there is only one photon in the idler mode.

Historically, the single-photon state was first verified using the measurement of the photon-number statistics, such as second-order coherence or coincidence. The measurement of the coincidence reveals the photon statistics of the incident light. This measurement allows us to differentiate between the single-photon state $|1\rangle$ and the semi-classical coherent state $|\alpha\rangle$, whose mean photon number $\langle\alpha|\hat{n}|\alpha\rangle$ is 1.

The measurement of the coincidence, however, is not sufficient to utilize and characterize the single-photon state for CV quantum computation. As we have previously mentioned, the herald generation of the non-Gaussian states makes the heralded states to exist in a localized temporal mode and we want to extract information on the quadrature values and their distribution. In the pulsed-laser experiments, the pulses used in both the generation of the single-photon states and the local oscillator of the homodyne measurement originate from the same pulse [Fig. 5.2(a)]. This makes it seem that we should be able to achieve perfect interferometric visibility in the homodyne detector. In reality, this is usually not

07 December 2024 17:52:47

the case, as the wave packet shapes of short laser pulses (such as femtosecond pulses) are affected by various factors such as dispersion of medium and require precise adjustment.

On the other hand, Fig. 5.2(b) shows the typical setup for the generation and homodyne measurement of the single-photon states in the CW regime. Unlike the pulsed-laser regime where the single-photon states can be generated only at the timing of the pulses, the single-photon state generation in the CW regime is completely random. Moreover, the local oscillators for the CW laser experiments are, naturally, CW lasers. Therefore, the continuous electrical signals from the homodyne detectors do not directly give the quadrature values of the wave packet modes and an additional step is required. If we recall, the quadrature of the wave packet mode can be obtained by integrating the continuous signals from the homodyne detector using the appropriate mode function that corresponds to the shape of the wave packet. Then, the problem of obtaining the quadrature values in the CW experiments is reduced to determining the mode function. Although we can theoretically select a mode function and use it to obtain the quadrature values, it would be convenient if we can determine the mode functions using the experimentally obtained data as the actual experimental situations could differ from the expected parameters.

The mode function estimation from the experimental data was first done by Morin *et al.* (2013) for the mode function that is a real function. After this, there is also an extension to the complex-valued mode functions (Takase *et al.*, 2019). As the details are rather technical, we will not delve into them here, but we will provide some physical intuitions. In the CW experiments, the electrical signals from the homodyne are obtained continuously. For most of the time, as the single-photon states are not generated, we will be just measuring vacuum states (or squeezed vacuum state in the photon subtraction). Thus, if we are using the mode function whose shape does not match with that of the single-photon state, we will be retrieving the quadrature values of the mixed states between the vacuum states and the single-photon states. As the background vacuum state and the single-photon state are uncorrelated (ideally), the problem of finding the shape of the wave packet is equivalent to the problem in the signal processing where we want to separate the signals from the uncorrelated noises. Moreover, the variance of the quadrature values of the single-photon state is larger than that of the vacuum state. Therefore, a method that is usually used for this task is called *principal component analysis (PCA)*. By using PCA, we can estimate the shape of the wave packet of the generated states. PCA is widely used for the estimation of the shape of the wave packet of the non-Gaussian states such as a single-photon state, superpositions of Fock states, and cat states generated in the CW regime.

Now that we have the shape of the temporal mode, we can obtain the quadrature values and their distributions. In most experiments, however, we want to know whether the generated quantum states match with the target quantum states. If we recall basic quantum mechanics, the quantum states dictate the probability distributions of the physical quantities that are measured. As such, we have to infer the quantum state from the probability distributions of various physical quantities, a process called *quantum state tomography*. In the CV system, as the Wigner function contains all information regarding the quantum state, there is a method called inverse radon transformation that reconstructs the Wigner

07 December 2024 17:52:47

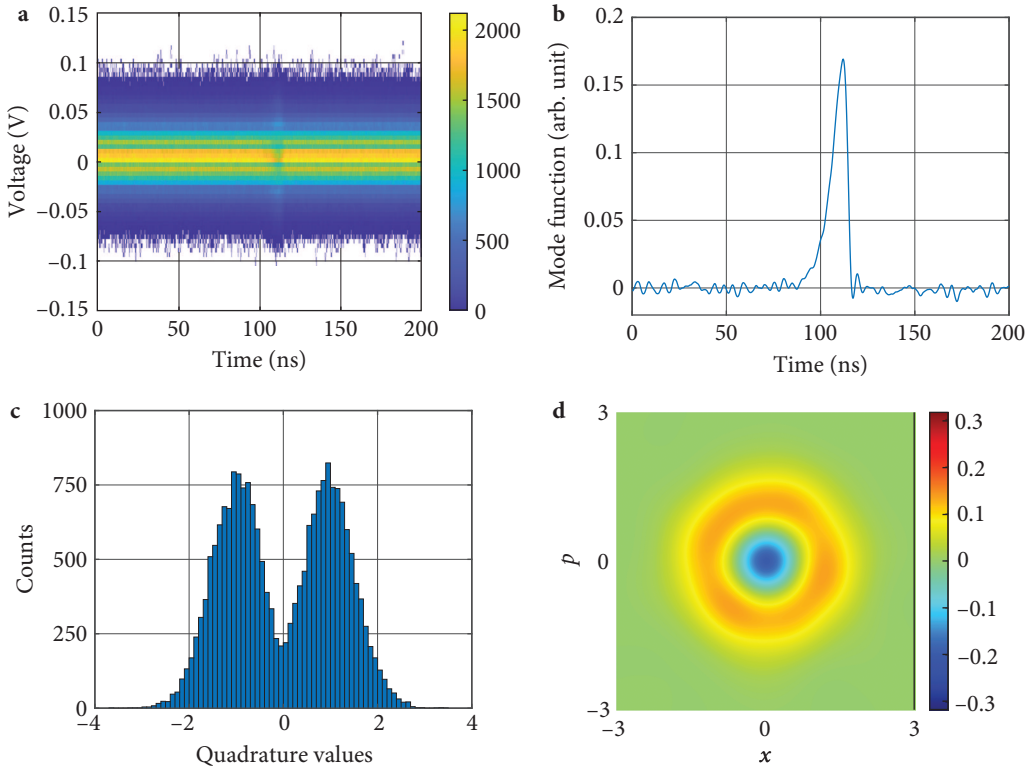

FIG. 5.3
Experimental data of the generation and verification of the single-photon state (Data: Shunya Konno). (a) Overlay of the electric signals from the homodyne detectors. (b) Estimated mode function of the single-photon state using principal component analysis. (c) Histogram of the quadrature values of the single-photon states. (d) Reconstructed Wigner function using the maximum likelihood method. We use the unit where $\hbar = 1$ here.

function directly from the experimentally obtained quadrature distributions. This method, however, usually performs poorly numerically and the resultant Wigner functions can be unphysical as no constraints are imposed. A more widely used method is the maximum likelihood method. This method reconstructs a physical density matrix that is most likely to give the quadrature distributions obtained in the experiments (Lvovsky, 2004). Figure 5.3 shows an example of the actual experimental data and analysis of the single-photon state that is generated experimentally using the heralding method. In the CV optical experiment, the negative regions of the Wigner functions are the concrete evidence that the generated states are the nonclassical states. In particular, for the single-photon state, the value of the Wigner function at the origin—also called *negativity*—is usually used as a simple figure of merit

07 December 2024 17:52:47

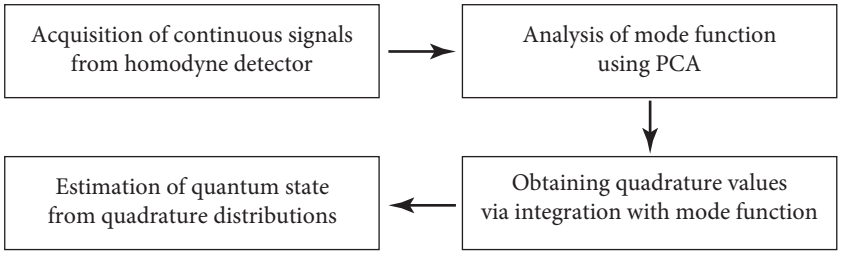
Acquisition of continuous signals from homodyne detector
Analysis of mode function using PCA
Obtaining quadrature values via integration with mode function
Estimation of quantum state from quadrature distributions

FIG. 5.4
Data processing in the CW non-Gaussian state generation experiments.

to show the nonclassicality of the state. Figure 5.4 summarizes a typical flow of the processing of the electrical signals from the homodyne measurements in the CW laser experiments.

5.3.2 Other single-photon sources

In addition to the heralding method, there are also various other methods to generate the single-photon state. For example, one of the well-known single-photon sources is a quantum dot that utilizes an emitter to generate single photons deterministically. Another type of the single-photon source is that which is based on atomic transitions. In comparison, the single-photon source using the heralding method explained here is usually referred to as a *spontaneous parametric down conversion (SPDC) source*. For a review of various single-photon sources, we refer the readers to Ref. Eisaman *et al.* (2011).

5.3.3 Superposition of the Fock state using displacement beams

In Sec. 5.2, we have given a general idea of how to herald arbitrary non-Gaussian states from the TMSSs. To show a more explicit example, let us first consider the generation of the superposition between vacuum state and single-photon state, $a|0\rangle + b|1\rangle$.

Figure 5.5 shows a typical setup to generate the $a|0\rangle + b|1\rangle$. In addition to the setup to generate the single-photon state, a displacement beam is added to the idler path. The physical intuition of how this system can generate the superposition states is as follows. To generate the superposition state, we need to create a situation where the clicks at the photon detector do not reveal whether it is due to the single-photon state in the idler path (which heralds the single-photon state on the signal path) or the photon from the displacement beam (which results in the vacuum state on the signal path). This process of hiding the information must be coherent, i.e., the information must be erased from the quantum level, as incoherent erasure would simply result in mixed states.

07 December 2024 17:52:47

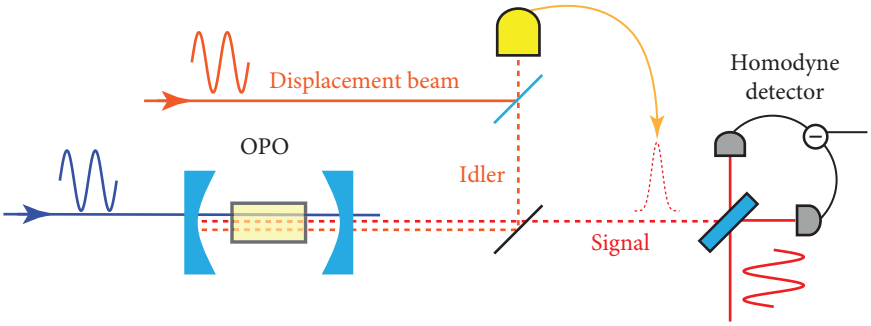

FIG. 5.5
Setup to generate the superposition between $|0\rangle$ and $|1\rangle$ by adding the displacement beam. Note that the blue beamsplitter at the idler path has high transmittivity ($T \sim 1$).

Now, let us do some more rigorous calculations. First, by using the weak-pump limit, we can write down the initial state as

$$|\psi_{\text{initial}}\rangle \propto |0\rangle_{\text{s}} \otimes |0\rangle_{\text{i}} + \lambda\, |1\rangle_{\text{s}} \otimes |1\rangle_{\text{i}} + \mathcal{O}(|\lambda|^2). \tag{5.21}$$

Then, if we do the displacement $\hat{D}(\alpha)$ on the idler mode and measure $|1\rangle_{\text{i}}$, we herald the following state on the signal mode,

$$|\psi_{\text{out}}\rangle \propto {}_{\text{i}}\langle 1|\, \hat{D}(\alpha)\, |0\rangle_{\text{i}}\, |0\rangle_{\text{s}} + \lambda_{\text{i}}\langle 1|\, \hat{D}(\alpha)\, |1\rangle_{\text{i}}\, |1\rangle_{\text{s}} + \mathcal{O}(|\lambda|^2). \tag{5.22}$$

We notice that the superposition coefficients depend on the matrix elements of the displacement operators $\hat{D}(\alpha)$ in the Fock basis. We can also assume further that α is small and do the approximation up to the first order of α,

$$\hat{D}(\alpha) \approx \hat{I} + \alpha\hat{a}^\dagger - \alpha^*\hat{a} + \mathcal{O}\big(|\alpha|^2\big). \tag{5.23}$$

Inserting Eq. (5.23) into Eq. (5.22) and keeping only the terms that are up to the first order in both α and λ, we have

$$|\psi_{\text{out}}\rangle \approx \alpha\, |0\rangle_{\text{s}} + \lambda\, |1\rangle_{\text{s}}. \tag{5.24}$$

Therefore, by adjusting the parameters λ and α, it is possible to generate arbitrary superposition in the form of $a|0\rangle + b|1\rangle$.

Experimentally, the parameters α and λ in Eq. (5.24) are adjusted as follows. First, their relative absolute values are adjusted by changing the power of the displacement beam. If we compare the counts at the photon detector for the cases with and without the displacement beam, the ratio $|\lambda|{:}|\alpha|$ can be easily calculated. Next, the phase factor can be adjusted by locking the relative phase between the idler path and the displacement beam. This is usually done by the injection of additional phase

07 December 2024 17:52:47

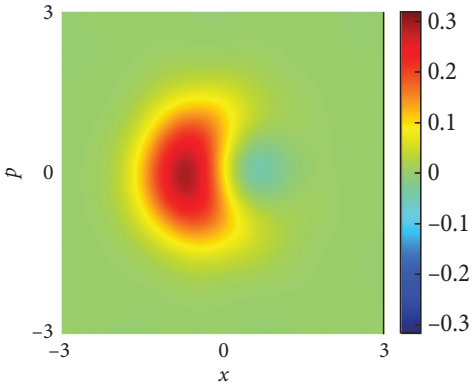

FIG. 5.6
Experimentally reconstructed Wigner function of the target state $(|0\rangle - |1\rangle)/\sqrt{2}$ (Data: Shunya Konno). We can see that the Wigner function of the state is phase sensitive and possesses a negative region. We use the unit where $\hbar = 1$ here.

reference beams into the optical system. Figure 5.6 shows an example of the experimentally reconstructed Wigner function of the quantum state of the form $a|0\rangle + b|1\rangle$.

Extending the idea that is shown here, the experimental generation of the Fock superposition up to two photons (Bimbard *et al.*, 2010) and three photons (Yukawa *et al.*, 2013) are demonstrated. In both experiments, the superposition coefficients are adjusted by adding two and three displacement beams in the idler path, respectively. Even more recently, there is a theoretical extension in which photon-number measurements on some of the modes of the multimode Gaussian state herald an arbitrary superposition of Fock states (Su *et al.*, 2019). In principle, by the implementation of a more generalized measurement using displacement operations, beamsplitter network, and photon-number-resolving detectors, the generation of various superpositions of Fock states can be achieved. Furthermore, by combining this generalized measurement with the quantum memory (which we will explain in Sec. 5.3.4), a deterministic state synthesizer using an optical system can be realized.

5.3.4 Multimode non-Gaussian states and their interferences

We have discussed generations of single-mode non-Gaussian states. Although it might be possible to extend the idea to realize multimode non-Gaussian states, there are also some instances where we want to realize multimode non-Gaussian states by interfering them on the linear optics network. Moreover, there exists many applications that require interferences between non-Gaussian states. For example, one of the methods to realize a logical qubit in the optical CV system requires interferences between cat states (Weigand and Terhal, 2018). Another application outside the CV quantum computation is a photonic qubit quantum computation scheme called KLM scheme that requires interferences between single-photon states (Knill *et al.*, 2001).

When compared to the other methodologies, the heralding generation of non-Gaussian state offers the generation of relatively purer quantum states with the possibility of extending the generation of a more complex state. The state generation with the heralding method is, however, probabilistic, which makes their direct applications to the interference experiments give a rather low success probability. Moreover, as the overall success probability roughly scales exponentially with the number of the non-Gaussian states required, this highly limits the range of the possible applications.

07 December 2024 17:52:47

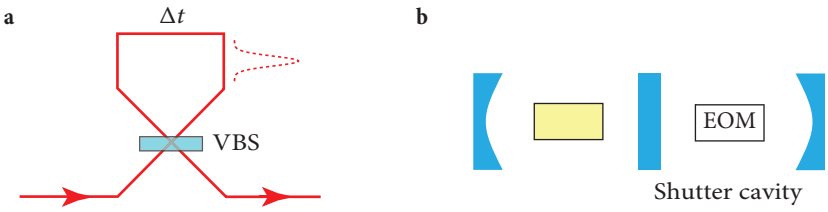

FIG. 5.7
Examples of an all-optical quantum memory. (a) Memory with a discrete storage time using the fixed delay line. (b) Memory with a continuous storage time using concatenate optical cavity. VBS, variable beamsplitter; EOM, electro-optics modulator.

The experimental difficulties due to the probabilistic nature of the heralding method can be elevated by using *quantum memories*. A quantum memory can be considered as a device that can store quantum states while keeping coherence. As we are considering the optical non-Gaussian states that exist in the wave packets, the quantum memory of our interest should be able to handle the wave packet mode. Therefore, the quantum memory that can store optical quantum states must be able to convert quantum states into propagating waves to a stationary system. We can also divide the quantum memory into two types based on whether the storage time of the memory is discrete or continuous. The most basic form of the quantum memory with a discrete storage time is a fiber loop with a variable beamsplitter [Fig. 5.7(a)]. In this type of memory, the storage time is an integer of the time width determined by the length of the fiber loop. For pulsed-laser experiments, this type of memory can be useful as the generation timing of the non-Gaussian state is determined by the pulse timing. For CW experiments, however, we would need a memory whose storage time can be continuously tuned.

Regarding the memory with continuous storage time, various media, such as atomic system, solid-state system, and optical system, are being researched, and each approach has different advantages and disadvantageous (Heshami *et al.*, 2016). For example, as the atomic system and the solid-state system utilize the energy level that is stable, they tend to offer a longer storage time. On the other hand, as these types of memory rely on the atomic transitions with a sharp linewidth, they are not applicable to optical quantum states of arbitrary wavelength and are unlikely to be able to handle wave packet mode. All-optical memory using the concatenated cavity depicted in Fig. 5.7(b), on the other hand, can store a quantum state of arbitrary wavelength. However, as the overall memory becomes a high-Finesse cavity during the storage, they tend to be susceptible to optical losses, making the storage time relatively limited compared to the other systems.

As an example of the interference experiment, Fig. 5.8 shows the setup for the interference of the single-photon states assisted by the all-optical quantum memories (Makino *et al.*, 2016). This experiment is based on the famous *Hong–Ou–Mandel (HOM) effect*. The HOM effect is when two single-photon

07 December 2024 17:52:47

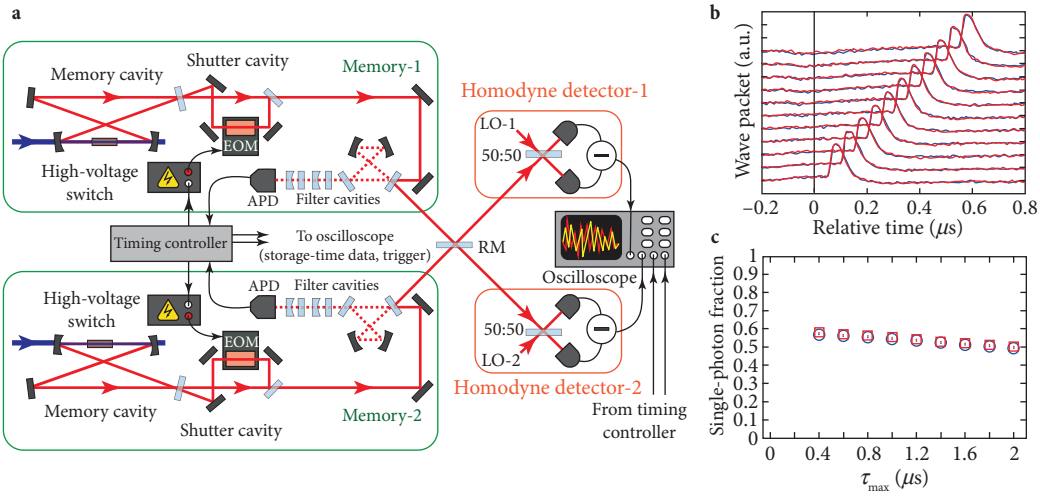

FIG. 5.8
An experimental setup to generate and verify the HOM state assisted by all-optical quantum memory (Makino *et al.*, 2016).

states are interfered at the beamsplitter, and both photons come out from the same port of the beamsplitter (bunching). If we write down the quantum state after the beamsplitter, we have

$$|\psi_{\mathrm{HOM}}\rangle = \frac{1}{\sqrt{2}}\left(|2\rangle \otimes |0\rangle - |0\rangle \otimes |2\rangle\right), \tag{5.25}$$

which we will call the HOM state. We observe that there are no $|1\rangle \otimes |1\rangle$ terms, which is due to the *bunching* of the photons that are Bosons. If we do not use the quantum memories, the HOM state is successfully generated only when the two single-photon states are heralded at the same timing. Therefore, the success probability in this case will be the square of the success rate of a single source. On the other hand, if we utilize quantum memories, we can adjust the timing between the two single-photon sources, which improves the generation rate by roughly a square root. In addition to the use of the optical memory to realize the HOM state, the same type of memory has been used to store superposition states (Hashimoto *et al.*, 2019) and two-mode quantum entanglement (Okamoto *et al.*, 2020).

Characterization of the multimode non-Gaussian states is also difficult. For the multimode Gaussian states, we can simply measure the nullifiers whose number scales linearly with a number of modes. For non-Gaussian states, the scaling of the number of the measurements required to accurately perform the quantum state tomography is much worse. As the characterization of the non-Gaussian states is usually based on the density matrix, the number of the measurements required scales exponentially with a number of modes. Moreover, the base of this exponential scaling would increase as the number

07 December 2024 17:52:47

of the photons in the system increases. As an example, although there are only two modes with at most two photons, 36 bases (between two modes) were used to characterize the HOM states (Makino *et al.*, 2016).

Generation and characterization of the multimode non-Gaussian states are crucial topics in the CV quantum computing as these states are indispensable resources to realize universal and fault-tolerant CV quantum computation. In recent research studies, there are efforts to make the quantum state tomography of the non-Gaussian states more efficient by using the technique in machine learning (Tiunov *et al.*, 2020).

5.4 PHOTON SUBTRACTION AND CAT STATE

In Sec. 5.3, we discussed the generation of the Fock superposition state using the TMSS and displacement beams. In this section, we will discuss another basic method called *photon subtraction*. Photon subtraction is one of the most basic and widely used methods to generate quantum states that approximate the cat state (Dakna *et al.*, 1997). Although photon subtraction is one of the special cases shown in Fig. 5.1(a) as it offers many insights and understandings into various research studies on the optical generations of non-Gaussian states, we will dedicate this chapter for its explanation.

5.4.1 Basic formulation

Figure 5.9 shows the typical setup of the photon subtraction. First, let us consider the case where the input state $|\psi\rangle = \sum_n c_n |n\rangle$ is an arbitrary pure state. In this case, the state $|\psi'\rangle$ after the beamsplitter is given by

$$\begin{aligned}|\psi'\rangle &= \hat{B}(\sqrt{T})\,|\psi\rangle \otimes |0\rangle_{\text{anc}} \\ &= \sum_{n=0}^{\infty} \hat{B}(\sqrt{T}) c_n \frac{\hat{a}^{\dagger n}}{\sqrt{n!}} |0\rangle \otimes |0\rangle_{\text{anc}}\end{aligned}$$

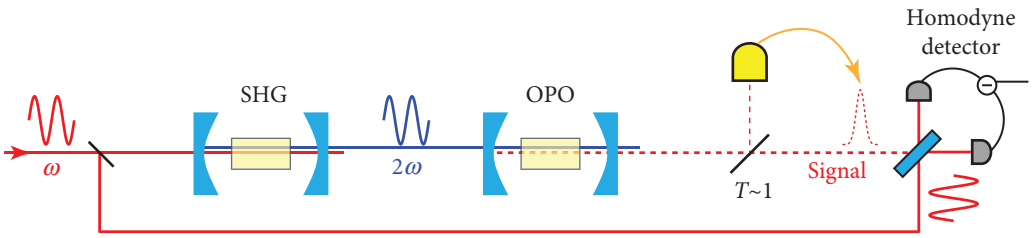

FIG. 5.9
Typical setup of the photon subtraction experiment. Note that the TMSS is replaced with a squeezed vacuum state.

07 December 2024 17:52:47

$$
\begin{aligned}
&= \sum_{n=0}^{\infty} c_n \frac{\left(\sqrt{T}\hat{a}^\dagger - \sqrt{R}\hat{a}_{\text{anc}}^\dagger\right)^n}{\sqrt{n!}} \hat{B}(\sqrt{R})\,|0\rangle \otimes |0\rangle_{\text{anc}} \\
&= \sum_{n=0}^{\infty} c_n (\sqrt{T})^n\,|n\rangle \otimes |0\rangle_{\text{anc}} - \sqrt{R}\sum_{n=1}^{\infty} c_n (\sqrt{T})^{n-1}\sqrt{n}\,|n-1\rangle \otimes |1\rangle_{\text{anc}} + \cdots.
\end{aligned} \tag{5.26}
$$

Note that in Eq. (5.26), we use the fact that the beamsplitter interaction on the vacuum state inputs results in the vacuum state. Now, let us consider the case where the ancillary mode is measured and the output state is heralded. If we measure the ancillary mode and find that there is no photon in the ancillary state, the output state becomes the first term of the last line in Eq. (5.26). We observe that the superposition coefficients are similar to $|\psi\rangle$, but the coefficients are "attenuated" by the factor $(\sqrt{T})^n$. On the other hand, if the ancillary mode is projected to $|1\rangle_{\text{anc}}$, the superposition coefficient of the term $|n\rangle$ is now the coefficient c_{n+1} of the original state (with additional factors).

For the sake of the physical intuition, let us consider the case where $T \approx 1$, i.e., the beamsplitter is highly transmittive. In this case, Eq. (5.26) can be approximated as

$$
|\psi'\rangle \approx |\psi\rangle \otimes |0\rangle_{\text{anc}} - \sqrt{R}\hat{a}\,|\psi\rangle \otimes |1\rangle_{\text{anc}} + \cdots. \tag{5.27}
$$

Equation (5.27) shows that, in this approximation, the input state does not change when no photon is detected in the ancillary mode and the annihilation operator is applied to $|\psi\rangle$ when a single photon is detected at the ancillary state (thus the term photon subtraction). Therefore, by using the photon subtraction setup, we can apply the annihilation operator to the input state to change it from the Gaussian state to the non-Gaussian state.

If we use the approximation in Eq. (5.27) and let the input state be the squeezed vacuum state, the output state $|\psi_{\text{out}}\rangle$ when a single-photon state is projected at the ancillary mode is

$$
\begin{aligned}
|\psi_{\text{out}}\rangle &\propto \hat{a}\,|S\rangle\,(r)\,|0\rangle \\
&= \hat{S}(r)\,|1\rangle,
\end{aligned} \tag{5.28}
$$

which is a squeezed single-photon state. This state is known to be a good approximation to the cat state $|\alpha\rangle - |-\alpha\rangle$ with small amplitude ($\alpha \sim 1$, also called Schrödinger kitten). There are many photon subtraction experiments that realize this type of state and the early cat state generation experiments generated mainly this type of state (Ourjoumtsev *et al.*, 2006; Neergaard-Nielsen *et al.*, 2006; and Wakui *et al.*, 2007). There is also an experiment that implements the squeezing operation on the single-photon state, which results in a state that can approximate the cat state well (Miwa *et al.*, 2014).

To move from the physical intuition, let us consider the case where the input state is the squeezed state. In this case, we can write down an exact form of the state $|\psi'\rangle$ after the beamsplitter interaction as

$$
|\psi_{\text{out}}\rangle = \frac{1}{\sqrt{\cosh r}} \sum_{n=0}^{\infty}\sum_{m=0}^{2n} \left(-\frac{\tanh r}{2}\right)^n \frac{(-1)^m (2n)!(\sqrt{T})^{2n-m}(\sqrt{R})^m}{n!\sqrt{(2n-m)!m!}}\,|2n-m\rangle \otimes |m\rangle_{\text{anc}}. \tag{5.29}
$$

07 December 2024 17:52:47

From Eq. (5.29), we can immediately observe that when the ancillary mode is projected into $|m\rangle_{\text{anc}}$, then if m is odd (even), the heralded state is the superposition of the Fock state with only odd (even) photon number.

We can also write down the conditioned state $|\psi_{\text{cond}}(m)\rangle$ when the ancillary mode is projected to $|m\rangle_{\text{anc}}$ as

$$|\psi_{\text{cond}}(m)\rangle = \frac{1}{\sqrt{p(m)}} \sum_{k=0}^{\infty} \frac{1+(-1)^{m+k}}{2\sqrt{\cosh r}} \frac{(m+k)!}{\sqrt{m!k!}\left(\frac{m+k}{2}\right)!} \left(\frac{R}{T}\right)^{\frac{m}{2}} \left(-\frac{T\tanh r}{2}\right)^{\frac{m+k}{2}} |k\rangle, \tag{5.30}$$

where $p(m)$ is the probability of obtaining the result m at the ancillary mode. This probability depends on both the squeezing parameter r and the splitting ratio T and R of the beamsplitter (which satisfies $R+T=1$).

Although we can further do the full calculation to show that the generated states indeed possess high fidelity to cat states when the parameters are optimized, let us do some calculations to intuitively show that Eq. (5.30) does give a good approximation to the cat states. First, using the identity of the Gamma function, let us rewrite the term $(m+k)!/[(m+k)/2]!$ as

$$\frac{(m+k)!}{\left(\frac{m+k}{2}\right)!} = \frac{2^{m+k}}{\sqrt{\pi}}\Gamma\left(\frac{m+k}{2}+\frac{1}{2}\right), \tag{5.31}$$

where $\Gamma(\cdot)$ is a gamma function. In the limit where m is large compared to the summation range of k, we can approximate the gamma function as $\Gamma(z+1) \sim \sqrt{2\pi z}\left(\frac{z}{e}\right)^z$. Then, we can approximate the conditioned state as

$$|\psi_{\text{cond}}\rangle \sim N_m \sum_{k=0}^{\infty} \frac{1+(-1)^{m+k}}{\sqrt{k!}} \left(-\frac{mT\tanh r}{e}\right)^{\frac{k}{2}} |k\rangle, \tag{5.32}$$

where N_m is a constant that does not depend on k. The plus and minus cat state with amplitude α, $|\psi_{\text{cat},\pm}(\alpha)\rangle$, can be written using Fock basis as

$$\left|\psi_{\text{cat},\pm}(\alpha)\right\rangle = N_{\alpha,\pm}(|\alpha\rangle \pm |-\alpha\rangle) \propto \sum_{k=0}^{\infty} \frac{1\pm(-1)^k}{\sqrt{k!}}\alpha^k |k\rangle. \tag{5.33}$$

Therefore, we observe that the values of m determine whether the generated cat state is a plus cat or a minus cat state and the parameter α is given by

$$\alpha = \sqrt{-\frac{mT\tanh r}{e}}. \tag{5.34}$$

For $r>0$ that corresponds to antisqueezing in p, α is purely imaginary, which means that the amplitudes of the cat states are in the p direction. For $r<0$ that corresponds to antisqueezing in x, α is real and the amplitudes of the cat states are in x direction. In general, when we do the photon subtraction on the squeezed vacuum states, the amplitude of the cat states will be in the antisqueezing direction.

07 December 2024 17:52:47

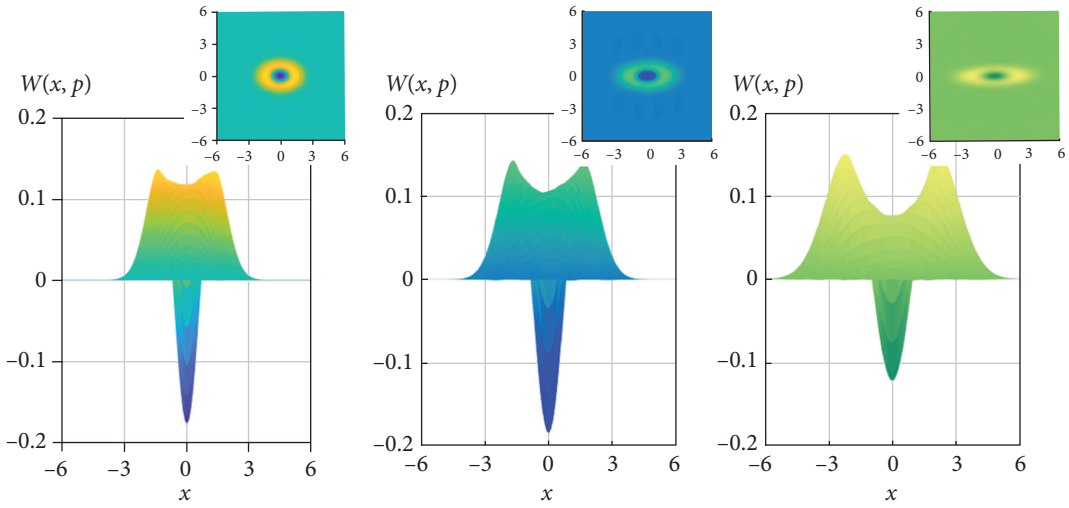

FIG. 5.10
Reconstructed Wigner functions of experimentally generated photon-subtracted squeezed vacuum states with different squeezing levels. Adapted from Asavanant *et al.*, Opt. Express **25**(26), 32227–32242 (2017). We use the unit where $\hbar = 1$ here.

Figure 5.10 shows the experimental reconstructed Wigner function of the photon-subtracted squeezed states where the ON/OFF detector is used to detect photons. As we can see, the larger the initial squeezing becomes, the further apart the two peaks of the Wigner functions are. Nevertheless, they remained somewhat of the same shape due to the fact that the subtraction of a single photon from a squeezed vacuum state can only result in a squeezed single-photon state. Therefore, to generate a larger cat state, we need a capability to resolve a larger photon number.

5.4.2 Experimental consideration

In Sec. 5.4.1, we gave the explanations of how photon subtraction on the squeezed vacuum state can be used to generate the cat state. In this section, we will direct our focus to the experimental consideration regarding the photon subtraction experiment.

Throughout this chapter, we have assumed that we can do an ideal photon counting on the idler mode. But as we have already explained, most of the currently available photon detector are either the ON/OFF detector or can count up to only a few photons. Therefore, most of the photon subtraction experiments use T that is close to one and $|r|$ that is sufficiently small so that the $p(m)$ for the case where $m > 1$ is negligible. Although the schematic in Fig. 5.9 shows the squeezed light passing through a beamsplitter, in the actual experiments, it is often the case that we use a highly reflective beamsplitter

07 December 2024 17:52:47

to tap some of the light and perform photon subtraction. For a fixed value of m, it is usually the case that we can tune r and T so that the generated state has high fidelity to a cat state with a certain α. In general, if we want to a generate cat state with a large α, we have to increase the value of m. For the case where $m = 1$, the antisqueezing of about 3 dB produces a state that has high fidelity to a cat state of $\alpha \sim 1$.

Another factor that we have to take into consideration is the generation rate. In the typical photon subtraction experiment, it is usually desirable that T is kept close to 1. But such constraint limits the generation rate, making it difficult to generate a cat state with a large amplitude. There is a protocol that can generate a cat state with a large amplitude using cat states with small amplitude (Sychev *et al.*, 2017). In this protocol, by interfering two cat states on a beamsplitter and do the homodyne conditioning on one of the mode, a cat state whose amplitude is larger than the initial states can be realized. The success rate of the breeding protocol, however, is relatively limited as it requires two cat states and homodyne conditioning that are all probabilistic. There is also a theoretical proposal that relaxes the condition $T \sim 1$ by replacing the ancillary vacuum state with a squeezed vacuum state (Takase *et al.*, 2021).

5.4.3 Superposition between cat state and squeezed vacuum state

In Sec. 5.3.3, we have shown that by adding the displacement beams to the idler path, various superpositions of Fock states can be generated. In particular, by adding the displacement beam to the single-photon-state generation system, the superpositions between the vacuum state and the single-photon state can be realized. In the photon subtraction system, a similar phenomenon occurs when a displacement beam is added to the ancillary mode: a superposition of the cat state and the squeezed vacuum state can be generated. The physical intuition here is also similar: by adding the displacement beam, we cannot distinguish whether the clicks at the photodetector are due to the photons from the initial squeezed states or the displacement beam. This type of state has been generated in Neergaard-Nielsen *et al.* (2010).

One of the interesting things about the superpositions between the minus cat state and the squeezed vacuum state is that they form a qubit. This is because they have a different photon number parity, i.e., the minus cat state is the superposition of the odd photon number Fock states, while the squeezed state is the superposition of the even photon number Fock states. The minus cat state and the plus cat state are a more popular choice for the qubit encoding of the CV system than the minus cat state and the squeezed vacuum state based on the cat state or coherent state (Ralph *et al.*, 2003). The important idea here is that to build qubits and error-correcting code using the CV system, we obviously need non-Gaussian states as all Gaussian states are nonorthogonal to each other as the Wigner functions of the Gaussian states (and their mixed states) are always positive. We will see in the next chapter how to use non-Gaussian states in the quantum error correction.

07 December 2024 17:52:47

REFERENCES

Asavanant, W., Nakashima, K., Shiozawa, Y., Yoshikawa, J. I., and Furusawa, A., "Generation of highly pure Schrödinger's cat states and real-time quadrature measurements via optical filtering," Opt. Express **25**(26), 32227–32242 (2017).

Bartlett, S. D., Sanders, B. C., Braunstein, S. L., and Nemoto, K., "Efficient classical simulation of continuous variable quantum information processes," Phys. Rev. Lett. **88**, 097904 (2002).

Bimbard, E., Jain, N., MacRae, A., and Lvovsky, A. I., "Quantum-optical state engineering up to the two-photon level," Nat. Photon. **4**(4), 243–247 (2010).

Dakna, M., Anhut, T., Opatrný, T., Knöll, L., and Welsch, D. G., "Generating Schrödinger-cat-like states by means of conditional measurements on a beam splitter," Phys. Rev. A **55**, 3184–3194 (1997).

Eisaman, M. D., Fan, J., Migdall, A., and Polyakov, S. V., "Invited review article: Single-photon sources and detectors," Rev. Sci. Instrum. **82**(7), 071101 (2011).

Hashimoto, Y., Toyama, T., Yoshikawa, J., Makino, K., Okamoto, F., Sakakibara, R. *et al.*, "All-optical storage of phase-sensitive quantum states of light," Phys. Rev. Lett. **123**, 113603 (2019).

Heshami, K., England, D. G., Humphreys, P. C., Bustard, P. J., Acosta, V. M., Nunn, J. *et al.*, "Quantum memories: Emerging applications and recent advances," J. Modern Opt. **63**(20), 2005–2028 (2016).

Hong, C. K., Ou, Z. Y., and Mandel, L., "Measurement of subpicosecond time intervals between two photons by interference," Phys. Rev. Lett. **59**, 2044–2046 (1987).

Knill, E., Laflamme, R., and Milburn, G. J., "A scheme for efficient quantum computation with linear optics," Nature **409**(6816), 46–52 (2001).

Lvovsky, A. I., "Iterative maximum-likelihood reconstruction in quantum homodyne tomography," J. Optics B **6**(6), S556–S559 (2004).

Makino, K., Hashimoto, Y., Yoshikawa, J., Ohdan, H., Toyama, T., van Loock, P. *et al.*, "Synchronization of optical photons for quantum information processing," Sci. Adv. **2**(5), (2016).

Miwa, Y., Yoshikawa, J., Iwata, N., Endo, M., Marek, P., Filip, R. *et al.*, "Exploring a new regime for processing optical qubits: Squeezing and unsqueezing single photons," Phys. Rev. Lett. **113**, 013601 (2014).

Morin, O., Fabre, C., and Laurat, J., "Experimentally accessing the optimal temporal mode of traveling quantum light states," Phys. Rev. Lett. **111**, 213602 (2013).

Neergaard-Nielsen, J. S., Nielsen, B. M., Hettich, C., Mølmer, K., and Polzik, E. S., "Generation of a superposition of odd photon number states for quantum information networks," Phys. Rev. Lett. **97**, 083604 (2006).

Neergaard-Nielsen, J. S., Takeuchi, M., Wakui, K., Takahashi, H., Hayasaka, K., Takeoka, M. *et al.*, "Optical continuous-variable qubit," Phys. Rev. Lett. **105**, 053602 (2010).

Ogawa, H., Ohdan, H., Miyata, K., Taguchi, M., Makino, K., Yonezawa, H. *et al.*, "Real-time quadrature measurement of a single-photon wave packet with continuous temporal-mode matching," Phys. Rev. Lett. **116**, 233602 (2016).

07 December 2024 17:52:47

Okamoto, F., Endo, M., Matsuyama, M., Ishizuka, Y., Liu, Y., Sakakibara, R. *et al.*, "Phase locking between two all-optical quantum memories," Phys. Rev. Lett. **125**, 260508 (2020).

Ourjoumtsev, A., Tualle-Brouri, R., Laurat, J., and Grangier, P., "Generating optical Schrödinger kittens for quantum information processing," Science **312**(5770), 83–86 (2006).

Ralph, T. C., Gilchrist, A., Milburn, G. J., Munro, W. J., and Glancy, S., "Quantum computation with optical coherent states," Phys. Rev. A **68**, 042319 (2003).

Su, D., Myers, C. R., and Sabapathy, K. K., "Conversion of Gaussian states to non-Gaussian states using photon-number-resolving detectors," Phys. Rev. A **100**, 052301 (2019).

Sychev, D. V., Ulanov, A. E., Pushkina, A. A., Richards, M. W., Fedorov, I. A., and Lvovsky, A. I., "Enlargement of optical Schrödinger's cat states," Nat. Photon. **11**(6), 379–382 (2017).

Takase, K., Okada, M., Serikawa, T., Takeda, S., Yoshikawa, J., and Furusawa, A., "Complete temporal mode characterization of non-Gaussian states by a dual homodyne measurement," Phys. Rev. A **99**, 033832 (2019).

Takase, K., Yoshikawa, J., Asavanant, W., Endo, M., and Furusawa, A., "Generation of optical Schrödinger cat states by generalized photon subtraction," Phys. Rev. A **103**, 013710 (2021).

Tiunov, E. S., Lvovsky, A. I., and Fedorov, A. K., "Experimental quantum homodyne tomography via machine learning," Optica **7**(5), 448–454 (2020).

Wakui, K., Takahashi, H., Furusawa, A., and Sasaki, M., "Photon subtracted squeezed states generated with periodically poled $KTiOPO_4$," Opt. Express **15**(6), 3568–3574 (2007).

Wang, H., Qin, J., Ding, X., Chen, M. C., Chen, S., You, X. *et al.*, "Boson sampling with 20 input photons and a 60-mode interferometer in a 10^14-dimensional hilbert space," Phys. Rev. Lett. **123**, 250503 (2019).

Weigand, D. J. and Terhal, B. M., "Generating grid states from Schrödinger-cat states without postselection," Phys. Rev. A **97**, 022341 (2018).

Yoshikawa, J., Asavanant, W., and Furusawa, A., "Purification of photon subtraction from continuous squeezed light by filtering," Phys. Rev. A **96**, 052304 (2017).

Yukawa, M., Miyata, K., Mizuta, T., Yonezawa, H., Marek, P., Filip, R. *et al.*, "Generating superposition of up-to three photons for continuous variable quantum information processing," Opt. Express **21**(5), 5529–5535 (2013).

07 December 2024 17:52:47

CHAPTER

6 QUANTUM ERROR CORRECTION IN CONTINUOUS-VARIABLE SYSTEM

6.1 "ANALOG" QUANTUM COMPUTER AND FAULT TOLERANCE

Continuous-variable quantum computation is sometimes associated with an analog computer. The reasons for this lie not only in the fact that the physical quantities, i.e., the quadratures, take continuous values, but also in its formalism. For example, if we look at the input–output relation of the quantum teleportation circuit, we have

$$\hat{x}_{\text{out}} = \hat{x}_{\text{in}} + \sqrt{2}\hat{x}_{\text{vac},1}e^{-r}, \tag{6.1}$$

$$\hat{p}_{\text{out}} = \hat{p}_{\text{in}} + \sqrt{2}\hat{p}_{\text{vac},2}e^{-r}, \tag{6.2}$$

where the second terms on the right are due to the ancillary states. From the perspective of signal processing, the above equations can be interpreted as the output signal (quadrature) being equal to the input signal plus random noise due to the ancillary state. As the quadrature operators of the vacuum state follow Gaussian distribution, the noise terms here can be considered as Gaussian noises. Note that unlike classical signals, the values of the input quadrature operators here are also random and follow probability distributions given by the initial input state.

From the parallelism between CV quantum computation and analog circuit, some readers might be doubtful that it is possible to build a fault-tolerant CV quantum computer; the modern day computers are mostly, if not all, digital computers. This is because it is difficult to manipulate and store analog information faithfully. In principle, manipulation and storage of analog information require infinite precision. Therefore, when analog information is processed, they degrade little by little, until the information becomes unrecognizable.

On the other hand, classical digital computers circumvent these degradations by the "quantization"[1] of the analog information. The conceptual diagram of this process is shown in Fig. 6.1. It is obvious that

[1] Although the same words are used as technical terms, "quantization" here does not mean the quantization of the electromagnetic fields in quantum mechanics, but the digitization of the analog information in computational science.

https://doi.org/10.1063/9780735424074_006

Optical Quantum Computers: A Route to Practical Continuous Variable Quantum Information Processing, W. Asavanant and A. Furusawa
© 2022 AIP Publishing, published by AIP Publishing

07 December 2024 17:52:47

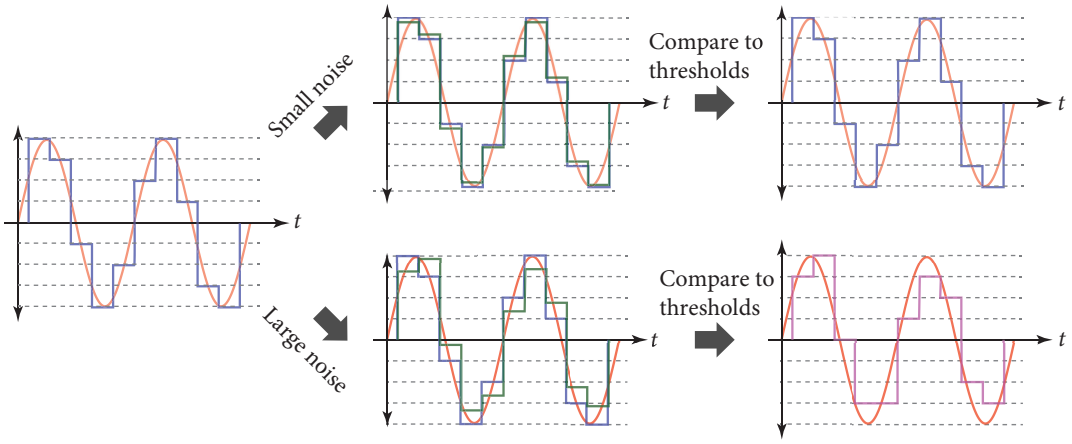

FIG. 6.1
Quantization of classical analog signals. The original signal (red) is compared to the threshold and is digitized (blue). When there are noises, the digitized signal is also changed (green). If the noises are relatively small, by comparing the threshold again, the original signal is recovered. If the noises are large, the recovered signal differs from that of the original one (magenta).

07 December 2024 17:52:47

most of the physical quantities used in the computer (for example, voltages and electrical currents) take continuous values. However, by adding a threshold, we can bin and digitize the information. The powerful thing about digitized information is that even if we do the information processing (for example, manipulating the electrical voltages using circuits) and a small amount of noises are added, as long as the noises are sufficiently small, we can again compare the electrical voltage to the threshold, do the digitization again, and remove the effects of the noises.

Then, the main problem we have to deal with is how to correct the information when the noises are larger than the thresholds. For example, in the usual digital computer, the information is digitized and encoded using a binary number where each bit is either 0 or 1. Then, we should consider how to correct the information when some of the bits flip, i.e., 0 becomes 1 and vice versa. The most basic way is to add redundancy.

For example, instead of using a single bit to represent informational 0 and 1 (which we denote by 0_L and 1_L), we can use three bits, 000 and 111, to represent informational 0 and 1, respectively (Fig. 6.2). To distinguish between the information level and the physical level, the term *logical bit* and *physical bit* are often used. If the probability of having a bit flip for each physical bit is sufficiently low, for most of the time, at most only a single physical bit will flip. Then, by looking at the values of three physical bits and using the majority vote, we can retrieve the logical level information and correct the physical bit that flipped. Of course, there is also a possibility that two or more bits flip and we misidentify the

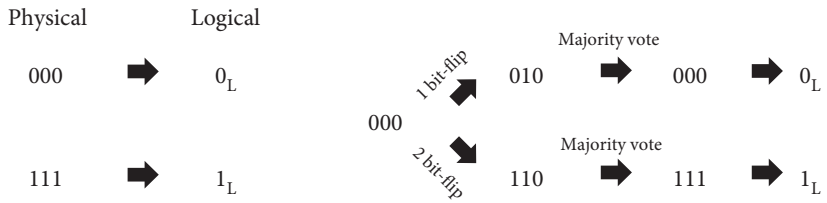

FIG. 6.2
A simple example where three physical bits are used as a single logical bit. This encoding can correct one bit flip. When there are two or more bit flips, the physical-level errors propagate to the logical level.

error, retaining the bit flip errors. Hence, this encoding will be useful only if it reduces the errors on the logical level compared to the physical-level error. The level or the threshold of the physical error that allows a particular encoding to mitigate the error is called *fault-tolerant threshold*.

As a concrete example, let us consider the three physical bits case above. If the probability of bit flip at each physical bit is p, then the probability of misidentifying the error at the logical level p_{err} is given by

$$p_{\text{err}} = 3p^2(1-p) + p^3 = p^2(3-2p). \tag{6.3}$$

For p_{err} to be below the bit flip probability p, this bit flip probability must satisfy $p < p_{\text{th}}$ where p_{th} is the threshold probability where in this case $p_{\text{th}} = 1/2$. On the other hand, if $p > p_{\text{th}}$, then this error encoding results in more logical level errors than the initial physical bit. Therefore, when considering the error correcting code, it is favorable that p_{th} is as high as possible.

Another important aspect of the error correction is how computations are done. For most of the cases, we want to manipulate the information on the logical level. However, the actual actions are done on the physical level. Therefore, a good error correcting code should allow for relatively easy computation on the physical level, in addition to the capability of mitigating the errors.

Up until now, we have kept our discussions to the classical error correction. In the CV quantum computation, the necessary step is similar to the classical error correction; first, as the information in the CV quantum computation is encoded in quadratures and wave functions that give continuous values, we need to "quantize" our information. In the classical case, the quantization (or the digitization) is done on physical quantities. For quantum computation, as the information is encoded on the quantum state, we have to do the digitization on the Hilbert space. In the case of discrete variables or qubits, the Hilbert space is already spanned by $|0\rangle$ and $|1\rangle$. For the CV system, this is usually done by dividing or compartmentalizing the vast CV Hilbert space into subspaces that are mutually orthogonal and consider "qubits" on those subspace. We will show some concrete examples in Sec. 6.2. This process is similar to that of the quantization of the classical analog signals.

07 December 2024 17:52:47

Next, we need to use these *physical qubits* to form *logical qubits* and encodings that allow quantum error correction on the logical level. Unlike the classical computation where bits can be measured as much as we want, we have to be careful about the measurements in the quantum system. Measurements of quantum systems can affect the post-measurement quantum states. As such, the quantum error correction needs to be carefully crafted so that the measurement on logical qubits can reveal the errors without affecting the logical information. Such measurements are called *syndrome measurements*. Note that for the CV system, the term syndrome measurement refers to both measurements to correct the analog errors (similar to Fig. 6.1) and the errors on the logical level (similar to Fig. 6.2). As a measurement on a single qubit or mode usually destroys the coherence or the superposition information, some sort of entangling operations are usually used in the syndrome measurements. After the syndrome measurements, the logical qubits that are moved outside of the logical subspace due to errors are returned to the logical subspace via *recovery operation*. Figure 6.3 summarizes the flow of the quantum error correction in the CV system.

As the CV optical system naturally does not strongly interact with the environment, the most dominant (or maybe the only) source of noise is called Gaussian noise or the Gaussian channel. The Gaussian channel includes optical losses, attenuation channel, amplification channel, and so on. Although we

07 December 2024 17:52:47

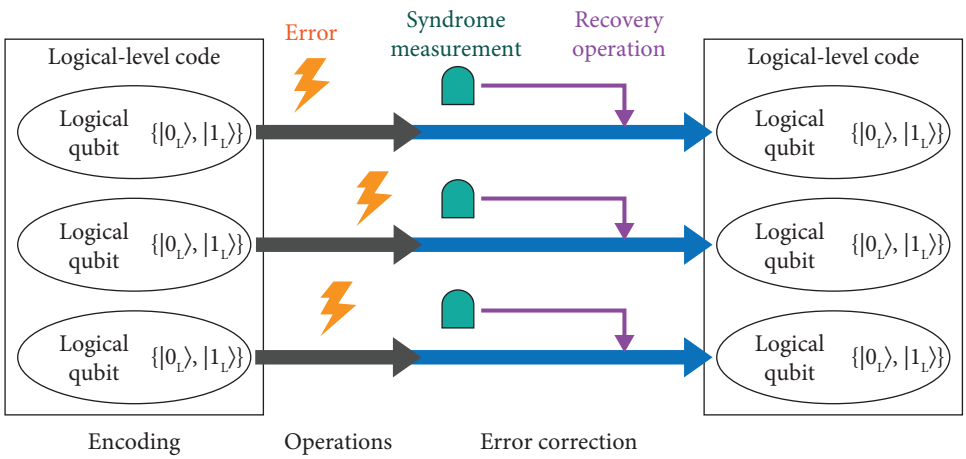

FIG. 6.3
A conceptual diagram of quantum error correction in the CV system. First, a logical subspace within the broad CV Hilbert space is used to encode the logical qubits and these logical qubits are concatenated with a logical-level code. Then, the logical-level operations are implemented by quantum operations on the physical qubits. In this process, there could be some errors that are detected via syndrome measurements and corrected. The quantum error correction must reveal the errors without destroying the coherence, i.e., the quantum states are still encoded in the logical subspace after the quantum error correction.

will not go into the details here, a rough definition of the Gaussian channel is a channel that can be equivalently formulated as a result of only Gaussian resources. Then, for the CV system, we should use an encoding that can protect information against the Gaussian noises. There exists a no-go theorem stating that the effects of the small Gaussian noises cannot be mitigated using only Gaussian components (Niset *et al.*, 2009). As such, the encoding for CV error correction requires non-Gaussian states.

In the encoding of the CV system, although the logical level uses qubits, the actual computations are done at a physical level using CV systems. Thus, it is favorable that the relatively "easy" operations at the logical level, i.e., Clifford operations, can be easily implemented at the physical level. For the CV system, Gaussian operations can be implemented relatively easily and deterministically. Therefore, an encoding that allows the logical-level Clifford operations to be implemented using physical-level Gaussian operations will be a very powerful encoding.

In this chapter, we will first introduce various types of "qubits" in the CV system. As this subject is very broad, we only pick some of the nominal examples of the qubits. Then, we focus mainly on the Gottesman–Kitaev–Preskill (GKP) qubit (Gottesman *et al.*, 2001) and discuss how to do the operations and how to implement syndrome measurements and error corrections using GKP qubits. GKP qubit is currently one of the most promising and widely studied encodings in the CV systems due to many of its traits and characteristics, which we will see in detail later. We will also be discussing some of the experiments (or experimental proposals) to generate the GKP qubits. At the end of this chapter, we will also discuss how the analog information at the physical level can also be used in the quantum error correction at the logical level (Fukui *et al.*, 2018). This property is, in a manner of speaking, unique to the CV system where the quantities of interest at the physical level takes continuous values, while those at the logical level take discretized values.

07 December 2024 17:52:47

6.2 EXAMPLES OF LOGICAL QUBITS IN THE CV OPTICAL SYSTEM

In this section, we will look at some examples of the logical qubits in the CV optical system. Here, we will mainly show how to encode the information and how do these encodings protect against noises.

6.2.1 Qutrit

As the dominant form of noises in the CV optical system is the optical loss, here we will show a code that can protect against a single-photon loss (Chuang *et al.*, 1997). In this encoding, information is digitized in a form $|\psi\rangle = a|0_L\rangle + b|1_L\rangle$, where $|0_L\rangle$ and $|1_L\rangle$ are the logical qubits given by

$$|0_L\rangle = \frac{1}{\sqrt{2}}(|0\rangle \otimes |4\rangle + |4\rangle \otimes |0\rangle), \tag{6.4}$$

$$|1_L\rangle = |2\rangle \otimes |2\rangle. \tag{6.5}$$

For this system, when there is a small loss probability L on each mode, the first (unnormalized) order term is given by

$$|\psi_{00}\rangle \propto |\psi\rangle, \tag{6.6}$$

which corresponds to the case where there is no optical loss. For the case where there is a single-photon loss, the output state is given by

$$|\psi_{01}\rangle \propto a\,|0\rangle \otimes |3\rangle + b\,|2\rangle \otimes |1\rangle, \tag{6.7}$$
$$|\psi_{10}\rangle \propto a\,|3\rangle \otimes |0\rangle + b\,|1\rangle \otimes |2\rangle, \tag{6.8}$$

where $|\psi_{10}\rangle$ ($|\psi_{01}\rangle$) corresponds to the case with single-photon loss from the first (second) mode. Note that for here, we will ignore higher order terms. From this example, we notice the following. First, even after the single-photon loss, the new bases on which the information regarding a and b are encoded remain orthogonal. Even after the bases are changed, information on coefficients is still the same as their ratios and phase information are not changed by the photon loss. Moreover, for any arbitrary initial state $|\psi\rangle$, the resulting states $|\psi_{00}\rangle$, $|\psi_{01}\rangle$, and $|\psi_{10}\rangle$ are mutually orthogonal. Therefore, if we can detect which subspace the state is in without directly revealing the quantum state, then it is possible to implement a unitary transformation to return the state to the initial state. This, in a way, is similar to the description in the previous section where we discuss the fact that by digitizing the analog information, it is possible to add tolerance to the noises.

From this example, one might be tempted to use any Fock basis. For example, we might want to use $|0_{\mathrm{L}}\rangle = |1\rangle$ and $|1_{\mathrm{L}}\rangle = |2\rangle$ as our encoding which seems, at the first glance, to be usable as a Bosonic code against a single-photon loss. We will show below that this is, in fact, not the case. To illustrate the effect of the optical losses, let us added another ancillary vacuum state for losses. Then, we can show that when there is optical loss, the state is transformed to

$$\begin{aligned}(a\,|1\rangle + b\,|2\rangle) \otimes |0\rangle_{\mathrm{anc}} \to{}& \sqrt{1-L}\left(a\,|1\rangle + b\sqrt{1-L}\,|2\rangle\right) \otimes |0\rangle_{\mathrm{anc}} \\ &+ \sqrt{L}\left(a\,|0\rangle + b\sqrt{1-L}\,|1\rangle\right) \otimes |1\rangle_{\mathrm{anc}} + bL\,|0\rangle \otimes |2\rangle_{\mathrm{anc}}.\end{aligned} \tag{6.9}$$

The ancillary mode will be traced out and cannot be detected. Unlike the previous example, even if we ignore the last term that corresponds to a two-photon loss, the state of our interest in the first term and the second term on the right are not orthogonal. Therefore, in principle, we cannot have a measurement that can ideally distinguish these two subspaces. Moreover, the ratio of the superposition coefficients is dependent on the level of the loss, meaning that unless we have sufficient knowledge regarding the noise channel, it is not so easy to return the state from the photon loss.

This simple example illustrates that it is important that the logical subspace and the subspace after the noises occur are mutually orthogonal or sufficiently distinguishable. Note that the above example can be further generalized to protect against more photon losses as well (Bergmann and van Loock, 2016).

07 December 2024 17:52:47

6.2.2 Coherent state encoding

As we are using the CV system, another type of encoding that we might be tempted to implement is an encoding using coherent states (Ralph *et al.*, 2003). Coherent state quantum computation uses the logical qubits

$$|0_{\mathrm{L}}\rangle = |\alpha\rangle, \tag{6.10}$$

$$|1_{\mathrm{L}}\rangle = |-\alpha\rangle, \tag{6.11}$$

where $|\alpha\rangle$ and $|-\alpha\rangle$ are coherent states and α in general is a complex number. Note that because coherent states are nonorthogonal, these logical qubits are also nonorthogonal, i.e., $|\langle\alpha| - \alpha\rangle|^2 = \exp(-4\alpha^2)$. For a sufficiently large α (which is usually taken as $\alpha \geq 2$), however, they can be approximately orthogonal. We can also consider the superposition of the coherent states (the cat states), which gives orthogonal qubits, but as we will see, this is equivalent to the implementation of the Hadamard gate on our logical qubits here.

To show photon loss act on the coherent state encoding, we first recall that the beamsplitter interaction transforms the coherent states as follows:

$$\hat{B}(\sqrt{R})\,|\alpha_1\rangle \otimes |\alpha_2\rangle = \left|\sqrt{R}\alpha_1 + \sqrt{T}\alpha_2\right\rangle \otimes \left|\sqrt{R}\alpha_2 - \sqrt{T}\alpha_1\right\rangle. \tag{6.12}$$

Then, applying this to coherent-encoded logical qubit, we have

$$\begin{aligned}&(a\,|0_{\mathrm{L}}\rangle + b\,|1_{\mathrm{L}}\rangle) \otimes |0\rangle_{\mathrm{anc}} \\ &\quad \to a\left|\sqrt{1-L}\alpha\right\rangle \otimes \left|-\sqrt{L}\alpha\right\rangle_{\mathrm{anc}} + b\left|-\sqrt{1-L}\alpha\right\rangle \otimes \left|\sqrt{L}\alpha\right\rangle_{\mathrm{anc}}.\end{aligned} \tag{6.13}$$

For a sufficiently small $|\sqrt{L}\alpha|$, we can do an approximation:

$$\left|\pm\sqrt{L}\alpha\right\rangle \approx |0\rangle \pm \sqrt{L}\alpha\,|1\rangle. \tag{6.14}$$

Therefore, the right-hand side of Eq. (6.13) becomes

$$\left(a\left|\sqrt{1-L}\alpha\right\rangle + b\left|-\sqrt{1-L}\alpha\right\rangle\right) \otimes |0\rangle_{\mathrm{anc}} - \sqrt{L}\alpha\left(a\left|\sqrt{1-L}\alpha\right\rangle - b\left|-\sqrt{1-L}\alpha\right\rangle\right) \otimes |1\rangle_{\mathrm{anc}}. \tag{6.15}$$

Equation (6.15) indicates that for coherent state encoding, the photon loss results in amplitude damping of the coherent state, along with a small probability of sign-flip errors (the so-called Pauli-Z error). By concatenating with a code to protect against sign-flip error, the error due to the photon loss on the physical level can be mitigated. One of the problems with this encoding is that, although we require α to be large so that our logical qubits are orthogonal, a large α also translates to a large error probability.

Regarding the operations on the coherent-state-encoded logical qubits, the Pauli-X gate (the bit flip) can be implemented relatively easily by using π phase rotation. On the other hand, the Pauli-Z gate (the sign flip) is relatively difficult and requires the quantum teleportation using cat-state Bell

07 December 2024 17:52:47

pairs. The most problematic gate is the Hadamard gate that takes the basis $\{|0_L\rangle, |1_L\rangle\}$ to the basis $\{|+_L\rangle, |-_L\rangle\}$, which can be written as

$$|+_L\rangle \propto |\alpha\rangle + |-\alpha\rangle, \tag{6.16}$$
$$|-_L\rangle \propto |\alpha\rangle - |-\alpha\rangle. \tag{6.17}$$

As we can see, the transformation between the basis $\{|0_L\rangle, |1_L\rangle\}$ to the basis $\{|+_L\rangle, |-_L\rangle\}$ does not preserve norm, meaning that this transformation must be non-unitary. Non-unitary transformation in quantum mechanics implies probabilistic transformations, meaning that the Hadamard gate in this encoding can be implemented only probabilistically.

6.3 GOTTESMAN–KITAEV–PRESKILL QUBIT

Now that we have looked at two types of logical qubits, we will turn our attention to the Gottesman–Kitaev–Preskill (GKP) qubits (Gottesman *et al.*, 2001), which will be our main subject for the rest of this chapter. As we have mentioned in Sec. 6.1, quantum error correction in the CV system involves some kind of "quantization" of our Hilbert space. In the previous examples, the discretization is achieved by using either the Fock basis or the coherent state basis. As our quantities of interest are the quadrature $\hat{x}$ and $\hat{p}$, we should also consider the discretization of the quadrature values. Using the unit where $\hbar = 1$, the logical basis of the GKP qubit is defined as follows.

Definition 6.1. The basis of the GKP qubit $|0_L\rangle$ and $|1_L\rangle$ is given in the quadrature basis by

$$|0_L\rangle = \sum_{s=-\infty}^{\infty} \left|x = 2s\sqrt{\pi}\right\rangle = \sum_{s=-\infty}^{\infty} \left|p = s\sqrt{\pi}\right\rangle, \tag{6.18}$$
$$|1_L\rangle = \sum_{s=-\infty}^{\infty} \left|x = (2s+1)\sqrt{\pi}\right\rangle = \sum_{s=-\infty}^{\infty} (-1)^s \left|p = s\sqrt{\pi}\right\rangle, \tag{6.19}$$

where the summations over s are summations over integers, and $|x\rangle$ and $|p\rangle$ are the quadrature eigenvector of x and p quadrature, respectively.

The wave functions and the Wigner functions of various bases of the GKP states are shown in Fig. 6.4. For the derivations, see Appendix A. In both the x and p basis, the wave functions of the GKP qubits are periodic delta functions.

From Eqs. (6.18) and (6.19), it is obvious that any superposition $|\psi\rangle = a|0_L\rangle + b|1_L\rangle$ is the translational invariant in both x and p directions for a displacement of an integer time of $2\sqrt{\pi}$. In other words, any $|\psi\rangle$ encoded with GKP is *stabilized* by the operators

$$\hat{S}_x = \exp(-i2\sqrt{\pi}\hat{p}), \tag{6.20}$$
$$\hat{S}_p = \exp(i2\sqrt{\pi}\hat{x}). \tag{6.21}$$

07 December 2024 17:52:47

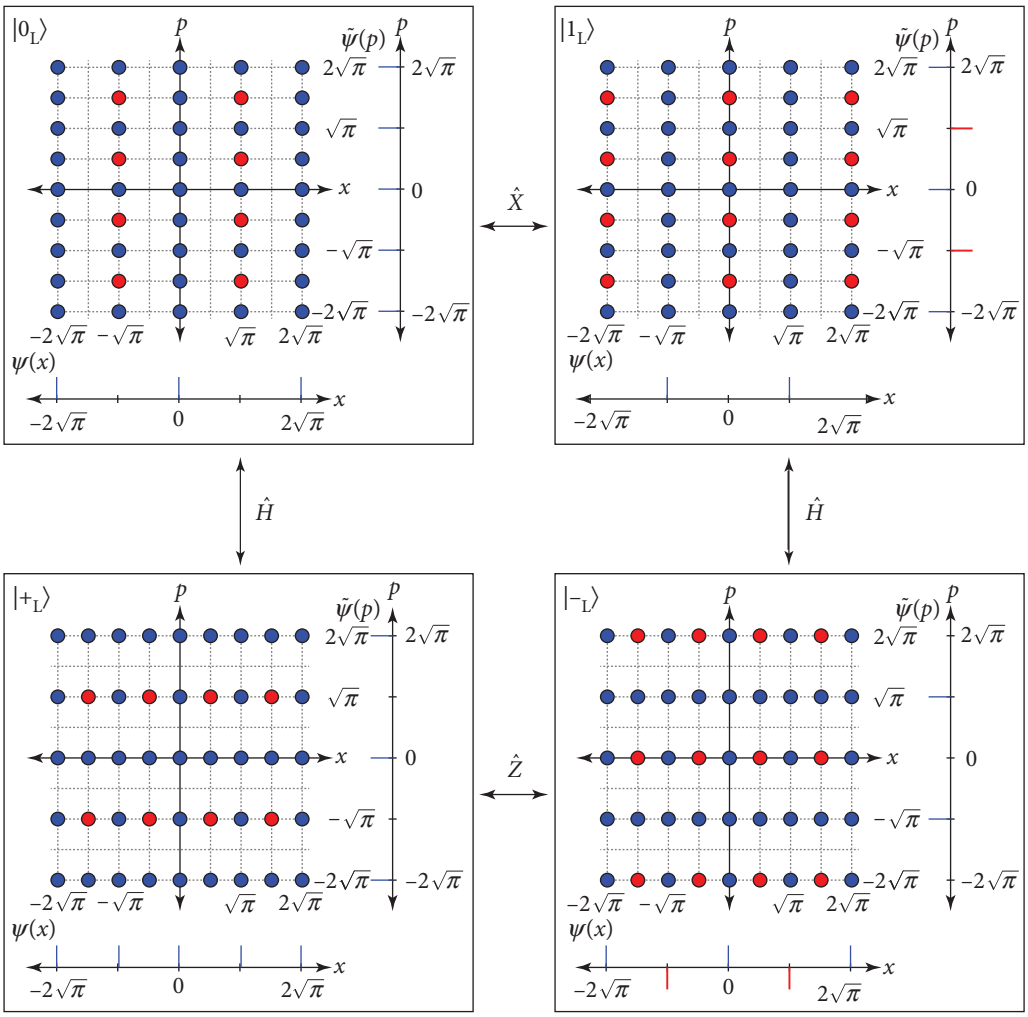

FIG. 6.4
Various bases of GKP qubit. The blue (red) dots are positive (negative) delta function peaks.

We note that as $[\hat{S}_x, \hat{S}_p] = 0$, there exist simultaneous eigenvectors of both operators. This is the concept of the *stabilizer formalism* where instead of using the basis vector, operators called stabilizers are used to show the logical subspace where the information is encoded. Stabilizer formalism is one of the basic tools in describing the quantum error corrections, and we refer the readers to, for example, Nielsen and Chuang (2000) for more details on stabilizers.

07 December 2024 17:52:47

To see how GKP qubits digitize the Hilbert space, let us consider a simple example of the measurement of x quadrature on $|0_L\rangle$. For an ideal $|0_L\rangle$, if we do the x quadrature measurement, our measurement results will be a multiple of $2\sqrt{\pi}$. Conversely, if we do the x quadrature measurement and find that the measurement result is a multiple of $2\sqrt{\pi}$, then the digital information we obtain is the logical 0. Now, let us consider the case where there is a small displacement. The source of the small displacement could be, for example, Gaussian noises due to finite squeezing of the cluster states if the cluster states are used to implement operations on the GKP qubits. In such a case, our measurement results would most likely be near the multiple of $2\sqrt{\pi}$, but slightly shifted. If the shifts are sufficiently small, i.e., closer to the peaks of $|0_L\rangle$ than that of $|1_L\rangle$, we would still conclude that the digital information we obtain is 0. In a rare case where the shifts are large, we would wrongly conclude that the digital information is 1. As such, we would need another level of *concatenation* to deal with these large shifts, even after we digitize the Hilbert space.

In the previous paragraph, we have discussed how GKP qubits help digitize the measurement results. As the quantum information lies in the superposition coefficients, however, we need to be able to mitigate the effects of the small displacements, i.e., the diffusion noises, without directly measuring the quantum states.

07 December 2024 17:52:47

6.3.1 Operations and error corrections on GKP qubit

In this section, we will discuss how to implement logical-qubit-level operations and measurements on the GKP qubits. We will also discuss what the physical GKP qubit looks like, as Eqs. (6.18) and (6.19) are obviously unphysical states and unnormalizable. At the end, we will show how to do the error correction on the GKP qubits.

6.3.1.1 Clifford operations

First, let us consider the logical-level Clifford operations. As a reminder, the logical-level Pauli-Z gate $\hat{Z}$, Pauli-X gate $\hat{X}$, Hadamard gate $\hat{H}$, and phase gate $\hat{P}$ form a universal gate set for single-qubit clifford operations, and they transform the logical qubits as

$$\hat{Z} : a|0_L\rangle + b|1_L\rangle \to a|0_L\rangle - b|1_L\rangle, \tag{6.22}$$
$$\hat{X} : a|0_L\rangle + b|1_L\rangle \to b|0_L\rangle + a|1_L\rangle, \tag{6.23}$$
$$\hat{H} : a|0_L\rangle + b|1_L\rangle \to a|+_L\rangle + b|-_L\rangle, \tag{6.24}$$
$$\hat{P} : a|0_L\rangle + b|1_L\rangle \to a|0_L\rangle + ib|1_L\rangle, \tag{6.25}$$

where $|+_L\rangle$ and $|-_L\rangle$ are defined as follows.

Definition 6.2. Another set of basis of the GKP qubits, $|+_L\rangle$ and $|-_L\rangle$, are given by

$$|+_L\rangle = \sum_{s=-\infty}^{\infty} |x = s\sqrt{\pi}\rangle = \sum_{s=-\infty}^{\infty} |p = 2s\sqrt{\pi}\rangle, \tag{6.26}$$

$$|-_{\mathrm{L}}\rangle = \sum_{s=-\infty}^{\infty} (-1)^s \left|x = s\sqrt{\pi}\right\rangle = \sum_{s=-\infty}^{\infty} \left|p = (2s+1)\sqrt{\pi}\right\rangle. \tag{6.27}$$

Based on Definition 6.2, we can write a set of operations that generate arbitrary Clifford operations on the GKP qubits as

$$\hat{Z} = \exp(-i\sqrt{\pi}\hat{x}), \tag{6.28}$$

$$\hat{X} = \exp(i\sqrt{\pi}\hat{p}), \tag{6.29}$$

$$\hat{H} = \exp\left(i\frac{\pi}{2}\hat{a}^\dagger\hat{a}\right), \tag{6.30}$$

$$\hat{P} = \exp\left(\frac{i}{2}\hat{x}^2\right). \tag{6.31}$$

Note that as GKP qubits have translational symmetry, the above operations are not unique. We can see that the Pauli-Z gate and Pauli-X gate are simply displacements of $\sqrt{\pi}$ in p and x quadrature, respectively. This is rather obvious when we look at the Wigner functions in Fig. 6.4. The Hadamard gate, which is the transformation between the basis $\{|0_{\mathrm{L}}\rangle, |1_{\mathrm{L}}\rangle\}$ and $\{|+_{\mathrm{L}}\rangle, |-_{\mathrm{L}}\rangle\}$, is a Fourier transformation, i.e., a 90° rotation on phase space. This is also obvious from the Wigner functions of the GKP qubits. For the phase gate, as we want additional phase factor of i in front of $|1_{\mathrm{L}}\rangle$ which has peaks at the places where the x quadratures are odd multiples of $\sqrt{\pi}$, we can use the shear operation to add the differences between the odd and the even multiples of $\sqrt{\pi}$.

To implement multi-qubit Clifford operations, we have to add two-qubit gates. One of the main examples is the logical level controlled-NOT gate $\hat{C}_{\mathrm{NOT}}$, which transforms the logical qubits as

$$\begin{aligned}\hat{C}_{\mathrm{NOT}} : {} & c_{00}|0_{\mathrm{L}}\rangle \otimes |0_{\mathrm{L}}\rangle + c_{01}|0_{\mathrm{L}}\rangle \otimes |1_{\mathrm{L}}\rangle + c_{10}|1_{\mathrm{L}}\rangle \otimes |0_{\mathrm{L}}\rangle + c_{11}|1_{\mathrm{L}}\rangle \otimes |1_{\mathrm{L}}\rangle \\ & \to c_{00}|0_{\mathrm{L}}\rangle \otimes |0_{\mathrm{L}}\rangle + c_{01}|0_{\mathrm{L}}\rangle \otimes |1_{\mathrm{L}}\rangle + c_{11}|1_{\mathrm{L}}\rangle \otimes |0_{\mathrm{L}}\rangle + c_{10}|1_{\mathrm{L}}\rangle \otimes |1_{\mathrm{L}}\rangle.\end{aligned} \tag{6.32}$$

This gate induces Pauli-X gate on the second qubit only when the first qubit is $|1_{\mathrm{L}}\rangle$. Then, we could write down the controlled-NOT gate as

$$\hat{C}_{\mathrm{NOT}} = \exp(-i\hat{x}_1 \otimes \hat{p}_2), \tag{6.33}$$

which is the quantum nondemolition gate or SUM gate which we introduced in Chap. 2. The intuition for this is as follows. Depending on whether the first qubit is $|0_{\mathrm{L}}\rangle$ or $|1_{\mathrm{L}}\rangle$, when we act $\hat{C}_{\mathrm{NOT}}$ on the qubits, the operator $\hat{x}$ will take either even or odd multiple of $\sqrt{\pi}$. When $\hat{x}$ is the even multiple, the $\hat{C}_{\mathrm{NOT}}$ operator is simply equivalent to the stabilizer in Eq. (6.20) and does not change the qubit. On the other hand, when $\hat{x}$ is the odd multiple, this $\hat{C}_{\mathrm{NOT}}$ becomes equivalent to the Pauli-X gate in Eq. (6.29) (with additional displacement that is just the stabilizer part).

From the aforementioned results, we can summarize the important feature of the Clifford operations on GKP qubits below:

Theorem 6.1. *Arbitrary multi-qubit Clifford operations on the GKP qubits can be implemented using only multimode Gaussian operations.*

07 December 2024 17:52:47

This feature makes the GKP qubit one of the most powerful encodings for the optical quantum computer; the logical-qubit-level Clifford operations are implemented via Gaussian operations that can be (relatively) easy to implement deterministically on the optical system. In addition, as the large-scale cluster states that can be used to easily implement multimode Gaussian operations have been demonstrated in optical systems (Asavanant *et al.*, 2019; and Larsen *et al.*, 2019), the GKP qubit is a very appealing choice as the logical qubit in the optical system.

6.3.1.2 Measurements

When doing the computations on the logical level, at the end of the computation, we would want to do the projection measurement on either the basis $\{|0_L\rangle, |1_L\rangle\}$ or $\{|+_L\rangle, |-_L\rangle\}$. Although we briefly discussed this in Sec. 6.3 already, let us summarize this again here. For the GKP qubit, projection measurements on the eigenvectors of the Pauli-X and Pauli-Z operators can be done via homodyne measurement (Fig. 6.5):

Theorem 6.2. *Measurements on $\{|0_L\rangle, |1_L\rangle\}$ basis. By doing the homodyne measurement on x quadrature and obtaining the measurement values m_x, the logical level information a_L (which is either 0 or 1) is given by $a_L = \frac{m_x}{\sqrt{\pi}} \pmod 2$. For the measurement on $\{|+_L\rangle, |-_L\rangle\}$, the same procedure is used, where the measured quadrature is p.*

Using homodyne measurements for the qubit-level measurement is relatively easy to understand if we look at the wave function in the quadrature x of the basis $\{|0_L\rangle, |1_L\rangle\}$ and $\{|+_L\rangle, |-_L\rangle\}$. In this sense, encoding in GKP qubits also implies the digitization of the quadrature values as well. As the homodyne measurements can be easily implemented on the optical system, projection measurements are also relatively easy tasks for the GKP qubit. This is in contrast to, for example, coherent state encoding in

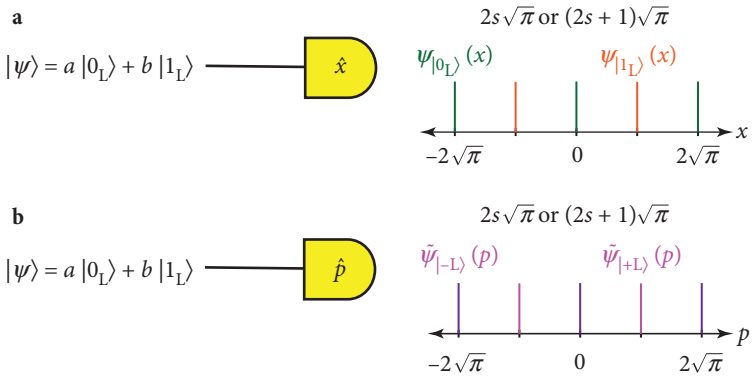

FIG. 6.5
Measurements in GKP basis (a) $\{|0_L\rangle, |1_L\rangle\}$ and (b) $\{|+_L\rangle, |-_L\rangle\}$ using homodyne measurements.

07 December 2024 17:52:47

Sec. 6.2.2 where measurements that distinguish cat states of different parity or coherent states with different phases are needed.

6.3.1.3 Non-Clifford operations

To implement universal quantum computation on the logical qubit, non-Clifford operations are also necessary. As an example of the non-Clifford gate, we consider the implementation of the $\pi/8$ phase gate $\hat{T}$, which transforms the qubit as

$$\hat{T} : a|0_L\rangle + b|1_L\rangle \rightarrow a|0_L\rangle + b\exp\left(i\frac{\pi}{4}\right)|1_L\rangle. \tag{6.34}$$

In the particular case of the GKP qubits, two methodologies to realize $\hat{T}$ have been proposed.

The first methodology utilizes the cubic phase gate. For example, we consider a unitary operation of a form

$$\hat{U} = \exp\left[i\left(c_3\hat{x}^3 + c_2\hat{x}^2 + c_1\hat{x}\right)\right] \tag{6.35}$$

for $c_1, c_2, c_3 \in \mathbb{R}$. With the right parameters, we should be able to implement the $\pi/8$ phase gate where the phases are added only to the peaks that are odd multiples of $\sqrt{\pi}$. In the original GKP paper, they showed one of the possible parameters for Eq. (6.35). However, recently it has been shown that those parameters do not give a sufficiently good performance as a non-Clifford gate when physical GKP qubits (see Sec. 6.3.1.5) are considered (Hastrup *et al.*, 2021).

The second methodology is based on the qubit version of the gate teleportation protocol (Gottesman and Chuang,1999) and is shown in Fig. 6.6. In this method, besides the ancillary state given by $|\psi_{anc}\rangle = \hat{T}|+_L\rangle$, the required components are Clifford operations, measurements on the basis $\{|0_L\rangle, |1_L\rangle\}$, and feedforward operations. In terms of the physical realizations, this means that if we can generate the ancillary states, the rest of the required components are Gaussian operations and homodyne measurements.

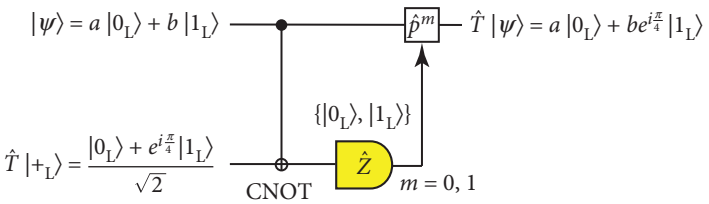

FIG. 6.6
Implementation of the $\pi/8$ gate using qubit gate teleportation. For GKP qubits, all components besides the ancillary state are Gaussian.

07 December 2024 17:52:47

6.3.1.4 Error correction

When an arbitrary quantum state encoded using GKP qubits $|\psi\rangle = a|0_L\rangle + b|1_L\rangle$ and there is a small displacement noise, we wish to detect the amount of the displacement noise without destroying the coherence between $|0_L\rangle$ and $|1_L\rangle$. To achieve this, the syndrome measurement and correction is implemented using the circuit shown in Fig. 6.7.

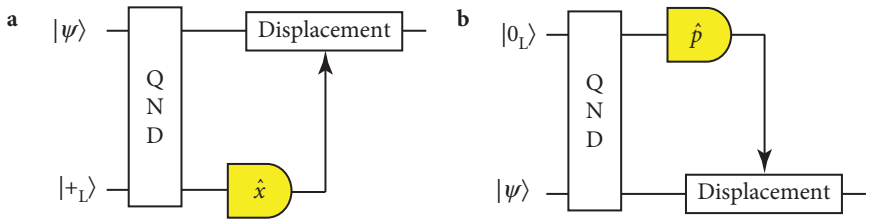

FIG. 6.7
Circuit for syndrome measurement and error correction for displacement in (a) *x* quadrature and (b) *p* quadrature using quantum nondemolition (QND) interaction, homodyne measurement, and displacement operation.

To illustrate the idea of the error correction using GKP qubits, let us consider the circuit in Fig. 6.7(a) using the Heisenberg picture. We denote mode "1" as the input GKP encoded state $|\psi\rangle = a|0_L\rangle + b|1_L\rangle$, and mode "anc" as the ancillary $|+_L\rangle$ state. The transformation of the quadrature operator after the quantum nondemolition gate is

$$\hat{x}_1' = \hat{x}_1, \tag{6.36}$$
$$\hat{p}_1' = \hat{p}_1 - \hat{p}_{\text{anc}}, \tag{6.37}$$
$$\hat{x}_{\text{anc}}' = \hat{x}_{\text{anc}} + \hat{x}_1, \tag{6.38}$$
$$\hat{p}_{\text{anc}}' = \hat{p}_{\text{anc}}. \tag{6.39}$$

Now, let us consider what happens when we measure $\hat{x}_{\text{anc}}'$. For any arbitrary initial state $|\psi\rangle$, if there are no displacement noises, $\hat{x}_1$ will take the values of $s\sqrt{\pi}$, where $s \in \mathbb{I}$. For $|+_L\rangle$, it is also evident from Eq. (6.26) that the measurement of $\hat{x}_{\text{anc}}$ would result in $s'\sqrt{\pi}$ where $s' \in \mathbb{I}$. Therefore, when $\hat{x}_{\text{anc}}'$ is measured, the obtained quadrature values will be $s''\sqrt{\pi}$ where $s'' \in \mathbb{I}$. This measurement does not reveal the individual values of $\hat{x}_1$ and $\hat{x}_{\text{anc}}$. Suppose that due to some reasons (such as noises in the computations), there are some displacements that can be written using an operator $\hat{\delta}$ added to mode 1 before we do the syndrome measurement. Then, the measurement results of $\hat{x}_{\text{anc}}'$ will no longer be $s''\sqrt{\pi}$, but will become $m = s''\sqrt{\pi} + \delta$.

From the measurement result m, we try to infer the value δ. Note that in principle, δ takes random values that follow a probability distribution dictated by the property of the noise. Through the syndrome measurement, in a way, we fix the values of δ and reveal the errors. There is, however, an ambiguity

07 December 2024 17:52:47

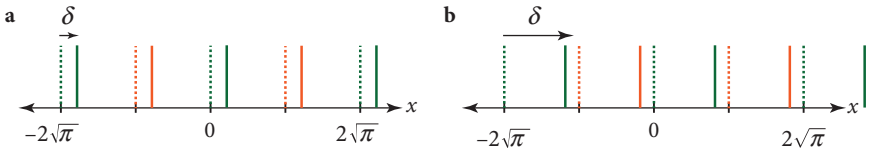

FIG. 6.8
When the shifts δ are small, the syndrome measurements will predict correct displacements as the shifted peaks (solid lines) are near the original position (a). When the shifts are large, however, the shifted peaks will be nearer to the peaks with different parity, resulting in the bit flip error after the syndrome measurement and recovery operations (b).

regarding how to determine δ, which is shown in Fig. 6.8. As the measurement result m should be equal to $s''\sqrt{\pi}$, we could look at the distance from the nearest peak. For $|\delta| < \sqrt{\pi}/2$, this gives us a correct value of δ. On the other hand, for $|\delta| > \sqrt{\pi}/2$, we will instead predict the wrong amount of displacement. When we correct the displacement using this wrong displacement, it will result in additional $\sqrt{\pi}$ shift, i.e., the Pauli-X error.

If we look at the output mode, however, we observe that the quadrature $\hat{p}_1'$ is changed from the original $\hat{p}_1$ due to the ancillary state. As our ancillary state is $|+_L\rangle$, however, this does not change the peak position in p quadrature as $\hat{p}_{\text{anc}}$ takes values of even multiples of $\sqrt{\pi}$. This fact is important as the syndrome measurement will be not so useful if syndrome measurement in one quadrature induces errors in another quadrature.

For the circuit for correcting p quadrature, the analysis is also the same and for a large displacement in p, the error correction will result in Pauli-Z error. Therefore, by using the GKP qubits, we can correct small displacement errors and for the large displacement error, the "analog" displacement error is transformed into the Pauli error on the logical level. Hence, by adding (concatenating) another level of encoding that can deal with Pauli error, we can mitigate the effects of the physical-level errors.

Experimentally, as beamsplitter interaction is much easier to implement than the QND interaction, it is important to consider whether we could simplify the QND interaction into something simpler. In terms of back action, as the beamsplitter interaction couples both x quadrature and p quadrature, it is expected that we would require some squeezing to evade this back action. Nevertheless, it is important from the experimental point of view that the syndrome measurement and the recovery operation can be easily and accurately implemented.

6.3.1.5 Physical GKP qubits

We have assumed the ideal GKP states with delta function peaks. As these GKP states are unphysical, we have to consider the physical or the approximated version of the GKP states. There are various [but

07 December 2024 17:52:47

equivalent (Matsuura *et al.*, 2020)] approximations of the GKP states, but here we will consider the approximated GKP qubits $|0_\Delta\rangle$ and $|1_\Delta\rangle$ which are defined as follows.

Definition 6.3. Basis of the physical GKP qubits, $|0_\Delta\rangle$ and $|1_\Delta\rangle$ are given by

$$|0_\Delta\rangle \propto \sum_{s=-\infty}^{\infty} \exp\left[-\pi(2s)^2\Delta^2\right] \int_{-\infty}^{\infty} dx \exp\left[-\frac{(x-2s\sqrt{\pi})^2}{4\Delta^2}\right]|x\rangle, \tag{6.40}$$

$$|1_\Delta\rangle \propto \sum_{s=-\infty}^{\infty} \exp\left[-\pi(2s+1)^2\Delta^2\right] \int_{-\infty}^{\infty} dx \exp\left[-\frac{(x-(2s+1)\sqrt{\pi})^2}{4\Delta^2}\right]|x\rangle, \tag{6.41}$$

where Δ^2 is the variance of each peak and $1/\Delta^2$ is the variance of the Gaussian envelope.

Figure 6.9 shows the wave functions of these physical GKP qubits. In this approximated version of the GKP qubits, each delta function peak is now replaced by displaced x-squeezed states and they are then weighted by a Gaussian envelope. The approximation in Eqs. (6.40) and (6.41) means that the physical GKP qubits are the superpositions of the displaced squeezed vacuum states. In the limit where $\Delta \to 0$, each peak becomes infinitesimally small and the envelope becomes infinitely broad, making the state approaching the ideal GKP states.

In the physical limit, however, we observe that the wave functions are no longer translational invariant. As such, in a strict manner, the operations in Sec. 6.3.1, no longer holds. For example, displacement in x by $\sqrt{\pi}$ does not transform $|0_\Delta\rangle$ to $|1_\Delta\rangle$. Even then, Gaussian operations on physical GKP qubits correspond to (noisy) logical-level Clifford operations. We also have to consider whether encoding using these approximated GKP states allows fault-tolerant quantum computation. The main difference between the ideal GKP states and the approximated GKP states is that even without the displacement noise, there is a finite probability that when we measure $|0_\Delta\rangle$, we misidentify it as $|1_\Delta\rangle$ and vice versa. This is due to the finite size of the peak, which means that even if the state is $|0_\Delta\rangle$, we might get a measurement result that is close to $(2s+1)\sqrt{\pi}$. We might be tempted to, for example, make a GKP qubits that, even with finite peak widths, is contained within the bins of our interest. However, this is not necessarily the best strategy as containing the peak in, for example, x-quadrature basis would result in a broadening in the peak width in the p-quadrature basis.

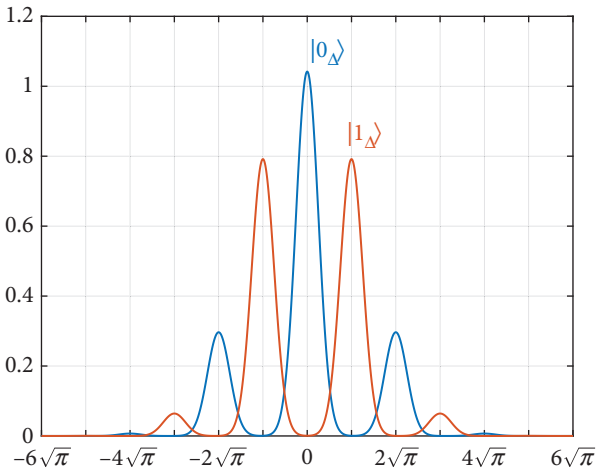

FIG. 6.9
Wave functions of physical GKP qubits with $\Delta^2 = 0.1$.

07 December 2024 17:52:47

To show the error correction using the physical GKP qubits, let us consider again the circuit in Fig. 6.7, but this time with the physical GKP qubits instead of the ideal GKP qubits. In such a case, as the physical GKP qubits are parametrized by the peak positions and distribution near the peak, it is convenient to write the quadrature operator as

$$\hat{x} = \hat{x}_{\text{peak}} + \hat{\sigma}, \tag{6.42}$$

where $\hat{x}_{\text{peak}}$ is the peak position that takes discrete values and $\hat{\sigma}$ shows the distribution around the peak. The same can be done for p quadrature. With this image in mind, it can be shown that when quantum states encoded using physical GKP qubits go through a noisy quantum operation (for example, CV quantum teleportation with finite squeezing resources), the additional noise increases the peak width. This effect is somewhat obvious when we use the Heisenberg picture, which shows the noise term being added to the quadrature operator. By using the circuit in Fig. 6.7 and doing a similar calculation to Sec. 6.3.1.4, we can easily show that, if we prepare "clean" ancillary states, even with a finite peak width, we can reduce the width of the peaks of the noisy GKP states to that of the clean ancillary state, at a cost of having some logical level Pauli error. The Pauli error here is not only due to the external displacement noise, but also due to the finite peak width of the GKP qubits. As such, by adding (or concatenating) another level of encoding, the Pauli error can be reduced if the initial error probability is sufficiently low.

6.3.1.6 Fault-tolerant quantum computation with GKP qubits

In the CV quantum computation using GKP qubits, in addition to the imperfection of the physical GKP qubits, we also have noise from the non-ideal computation. One of the main sources of the imperfection comes from the finite squeezing of the squeezed lights. Squeezed lights are indispensable resources for CV quantum computation and the universal resource states called cluster states are generated via squeezed lights and linear optics. As it is impossible to achieve perfect squeezing even theoretically, however, fault-tolerant CV quantum computation seems nonviable at the first glance.

This skepticism disappeared in 2014 when Menicucci showed that even with finite squeezing, combining the cluster state with the physical GKP qubits allows fault-tolerant quantum computation (Menicucci, 2014). At that point, it was shown that even in the worst case (i.e., without any additional technique or optimization), around -20.5 dB of squeezing should be sufficient. After this fault tolerance with finite squeezing was shown, there have been many subsequent works that reduce this threshold and introduce many new techniques in the error correction using GKP qubits. Covering all topics in the quantum error correction using GKP qubits would likely require another textbook; thus, we direct the readers to other papers for the recent progress made in the GKP qubits (Tzitrin *et al.*, 2020).

07 December 2024 17:52:47

6.3.2 Research studies on the generation of GKP qubits

Although many of the advances in the CV quantum computation have been achieved via the optical systems, as optical nonlinearities are relatively weak, the generation of the exotic quantum state is somewhat more progressed in the superconducting system and the ion-trapped system, where the nonlinearities are stronger.

From this point of view, the generation of the GKP qubits is also the case. In 2019, GKP qubits are experimentally generated in the superconducting system (Campagne-Ibarcq *et al.*, 2020) and the ion-trapped system (Flühmann *et al.*, 2019), using the existing nonlinearities and interactions in such systems. For the optical system, as there are no natural strong nonlinearities as the superconducting system and the ion-trapped system, a different strategy is required. A standard method to generate an optical non-Gaussian state is via photon-number measurements on multimode Gaussian entanglements. For GKP states, optical generation using photon-number measurement has been proposed (Tzitrin *et al.*, 2020). There are also other generation methods such as a breeding protocol that uses cat states and homodyne measurements (Weigand and Terhal, 2018) and Fock state filtering that utilizes single-photon states and coherent states (Eaton *et al.*, 2019). Regardless of the methodology, the key technology is the photon-number-resolving detectors. Therefore, the development of a photon-number-resolving detector holds the key to achieving the fault-tolerant universal CV optical quantum computer.

6.4 ANALOG INFORMATION IN CV QUANTUM ERROR CORRECTION

For CV quantum computation that uses physical quantities whose spectra take continuous values, discretization or quantization is required to realize fault-tolerant quantum computation. In the process of quantization, in a way, we are throwing away some of the information. For example, in the GKP qubit encoding, even though we are using homodyne measurements, in the end, we bin the quadrature values and do not use the continuous-valued quadratures.

When we consider only a single GKP qubit, it might not be necessary to keep the quadrature values. When we consider an upper level concatenation, however, the situation involves multiple logical qubits. It has been shown that the analog information from the homodyne measurement, can be used to improve the fault-tolerant threshold when GKP qubits are used. Figure 6.10 shows the idea of using the analog information in the work by Fukui *et al.* (2017). In their idea, when we bin the quadrature values, rather than just comparing the values to a threshold, it is more advantageous to consider the actual probability (or, in their paper, likelihood) to obtain certain measurement values. This idea is, in particular, important when we consider multiple physical GKP qubits where each peak has finite width and the most likely displacements are not necessarily found using the digital binning explained in Sec. 6.3.1.4.

07 December 2024 17:52:47

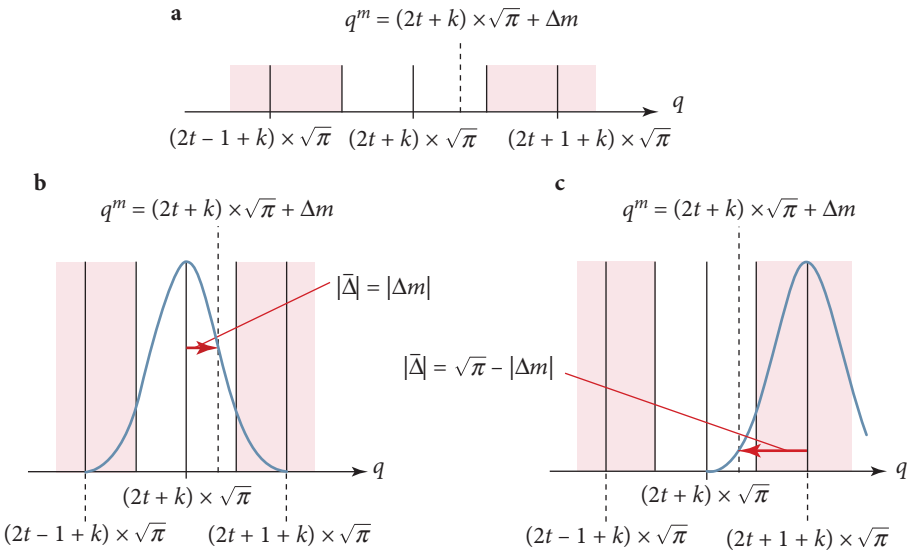
a
$q^m = (2t + k) \times \sqrt{\pi} + \Delta m$
q
$(2t - 1 + k) \times \sqrt{\pi}$
$(2t + k) \times \sqrt{\pi}$
$(2t + 1 + k) \times \sqrt{\pi}$
b
$q^m = (2t + k) \times \sqrt{\pi} + \Delta m$
$|\bar{\Delta}| = |\Delta m|$
q
$(2t + k) \times \sqrt{\pi}$
$(2t - 1 + k) \times \sqrt{\pi}$
$(2t + 1 + k) \times \sqrt{\pi}$
c
$q^m = (2t + k) \times \sqrt{\pi} + \Delta m$
$|\bar{\Delta}| = \sqrt{\pi} - |\Delta m|$
q
$(2t + k) \times \sqrt{\pi}$
$(2t - 1 + k) \times \sqrt{\pi}$
$(2t + 1 + k) \times \sqrt{\pi}$

FIG. 6.10
Introduction of likelihood into physical GKP qubits error correction where each peak is not a delta function, but a Gaussian function with finite width (Fukui *et al.*, 2017).

The work by Fukui *et al.* is a simple example that shows that utilizing a CV system is not as simple as just encoding the information using logical qubits and applying the results in the qubit-based quantum computation. As such, it is likely the case that the "analog" aspect of the CV system should be utilized as well. In the experimental work by Aoki *et al.* (2009), they demonstrate the Shor nine-qubit code, where instead of qubits, they used squeezed lights, which is also an example of using the analog aspect for error correction in the CV system.

As GKP qubits are difficult to generate for any physical system, which is not limited to the optical system, a practical method for CV error correction and fault tolerance should minimize the number of required GKP qubits as much as possible. In recent research (Bourassa *et al.*, 2021), it has been shown that even if we do the concatenation at the logical level, it is possible to achieve fault tolerance even when some of the logical GKP qubits are replaced with squeezed vacuum states. This result is crucial in the sense that squeezed vacuum states are highly "cheap" resources in the CV optical system; they can be deterministically generated with relative ease. Therefore, the search for a method to reduce the number of the required GKP qubits and incorporation of the analog aspect of CV systems is crucial if we are to realize a full-fledged quantum computer that has practical applications.

07 December 2024 17:52:47

REFERENCES

Aoki, T., Takahashi, G., Kajiya, T., Yoshikawa, J., Braunstein, S. L., and van Loock, P., "Quantum error correction beyond qubits," Nat. Phys. **5**(8), 541–546 (2009).

Asavanant, W., Shiozawa, Y., Yokoyama, S., Charoensombutamon, B., Emura, H., and Alexander, R. N., "Generation of time-domain-multiplexed two-dimensional cluster state," Science **366**(6463), 373–376 (2019).

Bergmann, M. and van Loock, P., "Quantum error correction against photon loss using NOON states," Phys. Rev. A **94**, 012311 (2016).

Bourassa, J. E., Alexander, R. N., Vasmer, M., Patil, A., Tzitrin, I., and Matsuura, T., "Blueprint for a scalable photonic fault-tolerant quantum computer," Quantum **5**, 392 (2021).

Campagne-Ibarcq, P., Eickbusch, A., Touzard, S., Zalys-Geller, E., Frattini, N. E., Sivak, V. V. *et al.*, "Quantum error correction of a qubit encoded in grid states of an oscillator," Nature **584**(7821), 368–372 (2020).

Chuang, I. L., Leung, D. W., and Yamamoto, Y., "Bosonic quantum codes for amplitude damping," Phys. Rev. A **56**, 1114–1125 (1997).

Eaton, M., Nehra, R., and Pfister, O., "Non-Gaussian and Gottesman–Kitaev–Preskill state preparation by photon catalysis," New J. Phys. **21**(11), 113034 (2019).

Flühmann, C., Nguyen, T. L., Marinelli, M., Negnevitsky, V., Mehta, K., and Home, J. P., "Encoding a qubit in a trapped-ion mechanical oscillator," Nature **566**(7745), 513–517 (2019).

Fukui, K., Tomita, A., and Okamoto, A., "Analog quantum error correction with encoding a qubit into an oscillator," Phys. Rev. Lett. **119**, 180507 (2017).

Fukui, K., Tomita, A., Okamoto, A., and Fujii, K., "High-threshold fault-tolerant quantum computation with analog quantum error correction," Phys. Rev. X **8**, 021054 (2018).

Gottesman, D. and Chuang, I. L., "Demonstrating the viability of universal quantum computation using teleportation and single-qubit operations," Nature **402**(6760), 390–393 (1999).

Gottesman, D., Kitaev, A., and Preskill, J., "Encoding a qubit in an oscillator," Phys. Rev. A **64**, 012310 (2001).

Hastrup, J., Larsen, M. V., Neergaard-Nielsen, J. S., Menicucci, N. C., and Andersen, U. L., "Unsuitability of cubic phase gates for non-Clifford operations on Gottesman–Kitaev–Preskill states," Phys. Rev. A **103**, 032409 (2021).

Larsen, M. V., Guo, X., Breum, C. R., Neergaard-Nielsen, J. S., and Andersen, U. L., "Deterministic generation of a two-dimensional cluster state," Science **366**(6463), 369–372 (2019).

Matsuura, T., Yamasaki, H., and Koashi, M., "Equivalence of approximate Gottesman–Kitaev–Preskill codes," Phys. Rev. A **102**, 032408 (2020).

Menicucci, N. C., "Fault-tolerant measurement-based quantum computing with continuous-variable cluster states," Phys. Rev. Lett. **112**, 120504 (2014).

Nielsen, M. A. and Chuang, I. L., *Quantum Computation and Quantum Information* (Cambridge University Press, Cambridge, 2000).

07 December 2024 17:52:47

Niset, J., Fiurášek, J., and Cerf, N. J., "No-go theorem for Gaussian quantum error correction," Phys. Rev. Lett. **102**, 120501 (2009).

Ralph, T. C., Gilchrist, A., Milburn, G. J., Munro, W. J., and Glancy, S., "Quantum computation with optical coherent states," Phys. Rev. A **68**, 042319 (2003).

Tzitrin, I., Bourassa, J. E., Menicucci, N. C., and Sabapathy, K. K., "Progress towards practical qubit computation using approximate Gottesman–Kitaev–Preskill codes," Phys. Rev. A **101**, 032315 (2020).

Weigand, D. J. and Terhal, B. M., "Generating grid states from Schrödinger-cat states without postselection," Phys. Rev. A **97**, 022341 (2018).

07 December 2024 17:52:47

07 December 2024 17:52:47

CHAPTER

7 INTEGRATED OPTICS FOR QUANTUM COMPUTER

7.1 MOVING FROM TABLE-TOP TO INTEGRATED OPTICS

Quantum optics began from free-space optics. Generations of various quantum states (such as a single-photon state, squeezed states, and cluster states), demonstrations of basic quantum protocols (such as quantum teleportation), and implementation of basic quantum algorithms were first realized using free-space optics. The main reason that free-space optics are widely used for the proof-of-principle experiments is that they can be easily realigned and rearranged to realize various different experiments. Another benefit is that optical losses in free-space are very low compared to, for example, optical fibers. When we consider the development of the optical quantum computer in a long term, free-space optics are, however, unlikely the best choices as they required daily maintenance (such as alignments and cleanings). Moreover, building a free-space optics setup is, in a sense, a form of art; practices and trainings are required, and even then, completely reproducing another setup is not at all an easy feat.

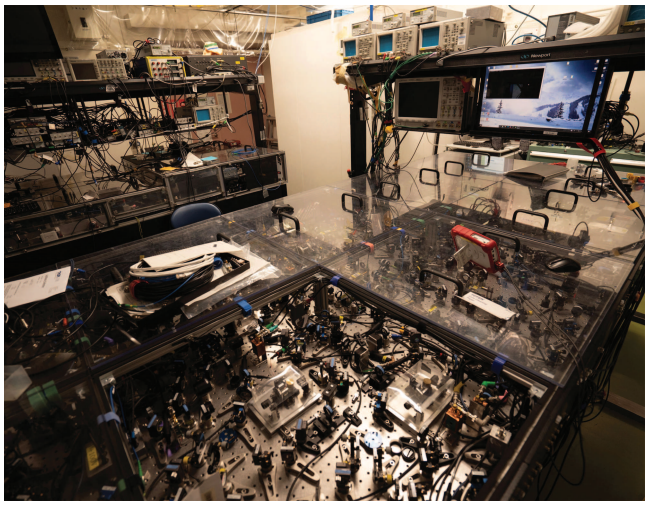

FIG. 7.1
Free-space optical setup for generation of two-dimensional cluster states (photo taken by Mamoru Endo).

To move from the proof-of-principle free-space optics to a more practical system, many possibilities are being explored. To make the free-space optics more maintenance free and manageable, we could employ some sort of an auto-alignment system. Even then, for a very complex optical system such as the one in Fig. 7.1, adding auto-alignment capability to all the mirrors and lenses is obviously not feasible. A more viable approach is to integrate free-space optical components into a more manageable system.

A typical optical system usually looks like the following. Any optical system would start with *light sources* such as master lasers,

07 December 2024 17:52:47

https://doi.org/10.1063/9780735424074_007

Optical Quantum Computers: A Route to Practical Continuous Variable Quantum Information Processing, W. Asavanant and A. Furusawa
© 2022 AIP Publishing, published by AIP Publishing

squeezed-light sources, and single-photon sources. Then, lights from these light sources are passed through an *optical circuit*, which determines the operations, protocols, or applications we wish to implement. Optical circuits usually consist of components such as beamsplitters, phase shifters, polarizer, optical delay line, and optical cavity. Finally, lights are measured by *detectors*. For most of the time, the detectors of our concern will be homodyne detectors, avalanche photodiodes, or photon-number-resolving detectors. Integration of optical systems is concerned with integrating some or all of these components.

In addition to the categorizations in the last paragraph, optical components can also be divided into passive components and active components. Passive components, as the name suggests, are components that do not require additional energy. Examples of passive components are beamsplitters, polarizers, and optical delay line. On the other hand, examples of active components are squeezed-light sources, single-photon sources, and phase shifters. In general, integration of active components tends to be more difficult than passive components as they need to be actively controlled.

A typical approach to the integration of the optical system is by using either an optical fiber or a waveguide system (Fig. 7.2). An optical fiber is a fiber made of glass (usually silica) and consists of a circular core and cladding where the refractive index of the core is slightly larger. On the other hand, the waveguides can be roughly considered an optical version of the electrical printed circuit board (also called a planar light circuit or PLC). The waveguide system also utilizes the difference between the strips and the surrounding area to contain and bend the lights as needed. Regarding the full analysis of the electromagnetic fields in the optical fiber and waveguide, we refer the readers to a classical optics textbook (Yariv and Yeh, 2006). We do note that one of the main differences between the free-space optics and the integrated optics is that the integrated optics support beams with only a particular spatial mode. As the modes in the integrated optics are different from that of the free-space, interfacing between free-space optics and integrated optics requires special care.

As optical industry is a huge industry ranging from telecommunications and manufacturing processes to biomedical applications, integrations of various optical components have been researched.

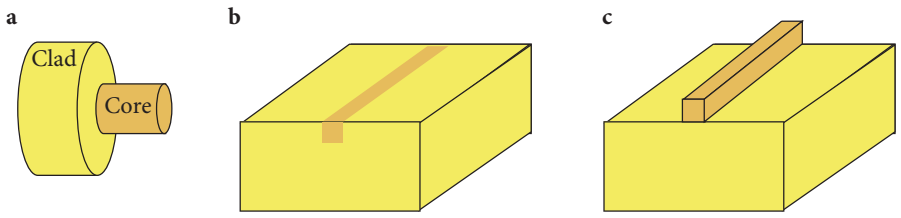

FIG. 7.2
Conceptual diagram of a fiber and a waveguide. (a) A circular fiber. (b) Stripped waveguide embedded in the medium with lower refractive index. (c) Stripped waveguide on a substrate.

07 December 2024 17:52:47

For quantum applications, however, there are a few requirements that are quite different from other fields. Compared to the usual applications, integrated components for quantum applications should have very low losses. To be more explicit, for example, if we wish to measure squeezed lights with the squeezing level of −20 dB, then the total optical losses of the whole system must be below 1%, which is equal to about 0.04 dB. This level is much lower than optical losses in the typical "low-loss" integrated optical components. Also, as most of the quantum operations in the optical systems involve interference, it is preferable (necessary) that integrated optical components only support a single spatial mode and that the interferometric visibility is as high as possible. In the optical fiber or the wave guide, the dimensions and boundary conditions determine the eigenmodes that can propagate through them. If there is only one eigenmode, then such a component is called a single-mode (for example, a single-mode optical fiber only supports a single spatial mode). Note that there is also a multimode optical fiber that supports multiple modes. Components that support multiple modes are rather difficult to deal with as it makes the modes of our interest become not well defined. This is similar to how optical cavity of the optical parametric oscillator (OPO) is useful as it also determines the spatial mode for the free-space experiments.

In this chapter, we will introduce integrations of various components required in the optical quantum computer. As the subject of the integrated optics is very broad, it is not possible to cover everything here. We will try to, however, give the readers the perspectives and concepts and encourage the readers to pursue further in the topic they are interested in.

07 December 2024 17:52:47

7.2 INTERFEROMETER

An interferometer is the most basic optical instrument. In free-space optics, an interferometer is composed of beamsplitters and phase shifters. A beamsplitter is usually a plate of glass with coating to realize desired reflectivity. On the other hand, the phase shifter is realized in various ways such as a mirror attached to a piezo actuator, an electro-optics phase modulator, and an acousto-optics modulator. To build an integrated interferometer, a beamsplitter and a phase shifter must be integrated.

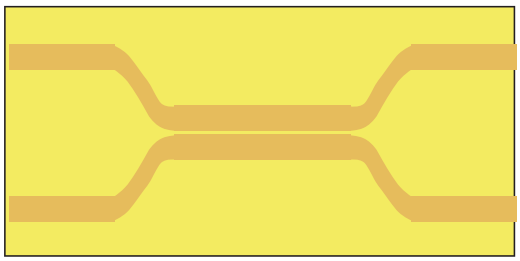

FIG. 7.3
Conceptual diagram of evanescent coupling on the waveguide.

When considering the integration of quantum optics experiments, there are two approaches. The first approach is to use the fiber-based component. The second approach is to use the waveguide or waveguide chip. For the beamsplitter, although the free-space beamsplitter uses the reflection between the medium with a different refractive index, beamsplitters in fiber-based and waveguide-based systems are realized via an evanescent wave. Figure 7.3 shows the conceptual diagram of coupling via an evanescent wave: when lights are contained inside the optical fiber or waveguide, it can couple to another fiber or

waveguide if the cores or the strips are brought close to each other. By designing the distance between two fibers/waveguides and adjust their lengths appropriately, various coupling ratios (reflectivity of the beamsplitter in the free-space) can be realized.

On the other hand, integration of the phase shifter is usually done by using electro-optic (EO) effects. In the nonlinear medium, by applying electric fields to the medium, the phases of the light passing through it can be adjusted by the strength of the electric fields. Such a nonlinear medium with EO effects can be incorporated onto a waveguide such as lithium niobate (Zhu *et al.*, 2021). For operations that do not require high-speed phase shifting, it is also possible add a heater to a particular strip of the waveguide, which allows changing of the refractive index (thus the phase) via temperature.

Using the beamsplitters and the phase shifters, an arbitrary interferometer can be implemented. For an N-input N-output interferometer, there is a configuration composed of $\sim N^2$ variable beamsplitters and phase shifters that can realize an arbitrary interferometer (Reck *et al.*, 1994). Note that a variable beamsplitter can be realized using a Mach–Zehnder interferometer with a phase shifter on one of its

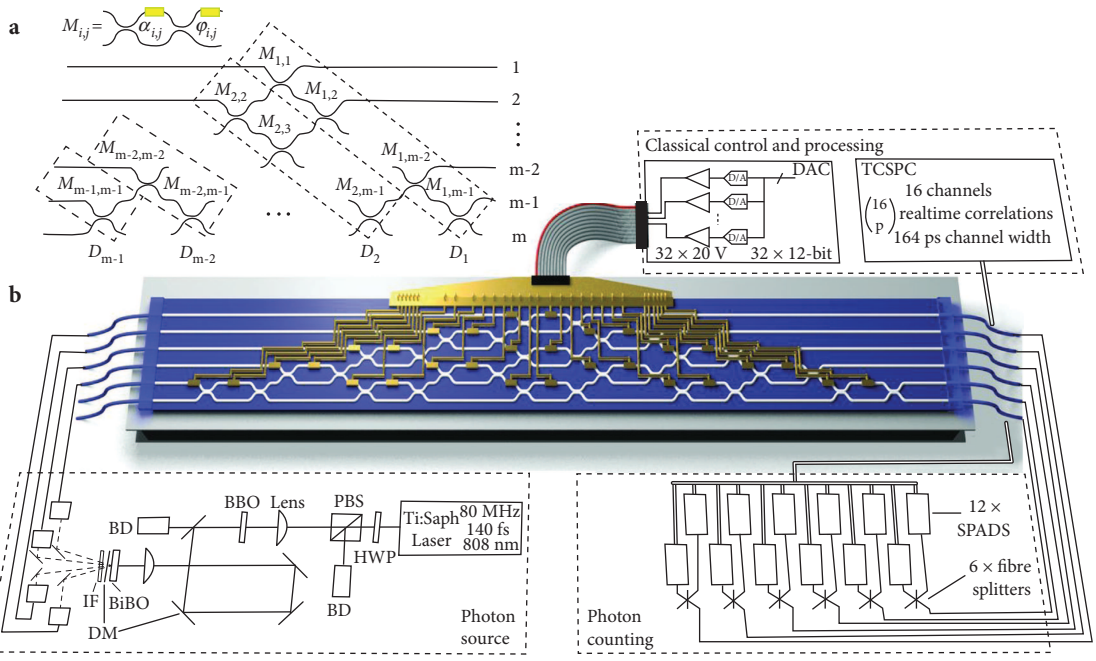

FIG. 7.4
Universal linear optics on the silica-on-silicon waveguide. Reprinted with permission from Carolan, J. *et al.*, Science **349**(6249), 711–716 (2015). Copyright 2015 AAAS.

07 December 2024 17:52:47

arms. The main obstacle regarding the beamsplitter network in the quantum computing is that if we use a quantum computation paradigm that requires fully programmable linear optics networks, the number of the parameters that needs to be adjusted would increase on the order of N^2 as the number of the input N increases. Also, the beamsplitter network must be fabricated and tailored to a specific N. This difficulty does not arise in the time-domain methodology where the beamsplitter network (i.e., the generation system of the cluster state) remains the same as N increases. The demonstration of the universal beamsplitter network and its applications in quantum computation was demonstrated by using a silica-on-silicon waveguide (Carolan *et al.*, 2015) (Fig. 7.4).

7.3 OPTICAL DELAY LINE

As we discussed in Chap. 4, optical delay lines are an important component for the time-domain multiplexing method. Figure 7.5 shows some of the configurations to realize an integrated optical delay line. In the integrated optical system, making a long optical delay line on a waveguide is somewhat difficult as we would need either a very large substrate or we have to coil the optical delay line on the waveguide. The optical fiber is a more popular option for an optical delay line. The length of the optical delay line that can be achieved using an optical fiber is limited by the propagation losses. The propagation loss in an optical fiber depends on the type of the fibers and the wavelength. For a typical optical fiber, the C-band (i.e., around 1550 nm used for optical communication) has the lowest optical losses of about ~0.2 dB/km. On the other hand, historically, quantum optics experiments usually used a shorter wavelength such as 852 nm, which corresponds to the transitions of silicon photodiodes and a transition line of a cesium atom. For optical quantum computer, when we consider the affinity to the optical telecommunication and the optical delay lines for the time-domain multiplexing method, it is important that the wavelengths of many components are moved to the C-band. Another important aspect is that the spatial mode of the light inside the waveguide and that of the fiber is usually different. This is because while the optical fibers are usually circular, the strips on the waveguides are usually rectangular stripes. Therefore, if we want to couple the light from the waveguide to the optical fiber and realize a long optical delay line, we need to be careful regarding mode matching. There are research studies that achieve interfacing between waveguides and optical fibers by adiabatically tapering the waveguide or using a tapered fiber to couple the waveguide. We refer the readers to Son *et al.* (2018) for a more comprehensive review of such interfacing.

7.4 SINGLE-PHOTON SOURCE

The most basic quantum light source for optical quantum computer using qubits is a single-photon source. For a quantum optics experiment, spontaneous parametric down conversion (SPDC) sources are widely used in free-space experiments. To achieve the integration of a single-photon source, the

07 December 2024 17:52:47

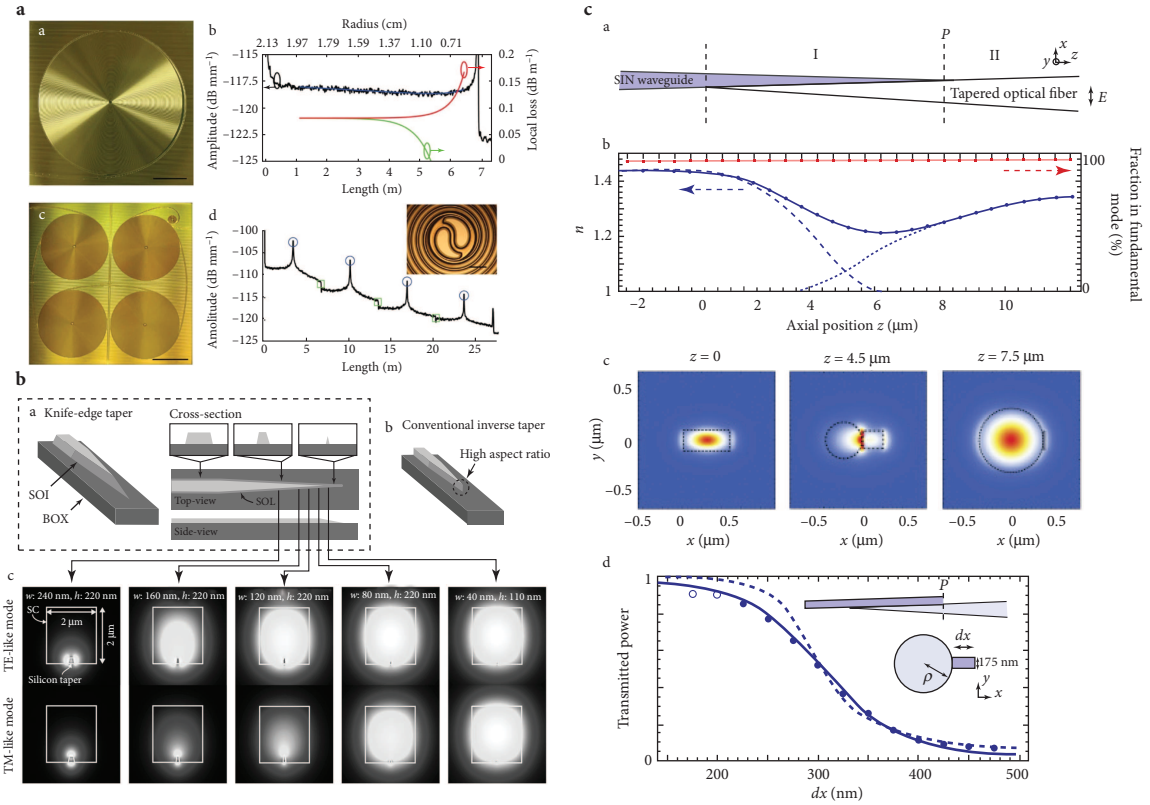

FIG. 7.5
Various configurations capable to implement optical delay lines. (a) Optical delay line on silicon chip. Reprinted with permission from Lee, H. *et al.*, Nat. Commun. **3**(1), 867 (2012). Copyright 2012 Springer Nature Customer Service Centre GmbH, Springer Nature. (b) Tapered waveguide converting between two modes. Reprinted with the permission from Takei, R. *et al.*, Appl. Phys. Lett. **102**(10), 101108 (2013). Copyright 2013 AIP publishing LLC. (c) Fiber–waveguide interfacing using a tapered fiber and evanescent coupling. Adapted with permission from Tiecke, T. G. *et al.*, Optica **2**(2), 70–75 (2015). Copyright 2015 The Optical Society.

most basic approach one could think of is making a compact free-space SPDC source that is coupled to an optical fiber. A different approach would be to build a SPDC source on the waveguide. For the silica waveguide, this is sometimes achieved by utilizing the third-order nonlinearity, which naturally occurs in the silica (Sharping *et al.*, 2006).

Another type of an integrated single-photon source is an artificial particle called a quantum dot. A quantum dot is a semiconductor, which is fabricated in a way that when it is shined on by the laser

07 December 2024 17:52:47

light, a single photon is emitted in a single direction. A quantum dot is considered one of the promising candidates for a deterministic single-photon source. Some of the downfalls for the quantum dots are that they operate at a low-temperature environment, and as they are semiconductors, making and tuning quantum dots at an arbitrary frequency is not a trivial task. For a more comprehensive review on single-photon sources, see, for example, Eisaman *et al.* (2011).

7.5 SQUEEZED-LIGHT SOURCE

For continuous-variable (CV) quantum computation, squeezed-light sources are essential components. Figure 7.6 shows some examples of integrations of squeezed-light sources. The most basic type of the integration is to build an OPO with a compact space designed for coupling to the optical fiber

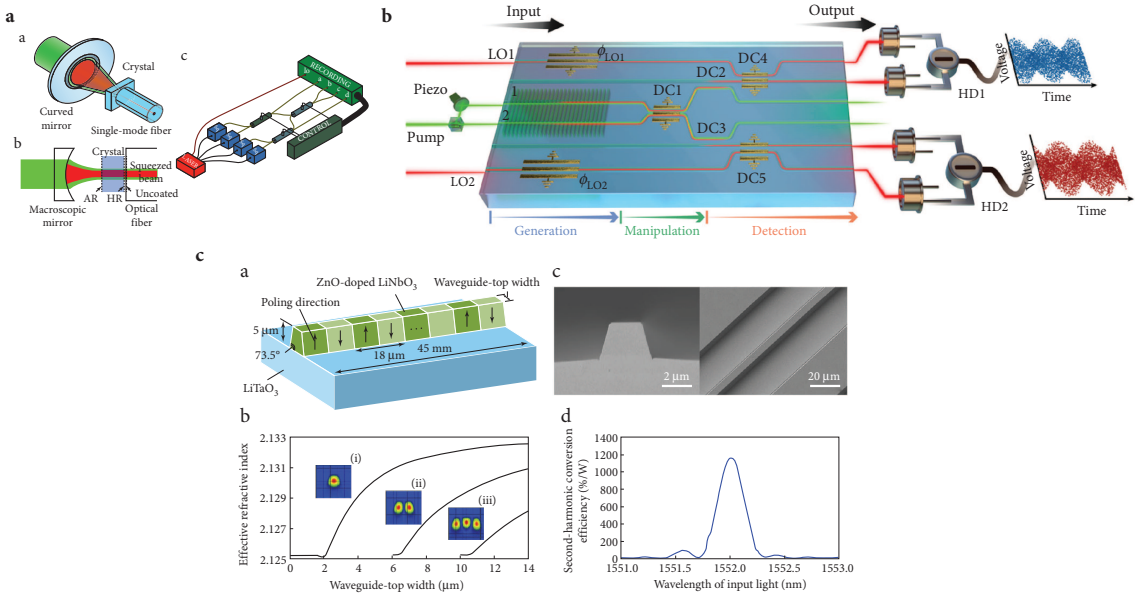

FIG. 7.6
Integrations of the squeezed-light sources. (a) Fiber-coupled cavity-based free-space squeezed-light source. Adapted with permission from Brieussel, A *et al.*, Opt. Lett. **43**(6), 1267–1270 (2018). Copyright 2018 The optical Society. (b) Squeezed lights and two-mode squeezed state generation using a lithium niobate waveguide patterned by reverse proton exchange. Reprinted with permission from Lenzini, F. *et al.*, Sci. Adv. **4**(12) (2018). Copyright Author(s), exclusive licensee AAAS. Distributed under a CC BY-NC 4.0 License (http://creativecommons.org/licenses/by-nc/4.0/). (c) PPLN waveguide for THz-order squeezed-light generation [Kashiwazaki, T. *et al.*, APL Photonics **5**(3) (2020), 036104. Copyright 2020 Author(s), licensed under a Creative Commons Attribution (CC BY) license].

07 December 2024 17:52:47

or the waveguide. In this type of architecture, one of the most important considerations is that while the spatial modes of the laser beams or the light from the OPO are usually Hermite–Gaussian modes (and for the most cases TEM_{00} modes), the modes supported by optical fibers and waveguides are not Gaussian (for example, the mode of the optical fiber is usually LP_{01}). As such, the mode matching between free-space and integrated optics must be maximized in order to reduce coupling losses. There are a few examples of this type of architecture (Brieussel *et al.*, 2018).

There are also integrated squeezed-light sources built on the waveguide using material such as periodically-poled potassium titanyl phosphate (PPKTP) or periodically-poled lithium niobate (PPLN). The squeezed-light source that does not have a cavity structure is usually called an optical parametric amplifier (OPA). One of the advantages of an OPA over an OPO is that OPA can generate squeezed lights with a much broader frequency bandwidth than an OPO as it does not require an optical cavity structure. Regarding the recent experimental work on integrated squeezed-light sources, there is a demonstration of −6 dB squeezing generated with waveguide OPA (Kashiwazaki *et al.*, 2020). On-chip generation and measurement of two-mode-squeezed states have also been demonstrated (Lenzini *et al.*, 2018).

7.6 PHOTON DETECTORS

Regarding the detection, we will first discuss the integration of photon detections. For the detectors such as transition edge sensors (TESs) and superconducting nanostrip photon detectors (SNSPDs), as they usually operate at the cryogenic temperature, these components are positioned inside the cryostats and are connected to light sources via an optical fiber. In this aspect, coupling to the optical fiber is required to use these devices. Another approach that has been taken is where the TESs or the SNSPDs are integrated on the waveguide (Fig. 7.7) Höpker *et al.* (2019).

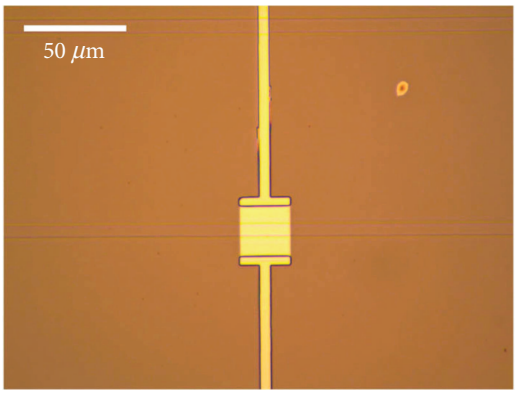

FIG. 7.7
Integration of TES on the waveguide [Höpker, J. P. *et al.*, APL Photonics **4**(5), 056103, (2019). Copyright Author(s), licensed under a Creative Commons Attribution (CC BY) license.]

07 December 2024 17:52:47

7.7 HOMODYNE MEASUREMENT

Figure 7.8 shows some experimental examples of an integrated homodyne measurement. As a homodyne detector is composed of a 50:50 beamsplitter, a local oscillator, and two photodiodes, integration of the homodyne measurement is rather straightforward. Note that in the homodyne measurement, it is crucial that the splitting ratio of the beamsplitter is adjusted so that it is balanced and the common-mode noise is rejected (usually expressed as a common-mode rejection ratio). As such, rather than a fixed 50:50 beamsplitter, a beamsplitter for the homodyne measurement in the waveguide system is usually made of a Mach–Zehnder interferometer with a phase shifter on one arm. This is in contrast to the free-space homodyne measurement where we can easily adjust the reflectivity.

After the beamsplitter, lights enter the photodiodes. There are many ways to achieve this. First, we can simply let the light out of the waveguide and coupling them to the photodiodes using free-space optics. Such a system is demonstrated in, for example, Masada *et al.* (2015). Another approach is that we could attach the photodiode to the output of the strips of the waveguide. In this method, we have to match the difference between each interface so that all lights are absorbed by the photodiodes. Recently, there is also a report of integration of homodyne detectors where all components, including the photodiodes, are integrated (Tasker *et al.*, 2021).

7.8 FEEDFORWARD OPERATION

Many protocols in the CV system require feedforward operations. The term feedforward usually means one of the following. First, it could mean the displacement operations where the amount of displacement depends on the prior measurement results. Another meaning is in the measurement-based quantum computation where the measurement basis depends on the prior measurement results. For both operations, it is essential to match the timing between the electrical signal processing and the optical mode where the feedforward operations are implemented. As the electrical signal processing is usually much slower, we need to add the optical delay lines and perfectly match the timing between the two. This is especially important for the quantum computation in the time-domain where the modes are encoded in a localized temporal wave packet. On the other hand, timing is unimportant for computation that takes place in the narrow frequency sideband as signals in such a sideband are periodic. As such, the integration of the feedforward operation on the waveguide has been done only for the frequency sideband mode, and integration of the feedforward system that can handle a temporal wave packet is crucial in the realization of the CV quantum computation in the time domain.

07 December 2024 17:52:47

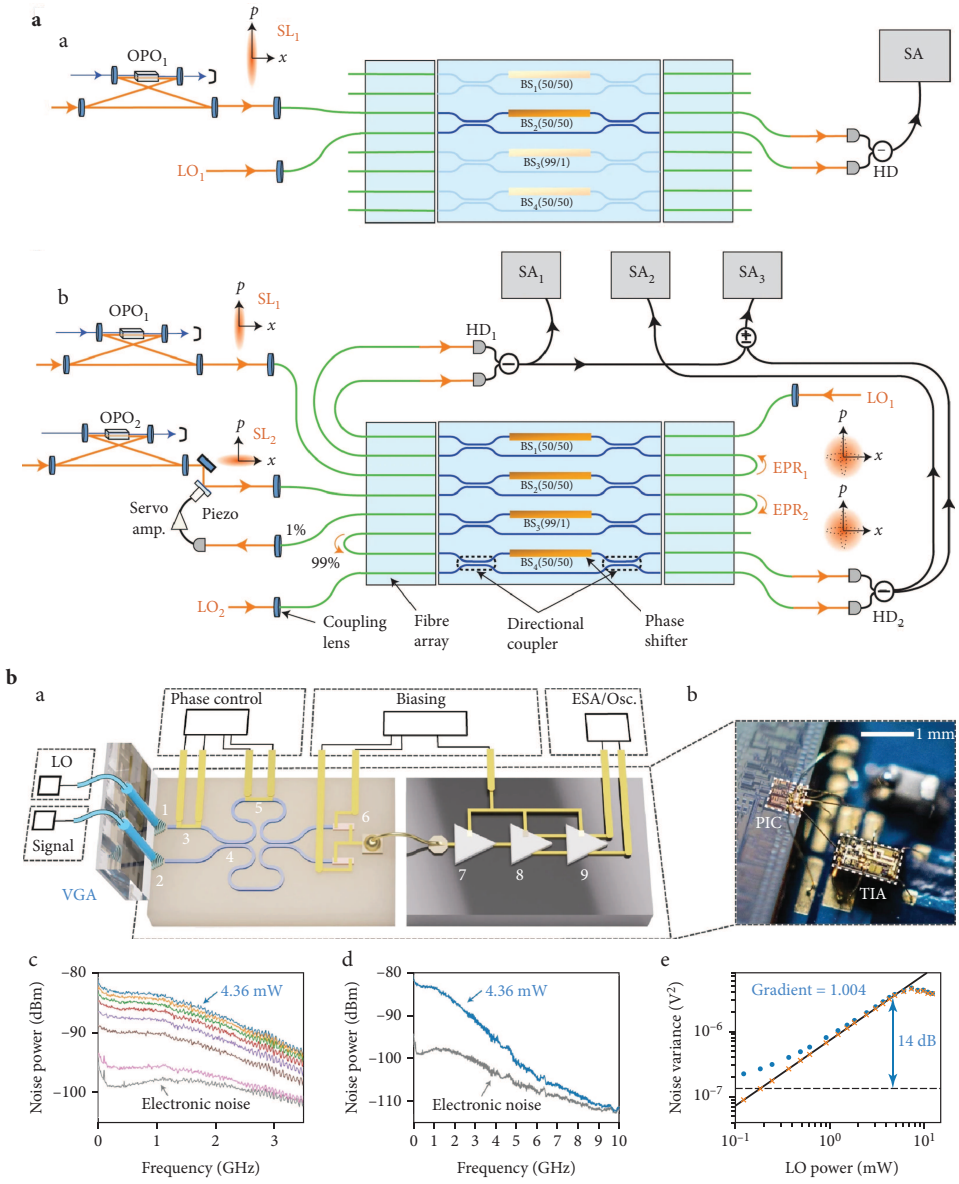

FIG. 7.8
Integration of homodyne detectors. (a) Homodyne measurements and entanglement generations using on-chip beam-splitters. [From Masada, G. *et al.*, Nat. Photonics **9**(5), 316–319 (2015). Copyright 2015 Springer Nature Publishing Group.] (b) Integrated homodyne measurements and electronics by CMOS-compatible silicon and germanium-on-silicon nanophotonics. [Reprinted with permission from Tasker, J. F. *et al.*, Nat. Photonics **15**(1), 11–15 (2021). Copyright 2021 Springer Nature Publishing Group.]

07 December 2024 17:52:47

REFERENCES

Brieussel, A., Ott, K., Joos, M., Treps, N., and Fabre, C., "Toward a compact fibered squeezing parametric source," Opt. Lett. **43**(6), 1267–1270 (2018).

Carolan, J., Harrold, C., Sparrow, C., Martín-López, E, Russell, N. J., and Silverstone, J. W., "Universal linear optics," Sciences **349**(6249), 711–716 (2015).

Eisaman, M. D., Fan, J., Migdall, A., and Polyakov, S. V., "Invited review article: Single-photon sources and detectors," Rev. Sci. Instrum. **82**(7), 071101 (2011).

Höpker, J. P., Gerrits, T., Lita, A., Krapick, S., Herrmann, H., and Ricken, R., "Integrated transition edge sensors on titanium in-diffused lithium niobate waveguides," APL Photonics **4**(5), 056103 (2019).

Kashiwazaki, T., Takanashi, N., Yamashima, T., Kazama, T., Enbutsu, K., and Kasahara, R, "Continuous-wave 6-dB-squeezed light with 2.5-THz-bandwidth from single-mode PPLN waveguide," APL Photonics **5**(3), 036104 (2020).

Lenzini, F., Janousek, J., Thearle, O., Villa, M., Haylock, B., and Kasture, S., "Integrated photonic platform for quantum information with continuous variables," Sci. Adv. **4**(12), (2018).

Masada, G., Miyata, K., Politi, A., Hashimoto, T., O'Brien, J. L., and Furusawa, A., "Continuous-variable entanglement on a chip," Nat. Photonics **9**(5), 316–319 (2015).

Reck, M., Zeilinger, A., Bernstein, H. J., and Bertani, P., "Experimental realization of any discrete unitary operator," Phys. Rev. Lett. **73**, 58–61 (1994).

Sharping, J. E., Lee, K. F., Foster, M. A., Turner, A. C., Schmidt, B. S., and Lipson, M., "Generation of correlated photons in nanoscale silicon waveguides," Opt. Express. **14**(25), 12388–12393 (Dec. 2006).

Son, G., Han, S., Park, J., Kwon, K., and Yu, K., "High-efficiency broadband light coupling between optical fibers and photonic integrated circuits," Nanophotonics **7**(12), 1845–1864 (2018).

Tasker, J. F., Frazer, J., Ferranti, G., Allen, E. J., Brunel, L. F., and Tanzilli, S., "Silicon photonics interfaced with integrated electronics for 9 GHz measurement of squeezed light," Nat. Photonics **15**(1), 11–15 (2021).

Yariv, A. and Yeh, P., in Photonics: Optical Electronics in Modern Communications, The Oxford Series in Electrical and Computer Engineering (Oxford University Press, Inc., 2006).

Zhu, D., Shao, L, Yu, M., Cheng, R., Desiatov, B., and Xin, C. J., "Integrated photonics on thin-film lithium niobate," Adv. Opt. Photonics **13**(2), 242–352 (2021).

07 December 2024 17:52:47

07 December 2024 17:52:47

CHAPTER

8 CONCLUSION AND FUTURE PERSPECTIVE

8.1 FROM QUBIT TO CONTINUOUS VARIABLE TO LOGICAL QUBIT

In the long history of the development of the quantum computer, it is inarguable that quantum computation starts with two-level, i.e., qubit, systems. In the course of the development of the qubits, a single qubit can now be fabricated and operations can be implemented with high fidelities. Now, the research studies on the qubit system focus on either how to scale up in a fault-tolerant fashion or what can be demonstrated with the current intermediate scale systems without the capabilities to do the error corrections.

Along with the developments of quantum computation using qubits, research has also given birth to quantum computation with an infinite level system, i.e., continuous variable (CV). In some sense, a continuous variable might be a more natural choice since there is rarely any system (without high level of engineering) that is naturally and truly two-level, and most of the physical quantities in nature are either continuous-valued or can take multiple values besides just 0 or 1.

In the beginning, many of the developments of the CV quantum computation simply followed the development of the qubit systems, where many theoretical developments are extensions of the qubit-version results into the CV version. Although there are some substantial differences between the finite and infinite dimension systems, these differences are usually subtle.

There are a few turning points in the development of the CV system, which makes it now an important concept in quantum computation and not just an alternative to the qubit system. Although we have explained many of them throughout this book, we would like to recall some of the important results here.

One of the first demonstrations of the advantage of the CV system over the qubit system is the demonstration of the unconditional quantum teleportation using the CV optical system (Furusawa *et al.*, 1998). This demonstration does not only show the usefulness of the CV system but also demonstrates the generation of quantum entanglement, phase locking, measurement, and feedforward operation, which form the basic technologies of the subsequent CV experiments.

07 December 2024 17:52:47

https://doi.org/10.1063/9780735424074_008 8-1

Optical Quantum Computers: A Route to Practical Continuous Variable Quantum Information Processing, W. Asavanant and A. Furusawa
© 2022 AIP Publishing, published by AIP Publishing

The next important result is regarding the fault tolerance. When theorems or protocols in the qubit system are imported to the CV system, many of them tend to require infinite squeezing and raise the skepticism of whether CV quantum computation can be made fault-tolerant. In 2013, it was shown that by using GKP qubits (Gottesman *et al.*, 2001) even with finite squeezing, it is possible to achieve universal and fault-tolerant quantum computation given that the squeezing level is sufficiently high (Menicucci, 2014).

Finally, there have been experimental demonstrations of various scalable platforms using the CV optical system. By using multiplexing, computational platforms where components and parameters that needed to be controlled do not increase with the number of inputs are demonstrated. These experimental results show a sheer advantage of the CV system over the qubit system regarding the scalability.

Therefore, it is suffice to say that when considering scaling-up of the quantum computation system, rather than building qubits one by one and trying to interfacing them, going for a system with built-in scalability such as the CV optical system could prove to be a better approach. Regarding fault tolerance, although we would require multiple qubits to make a single logical qubit in the qubit-based systems, as there are large Hilbert spaces in the CV system, a logical qubit can be made using the bosonic code, which requires only a single mode.

When using the CV system for fault-tolerant universal quantum computation, we need to encode the information using the logical qubits. It is somewhat interesting to see that while the quantum computation starts with qubits and then developed into continuous variables, we are now back to (logical) qubits. Some readers might feel that if we are going to encode information using "qubits" anyway, everything on the logical level would just follow the traditional qubits and we would not have to consider the CV aspects. This is not entirely true. For example, in some of the recent research studies, it has been shown that even if we do not replace every mode with logical qubits, fault tolerance can still be achieved (Bourassa *et al.*, 2021). Another example of this is the utilization of the analog information in the logical level error correction (Fukui *et al.*, 2017, 2018). These examples illustrate instances where rather than completely throwing away the CV aspects on the logical level, interplays between CV and qubits are important in the realization of a quantum computer. Therefore, hybridization between qubits and CV would be a significant step toward a quantum computer that retains the advantages of both worlds.

8.2 THE NEXT STEPS

Now that we have reached the last section of this book, let us summarize what we know about optical quantum computation using continuous variables. In terms of experiments, we have seen how the approach using time-domain multiplexing can allow the generation of large-scale cluster states and implementation of measurement-based quantum computation in a way that removes most of

07 December 2024 17:52:47

the experimental hurdles regarding the scalability. Moreover, there are also various demonstrations of non-Gaussian quantum states whose experimental techniques would be the foundation for the implementation of the fault-tolerant universal quantum computation. On the other hand, there are also many theoretical progresses regarding fault tolerance. It is not an exaggeration to say that the developments of fault tolerance and error corrections in CV systems centered around the GKP qubits and how to efficiently implement them in the actual setup.

To actually realize quantum computers, despite the impressive progresses, there are still many obstacles that need to be taken care of. Unlike the developments of a qubit-based quantum computer where the initial efforts are mainly put into the fabrication of a clean qubit with high gate fidelity, and the scaling-up coming later, the developments of the CV-based quantum computer are more focused on the demonstration of scalable and promising approaches while the improvement of the qualities of quantum operations comes later as encoding the logical qubits is the prerequisite before we can implement useful quantum computation on the CV system.

Therefore, the next crucial experimental step in the development of the CV optical quantum computer is how to improve the qualities of the quantum states so that they are sufficient for fault-tolerant universal quantum computation. For the Gaussian states such as two-mode-squeezed states and cluster states, this translates to the improvement of the squeezing level of the squeezed light sources. Despite the fact that there is already a demonstration of a 15 dB squeezed light source (Vahlbruch *et al.*, 2016) that has the squeezing level comparable to that required for fault tolerance, employing this light source in the generation of Gaussian states requires a more sophisticated technique such as high precision phase locking. On the other hand, for the non-Gaussian states, the key technology is the photon-number-resolving detector (PNRD). Although there have been many demonstrations of the non-Gaussian states generations using an ON/OFF detector, the generation of sophisticated non-Gaussian states such as GKP qubit requires PNRD. Experimental progresses are being made regarding the PNRD and the generation of cat state using PNRD whose resolvability of up to about three photons has been demonstrated (Gerrits *et al.*, 2010). However, it is expected that high quantum efficiency PNRD with better resolving power would be needed to realize GKP qubits in the optical system.

The next important theoretical step involves reducing and clarifying the experimental requirements to achieve universal fault-tolerant quantum computation. A good example of this is the generation of the GKP qubits. Although it is known that in principle using PNRDs and Gaussian entanglements should allow the generation of GKP qubits, it is not clear at all how the actual experimental setup should be and how many parameters and photon numbers are required to generate GKP qubits that are sufficient to realize universality and fault tolerance. There is some preliminary work toward this (Tzitrin *et al.*, 2020), but much improvement is still required for the experimentalists to be able to actually generate sufficiently good optical GKP qubits. Another example is regarding the requirement of the squeezing level of the cluster states in the actual experiments. In addition to the experimental efforts to increase the squeezing level of the cluster states (which is currently about 5 dB), it is important that the required threshold is brought down by the theoretical approach.

07 December 2024 17:52:47

8.3 FINAL REMARKS

In this book, we have discussed various topics in the continuous-variable optical quantum computation. We do not claim that we have covered every topic, but we do believe that we have covered sufficiently broad topics and basics so that the readers could further explore the regions of the optical quantum computation in their interests. As the frontiers of science are being pushed forward every day, we urge readers to use our book as a guideline in their studies or research studies, rather than as a textbook that contains all information. We hope that readers find our book interesting and we would be glad if our book helps them in understanding the excitement in optical quantum computation.

REFERENCES

Bourassa, J. E., Alexander, R. N., Vasmer, M., Patil, A., Tzitrin, I., and Matsuura, T., "Blueprint for a scalable photonic fault-tolerant quantum computer," Quantum **5**, 392 (2021).

Fukui, K., Tomita, A., and Okamoto, A., "Analog quantum error correction with encoding a qubit into an oscillator," Phys. Rev. Lett. **119**, 180507 (2017).

Fukui, K., Tomita, A., Okamoto, A., and Fujii, K., "High-threshold fault-tolerant quantum computation with analog quantum error correction," Phys. Rev. X **8**, 021054 (2018).

Furusawa, A., Sørensen, J. L., Braunstein, S. L., Fuchs, C. A., Kimble, H. J., and Polzik, E. S., "Unconditional quantum teleportation," Science **282**(5389), 706–709 (1998).

Gerrits, T., Glancy, S., Clement, T. S., Calkins, B., Lita, A. E., and Miller, A. J., "Generation of optical coherent-state superpositions by number-resolved photon subtraction from the squeezed vacuum," Phys. Rev. A **82**, 031802 (2010).

Gottesman, D., Kitaev, A., and Preskill, J., "Encoding a qubit in an oscillator," Phys. Rev. A **64**, 012310 (2001).

Menicucci, N. C., "Fault-tolerant measurement-based quantum computing with continuous-variable cluster states," Phys. Rev. Lett. **112**, 120504 (2014).

Tzitrin, I., Bourassa, J. E., Menicucci, N. C., and Sabapathy, K. K., "Progress towards practical qubit computation using approximate Gottesman–Kitaev–Preskill codes," Phys. Rev. A **101**, 032315 (2020).

Vahlbruch, H., Mehmet, M., Danzmann, K., and Schnabel, R., "Detection of 15 dB squeezed states of light and their application for the absolute calibration of photoelectric quantum efficiency," Phys. Rev. Lett. **117**, 110801 (2016).

07 December 2024 17:52:47

APPENDIX A: MISCELLANEOUS CALCULATIONS

A.1 DERIVATION OF THE HEISENBERG PICTURE TIME EVOLUTION OF $\hat{\mathbf{A}}$ AND $\hat{\mathbf{\Pi}}$

Here, we derive the evolutions of vector potential operator $\hat{\mathbf{A}}$ and its canonical momentum $\hat{\mathbf{\Pi}}$, which are given by

$$\frac{\mathrm{d}}{\mathrm{d}t}\hat{\mathbf{A}} = \frac{i}{\hbar}[\hat{H}, \hat{\mathbf{A}}] = \frac{1}{\varepsilon_0}\hat{\mathbf{\Pi}}, \tag{A.1}$$

$$\frac{\mathrm{d}}{\mathrm{d}t}\hat{\mathbf{\Pi}} = \frac{i}{\hbar}[\hat{H}, \hat{\mathbf{\Pi}}] = \frac{1}{\mu_0}\nabla^2\hat{\mathbf{A}}, \tag{A.2}$$

where the Hamiltonian $\hat{H}$ is

$$\hat{H} = \int \mathrm{d}^3\mathbf{r}\left[\frac{1}{2\varepsilon_0}\hat{\mathbf{\Pi}}^2 + \frac{1}{2\mu_0}\left(\nabla\times\hat{\mathbf{A}}\right)^2\right], \tag{A.3}$$

and the commutation relation becomes

$$[\hat{A}_j(\mathbf{r}, t), \hat{\Pi}_k(\mathbf{r}', t)] = i\hbar\delta_{jk}\delta^{\perp}(\mathbf{r}-\mathbf{r}'), \tag{A.4}$$

whereas the commutation relation between other pairs of operators are zeros.

The derivation of Eq. (A.1) is relatively easy as $\hat{\mathbf{A}}$ is commutative with $\nabla\times\hat{\mathbf{A}}$, meaning that we can write

$$\begin{aligned}\frac{i}{\hbar}[\hat{H}, \hat{A}_j(\mathbf{r}, t)] &= \frac{i}{2\hbar\varepsilon_0}\int \mathrm{d}^3\mathbf{r}'\,[\hat{\mathbf{\Pi}}^2(\mathbf{r}', t), \hat{A}_j(\mathbf{r}, t)] \\ &= \frac{1}{\varepsilon_0}\hat{\Pi}_j,\end{aligned} \tag{A.5}$$

where we have made use of the commutation relation in Eq. (A.4). This equation is simply the definition of the canonical momentum $\hat{\mathbf{\Pi}}$.

The derivation of Eq. (A.2) is a little bit more complicated. To write the equation more succinctly, let us introduce a Levi–Cività symbol ϵ_{ijk}, where the index i, j, and k can take the values from 1 to 3 and represent each component of the three-dimensional vector space. The values of Levi–Cività symbols

07 December 2024 17:52:47

https://doi.org/10.1063/9780735424074_app1

Optical Quantum Computers: A Route to Practical Continuous Variable Quantum Information Processing, W. Asavanant and A. Furusawa
© 2022 AIP Publishing, published by AIP Publishing

are given by

$$\epsilon_{ijk} = \begin{cases} 1, & (i,j,k) = (1,2,3) \text{ or } (2,3,1) \text{ or } (3,1,2), \\ -1, & (i,j,k) = (1,3,2) \text{ or } (2,1,3) \text{ or } (3,2,1), \\ 0, & \text{when any } i,\ j,\ \text{or } k \text{ takes the same values.} \end{cases} \tag{A.6}$$

We will also use the Einstein summation notation where it is understood that the summation is taken when there are same indices. Another abbreviation we will use is the abbreviation of the partial differentiation where we will denote ∂_m as partial differentiation with respect to the spatial component where $m = 1, 2, 3$ corresponds to x, y, and z, respectively.

Using the above notations, we can write down $[(\nabla \times \hat{\mathbf{A}}(\mathbf{r}', t))^2, \hat{\Pi}_j(\mathbf{r}, t)]$ as

$$\begin{aligned} [(\nabla \times \hat{\mathbf{A}})^2, \hat{\Pi}_j] &= [\epsilon_{klm}\epsilon_{knp}\partial_l \hat{A}_m \partial_n \hat{A}_p, \hat{\Pi}_j] \\ &= \epsilon_{klm}\epsilon_{knp}[\partial_l \hat{A}_m \partial_n \hat{A}_p, \hat{\Pi}_j] \\ &= (\delta_{ln}\delta_{mp} - \delta_{mn}\delta_{pl}) \left[(\partial_l \hat{A}_m)[\partial_n \hat{A}_p, \hat{\Pi}_j] + [\partial_l \hat{A}_m, \hat{\Pi}_j](\partial_n \hat{A}_p) \right], \end{aligned} \tag{A.7}$$

where we used the identity between the Levi–Cività symbol and the Kronecker delta, which can be easily checked. First, we consider the calculations of the commutation relation in Eq. (A.7) which can be equivalently written as

$$[\partial_n \hat{A}_p, \hat{\Pi}_j] = \partial_n \left([\hat{A}_p, \hat{\Pi}_j] \right) - [\hat{A}_p, \partial_n \hat{\Pi}_j]. \tag{A.8}$$

We will show that the first term in Eq. (A.8) contributes to the right-hand side of Eq. (A.2). We can calculate the following:

$$\int \mathrm{d}^3\mathbf{r}' \partial_l \hat{A}_m \partial_n \left([\hat{A}_p, \hat{\Pi}_j] \right) = -\int \mathrm{d}^3\mathbf{r}' (\partial_n \partial_l \hat{A}_m)[\hat{A}_p, \hat{\Pi}_j] = -i\hbar\delta_{pj}\partial_n \partial_l \hat{A}_m, \tag{A.9}$$

$$\int \mathrm{d}^3\mathbf{r}' \partial_l \left([\hat{A}_m, \hat{\Pi}_j] \right) \partial_n \hat{A}_p = -\int \mathrm{d}^3\mathbf{r}' [\hat{A}_m, \hat{\Pi}_j](\partial_l \partial_n \hat{A}_p) = -i\hbar\delta_{mj}\partial_l \partial_n \hat{A}_p. \tag{A.10}$$

Note that we use the integration by part and assume that the vector potentials vanish at the infinity. Including the Kronecker deltas in Eq. (A.7), we arrive at

$$\begin{aligned} -i\hbar(\delta_{ln}\delta_{mp} - \delta_{mn}\delta_{pl})(\delta_{pj}\partial_n \partial_l \hat{A}_m + \delta_{mj}\partial_l \partial_n \hat{A}_p) &= -2i\hbar \left[\partial_n \partial_n \hat{A}_j - \partial_j \left(\partial_n \hat{A}_n \right) \right] \\ &= -2i\hbar \left(\nabla^2 \hat{\mathbf{A}} \right)_j. \end{aligned} \tag{A.11}$$

The second term vanishes due to the Coulomb gauge. When proper coefficients are included, this is the contribution to the right-hand side of Eq. (A.2).

To conclude the derivation, we are left with proving that

$$(\delta_{ln}\delta_{mp} - \delta_{mn}\delta_{pl}) \int \mathrm{d}^3\mathbf{r}' \left(\partial_l \hat{A}_m [\hat{A}_p, \partial_n \hat{\Pi}_j] + [\hat{A}_m, \partial_l \hat{\Pi}_j] \partial_n \hat{A}_p \right) = 0. \tag{A.12}$$

07 December 2024 17:52:47

First, we simplify the expression into

$$\begin{aligned}(\delta_{ln}\delta_{mp} - \delta_{mn}\delta_{pl})\partial_l\hat{A}_m[\hat{A}_p, \partial_n\hat{\Pi}_j] &= (\partial_n\hat{A}_p - \partial_p\hat{A}_n)[\hat{A}_p, \partial_n\hat{\Pi}_j] \\ &= \epsilon_{rnp}\hat{B}_r[\hat{A}_p, \partial_n\hat{\Pi}_j],\end{aligned} \tag{A.13}$$

where $\hat{B}_r$ is a r-component of the magnetic field operator defined via the curl of the vector potential operator. By using the integration by part and assume that the magnetic field vanishes at the infinity, we have

$$\begin{aligned}\int \mathrm{d}^3\mathbf{r}'\epsilon_{rnp}\hat{B}_r[\hat{A}_p, \partial_n\hat{\Pi}_j] &= -i\hbar\delta_{jp}\epsilon_{rnp}\partial_n\hat{B}_r - \int \mathrm{d}^3\mathbf{r}'\hat{B}_r[\epsilon_{rnp}\partial_n\hat{A}_p, \hat{\Pi}_j] \\ &= i\hbar(\nabla\times\hat{\mathbf{B}})_j - \int \mathrm{d}^3\mathbf{r}'\hat{B}_r[\hat{B}_r, \hat{\Pi}_j] \\ &= i\hbar\varepsilon_0\mu_0\frac{\partial\hat{E}_j}{\partial t} - \int \mathrm{d}^3\mathbf{r}'\hat{B}_r[\hat{B}_r, \hat{\Pi}_j],\end{aligned} \tag{A.14}$$

where we use the Maxwell equations for the free space without electric charges here. Therefore, the right-hand side of Eq. (A.12) becomes

$$\begin{aligned}&2i\hbar\varepsilon_0\mu_0\frac{\partial\hat{E}_j}{\partial t} - \int \mathrm{d}^3\mathbf{r}'\left(\hat{B}_r[\hat{B}_r, \hat{\Pi}_j] + [\hat{B}_r, \hat{\Pi}_j]\hat{B}_r\right)\hat{B}_r\Big) \\ &\quad = 2i\hbar\varepsilon_0\mu_0\frac{\partial\hat{E}_j}{\partial t} - 2\mu_0[\hat{H}, \hat{\Pi}_j].\end{aligned} \tag{A.15}$$

The second term on the right is the time evolution of $\hat{\Pi}$. By invoking Eq. (A.1) and the relation between the vector potential and the electric field in the Coulomb gauge, we have

$$2\mu_0[\hat{H}, \hat{\Pi}_j] = -i2\hbar\varepsilon_0\mu_0\frac{\partial^2}{\partial t^2}\hat{A}_j = 2i\hbar\varepsilon_0\mu_0\frac{\partial\hat{E}_j}{\partial t}, \tag{A.16}$$

which finishes our derivations.

A.2 HAMILTONIAN OF THE MONOCHROMATIC MODE

Here, we prove that when we expand the vector potential using the monochromatic mode $\mathbf{A}_k(\mathbf{r}, t)$ given by

$$\mathbf{A}_k(\mathbf{r}, t) = \mathbf{A}_k(\mathbf{r})\exp(-i\Omega_k t), \tag{A.17}$$

the Hamiltonian can be written as

$$\hat{H} = \sum_k \hbar\Omega_k\left(\hat{a}_k^\dagger\hat{a}_k + \frac{1}{2}\right), \tag{A.18}$$

where $\hat{a}_k$ are the annihilation operators associated with mode k.

07 December 2024 17:52:47

To derive this result, let us first note that we are using a set of the vector potentials $\{\mathbf{A}_k(\mathbf{r},t), \mathbf{A}_k^*(\mathbf{r},t)\}$ that are orthonormal with respect to the inner product:

$$(\mathbf{A}_j, \mathbf{A}_k) = i\frac{\varepsilon_0}{\hbar}\int \mathrm{d}^3\mathbf{r}\left(\mathbf{A}_j^* \cdot \frac{\partial \mathbf{A}_k}{\partial t} - \frac{\partial \mathbf{A}_j^*}{\partial t}\cdot \mathbf{A}_k\right). \tag{A.19}$$

For the monochromatic mode, the orthonormal condition can be written using the spatial components as

$$(\mathbf{A}_j(\mathbf{r},t), \mathbf{A}_k(\mathbf{r},t)) = \frac{\varepsilon_0}{\hbar}(\Omega_j + \Omega_k)e^{i(\Omega_j-\Omega_k)t}\int \mathrm{d}^3\mathbf{r}\,\mathbf{A}_j^*(\mathbf{r})\cdot\mathbf{A}_k(\mathbf{r}) = \delta_{jk}, \tag{A.20}$$

$$(\mathbf{A}_j(\mathbf{r},t), \mathbf{A}_k^*(\mathbf{r},t)) = 0. \tag{A.21}$$

The spatial components also satisfy

$$\left(\nabla^2 + \frac{\Omega_k^2}{c^2}\right)\mathbf{A}_k(\mathbf{r}) = 0. \tag{A.22}$$

The vector potential $\hat{\mathbf{A}}(\mathbf{r},t)$ and its canonical momentum $\hat{\mathbf{\Pi}}(\mathbf{r},t)$ are expanded as

$$\hat{\mathbf{A}}(\mathbf{r},t) = \sum_k \left[\mathbf{A}_k(\mathbf{r})e^{-i\Omega_k t}\hat{a}_k + \mathbf{A}_k^*(\mathbf{r})e^{i\Omega_k t}\hat{a}_k^\dagger\right], \tag{A.23}$$

$$\hat{\mathbf{\Pi}}(\mathbf{r},t) = -i\varepsilon_0\sum_k \Omega_k\left[\mathbf{A}_k(\mathbf{r})e^{-i\Omega_k t}\hat{a}_k - \mathbf{A}_k^*(\mathbf{r})e^{i\Omega_k t}\hat{a}_k^\dagger\right]. \tag{A.24}$$

Let us calculate each part of the Hamiltonian $\hat{H}$. The first part concerning the canonical momentum is

$$\begin{aligned}\int \mathrm{d}^3\mathbf{r}\,\frac{1}{2\varepsilon_0}\hat{\mathbf{\Pi}}^2 = -\frac{\varepsilon_0}{2}\sum_{k,k'}\Omega_k\Omega_{k'}\int \mathrm{d}^3\mathbf{r}\,&\left[\mathbf{A}_k(\mathbf{r})e^{-i\Omega_k t}\hat{a}_k - \mathbf{A}_k^*(\mathbf{r})e^{i\Omega_k t}\hat{a}_k^\dagger\right]\\ &\cdot\left[\mathbf{A}_{k'}(\mathbf{r})e^{-i\Omega_{k'} t}\hat{a}_{k'} - \mathbf{A}_{k'}^*(\mathbf{r})e^{i\Omega_{k'} t}\hat{a}_{k'}^\dagger\right].\end{aligned} \tag{A.25}$$

By invoking the orthonormal condition in Eqs. (A.20) and (A.21), we have

$$\int \mathrm{d}^3\mathbf{r}\,\frac{1}{2\varepsilon_0}\hat{\mathbf{\Pi}}^2 = \frac{1}{4}\sum_k \hbar\Omega_k\left(\hat{a}_k\hat{a}_k^\dagger + \hat{a}_k^\dagger\hat{a}_k\right). \tag{A.26}$$

To calculate the second part of the Hamiltonian, we first notice the following relation:

$$\begin{aligned}(\nabla\times\mathbf{A}_k(\mathbf{r}))\cdot(\nabla\times\mathbf{A}_{k'}(\mathbf{r})) &= \nabla\cdot(\mathbf{A}_k\times(\nabla\times\mathbf{A}_{k'})) + \mathbf{A}_k\cdot(\nabla\times(\nabla\times\mathbf{A}_{k'}))\\ &= \nabla\cdot(\mathbf{A}_k\times(\nabla\times\mathbf{A}_{k'})) + \mathbf{A}_k\cdot[\nabla(\nabla\cdot\mathbf{A}_{k'}) - \nabla^2\mathbf{A}_{k'}]\\ &= \nabla\cdot(\mathbf{A}_k\times(\nabla\times\mathbf{A}_{k'})) + \frac{\Omega_k^2}{c^2}\mathbf{A}_k\cdot\mathbf{A}_{k'}.\end{aligned} \tag{A.27}$$

We have used the vector calculus identity, the Coulomb gauge, and the Helmholtz equation in the derivation above. Therefore, we have

$$\int \mathrm{d}^3\mathbf{r}\,\frac{1}{2\mu_0}\left(\nabla\times\hat{\mathbf{A}}\right)^2 = \frac{1}{4}\sum_k \hbar\Omega_k\left(\hat{a}_k\hat{a}_k^\dagger + \hat{a}_k^\dagger\hat{a}_k\right). \tag{A.28}$$

07 December 2024 17:52:47

We notice that the contributions due to the electric field and the magnetic field are equal. Hence, by using the commutation relation of the annihilation and the creation operator, we can write down the Hamiltonian as

$$\hat{H} = \sum_k \hbar\Omega_k \left(\hat{a}_k^\dagger \hat{a}_k + \frac{1}{2}\right). \tag{A.29}$$

A.3 EVOLUTION OF OPERATORS AND BAKER–CAMPBELL–HAUSDORFF FORMULA

In this section, we will first prove the following equation:

$$e^{\hat{A}}\hat{B}e^{-\hat{A}} = \hat{B} + [\hat{A},\hat{B}] + \frac{1}{2}[\hat{A},[\hat{A},\hat{B}]] + \cdots + \frac{1}{n!}[\underbrace{\hat{A},[\hat{A},\ldots,[\hat{A}}_{\text{n terms}},\hat{B}]\ldots] + \cdots. \tag{A.30}$$

This equation is useful for finding the Heisenberg picture evaluation of the operators. To prove this, let us first consider a following function $f(\lambda)$:

$$f(\lambda) = e^{\lambda\hat{A}}\hat{B}e^{-\lambda\hat{A}} = \sum_{\lambda=0}^{\infty} \lambda^n \hat{S}_n. \tag{A.31}$$

Operator $\hat{S}_n$ will correspond to each term in Eq. (A.30). If we consider the nth derivative of $f(\lambda)$ (denoted by $f^{(n)}(\lambda)$), we can easily show that

$$\hat{S}_n = \frac{1}{n!} f^{(n)}(0). \tag{A.32}$$

By actually doing the derivation of $f(\lambda)$ on the exponential terms, we can prove Eq. (A.30).

The Baker–Campbell–Hausdorff (BCH) formula, on the other hand, shows the relation between the product of the exponentials of two operators. We refer the readers to a general textbook on quantum mechanics for proof of the general cases and show only the proof of the case of our interest which is related to the displacement operators.

Theorem A.1. *For operators $\hat{X}$ and $\hat{Y}$ that satisfy*

$$[\hat{X},[\hat{X},\hat{Y}]] = [\hat{Y},[\hat{X},\hat{Y}]] = 0, \tag{A.33}$$

we have

$$e^{\hat{X}}e^{\hat{Y}} = e^{\hat{X}+\hat{Y}+\frac{1}{2}[\hat{X},\hat{Y}]}. \tag{A.34}$$

To prove this, we use a similar approach to the previous derivation and consider a function $g(\lambda)$

$$g(\lambda) = e^{\lambda\hat{X}}e^{\lambda\hat{Y}} = \exp\left(\sum_{n=1}^{\infty} \lambda^n \hat{R}_n\right). \tag{A.35}$$

07 December 2024 17:52:47

By doing the derivation with respect to λ, we have

$$g^{-1}(\lambda)\frac{\mathrm{d}}{\mathrm{d}\lambda}g(\lambda) = e^{-\lambda\hat{Y}}e^{-\lambda\hat{X}}\frac{\mathrm{d}}{\mathrm{d}\lambda}\left(e^{\lambda\hat{X}}e^{\lambda\hat{Y}}\right) = \hat{X} + \hat{Y} + \lambda[\hat{X}, \hat{Y}], \tag{A.36}$$

where we use Eq. (A.30) and the condition in Eq. (A.33). The above equation can be equivalently written as

$$g^{-1}(\lambda)\frac{\mathrm{d}}{\mathrm{d}\lambda}g(\lambda) = \exp\left(-\sum_{k=1}^{\infty}\lambda^n\hat{R}_n\right)\sum_{n=1}^{\infty}n\lambda^{n-1}\hat{R}_n\exp\left(\sum_{n=1}^{\infty}\lambda^n\hat{R}_n\right). \tag{A.37}$$

By comparing Eqs. (A.36) and (A.37), we notice that only the terms that contribute to the first-order of λ matter, and we can easily show that

$$\hat{R}_1 = \hat{X} + \hat{Y}, \tag{A.38}$$

$$\hat{R}_2 = \frac{1}{2}[\hat{X}, \hat{Y}], \tag{A.39}$$

and the rest of $\hat{R}_n$ are zeros which complete our proof. Note that this derivation can also be extended to the case where Eq. (A.33) does not hold.

A.4 PROOF OF THE OVERCOMPLETENESS OF THE COHERENT STATES

Here, we prove the overcompleteness of the coherent states given by

$$\int \mathrm{d}^2\alpha\, |\alpha\rangle\langle\alpha| = \pi\hat{I}, \tag{A.40}$$

where the integration is taken over the phase space. To derive this, let us use the Fock representation of the coherent state and write the left-hand side of Eq. (A.40) as

$$\int \mathrm{d}^2\alpha\, |\alpha\rangle\langle\alpha| = \sum_{m,n=0}^{\infty}\int \mathrm{d}^2\alpha\exp(-|\alpha|^2)\frac{\alpha^m\alpha^{*n}}{\sqrt{m!n!}}|m\rangle\langle n|. \tag{A.41}$$

If we change the parameter $\alpha = A\exp(i\theta)$ where $A \geq 0$ and $0 < \theta < 2\pi$ and use the polar coordinate, the integration becomes

$$\int \mathrm{d}^2\alpha\, |\alpha\rangle\langle\alpha| = \sum_{m,n=0}^{\infty}\int_0^{\infty}A\mathrm{d}A\int_0^{2\pi}\mathrm{d}\theta\exp(-A^2)\frac{A^{m+n}e^{i(m-n)\theta}}{\sqrt{m!n!}}|m\rangle\langle n|. \tag{A.42}$$

It is obvious that the integration with respect to θ becomes 0 when $m \neq n$. Therefore, the above equation is simplified to

$$\int \mathrm{d}^2\alpha\, |\alpha\rangle\langle\alpha| = 2\pi\sum_{n=0}^{\infty}\int_0^{\infty}\mathrm{d}A\exp(-A^2)\frac{A^{2n+1}}{n!}|n\rangle\langle n|. \tag{A.43}$$

07 December 2024 17:52:47

This is a Gaussian integral and can be easily shown to be

$$\int_0^\infty \mathrm{d}A\, A^{2n+1} \exp(-A^2) = \frac{n!}{2}, \tag{A.44}$$

which completes our proof.

A.5 MATHEMATICAL TREATMENT OF AN OPTICAL PARAMETRIC OSCILLATOR

Although we do not go into the details in the main text, we will briefly explain the mathematical treatment of an optical parametric oscillator (OPO) here as it is an important component in the CV optical quantum computation. For more details, we suggest that the readers refer to Collett and Gardiner (1984) and Gardiner and Collett (1985).

Figure A.1 depicts a schematic diagram of an OPO. OPO is an optical cavity with a second-order nonlinear optical crystal placed inside and is then pumped with a pump beam whose frequency is 2Ω, where Ω is the resonance angular frequency of the cavity.

One of the widely used explanations for how OPO generates squeezed light is that by pumping the nonlinear crystal, photon-pairs are generated and trapped inside the cavity and more photon is generated. Although this explanation is not entirely wrong, it does not capture the essence of the OPO. There are three fields involved in the OPO: intracavity field ($\hat{a}$), input field ($\hat{a}_{\mathrm{in}}$), and output field ($\hat{a}_{\mathrm{out}}$). The process of the generation of the squeezed light is an interplay between these three fields and not simply the photon-pair generation inside the cavity. Although they are written similarly, the intracavity mode is a mode of the standing wave, while the input and output modes are that of the propagating wave.

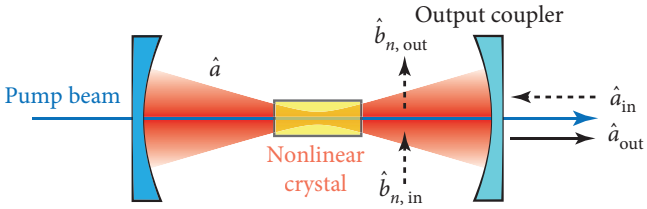

FIG. A.1
Schematic diagram of an optical parametric oscillator. Mode $\hat{a}$ is an intracavity mode. Mode $\hat{a}_{\mathrm{in}}$ is the input vacuum mode and $\hat{a}_{\mathrm{out}}$ is the output mode of our interest. Mode $\hat{b}$ represents the auxiliary mode besides the mode that we are interested in using as squeezed vacuum. Such examples are modes representing intracavity optical losses and mode of the injected phase reference beams.

07 December 2024 17:52:47

A more formal explanation would be that an OPO act as a phase-sensitive amplifier that amplifies the vacuum fluctuation of the input mode.

Now, we will give the mathematical description of the OPO. Here, we will consider the degenerated OPO whose Hamiltonian $\hat{H}_0$ of the intracavity field is given by

$$\hat{H} = \hat{H}_0 + \hat{H}_{\mathrm{DPDC}}, \tag{A.45}$$

where

$$\hat{H}_0 = \hbar\Omega \hat{a}^\dagger \hat{a}, \tag{A.46}$$

$$\hat{H}_{\mathrm{DPDC}} = \frac{1}{2} i\hbar\chi \left(\hat{a}_{\mathrm{p}}^\dagger \hat{a}^2 - \hat{a}_{\mathrm{p}} \hat{a}^{\dagger 2} \right). \tag{A.47}$$

$\hat{H}_0$ is the Hamiltonian of the free evolution of the intracavity field and $\hat{H}_{\mathrm{DPDC}}$ is the Hamiltonian of the degenerated parametric down conversion process of the crystal. The parameter χ corresponds to the strength of the interaction and $\hat{a}_{\mathrm{p}}$ is the annihilation operator of the pump beam mode. Since we are considering the case where the pump beam is a classical light, we replace $\hat{a}_{\mathrm{p}}$ with the complex amplitude of the pump beam and recast $\hat{H}_{\mathrm{DPDC}}$ into

$$\hat{H}_{\mathrm{DPDC}} = \frac{1}{2} i\hbar(\epsilon^* e^{i2\Omega t} \hat{a}^2 - \epsilon e^{-i2\Omega t} \hat{a}^{\dagger 2}), \tag{A.48}$$

with ϵ being a parameter that combines the pump power and the interaction strength together. We will shortly see that this parameter determines the squeezing level.

From the perspective of the intracavity field, in addition to the Hamiltonian $\hat{H}$, there are also effects of the external fields. To incorporate such effects and write down the time evolution of the intracavity field, we use quantum Langevin equation, which can be written down as

$$\frac{\mathrm{d}\hat{a}}{\mathrm{d}t} = \frac{i}{\hbar}[\hat{H}, \hat{a}] - \frac{1}{2} \sum_n \gamma_n \hat{a} + \sqrt{\gamma_0}\hat{a}_{\mathrm{in}} + \sum_{n \neq 0} \sqrt{\gamma_n} \hat{b}_{n,\mathrm{in}}. \tag{A.49}$$

Note that the operators here are not the time-dependent ($\hat{a}(t)$) version, which was discussed in Chap. 2. The first term on the right-hand side is the usual time evolution in the Heisenberg picture. The second term corresponds to the leakage of the cavity mode to the external fields. The third term and the fourth term are contributions from the external fields. Operator $\hat{b}_n$ with $n \geq 1$ corresponds to the fields that are not related to the squeezed light such as auxiliary vacuum states which are useful for consideration of the effect of the optical losses. Parameter γ_n is the decay rate of the intracavity mode to the external fields. Substituting Hamiltonian $\hat{H}$ into Eq. (A.49), we have

$$\frac{\mathrm{d}\hat{a}}{\mathrm{d}t} = -i\Omega\hat{a} - \epsilon e^{-i2\Omega t} \hat{a}^\dagger - \frac{1}{2} \sum_n \gamma_n \hat{a} + \sqrt{\gamma_0}\hat{a}_{\mathrm{in}} + \sum_{n \neq 0} \sqrt{\gamma_n} \hat{b}_{n,\mathrm{in}}. \tag{A.50}$$

To solve this, we move to the operator $\hat{a}(t)$ in the rotating reference frame of Ω and do the Fourier transform to the sideband mode $\tilde{\hat{a}}(\omega)$,

$$\hat{a} = \hat{a}(t) e^{-i\Omega t}, \tag{A.51}$$

07 December 2024 17:52:47

$$\hat{\tilde{a}}(\omega) = \frac{1}{\sqrt{2\pi}} \int \mathrm{d}t\, \hat{a}(t) e^{i\omega t}. \tag{A.52}$$

Therefore, we can write Eq. (A.49) as

$$-i\omega \hat{\tilde{a}}(\omega) = -\epsilon \hat{\tilde{a}}(-\omega) - \Gamma \hat{\tilde{a}}(\omega) + \sqrt{\gamma_0}\hat{\tilde{a}}_{\mathrm{in}}(\omega) + \sum_{n\neq 0} \sqrt{\gamma_n}\hat{\tilde{b}}_{n,\mathrm{in}}(\omega). \tag{A.53}$$

where $\Gamma = \frac{1}{2}\sum_n \gamma_n$. We point out some of the interesting features of Eq. (A.53). First, we observe that dependence on Ω is gone as we have moved into the rotating reference frame. Second, Eq. (A.53) contains only the dependence on $\pm\omega$. In particular, the term that contains $-\omega$ is generated via ϵ, meaning that the interaction due to the OPO in the frequency domain corresponds to the interactions between sideband mode. When $\varepsilon = 0$, we observe that there are only terms that depend on ω, which is expected for an empty cavity.

We can solve Eq. (A.53) for $\hat{\tilde{a}}(\omega)$ as

$$\begin{aligned}\hat{\tilde{a}}(\omega) = {} & \sqrt{\gamma_0}\frac{(-i\omega+\Gamma)\hat{\tilde{a}}_{\mathrm{in}}(\omega) - \epsilon\hat{\tilde{a}}^{\dagger}_{\mathrm{in}}(-\omega)}{(-i\omega+\Gamma)^2 - |\epsilon|^2} \\ & + \sum_{n\neq 0}\sqrt{\gamma_n}\frac{(-i\omega+\Gamma)\hat{\tilde{b}}_{n,\mathrm{in}}(\omega) - \epsilon\hat{\tilde{b}}^{\dagger}_{n,\mathrm{in}}(-\omega)}{(-i\omega+\Gamma)^2 - |\epsilon|^2}.\end{aligned} \tag{A.54}$$

Rather than the intracavity mode, the mode of our interest is the output mode. As we have explained, there is a subtle difference between these two modes: while the intracavity mode is a standing wave mode of the electromagnetic field inside the cavity, the output mode is a propagating electromagnetic field. The relationship between these two modes can be written as (Collett and Gardiner,1984)

$$\hat{\tilde{a}}_{\mathrm{out}}(\omega) = -\hat{\tilde{a}}_{\mathrm{in}}(\omega) + \sqrt{\gamma_0}\hat{\tilde{a}}(\omega). \tag{A.55}$$

Then, we can write down $\hat{\tilde{a}}_{\mathrm{out}}(\omega)$ as

$$\begin{aligned}\hat{\tilde{a}}_{\mathrm{out}}(\omega) = {} & \frac{[|\epsilon|^2 - (-i\omega+\Gamma)^2 + \gamma_0(-i\omega+\Gamma)]\hat{\tilde{a}}_{\mathrm{in}}(\omega) - \gamma_0\epsilon\hat{\tilde{a}}^{\dagger}_{\mathrm{in}}(-\omega)}{(-i\omega+\Gamma)^2 - |\epsilon|^2} \\ & + \sum_{n\neq 0}\sqrt{\gamma_0\gamma_n}\frac{(-i\omega+\Gamma)\hat{\tilde{b}}_{n,\mathrm{in}}(\omega) - \epsilon\hat{\tilde{b}}^{\dagger}_{n,\mathrm{in}}(-\omega)}{(-i\omega+\Gamma)^2 - |\epsilon|^2}.\end{aligned} \tag{A.56}$$

To understand Eq. (A.56) more clearly, we consider the case where there is only a single additional mode ($n = 1$), which corresponds to the auxiliary vacuum state of the optical loss, and rewrite the equation into

$$\hat{\tilde{a}}_{\mathrm{out}}(\omega) = A(\omega)\hat{\tilde{a}}_{\mathrm{in}}(\omega) - B(\omega)\hat{\tilde{a}}^{\dagger}_{\mathrm{in}}(-\omega) + C(\omega)\hat{\tilde{b}}(\omega) - D(\omega)\hat{\tilde{b}}^{\dagger}(-\omega), \tag{A.57}$$

with

$$A(\omega) = \frac{|\epsilon|^2 - (-i\omega+\Gamma)^2 + \gamma_0(-i\omega+\Gamma)}{(-i\omega+\Gamma)^2 - |\epsilon|^2}, \tag{A.58}$$

07 December 2024 17:52:47

$$B(\omega) = \frac{\gamma_0 \epsilon}{(-i\omega + \Gamma)^2 - |\epsilon|^2}, \tag{A.59}$$

$$C(\omega) = \frac{\sqrt{\gamma_0 \gamma_1}(-i\omega + \Gamma)}{(-i\omega + \Gamma)^2 - |\epsilon|^2}, \tag{A.60}$$

$$D(\omega) = \frac{\sqrt{\gamma_0 \gamma_1}\epsilon}{(-i\omega + \Gamma)^2 - |\epsilon|^2}. \tag{A.61}$$

Here, $\Gamma = (\gamma_0 + \gamma_1)/2$. We can see that when $\gamma_1 = 0$ and $C(\omega) = D(\omega) = 0$, which means that there are no interaction (or loss) with any other mode. We also observe that when $\epsilon = 0$, i.e., when there is no parametric down conversion, we have $B(\omega) = 0$ and

$$A(\omega) = \frac{i\omega + \frac{\gamma}{2}}{-i\omega + \frac{\gamma}{2}}, \tag{A.62}$$

meaning that the input field is subjected to the frequency-dependent phase shift. This is the case because the OPO has only one output coupler. We now turn our attention to the case where $\epsilon \neq 0$ and $\gamma_1 = 0$. In such a case, we have

$$\hat{\tilde{a}}_{\text{out}}(\omega) = A(\omega)\hat{\tilde{a}}_{\text{in}}(\omega) - B(\omega)\hat{\tilde{a}}^{\dagger}_{\text{in}}(-\omega), \tag{A.63}$$

with

$$|A(\omega)|^2 - |B(\omega)|^2 = 1. \tag{A.64}$$

Equations (A.63) and (A.67) have the same form as the squeezing operator where instead of the single-mode squeezing, the sideband modes are squeezed. As such, OPO acts as an amplifier that generates quantum correlation (i.e., squeezing) between the sideband mode.

To calculate the squeezing and antisqueezing levels, we calculate the power spectra measured by the homodyne measurement, which was discussed in Chap. 4 and is given by

$$\tilde{S}_\theta(\omega) = \left\langle \left| \hat{X}_\theta(\omega) \right|^2 \right\rangle, \tag{A.65}$$

where

$$\hat{X}_\theta(\omega) = \sqrt{\frac{\hbar}{2}} \left[\hat{\tilde{a}}(\omega) e^{-i\theta} + \hat{\tilde{a}}^{\dagger}(-\omega) e^{i\theta} \right]. \tag{A.66}$$

We will not show explicit proof here, but if we assume without loss of generality that ϵ is a non-negative real number, then the extrema of $\tilde{S}_\theta(\omega)$ which correspond to squeezing (denoted by $\tilde{S}_-(\omega)$) and antisqueezing (denoted by $\tilde{S}_+(\omega)$) can be calculated as

$$\tilde{S}_\pm(\omega) = \frac{\hbar}{2} \left[1 \pm \frac{\gamma_0}{\gamma_0 + \gamma_1} \frac{4x}{(1 \mp x)^2 + (\omega/\omega_0)^2} \right], \tag{A.67}$$

where $x = \epsilon/\Gamma$ is a normalized pump amplitude and $\omega_0 = \Gamma$ corresponds to the bandwidth of the squeezed light. If we assume that the additional mode to be the ancillary vacuum state corresponds to

07 December 2024 17:52:47

the intracavity loss L and the transmittivity of the output coupler to be T, Eq. (A.67) becomes

$$\tilde{S}_{\pm}(\omega) = \frac{\hbar}{2}\left[1 \pm \frac{T}{T+L}\frac{4x}{(1\mp x)^2 + (\omega/\omega_0)^2}\right]. \tag{A.68}$$

We observe that for all ω,

$$\tilde{S}_{+}(\omega)\tilde{S}_{-}(\omega) \geq \frac{\hbar^2}{4}, \tag{A.69}$$

where the equality is satisfied if $L = 0$.

A.6 MULTIMODE WIGNER FUNCTION AND ANALYSIS OF QUANTUM TELEPORTATION

In this section, we will discuss the mathematical descriptions of the multimode Wigner function and its usage in the analysis of quantum teleportation. First, the multimode Wigner function is defined as

Definition A.1. N-mode Wigner function $W(\mathbf{x}, \mathbf{p})$ of a density matrix ρ is given by

$$W(\boldsymbol{x}, \boldsymbol{p}) = \frac{1}{(2\pi\hbar)^N}\int \mathrm{d}^N\boldsymbol{\zeta}\left\langle \boldsymbol{x} + \frac{1}{2}\boldsymbol{\zeta}\middle|\hat{\rho}\middle|\boldsymbol{x} - \frac{1}{2}\boldsymbol{\zeta}\right\rangle \exp\left(-\frac{i}{\hbar}\boldsymbol{\zeta}^{\mathrm{T}}\boldsymbol{p}\right), \tag{A.70}$$

where $\boldsymbol{\zeta} = (\zeta_1, \zeta_2, \ldots, \zeta_N)^{\mathrm{T}}$, $\boldsymbol{x} = (x_1, x_2, \ldots, x_N)^{\mathrm{T}}$, $\boldsymbol{p} = (p_1, p_2, \ldots, p_N)^{\mathrm{T}}$, and the integration is taken with respect to the space of $\boldsymbol{\zeta}$. The ket vectors $|\boldsymbol{x}\rangle$ is an abbreviation for

$$|\boldsymbol{x}\rangle = |x_1\rangle_1 \otimes |x_2\rangle_2 \otimes \cdots \otimes |x_N\rangle_N. \tag{A.71}$$

The marginal distribution of the quadrature in each mode can be calculated similar to the single-mode case. To derive the input–output relation of the teleportation circuit, however, we have to consider what happens to the Wigner function when a certain mode is measured. To do so, we prove the following theorems.

Theorem A.2. *The Wigner function of the quantum state when the partial trace is taken can be calculated by integrating the original Wigner function with respect to both x and p of the modes that are traced out. For example, if we consider two-mode quantum state whose Wigner function is $W(x_1, x_2, p_1, p_2)$ and we trace out mode 2, the output Wigner function is*

$$W'(x_1, p_1) = \int\int \mathrm{d}x_2\mathrm{d}p_2\, W(x_1, x_2, p_1, p_2). \tag{A.72}$$

We show the proof for the case where $N = 2$ below, and the general case can be proved in a similar way.

07 December 2024 17:52:47

Proof. By using the definition of the Wigner function in Eq. (A.70), we can write down the right-hand side of Eq. (A.72) as

$$\frac{1}{(2\pi\hbar)^2}\int\int \mathrm{d}x_2\mathrm{d}p_2\int\int \mathrm{d}\zeta_1\mathrm{d}\zeta_2 \times\left\langle x_1+\frac{1}{2}\zeta_1\middle|\left\langle x_2+\frac{1}{2}\zeta_2\middle|\,\hat{\rho}\,\middle|x_2-\frac{1}{2}\zeta_2\right\rangle\middle|x_1-\frac{1}{2}\zeta_1\right\rangle \exp\left[-\frac{i}{\hbar}(\zeta_1 p_1+\zeta_2 p_2)\right]. \tag{A.73}$$

If we perform the integration with respect to p_2 first, we will have delta function in ζ_2 as

$$\frac{1}{2\pi\hbar}\int \mathrm{d}p_2\,\exp\left(-\frac{i}{\hbar}\zeta_2 p_2\right)=\delta(\zeta_2). \tag{A.74}$$

Therefore, Eq. (A.73) becomes

$$W'(x_1,p_1)=\frac{1}{2\pi\hbar}\int \mathrm{d}x_2\int \mathrm{d}\zeta_1\left\langle x_1+\frac{1}{2}\zeta_1\middle|\,\langle x_2|\,\hat{\rho}\,|x_2\rangle\,\middle|x_1-\frac{1}{2}\zeta_1\right\rangle \times\exp\left(-\frac{i}{\hbar}\zeta_1 p_1\right). \tag{A.75}$$

Now, we notice that the term regarding x_2 is equivalent to partial trace, i.e.,

$$\mathrm{Tr}_2(\hat{\rho})=\int \mathrm{d}x_2\,\langle x_2|\,\hat{\rho}\,|x_2\rangle. \tag{A.76}$$

Thus, the right-hand side of Eq. (A.72) is a Wigner function of the density matrix where mode 2 is traced out and hence complete our proof. □

Another theorem we have to prove beforehand is regarding the measurement of one of the modes of the Wigner function, which can be stated as follows.

Theorem A.3. *The unnormalized Wigner function of the quantum state when one of the modes is measured (for example, x) and the measurement result is obtained (for example, m_x) is given by replacing the appropriate quadrature with the measurement result m_x and integrating out the orthogonal quadrature. The norm of this new Wigner function is unnormalized and corresponds to the probability density of obtaining the measurement results.*

As an example, if we consider a two-mode quantum state whose Wigner function is $W(x_1, x_2, p_1, p_2)$ and we measure x_2 and obtain the result m_x, the resulting unnormalized Wigner function $W_{m_x}(x_1,p_1)$ is given by

$$W_{m_x}(x_1,p_1)=\int \mathrm{d}p_2\,W(x_1,p_1,m_x,p_2). \tag{A.77}$$

The proof of this theorem is almost the same as the proof of Eq. (A.72) where instead of integrating with respect to x_2, we replace x_2 with m_x. Moreover, the relation between the norm and the probability is evident from the relation between the Wigner function and the marginal distribution of the quadrature operator.

07 December 2024 17:52:47

Now that we have completed the preliminary preparation, we are ready to derive the results regarding the output of the quantum teleportation in Chap. 3 which states that the output Wigner function of the teleported input state $W_{\rm in}(x_{\rm in}, p_{\rm in})$ is given by

$$W_{\rm out}(x_{\rm out}, p_{\rm out}) = \int\int {\rm d}x{\rm d}p\, W_{\rm in}(x,p)\Phi(x_{\rm out}-x, p_{\rm out}-p), \tag{A.78}$$

where

$$\Phi(x_{\rm out}-x, p_{\rm out}-p) \equiv \int\int {\rm d}x'{\rm d}p'\, W_{AB}(x',p',x_{\rm out}-x+x', p_{\rm out}-p-p') \tag{A.79}$$

and $W_{\rm AB}(x_{\rm A}, p_{\rm A}, x_{\rm B}, p_{\rm B})$ is the Wigner function of the two-mode entangled resource state used in the quantum teleportation. The proof of Eq. (A.78) is given below.

Proof. The initial combined Wigner function of the input state and the two-mode entangled resource state is given by

$$W_{\rm ini}(x_{\rm in}, p_{\rm in}, x_A, p_A, x_B, p_B) = W_{\rm in}(x_{\rm in}, p_{\rm in}) W_{AB}(x_A, p_A, x_B, p_B). \tag{A.80}$$

Then, we use a 50:50 beamsplitter, which transforms the quadrature operator into

$$\begin{pmatrix} \hat{x}'_{\rm in} \\ \hat{x}'_{\rm A} \\ \hat{p}'_{\rm in} \\ \hat{p}'_{\rm A} \end{pmatrix} = \frac{1}{\sqrt{2}} \begin{pmatrix} 1 & -1 & 0 & 0 \\ 1 & 1 & 0 & 0 \\ 0 & 0 & 1 & -1 \\ 0 & 0 & 1 & 1 \end{pmatrix} \begin{pmatrix} \hat{x}_{\rm in} \\ \hat{x}_{\rm A} \\ \hat{p}_{\rm in} \\ \hat{p}_{\rm A} \end{pmatrix}. \tag{A.81}$$

If we use the transformation of the Wigner function due to Gaussian operations explained in Chap. 2 and we measure $\hat{x}'_{\rm in}$ and $\hat{p}'_{\rm A}$ and get the measurement results m_x and m_p, the (unnormalized) Wigner function of the output mode at this state is

$$\begin{aligned} W_{m_x,m_p}(x_{\rm B}, p_{\rm B}) = \int\int {\rm d}p'_{\rm in}{\rm d}x'_{\rm A}\, W_{\rm in}\left(\frac{m_x+x'_{\rm A}}{\sqrt{2}}, \frac{p'_{\rm in}+m_p}{\sqrt{2}}\right) \\ \times W_{\rm AB}\left(\frac{x'_{\rm A}-m_x}{\sqrt{2}}, \frac{m_p-p'_{\rm in}}{\sqrt{2}}, x_{\rm B}, p_{\rm B}\right). \end{aligned} \tag{A.82}$$

After the Bell measurement, mode B is displaced by the amount $\sqrt{2}m_x$ and $\sqrt{2}m_p$ and the classical information regarding (m_x, m_p) is used, which results in the output state,

$$\begin{aligned} W_{\rm out}(x_{\rm out}, p_{\rm out}) = \int\int {\rm d}m_x{\rm d}m_p \int\int {\rm d}p'_{\rm in}{\rm d}x'_{\rm A}\, W_{\rm in}\left(\frac{m_x+x'_{\rm A}}{\sqrt{2}}, \frac{p'_{\rm in}+m_p}{\sqrt{2}}\right) \\ W_{\rm AB}\left(\frac{x'_{\rm A}-m_x}{\sqrt{2}}, \frac{m_p-p'_{\rm in}}{\sqrt{2}}, x_{\rm out}-\sqrt{2}m_x, p_{\rm out}-\sqrt{2}m_p\right). \end{aligned} \tag{A.83}$$

To arrive at Eq. (A.78), we change the integration variables as

$$x = \frac{m_x + x'_{\rm A}}{\sqrt{2}}, \tag{A.84}$$

07 December 2024 17:52:47

$$p = \frac{p'_{\rm in} + m_p}{\sqrt{2}}, \tag{A.85}$$

$$x' = \frac{x'_{\rm A} - m_x}{\sqrt{2}}, \tag{A.86}$$

$$p' = \frac{m_p - p'_{\rm in}}{\sqrt{2}}. \tag{A.87}$$

Then, we arrive at

$$W_{m_x,m_p}(x_{\rm B}, p_{\rm B}) = \int\int {\rm d}x{\rm d}p\, W_{\rm in}(x,p) \int\int {\rm d}x'{\rm d}p' \times W_{\rm AB}(x', p', x_{\rm out} - x + x', p_{\rm out} - p - p'), \tag{A.88}$$

which completes our proof. □

A.7 WIGNER FUNCTIONS OF GKP QUBITS

In this section, we show the ideas of how to calculate the Wigner function of the GKP qubits. For convenience, we consider a unit system where $\hbar = 1$ and we write down again the bases of the GKP qubit,

$$|0_{\rm L}\rangle = \sum_{s=-\infty}^{\infty} \left|x = 2s\sqrt{\pi}\right\rangle = \sum_{s=-\infty}^{\infty} \left|p = s\sqrt{\pi}\right\rangle, \tag{A.89}$$

$$|1_{\rm L}\rangle = \sum_{s=-\infty}^{\infty} \left|x = (2s+1)\sqrt{\pi}\right\rangle = \sum_{s=-\infty}^{\infty} (-1)^s \left|p = s\sqrt{\pi}\right\rangle, \tag{A.90}$$

$$|+_{\rm L}\rangle = \sum_{s=-\infty}^{\infty} \left|x = s\sqrt{\pi}\right\rangle = \sum_{s=-\infty}^{\infty} \left|p = 2s\sqrt{\pi}\right\rangle, \tag{A.91}$$

$$|-_{\rm L}\rangle = \sum_{s=-\infty}^{\infty} (-1)^s \left|x = s\sqrt{\pi}\right\rangle = \sum_{s=-\infty}^{\infty} \left|p = (2s+1)\sqrt{\pi}\right\rangle. \tag{A.92}$$

As ideal GKP qubits are unnormalizable, the Wigner function of the GKP qubits are also unnormalizable and we are focused on the positions and the (relative) height of the delta function peaks. Although it is possible to calculate the ideal Wigner function using Dirac comb and its Fourier transform, we consider the finite squeezing approximation given by

$$|0_\Delta\rangle = N_{|0_\Delta\rangle} \sum_{s=-\infty}^{\infty} \exp\left[-\pi(2s)^2\Delta^2\right] \int_{-\infty}^{\infty} {\rm d}x\, \exp\left[-\frac{(x - 2s\sqrt{\pi})^2}{4\Delta^2}\right] |x\rangle, \tag{A.93}$$

$$|1_\Delta\rangle = N_{|1_\Delta\rangle} \sum_{s=-\infty}^{\infty} \exp\left[-\pi(2s+1)^2\Delta^2\right] \int_{-\infty}^{\infty} {\rm d}x\, \exp\left[-\frac{(x - (2s+1)\sqrt{\pi})^2}{4\Delta^2}\right] |x\rangle, \tag{A.94}$$

07 December 2024 17:52:47

where $N_{|0_\Delta\rangle}$ and $N_{|1_\Delta\rangle}$ are the normalization factors. In the limit where $\Delta \to 0$, we have the ideal GKP qubit. As such, we can calculate the Wigner function for the case where Δ is finite and then take the ideal limit to evaluate the Wigner function of the ideal GKP qubit. First, let us look at the Wigner function of $|0_\Delta\rangle$, which can be calculated as

$$W_{|0_\Delta\rangle\langle 0_\Delta|}(x,p) = \frac{\left|N_{|0_\Delta\rangle}\right|^2}{2\pi} \sum_{s,s'} \exp\left[-4\pi\Delta^2(s^2+s'^2)\right] \times \int \mathrm{d}\zeta \ \exp\left\{-\frac{1}{4\Delta^2}\left[\left(x+\frac{1}{2}\zeta-2s\sqrt{\pi}\right)^2+\left(x-\frac{1}{2}\zeta-2s'\sqrt{\pi}\right)^2\right]-i\zeta p\right\}. \tag{A.95}$$

The above integration is simply a Guassian integration, which can be easily solved using the fact that

$$\int \mathrm{d}x \ \exp(-ax^2+bx+c) = \sqrt{\frac{\pi}{a}} \exp\left(\frac{b^2}{4a}+c\right), \tag{A.96}$$

which holds for $a > 0$ even when b is a complex number. Comparing Eq. (A.95) with this formula, we have

$$a = \frac{1}{8\Delta^2}, \tag{A.97}$$

$$b = -\frac{1}{4\Delta^2}[2(s'-s)\sqrt{\pi}+i4\Delta^2 p], \tag{A.98}$$

$$c = -\frac{1}{4\Delta^2}[(x-2s\sqrt{\pi})^2+(x-2s'\sqrt{\pi})^2], \tag{A.99}$$

which means that the Wigner function is

$$W_{|0_\Delta\rangle\langle 0_\Delta|}(x,p) = \frac{\left|N_{|0_\Delta\rangle}\right|^2\sqrt{8\pi\Delta^2}}{2\pi} \sum_{s,s'} \exp\left[-4\pi\Delta^2(s^2+s'^2)\right] \times \exp\left\{-\frac{1}{4\Delta^2}[(x-2s\sqrt{\pi})^2+(x-2s'\sqrt{\pi})^2]\right\} \times \exp\left\{\frac{1}{8\Delta^2}[2(s'-s)\sqrt{\pi}+i4\Delta^2 p]^2\right\}. \tag{A.100}$$

We can observe that the x and p components are separated into two Gaussian functions. This can be further simplified as

$$\exp\left\{-\frac{1}{4\Delta^2}[(x-2s\sqrt{\pi})^2+(x-2s'\sqrt{\pi})^2]\right\} = \exp\left\{-\frac{1}{2\Delta^2}\left[x-(s+s')\sqrt{\pi}\right]^2\right\} \exp\left[-\frac{1}{2\Delta^2}\pi(s-s')^2\right], \tag{A.101}$$

$$\exp\left\{\frac{1}{8\Delta^2}[2(s'-s)\sqrt{\pi}+i4\Delta^2 p]^2\right\} = \exp\left[\frac{1}{2\Delta^2}\pi(s-s')^2\right] \times \exp\left[i2\sqrt{\pi}(s-s')p\right]\exp\left[-2\Delta^2 p\right], \tag{A.102}$$

07 December 2024 17:52:47

which gives

$$W_{|0_\Delta\rangle\langle 0_\Delta|}(x,p) = \frac{\left|N_{|0_\Delta\rangle}\right|^2 \sqrt{8\pi\Delta^2}}{2\pi} \exp\left[-2\Delta^2 p\right] \times \sum_{s,s'} \exp\left[-4\pi\Delta^2(s^2+s'^2)\right] \exp\left\{-\frac{1}{2\Delta^2}\left[x-(s+s')\sqrt{\pi}\right]^2\right\} \times \exp\left[i2\sqrt{\pi}(s-s')p\right]. \tag{A.103}$$

We observe that for x, the Wigner function is a sum of Gaussian functions that are localized near an integer time of $\sqrt{\pi}$, and become delta peaks when $\Delta \to 0$. On the other hand, the Wigner function has an oscillatory term in p. In the limit where $\Delta \to 0$, the only term that matters for p is $\exp[i2\sqrt{\pi}(s-s')p]$. For most of the time, when we do the summation with respect to $s-s'$, the resulting values will be small. However, when p is an integer time of $\sqrt{\pi}$ or $\sqrt{\pi}/2$, the values of the exponential will be either 1 or -1 regardless of $s-s'$. Whether the output values will be 1 or -1 depends on the position of x, i.e., $s+s'$. When $s+s'$ is an even number, both s and s' must be either odd or even, meaning that regardless of the actual value of s and s', $s-s'$ will be even. On the other hand, when $s+s'$ is an odd number, $s-s'$ will be an odd number.

For $|1_\Delta\rangle$, a similar calculations can be done where s and s' are replaced by $s+1/2$ and $s'+1/2$, which results in a shift in the position of x. For a more general state that can be written using the GKP qubit basis, we can borrow the idea of the qubit and write down a general density matrix $\hat{\rho}$ as

$$\hat{\rho} = \frac{1}{2}(a_0\hat{I} + a_x\hat{\sigma}_x + a_y\hat{\sigma}_y + a_z\hat{\sigma}_z), \tag{A.104}$$

where each parameter is an identity operator and a Pauli operator on the basis of the ideal GKP qubit $\{|0_L\rangle, |1_L\rangle\}$. These operators can be written as

$$\hat{I} = |0_L\rangle\langle 0_L| + |1_L\rangle\langle 1_L|, \tag{A.105}$$
$$\hat{\sigma}_x = |0_L\rangle\langle 1_L| + |1_L\rangle\langle 0_L|, \tag{A.106}$$
$$\hat{\sigma}_y = -i|0_L\rangle\langle 1_L| + i|1_L\rangle\langle 0_L|, \tag{A.107}$$
$$\hat{\sigma}_z = |0_L\rangle\langle 0_L| - |1_L\rangle\langle 1_L|. \tag{A.108}$$

Note that this notation is useful only for writing down any quantum state that is within the region represented by the ideal GKP qubits; most of the states (e.g., finite squeezing GKP qubits) will not be within this region. Nevertheless, this notation is useful for writing down the Wigner function of various GKP qubits as the Wigner function of $\hat{\rho}$ is simply the combination of the Wigner function of each part.

Although we will omit the calculations and refer the readers to Mensen *et al.* (2020) for more details regarding the phase-space representation of the GKP qubits, some of the basic ideas of the calculations are similar to the arguments shown here and the Wigner functions of each operator are shown in Fig. A.2. We notice that the spacing for all the bases is $\sqrt{\pi}$. We also notice some other properties regarding displacement. For example, the displacement in the x direction by $\sqrt{\pi}$ (Pauli-X operation)

07 December 2024 17:52:47

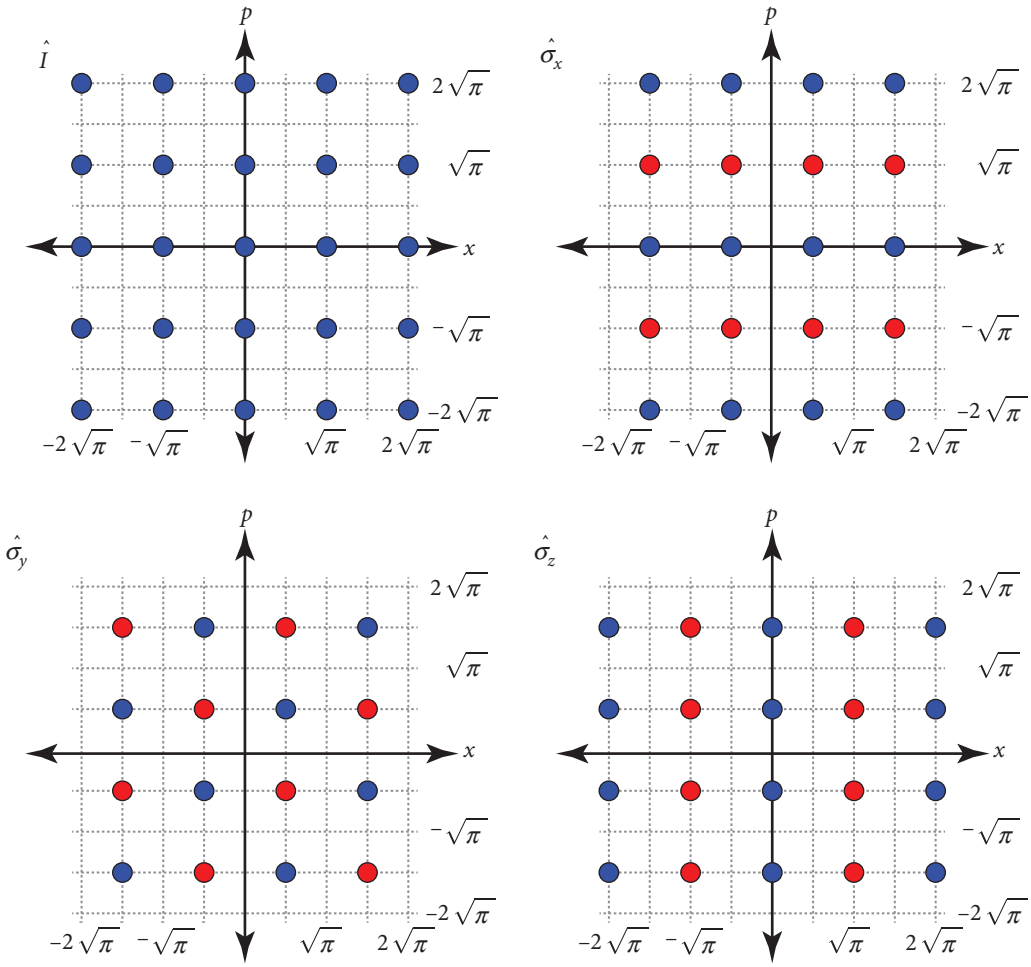

FIG. A.2
Wigner function plots of the identity and the Pauli operators in the ideal GKP basis. Blue dots are positive delta functions, while red dots are negative delta functions. The heights of the delta functions are uniform and depend on the normalization condition as the GKP qubits are unnormalizable.

flips the sign of $\hat{\sigma}_y$ and $\hat{\sigma}_z$, while the displacement in the p direction by $\sqrt{\pi}$ (Pauli-Z operation) flips the sign of $\hat{\sigma}_y$ and $\hat{\sigma}_x$. On the other hand, $\hat{\sigma}_y$ returns to itself after the implementation of consecutive displacement by $\sqrt{\pi}$ in both directions.

07 December 2024 17:52:47

REFERENCES

Collett, M. J. and Gardiner, C. W., "Squeezing of intracavity and traveling-wave light fields produced in parametric amplification," Phys. Rev. A **30**, 1386–1391 (1984).

Gardiner, C. W. and Collett, M. J., "Input and output in damped quantum systems: Quantum stochastic differential equations and the master equation," Phys. Rev. A **31**, 3761–3774 (1985).

Mensen, L. J., Baragiola, B. Q., and Menicucci, N. C., "Phase-space methods for representing, manipulating, and correcting Gottesman–Kitaev–Preskill qubits," arXiv:2012.12488 (2020).

07 December 2024 17:52:47

APPENDIX B: EXPERIMENTAL METHODS IN QUANTUM OPTICS EXPERIMENTS

B.1 GAUSSIAN BEAM

In many of the introductory textbooks, electromagnetic waves are usually considered as a plane wave. In the actual physical situations, however, the lights are not spread throughout the whole region but are contained near a certain axis. In general, the electric fields of the electromagnetic wave in free space follow the wave equation

$$\nabla^2 \mathbf{E} - \frac{1}{c^2}\frac{\partial^2 \mathbf{E}}{\partial t^2} = 0. \tag{B.1}$$

If we consider an electromagnetic wave propagating in the z axis and consider one of the electrical field components $E(\mathbf{r}, t)$, we can consider a solution that has a form

$$E(\mathbf{r}, t) = \mathcal{E}(x, y, z)\exp[i(kz - \omega t)], \tag{B.2}$$

where the phase term is the phase term of a plane wave. Substituting this into the wave equation, we have

$$\frac{\partial^2 \mathcal{E}}{\partial x^2} + \frac{\partial^2 \mathcal{E}}{\partial y^2} + \frac{\partial^2 \mathcal{E}}{\partial z^2} + 2ik\frac{\partial \mathcal{E}}{\partial z} = 0. \tag{B.3}$$

Although this equation is exact, for most of the cases, the following approximation holds:

$$\left|\frac{\partial^2 \mathcal{E}}{\partial z^2}\right| \ll 2k\left|i\frac{\partial \mathcal{E}}{\partial z}\right|. \tag{B.4}$$

This approximation is that $\mathcal{E}$ does not rapidly change with z and the main contributor of z dependence comes from the exponential term. In this approximation, we ignore the second-order derivative of $\mathcal{E}$ in Eq. (B.3), which makes us able to solve the differential equation. One of the possible sets of a complete solution is called the *Hermite–Gaussian mode* (or simply Gaussian beam) and has a form

$$\begin{aligned}\mathcal{E}_{mn}(\mathbf{r}, t) = \mathcal{E}\frac{w_0}{w(z)}H_m\left(\frac{\sqrt{2}x}{w(z)}\right)H_n\left(\frac{\sqrt{2}y}{w(z)}\right)\exp\left[-\frac{x^2+y^2}{w^2(z)}\right] \\ \times \exp\left[ik\frac{x^2+y^2}{2R(z)} + i\left[kz - (m+n+1)\arctan\left(\frac{z}{z_0}\right)\right] - i\omega t\right],\end{aligned} \tag{B.5}$$

07 December 2024 17:52:47

Optical Quantum Computers: A Route to Practical Continuous Variable Quantum Information Processing, W. Asavanant and A. Furusawa
© 2022 AIP Publishing, published by AIP Publishing

where m and n are non-negative integers, $H_m(\cdot)$ is a Hermite polynomial of the order n. The parameters defining Eq. (B.5) are given by

$$w(z) = w_0\sqrt{1+\frac{z^2}{z_0^2}}, \tag{B.6}$$

$$R(z) = z\left(1+\frac{z_0^2}{z^2}\right), \tag{B.7}$$

$$z_0 = \frac{\pi w_0^2}{\lambda}, \tag{B.8}$$

with λ being the wavelength and we assume that the beam waist (i.e., the location where the beam is most concentrated around z axis) is located at $z = 0$. We are usually interested in the parameter $w(z)$ (and its position). This parameter is called the beam waist and z_0 is called the Rayleigh range.

The Hermite–Gaussian mode is usually denoted by TEM_{mn} and the laser light is usually a mode where $m = n = 0$, which corresponds to the case where the intensity of the beam in xy plane has a Gaussian function. When a Gaussian beam passes through optical components such as lenses and mirrors, it is transformed into another Gaussian beam. In the quantum optics experiments, because the interference visibility has to be kept high, it is important to keep track of the shape of the Gaussian beams as Gaussian beams with different shapes (i.e., different parameters) do not perfectly interfere. The shape of the Gaussian beam and its transformation can be tracked using a single parameter called beam parameter $q(z)$ given by

$$\frac{1}{q(z)} = \frac{1}{R(z)} + i\frac{\lambda}{\pi w^2(z)}. \tag{B.9}$$

In the paraxial limit, an optical component can be characterized using a 2×2 matrix called the ABCD matrix. The beam parameters q' after a system with ABCD matrix $\left(\begin{smallmatrix} A & B \\ C & D \end{smallmatrix}\right)$ is related to the initial beam parameter q by

$$q' = \frac{Aq+B}{Cq+D}. \tag{B.10}$$

For more details regarding the Gaussian beam, we refer the readers to textbooks in classical optics such as Yariv and Yeh (2006).

B.2 OPTICAL CAVITY

An optical cavity has various applications in quantum optics experiments. It can be used to amplify the field intensity inside the cavity and can also act as a filter for both frequency and spatial mode. In this section, we will discuss various aspects of the optical cavity. First, we will discuss about the frequency aspect (longitudinal mode) and the spatial mode aspect (transverse mode) of the cavity. Not all frequencies and all shapes of beams can be supported by the cavity, and such discussions are important when designing an experimental system. Next, we discuss how to stabilize (i.e., lock) an optical cavity.

07 December 2024 17:52:47

B.2.1 Longitudinal mode

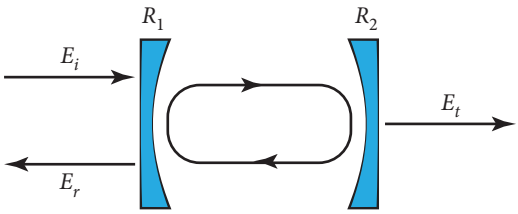

FIG. B.1
Schematic diagram of an optical cavity.

Figure B.1 shows a typical optical cavity with two mirrors whose energy reflectivities are R_1 and R_2. If we let the round-trip length of the cavity be $2l$ and the decay rate per length of the electric field amplitude inside the cavity be α, we can calculate the relation of the transmitted electric field amplitude E_t and reflected electric field amplitude E_r to the input electric field amplitude E_i as

$$E_t = \left[\frac{\sqrt{(1-R_1)(1-R_2)}e^{i\delta}e^{-\alpha l}}{1-\sqrt{R_1R_2}e^{2i\delta}e^{-2\alpha l}}\right]E_i, \tag{B.11}$$

$$E_r = \left[\frac{-\sqrt{R_1}+\sqrt{R_2}e^{i2\delta}e^{-\alpha l}}{1-\sqrt{R_1R_2}e^{2i\delta}e^{-2\alpha l}}\right]E_i, \tag{B.12}$$

with δ being an amount of phase accumulated during the half-trip inside the cavity. Note that this δ would depend on the frequency of the beam we are considering. If we use a round-trip intracavity loss $L = 1 - \exp(-4\alpha)$, we can further simplify the above equations into

$$E_t = \frac{\sqrt{(1-R_1)(1-R_2)}\sqrt[4]{(1-L)}e^{i\delta}}{1-\sqrt{R_1R_2}\sqrt{1-L}e^{2i\delta}}E_i, \tag{B.13}$$

$$E_r = \left[-\sqrt{R_1}+\frac{(1-R_1)\sqrt{R_2}\sqrt[4]{(1-L)}e^{i2\delta}}{1-\sqrt{R_1R_2}\sqrt{1-L}e^{2i\delta}}\right]E_i. \tag{B.14}$$

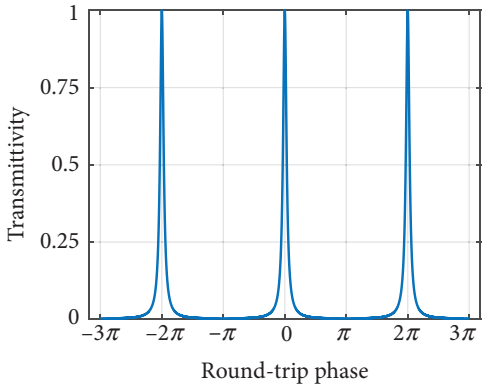

FIG. B.2
Transmittivity of an optical cavity as a function of round-trip phase (2δ) with parameters $R_1 = R_2 = 0.9$ and $L = 0$.

Let us look at the transmitted power, which can be calculated as

$$\frac{I_t}{I_i} = \left|\frac{E_t}{E_i}\right|^2 = \frac{(1-R_1)(1-R_2)\sqrt{1-L}}{1+R_1R_2(1-L)-2\sqrt{R_1R_2}\sqrt{1-L}\cos 2\delta} \tag{B.15}$$

and is plotted in Fig. B.2. It is obvious that the maximum transmitted power occurs at

$$2\delta = 2\pi p, \tag{B.16}$$

i.e, when the phase accumulated during a round trip inside the cavity is an integer time of 2π. On the other hand, we see from Fig. B.2 that when 2δ is sufficiently far from a multiple of 2π, most of the lights are reflected off the cavity and are not transmitted, making the optical cavity work as a frequency filtering. The maximum transmitted power is given by

$$\left(\frac{I_t}{I_i}\right)_{\max} = \frac{(1-R_1)(1-R_2)\sqrt{1-L}}{\left(1-\sqrt{R_1R_2(1-L)}\right)^2}. \tag{B.17}$$

07 December 2024 17:52:47

At the condition where $R_1 = R_2$ and the cavity is lossless ($L = 0$), all the lights are transmitted. This condition is sometimes called impedance matching condition, similar to the impedance matching in the electrical circuits. Therefore, if we want a cavity to transmit as much power as possible, rather than the actual values of the reflectivity, it is important that the reflectivities of the input and output mirror are matched.

Equation (B.16) shows that there are many resonant frequencies in a single cavity. One of the important parameters defining the longitudinal mode of the cavity is the spacing between the resonant points—free spectral range (FSR)—given by

$$\mathrm{FSR} = \frac{c}{2l}. \tag{B.18}$$

Therefore, if we want to make a cavity with large spacing between the resonant frequencies (i.e., large FSR), we have to make a cavity that is small. Another important parameter is the full-width half-maximum (FWHM) of the resonant peaks. If we let $2\delta = \pm\Delta$ be a point where the transmitted power is half of the maximum level, we have

$$\cos\Delta = 1 - \frac{1}{2}\left(\frac{1-\sqrt{R_1R_2(1-L)}}{\sqrt[4]{R_1R_2(1-L)}}\right)^2. \tag{B.19}$$

For the case of our interest where L is sufficiently small and the reflectivities of the mirrors are closed to 1, we can approximate Δ as

$$\Delta = \frac{1-\sqrt{R_1R_2(1-L)}}{\sqrt[4]{R_1R_2(1-L)}}, \tag{B.20}$$

and the FWHM becomes

$$\mathrm{FWHM} = \frac{1}{\pi}\frac{1-\sqrt{R_1R_2(1-L)}}{\sqrt[4]{R_1R_2(1-L)}}\frac{c}{2l}. \tag{B.21}$$

FWHM by itself does not show how sharp the resonant peaks of the optical cavity are; we need to compare it with the distance between the peaks, i.e., the FSR, to quantify the sharpness. This quantity is called *Finesse* ($\mathcal{F}$), which is given by

$$\mathcal{F} = \frac{\mathrm{FSR}}{\mathrm{FWHM}} = \frac{\pi\sqrt[4]{R_1R_2(1-L)}}{1-\sqrt{R_1R_2(1-L)}}. \tag{B.22}$$

These parameters must be designed so that the optical cavity is appropriate for each application.

If we return to the definition of the Gaussian beam in Eq. (B.5), we see that there is a phase term that depends on m and n. This term is called *Gouy phase*. As we have briefly discussed, the positions of the resonant peaks depend on the accumulated phase during a round trip inside the cavity. Therefore, as the Hermite–Gaussian mode with different orders accumulates different phases, their resonant frequencies can be different, allowing the optical cavity to be used to filter out Hermite–Gaussian mode with different orders. As such, we also have to consider the resonant frequency of the higher order mode and make sure that they do not coincide with the mode of our interest.

07 December 2024 17:52:47

B.2.2 Transverse mode

In addition to the longitudinal mode, we have to consider the shape of the beam that an optical cavity can support. In principle, this is determined by the beam parameter. If we consider a single point in an optical cavity and consider a round-trip propagation inside the cavity where the ABCD matrix is $\left(\begin{smallmatrix} A & B \\ C & D \end{smallmatrix}\right)$, then the beam parameter must return to the initial beam parameter for that mode to be resonant to the optical cavity. For any other modes that the beam parameters do not return to the initial beam parameter, the beam parameters will keep changing and the resonance will not occur. This condition can be written down as

$$q = \frac{Aq + B}{Cq + D}. \tag{B.23}$$

In the case where our cavity has symmetry and it is obvious where the beam waist should be, if we start from the beam waist, we have

$$-iz_0 = \frac{-iAz_0 + B}{-iCz_0 + D}, \tag{B.24}$$

which gives the Rayleigh range

$$z_0 = \sqrt{-\frac{BD}{AC}}. \tag{B.25}$$

Therefore, from the shape of the cavity (hence its ABCD matrix), we can calculate and find the beam parameter that is supported by the cavity. Note that not all configurations and parameters of the optical cavity have the solution to z_0 and calculations of the dependence of the beam parameter to the parameters of the cavity gives us the idea of the precisions of each parameter of the cavity (such as cavity lengths) should be. In the actual experiment, when we build a cavity and try to couple the light to it, we need to tailor the beam parameter of the light to match the transverse mode of the cavity as well.

B.2.3 Locking optical cavity

When we build an optical cavity, the resonant frequency of the cavity depends on the length of the cavity, which has to be precise in the sub-wavelength order. On the other hand, we can also build a very stable cavity and use it as a frequency reference for our laser. In any case, we need a methodology to control the relation between the frequency of the light source and the resonant frequency of the cavity. This process is usually referred to as locking.

One might naively think that we can look at the transmitted power of the cavity and lock the cavity so that the transmitted power is maximum. This is, however, not a good approach as the transmitted power is symmetric to the change of the length of the cavity. In other words, the transmitted power always decreases when the length of the cavity shifts from the resonance, regardless of whether the length becomes too short or too long. Therefore, we need to generate an error signal that can differentiate the changes in the length of the cavity. Here, we introduce two methods: the Pound–Drever–Hall (PDH) method (Drever *et al.*, 1983; and Black, 2001) and the tilt locking method (Shaddock *et al.*, 1999).

07 December 2024 17:52:47

B.2.3.1 Pound–Drever–Hall method

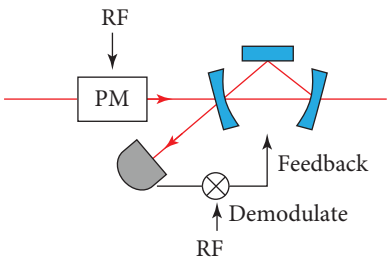

FIG. B.3
Schematic diagram of the PDH method where the light which is phase modulated is reflected of the cavity and the modulated signal is used to stabilize the cavity (or equivalently the frequency of the laser).

Figure B.3 shows the schematic diagram of the PDH method. In this method, we inject a laser light that is subjected to the phase modulation in to the optical cavity. If we let the carrier angular frequency be Ω and the modulating angular frequency be $\omega_{\rm mod}$, the modulated electric field is

$$E_{\rm mod}(t) = E_{\rm mod}\exp[-i\Omega t + i\beta\sin\omega_{\rm mod}t], \tag{B.26}$$

where β is the strength of the phase modulation. We can expand this using the Bessel function as

$$E_{\rm mod}(t) = E_{\rm mod}\sum_{n=-\infty}^{\infty} J_n(\beta)\exp[-i(\Omega - n\omega_{\rm mod})t], \tag{B.27}$$

with $J_n(\,\cdot\,)$ being a Bessel function of the order n. We observe that the phase modulation corresponds to the linear combination of various sideband components $\Omega \pm n\omega_{\rm mod}$ whose amplitudes are determined by β. For our purpose, we consider only the frequency component Ω and $\Omega \pm \omega_{\rm mod}$, meaning that

$$\begin{aligned} E_{\rm mod}(t) \approx{}& E_{\rm mod}\exp(-i\Omega t) \\ &\times [J_0(\beta) + J_1(\beta)\exp(i\omega_{\rm mod}t) + J_{-1}(\beta)\exp(-i\omega_{\rm mod}t)]. \end{aligned} \tag{B.28}$$

To generate the error signal, we look that the light reflected from the cavity. To simplify the equation, let us suppose that $R_1 = R_2$ and there are no losses in the cavity. Then, the coefficient of the reflected electrical field $r(\omega)$ in Eq. (B.12) can be written as

$$r(\omega) = \sqrt{R}\frac{-1 + \exp(i\theta_\omega)}{1 - R\exp(i\theta_\omega)}, \tag{B.29}$$

where θ_ω is a phase accumulated during the round-trip of the cavity. Note that although we do not explicitly write it down, θ_ω also depends on the length of the cavity as well. Therefore, the total reflected electric field E_r becomes

$$\begin{aligned} E_r = {}& E_{\rm mod}\exp(-i\Omega t)[r(\Omega)J_0(\beta) + r(\Omega - \omega_{\rm mod})J_1(\beta)\exp(i\omega_{\rm mod}t) \\ &+ r(\Omega + \omega_{\rm mod})J_{-1}(\beta)\exp(-i\omega_{\rm mod}t). \end{aligned} \tag{B.30}$$

The intensity of the electric field is then measured by the detector. As we are interested only in the signals that oscillate with the frequency $\omega_{\rm mod}$, such an output signal is given by

$$I_{\omega_{\rm mod}} \propto \Re[K(\Omega)]\cos\omega_{\rm mod}t + \Im[K(\Omega)]\sin\omega_{\rm mod}t, \tag{B.31}$$

where

$$K(\Omega) = r(\Omega)r^*(\Omega - \omega_{\rm mod}) - r^*(\Omega)r(\Omega + \omega_{\rm mod}), \tag{B.32}$$

07 December 2024 17:52:47

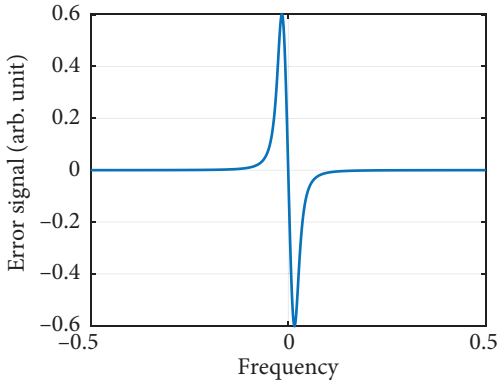

FIG. B.4
An example of the error signal for the PDH method where we use $R = 0.9$ and the demodulation frequency is the frequency corresponding to the half-width half-maximum. The x axis is normalized by the FSR of the cavity.

and we used the fact that $J_{-1}(\beta) = -J_1(\beta)$. We observe that $K(-\Omega) = -K(\Omega)$. Therefore, if we consider the region at the resonant, then we find that the amplitude of both sine and cosine parts of $I_{\omega_{\text{mod}}}$ are antisymmetric with respect to the resonant frequency. We can obtain this amplitude by doing the demodulation, and this amplitude can be used as an error signal to stabilize the laser (or equivalently, the cavity). Figure B.4 shows an example of the error signal by the PDH method.

B.2.3.2 Tilt locking method

Another locking method that is usually used is called the tilt locking method. In this method, instead of using phase modulation to generate sideband components to act as a phase reference, a high-order Hermite–Gaussian mode is used as a phase reference. Figure B.5 shows a schematic idea of the tilt-locking method. When considering the reflection from the cavity near the resonance of the Gaussian beam (TEM_{00}) and when the frequency of the beam slightly changes, the phase of the reflected beam will also change. However, in most of the situations, we cannot detect this phase without other phase reference. On the other hand, the mode TEM_{10} will be nonresonant at the resonance of TEM_{00} and can be used as a phase reference. To detect the change in the phase (frequency) of the mode TEM_{00}, a bi-cell photodiode is used and the difference between the intensity of the incident lights on each cell is the error signal that can be used to stabilize the frequency (or equivalently, the cavity length).

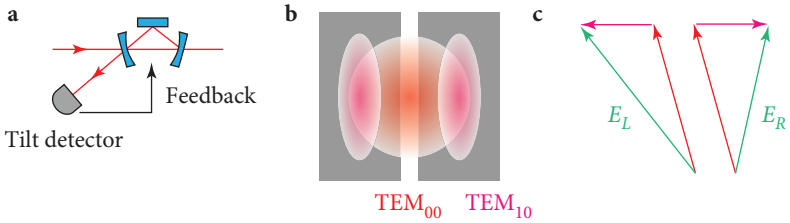

FIG. B.5
Schematic diagram of tilt locking. (a) A reflected light from the cavity enters the tilt locking detector. (b) Interference of TEM_{00} and TEM_{10} on a bi-cell photodiode. (c) Differences between the electric fields of each cell when the cavity length is slightly shifted from the resonance.

07 December 2024 17:52:47

The readers might wonder how can we make the TEM_{10} mode required in the tilt locking. This can be easily done by misaligning the TEM_{00} mode. When we misalign (for example, by changing the angle of a mirror) the beam, although the new beam is simply a Gaussian beam that is reflected in another direction if we expand the beam around the original axis, this is the same as having additional high-order modes. For example, if we slightly shift the beam in xy-plane by an angle $\delta\theta$, then the parameters are transformed as $x \to x + \delta\theta z$ and $z \to z - \delta\theta x$, meaning that the exponential term of Eq. (B.5) becomes

$$\exp\left[-\frac{x^2+y^2}{w^2(z)}\right] \sim \left(1 - 2\frac{x\delta\theta z}{\omega^2(z)}\right)\exp\left[-\frac{x^2+y^2}{w^2(z)}\right], \tag{B.33}$$

which has a first-order term in x as expected of the TEM_{10} mode. Note, however, that this misalignment also gives an additional phase term due to the second exponential in Eq. (B.5). Therefore, to achieve a situation depicted in Fig. B.5(c), an appropriate alignment is required.

B.3 PHASE LOCKING OF THE INTERFEROMETER

Interferometer is the most common component of quantum optics experiments. When we interfere with two beams or modes, the relative phase between them plays an important role and this must be controlled and stabilized. As directly measuring the quantum states of lights and using themeasurement results to stabilize the phases in the interferometer are not experimentally easy, the most common method to stabilize the phase is via injections of the classical phase reference beams. The reason that this method works is that the phases that are accumulated by the classical phase reference beams are the same as that of the quantum states when their spatial modes are the same.

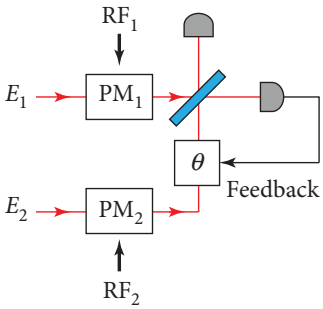

FIG. B.6
General scheme for locking the relative phase (θ) at a beamsplitter. The error signal is the interference signal (or its demodulation) of the signal at one of the output ports. In the actual system, as quantum states are susceptible to losses, we use a mirror to tap only a small portion of light (which is not shown here).

Figure B.6 shows a schematic of the methodology to stabilize the relative phase at a beamsplitter and we will discuss these methods in detail.

B.3.1 Phase locking with carrier interferences

First, let us assume that there are no phase modulations on both beams. Then, the resultant electric field at one of the outputs of the beamsplitter becomes

$$E_{\mathrm{out}} = e^{-i\Omega t}\left[\sqrt{R}E_1 + \sqrt{T}E_2 e^{i\theta}\right], \tag{B.34}$$

where θ is the relative phase we want to lock and we assume that E_1 and E_2 are real. If we tap a small portion of this light by using a highly reflective mirror and measure it using a photodetector, we have the output signal

$$I \propto R|E_1|^2 + T|E_2|^2 + 2\sqrt{RT}E_1E_2\cos\theta. \tag{B.35}$$

07 December 2024 17:52:47

Therefore, if we remove the DC component, we will obtain an error signal that is proportional to $\cos\theta$. This signal is appropriate for locking at $\theta = \pm\pi/2$ as the cosine function is sensitive to the change in θ around that point.

One of the experimental drawbacks of this method is that it required that we remove the DC offset in Eq. (B.35). This DC offset depends on the power of each phase reference beam, which means that the fluctuations in their power become the fluctuations in the phase locking.

B.3.2 Phase locking with phase modulations

In addition to locking the phase at $\theta = \pm\pi/2$, we would also want to lock the phase at other θ such as $\theta = 0, \pi$, which corresponds to the case where the two beams are parallel (or anti-parallel). To do this, let us include the phase modulations of angular frequencies ω_1 and ω_2 on each beam and calculate the resultant electric field,

$$E_{\text{out}} = e^{-i\Omega t}\big[\sqrt{R}E_1\big(1 + J_1(\beta_1)e^{i\omega_1 t} - J_1(\beta_1)e^{-i\omega_1 t}\big) + \sqrt{T}E_2 e^{i\theta}\big(1 + J_1(\beta_2)e^{i\omega_2 t} - J_1(\beta_2)e^{-i\omega_2 t}\big)\big]. \tag{B.36}$$

Similarly, we tap some of the beam and measure the intensity using a photodetector, which result in the signal

$$I \propto I_{\text{DC}} + I_{\omega_1} + I_{\omega_2} + I_{\omega_1-\omega_2} + I_{\omega_1+\omega_2} + I_{2\omega_1} + I_{2\omega_2}, \tag{B.37}$$

where each part is given by

$$I_{\text{DC}} = R[1 + 2J_1^2(\beta_1)]|E_1|^2 + T[1 + 2J_1^2(\beta_2)]|E_2|^2 + 2\sqrt{RT}E_1E_2\cos\theta, \tag{B.38}$$

$$I_{\omega_1} = 4\sqrt{RT}J_1(\beta_1)E_1E_2\sin\theta\sin\omega_1 t, \tag{B.39}$$

$$I_{\omega_2} = -4\sqrt{RT}J_1(\beta_2)E_1E_2\sin\theta\sin\omega_2 t, \tag{B.40}$$

$$I_{\omega_1-\omega_2} = 4\sqrt{RT}J_1(\beta_2)J_2(\beta_2)E_1E_2\cos\theta\cos[(\omega_1-\omega_2)t], \tag{B.41}$$

$$I_{\omega_1+\omega_2} = -4\sqrt{RT}J_1(\beta_2)J_2(\beta_2)E_1E_2\cos\theta\cos[(\omega_1+\omega_2)t], \tag{B.42}$$

$$I_{2\omega_1} = -2R|E_1|^2J_1^2(\beta_1)\sin(2\omega_1 t), \tag{B.43}$$

$$I_{2\omega_2} = -2T|E_2|^2J_1^2(\beta_2)\sin(2\omega_2 t). \tag{B.44}$$

We can see that among various terms that oscillate with different frequencies, the amplitudes of the terms that oscillate with frequency ω_1, ω_2, and $\omega_1 \pm \omega_2$ are dependent on θ. First, the terms that oscillate with frequencies ω_1 and ω_2 both are dependent on $\sin\theta$. Therefore, if we can extract the information regarding the amplitude, we can realize an error signal that would allow us to do the phase locking at $\theta = 0, \pi$. This can be achieved by using an electrical mixer and multiplying I_{ω_1} (I_{ω_2}) with $\sin\omega_1 t$ ($\sin\omega_2 t$), which downconverts the signals and lets us extract the $\sin\theta$ part. This process is called demodulation. The ω_1 (or ω_2) component is the interference between phase modulation and the carrier of the two beams.

07 December 2024 17:52:47

On the other hand, the $\omega_1 \pm \omega_2$ component is dependent on $\cos\theta$, which, when we do the demodulation, will allow us to do the phase locking similar to Eq. (B.35). There are, however, two technical differences. First, in the phase locking using the demodulation of the sum and the difference frequency component of I, the lock point does not change with the power fluctuation of the two beams as such fluctuations only change the amplitude of the error signals. Second, as these signals are the results of the interferences between the sideband modes due to the phase modulations, these signals are typically small, as we are considering the modulation amplitude that is sufficiently small so that we have to consider only the first sideband mode.

There are also cases where we want to lock at phase θ that is not the zero points of sine or cosine function. In principle, since we have the signals that are sine and cosine, by combining them at appropriate ratios, we can generate signals for phase locking at arbitrary θ. In this method, the ratio between two signals needs to be adjusted precisely since the lock points are sensitive to the change of this ratio. Moreover, the amplitudes of the original sine and cosine signals must be sufficiently stable as the combining ratio also depends on these amplitudes.

B.4 FEEDFORWARD AND CANCELLATION

Feedforward operations are one of the main components in quantum computation. This is especially the case for the measurement-based quantum computation where the randomness of the measurement outputs is taken care of by the feedforward operations.

It is often the case that the feedforward operations are regarded as simple processes in the theory as they are displacement operations or Pauli operations. From an experimental point of view, however, feedforward operations are experimentally challenging. The main reason for this is that while the measurements of the quantum states result in the classical values, to do the feedforward operations, these classical values need to be converted again to corresponding quantum operations. Interfacing between classical and quantum regimes requires an appropriate technique and calibration.

In the case of the CV optical system, the typical homodyne detectors give the electrical signals whose values are proportional to the quadrature values. The proportional constant depends on various parameters, such as power of the local oscillator, electrical current from the photodiodes, and electrical gains of the circuitry. From these electrical signals, we need to convert them to appropriate displacement operations. The calibration between the electrical signals of the homodyne and the appropriate amount of the displacements can be done using a method called *cancellation*.

Figure B.7 shows a conceptual diagram of cancellation. When we do the measurement and feedforward in the quantum teleportation (or half-teleportation), one of the ways to think about feedforward operation is that it erases the antisqueezing contribution due to the quantum resource whether it is two-mode-squeezed state or just squeezed state. Therefore, by using a classical probe beam with

07 December 2024 17:52:47

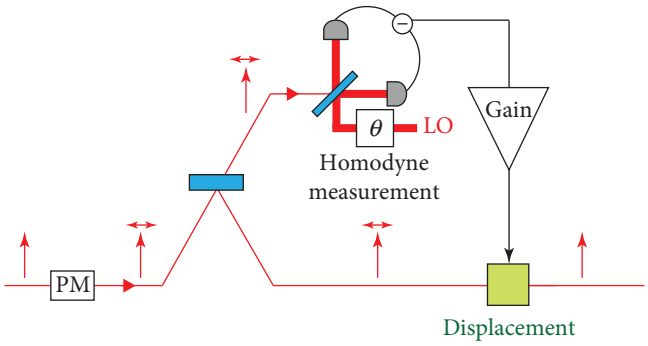

FIG. B.7
Schematic diagram of cancellation method for adjusting feedforward operation. When the electrical gain and timing is correct, we can cancel out the initial phase modulation by using the electrical signal of the homodyne detector. To use the wave packet mode (for example, in the time-domain method), the cancellation must be done on a broad range of frequencies that correspond to the bandwidth of the wave packet.

phase modulation, we can adjust the feedforward gain and the timing so that the phase modulation component is completely erased (which corresponds to erasing the antisqueezing component).

REFERENCES

Black, E. D., "An introduction to Pound–Drever–Hall laser frequency stabilization," Am. J. Phys. **69**(1), 79–87 (2001).

Drever, R. W. P, Hall, J. L., Kowalski, F. V., Hough, J., Ford, G. M., and Munley, A. J., "Laser phase and frequency stabilization using an optical resonator," Appl. Phys. B **31**(2), 97–105 (1983).

Shaddock, D. A., Gray, M. B., and McClelland, D. E., "Frequency locking a laser to an optical cavity by use of spatial mode interference," Opt. Lett. **24**(21), 1499–1501 (1999).

Yariv, A. and Yeh, P., in *Photonics: Optical Electronics in Modern Communications*, The Oxford Series in Electrical and Computer Engineering (Oxford University Press, Inc., 2006).

07 December 2024 17:52:47

07 December 2024 17:52:47

INDEX

$\pi/8$ gate, 2-34, 3-23, 6-13

Annihilation operator, 2-11

Baker–Campbell–Hausdorff formula, A-5
Beam parameter, B-2
Beamsplitter, 2-40, 2-41, 7-3
Bloch sphere, 2-15, A-16
Bloch–Messiah decomposition, 2-38, 3-15, 4-19
Bogoliubov transformation, 2-12, 2-26

Cancellation, B-10
Cat state, 2-31, 5-16
Classical information processing, 1-2
Clifford operation, 2-34, 2-36, 6-5, 6-10
Cluster state, 3-11, 3-15, 4-6, 6-17, 8-2
Coherent state quantum computation, 6-7
Coherent state, 2-22
Commutation relation, 2-13
Continuous variable, 1-4
Controlled-not gate, 2-35
Controlled-Z gate, 2-35, 2-42
Covariance matrix, 3-16
Creation operator, 2-11
Cubic phase gate, 2-43, 3-22, 6-13

Density matrix, 2-3
Discrete variable, 1-3
Displacement operator, 2-23, 2-37
Dynamic squeezing gate, 4-17

EPR state, 2-49, 3-4, 4-14, 4-9, 5-2

Feedforward operation, 3-2, 3-6, 3-12, 3-23, 4-15, 4-18, 7-9, B-10
Finesse, B-4
Fock state, 2-20, 5-6
Four wave mixing, 2-28
Free spectral range (FSR), B-4
Free-space optics, 7-1
Frequency domain, 4-2
Frequency multiplexing, 4-20
Full teleportation, 3-3, 3-9, 4-8
Full-width half-maximum (FWHM), B-4

Gate teleportation, 3-21, 6-13
Gaussian beam, B-1
Gaussian operation, 2-35, 2-37, 2-41, 4-14, 6-11
Gaussian parallelism, 3-13
Gaussian state, 3-14, 3-16, 3-17
Glauber–Sudarshan representation, 2-25
Gottesman–Kitaev–Preskill qubit, 6-5, 6-8, 6-16, 6-17, 6-18, 8-2, A-14
Gottesman–Knill theorem, 2-36
Graphical calculus, 3-16

Hadamard gate, 2-33
Half teleportation, 3-1, 3-8
Heisenberg picture, 2-2
Herald generation, 5-3, 5-7
Hermite–Gaussian mode, B-1
Homodyne measurement, 2-44, 4-2, 4-3, 4-14, 7-9

Inseparability, 2-50
Interferometer, 7-4

Logical qubit, 6-4, 8-1, 8-2
Loop-based quantum computation, 4-16

Macronode, 4-12
Marginal distribution, 2-17

07 December 2024 17:52:47

Measurement-based quantum computation (MBQC), 3-7, 3-18, 4-6, 4-12
Minimum uncertainty state, 2-19
Mode function, 2-10, 4-2, 4-6, 5-9
Mode, 2-10, 5-5
Monochromatic mode, A-3

Non-Clifford gate, 3-23
Non-Clifford operation, 2-34, 2-36, 6-13
Non-Gaussian ancillary state, 3-21, 3-24, 4-15, 5-2
Non-Gaussian measurement, 3-24, 4-18, 5-1
Non-Gaussian operation, 2-36, 2-43, 3-21, 4-14, 4-15, 5-1
Non-Gaussian state, 5-1
Nullifier, 3-14, 4-10

One-dimensional cluster state, 4-8
Optical cavity, B-2
Optical classical computer, 1-6
Optical delay line, 4-10, 4-13, 4-16, 4-18, 7-5
Optical fiber, 7-2
Optical parametric amplifier (OPA), 5-7, 7-8
Optical parametric oscillator (OPO), 2-30, 4-5, 5-7, 7-7, A-7
Overlap formula, 2-17

Partial transpose, 2-52
Passive linear optics, 2-39
Pauli operator, 2-15, 2-33
P-function, 2-25
Phase gate, 2-34
Phase rotation operation, 2-39
Phase shifter, 7-3
Phase shifting operation, 2-39
Phase-insensitive quantum state, 2-19
Phase-locking technique, 3-6, B-8
Photon number resolving detector, 2-45, 8-3
Photon subtraction, 5-16
Physical qubit, 6-4
Pound–Drever–Hall method, B-6
PPT criteria, 2-51
Projective measurement, 2-4
Purity, 2-3, 2-16, 2-17

Quadrature eigenstate, 2-18
Quadrature operator, 2-12, 2-44, 4-2
Quantization of electromagnetic field, 2-9
Quantum computer, 1-1
Quantum entanglement, 2-48, 2-50, 3-12
Quantum error correction, 6-14
Quantum Langevin equation, A-8
Quantum memory, 5-14
Quantum nondemolition, 4-19, 6-14
Quantum state tomography, 5-9, 5-15
Quantum teleportation, 1-7, 1-9, 3-1, 8-1, A-13
Quasiprobability distribution, 2-16
Qubit, 1-3
Qutrit, 6-5

Recovery operation, 6-4

Scalar potential, 2-8
Schrödinger picture, 2-2
Schrödinger's cat state, 2-31
Shear operation, 2-41
Sideband, 4-4
Single-photon source, 7-5
Single-photon state, 5-7
Spontaneous parametric down conversion, 2-28, 5-11, 7-5
Squeezed state, 2-25, 2-26, 3-2, 4-4
Squeezing level, 2-27
Squeezing operator, 2-26, 2-38
Squeezing parameter, 2-26
Superposition state, 5-11
Symplectic matrix, 2-12, 2-37, 3-16

07 December 2024 17:52:47

Symplectic transformation, 2-37, 3-20
Syndrome measurement, 6-4

Tilt locking method, B-7
Time domain, 4-1
Time-domain multiplexing, 3-18, 4-6, 8-2
Two-dimensional cluster state, 4-11
Two-mode squeezed state, 2-49, 3-4, 5-3

Uncertainty principle, 2-6, 2-17
Universality, 2-35, 2-36, 3-20

Vacuum state, 2-18
van Loock–Furusawa criteria, 2-53
Vector potential, 2-8, A-1

Wave equation, 2-8
Wave packet, 3-6, 4-1, 4-17, 5-6
Waveguide, 7-2
Weyl–Heisenberg group, 2-36
Wigner function, 2-16, 2-37, 2-42, 3-5, 3-17, 5-10, 5-19, A-11, A-12

07 December 2024 17:52:47

07 December 2024 17:52:47

This book is a current and rare treatment of the theoretical and experimental aspects of one of the most promising approaches to quantum computation—continuous-variable (CV) quantum computation using optical systems. In addition to its pedagogical value to those new to quantum computing, it is also a practical handbook for both experimentalists and theorists working in the field. ***Optical Quantum Computers: A Route to Practical Continuous Variable Quantum Information Processing*** summarizes many recent experimental developments and fills a gap in current literature.

This timely book:

- Provides up-to-date discussions based on experiments and expertise of the scientists building quantum computers
- Centers around the idea of time-domain quantum computation
- Highlights work by the team from the Furusawa–Yoshikawa Laboratory at The University of Tokyo—one of the leading quantum computing labs in the world

Researchers, graduate students, and those working in the quantum computing industry and its related fields will find this an invaluable resource.

Warit Asavanant, Ph.D., is an Assistant Professor of Applied Physics at The University of Tokyo, Japan. He earned his Ph.D. at the Furusawa–Yoshikawa Laboratory with research topics centering the usage of continuous-variable optical entanglement in quantum computation. He received an award for his outstanding M.S. thesis from the Department of Applied Physics, Graduate School of Engineering, The University of Tokyo.

Akira Furusawa, Ph.D., is a Professor of Applied Physics at The University of Tokyo and a Deputy Director of RIKEN Center for Quantum Computing, Japan. He is a pioneer in quantum teleportation and his research has ensured great progress toward the realization of optical quantum computers using quantum teleportation techniques. He is the recipient of numerous awards, including the Ryogo Kubo Memorial Award in 2006, the JSPS Prize and Japan Academy Medal in 2007, the International Quantum Communication Award in 2008, the Toray Science and Technology Prize in 2014, and the Medal of Honor with Purple Ribbon in 2016.

AIP Publishing

9 780735 424043

Not for resale

07 December 2024 17:52:47